



Durham E-Theses

Controls on the distribution of landslides triggered by the 2008 Wenchuan earthquake, Sichuan Province, China

PARKER, ROBERT,NEVILLE

How to cite:

PARKER, ROBERT,NEVILLE (2010) *Controls on the distribution of landslides triggered by the 2008 Wenchuan earthquake, Sichuan Province, China*, Durham theses, Durham University. Available at Durham E-Theses Online: <http://etheses.dur.ac.uk/365/>

Use policy

The full-text may be used and/or reproduced, and given to third parties in any format or medium, without prior permission or charge, for personal research or study, educational, or not-for-profit purposes provided that:

- a full bibliographic reference is made to the original source
- a [link](#) is made to the metadata record in Durham E-Theses
- the full-text is not changed in any way

The full-text must not be sold in any format or medium without the formal permission of the copyright holders.

Please consult the [full Durham E-Theses policy](#) for further details.

Academic Support Office, Durham University, University Office, Old Elvet, Durham DH1 3HP
e-mail: e-theses.admin@dur.ac.uk Tel: +44 0191 334 6107
<http://etheses.dur.ac.uk>

Controls on the distribution of
landslides triggered by the 2008
Wenchuan earthquake, Sichuan
Province, China

Robert Neville Parker

Institute of Hazard, Risk and Resilience

Department of Geography

University of Durham

Thesis submitted for the degree of Master of Science

Declaration

I confirm that no part of the material presented in this thesis has previously been submitted for a degree in this or any other university. In all cases the work of others, where relevant, has been fully acknowledged.

The copyright of this thesis rests with the author. No quotation from it should be published without prior written consent and information derived from it should be acknowledged.

Robert Parker

University of Durham

Abstract

Landsliding is the dominant mass wasting process in upland areas where the rate of river incision is higher than that of rock weathering of hillslopes. Although progressive erosional processes can provide sufficient conditions for slope failure, the majority of landslides are induced by earthquakes, rainstorms or a combination of these two. Landslides are also one of the most destructive geological processes, being the primary cause of damage and fatalities associated with severe storms and earthquakes in mountainous regions. On 12th May 2008 the magnitude 7.9 Wenchuan earthquake occurred in the Longmen Shan mountain range, on the northwest margin of the Sichuan Basin. Landsliding contributed greatly to the high death toll of over 70,000 and widespread infrastructural damage produced by the earthquake. The event offers an opportunity to both broaden the global database of seismically induced landslides and study the processes involved in earthquake-triggered landsliding, for a large continental thrust event with complex faulting mechanisms and diverse geophysical conditions. To achieve this, the following investigation builds upon recent advances in landslide remote sensing, to develop automated detection algorithms through which landslides can be accurately mapped using a range of satellite data. Using these techniques, a first order, regional landslide inventory map of slope failures triggered by the Wenchuan earthquake is produced, over an area of 12,000km² along the main rupture zone. The production of this dataset demonstrates the application of automated classification techniques for the rapid generation of landslide data, for both geomorphological research and hazard management applications. The data is used to examine the interaction of fault rupture dynamics, topography and geology on landslide failure location, and identify key characteristics of the landslide distribution. Findings of the study demonstrate high levels of landslide occurrence along the entire mapped length of the rupture zone, and an exponential decay in landslide density with distance from the co-seismic surface ruptures. This is superimposed over a marked hanging wall effect, along with clear geological and topographic controls on landslide occurrence. Through generalised linear modelling, peak ground acceleration attenuation patterns, hillslope gradient, relief, local elevation and geology are identified as core controls on the location of landslides. The results of this research shed light on some increasingly recognised

though poorly understood characteristics of seismically induced landslide distributions. The dataset produced contributes to the limited global database of earthquake-triggered landslide inventories, as well producing a widely applicable resource for further study of the Wenchuan earthquake and post-seismic landscape evolution.

Acknowledgements

There are many people to whom I own thanks for the assistance and advice I have received during this study. The role of the three supervisors involved in this project must not be understated; without their vision, guidance and encouragement this thesis would not have been possible. Dr Nick Rosser has been an invaluable source of advice, support and encouragement throughout the project. Like the rest of his students I have immensely valued the time Nick has for people, along with his willingness to discuss thorny concepts and help with technical problems. My sincere thanks also go to Professor Dave Petley for his clear focus and insightful discussions, as well as being prepared to let an overenthusiastic masters student jointly present his invited talk at the *Next generation of earthquake induced landslides conference*. This was an unbelievable opportunity, and I can't thank both Dave and Nick enough for helping it happen. A huge debt of gratitude also goes to Dr Alex Densmore for his enthusiasm, technical help, insightful discussions and willingness to share his intricate understanding of tectonic geomorphology and processes in the Sichuan region. Working with these individuals over the last year has been truly inspiring, and I greatly look forward to our continued work together over the next few years.

Additional thanks also go to members of the wider group of enthusiastic staff and postgraduate researchers at the Institute of Hazard, Risk and Resilience. Dr Patrice Carbonneau has been both an immense source of encouragement and technical advice. Particular thanks are due for his help in planning an award winning conference presentation at the RSPSoc student conference. Thanks also go to Dr Nick Cox for his invaluable help with statistical analysis; to Emma Norman, Peter Schuerch and Brian Cook for the insightful, problem solving discussions we have had over the last year; to Rosanna Schultz for her data contributions; to Harriet for her help, support, patience, understanding, little presents, hugs, smiles and much more; and to many other members of the student community at Durham University, for their support and friendship.

This thesis is also the product of attending numerous presentations by and discussions with delegates of the 2009 *International conference in commemoration of the 10th anniversary of the Chi-Chi earthquake*, entitled *The*

next generation of research on earthquake induced landslides. Therefore, my gratitude also goes to these leading members of the scientific community for their knowledge and insights.

Thanks to my examiners Dr Niels Hovius and Dr Mark Allen for their helpful feedback which added to the quality this thesis and other outputs from this work.

Finally it remains for me to thank my friends and family; they are my greatest inspiration to go out and explore this intriguing world, my most valued guides, roots and wings. I can't put into words what they mean to me, but it is to them that I dedicate this work.

Contents

Declaration		i
Abstract		ii
Acknowledgements		iv
Contents		vi
List of figures		x
List of tables		xv
Chapter 1	Introduction to the study	1
1.1	Context and justification of the thesis	2
1.2	Research aims and objectives	3
1.3	Organisation of the thesis	3
Chapter 2	Landslides: definition, causes and regional scale events	5
2.1	Landslide Definition	6
2.2	Landslide Mechanics	6
2.2.1	Hydrological Triggering of landslides	7
2.2.2	Seismic triggering of landslides	7
2.3	Regional scale landslide events	8
Chapter 3	Landslide inventories: data acquisition and analysis	9
3.1	Introduction to landslide Inventories	10
3.2	Use of remote sensing in landslide inventory mapping	12
3.3	Techniques for landslide inventory data analysis	17
3.4	Previous seismic landslide inventory investigations	18
3.5	Chapter summary	24
Chapter 4	Geophysical background to the Wenchuan earthquake	25
4.1	Tectonics and geology of the Longmen Shan	26
4.1.1	The India-Asia collision	26
4.1.2	Development of the Longmen Shan	29
4.1.3	Tectonic deformation	33
4.1.4	Faults and folding	34
4.1.5	Geological units and rock types	35
4.1.6	Climate	40
4.1.7	Hydrology	40
4.2	The Wenchuan earthquake	41
4.2.1	Coseismic fault ruptures	41
4.2.2	Distributed displacement and deformation	45
4.2.3	Seismic ground motion	50
4.2.4	Aftershocks	54
4.2.5	Summary	54

4.3	Landslides triggered by the Wenchuan earthquake	56
4.3.1	Investigations on the regional distribution of landslides	56
4.3.2	Total magnitude of the landslide impact	57
4.3.3	Key characteristics of the landslide distribution	60
4.3.4	Influence of hillslope gradient	63
4.3.5	Influence of Elevation	63
4.3.6	Influence of lithology	63
4.3.7	Areas of very high landslide concentration	68
4.3.8	Landslide dammed lakes	70
4.3.9	Summary	71
4.4	Chapter summary	72
Chapter 5	Production of a landslide inventory map	73
5.1	Acquisition of imagery for landslide mapping	74
5.2	Available satellite imagery	74
5.2.1	Quickbird and IKONOS	77
5.2.2	ALOS-PRISM	77
5.2.3	SPOT 5	77
5.2.4	EO-1 ALI	78
5.2.5	Landsat 7 ETM+	78
5.2.6	UK-DMC	79
5.2.7	Summary	79
5.3	Landslide mapping methodology	82
5.3.1	Image processing software and coordinate system	82
5.3.2	Temporal control: pre- and post- Wenchuan earthquake landslides	82
5.3.3	Pre-processing enhancements	83
5.3.4	Automated classification of landslides	83
5.3.5	Supervised classification	87
5.3.6	Unsupervised classification	87
5.3.7	Classification filtering	90
5.3.8	Panchromatic band thresholding	94
5.3.9	Exemptions	94
5.3.10	Full map compilation	97
5.3.11	Manual editing	97
5.3.12	Final classification algorithm summary	97
5.4	Validation and evaluation of automated landslide mapping	100
5.4.1	Comparison of classified and manually mapped landslides	100
5.4.2	Comparison of landslide maps derived from different resolution images	107
5.4.3	Image condition limitations	113
5.4.4	Summary	114
5.5	Data format and resampling	115
5.5.1	Matrix grid sampling	116

5.5.2	Non-cumulative and cumulative distributions	117
5.5.3	Discussion	118
Chapter 6	Results: The landslide distribution	122
6.1	Overall landslide inventory map	123
6.2	Data characteristics of the landslide distribution	123
6.3	Landslides relative to geophysical variables	124
6.4	Ground acceleration triggering of slope failures	126
6.4.1	Across-strike pattern of landslide occurrence	127
6.4.2	Along-strike pattern of landslide occurrence	128
6.4.3	Two dimensional spatial variations in landslide occurrence	132
6.5	Landslide occurrence relative to geophysical causes of slope instability	135
6.5.1	Landslide occurrence relative to geological units	135
6.5.2	Landslide occurrence relative to topographic attributes	140
6.5.2.1	Elevation	141
6.5.2.2	Hillslope gradient	141
6.5.2.3	Relative relief	145
6.5.2.4	Local elevation	145
6.5.2.5	Slope curvature	148
6.5.2.6	Aspect	154
6.5.2.7	Upslope contributing area	154
6.5.2.8	Distance from major river channels	157
6.6	Chapter summary	160
Chapter 7	Statistical modelling of landslide occurrence	162
7.1	Data format	163
7.2	Bivariate relationships	163
7.3	Introduction to generalised linear modelling of landslide probability: logistic regression	167
7.4	Landslide probability modelling	168
7.5	Comparison of landslide occurrence and modelled probabilities	170
7.6	Relative significance of predictor variables and logistic model simplification	175
7.7	Probabilistic landslide occurrence for the full rupture zone	182
7.8	Full rupture zone model evaluation and considerations	184
7.9	Chapter summary	184
Chapter 8	Analysis and Discussion	186
8.1	Processes and mechanisms governing the occurrence of earthquake triggered landslides	187
8.2	Seismological triggering parameters	187
8.2.1	Seismic moment release: seismic wave generation	188

8.2.2	Directivity	191
8.2.3	Attenuation of seismic waves	191
8.2.4	Hanging wall effect	191
8.2.5	Attenuation effects with distance from seismic sources	193
8.2.6	Constraining the seismic energy source	194
8.3	Topographic site effects	197
8.3.1	Amplification of ground accelerations at topographic convexities	197
8.3.2	Amplification or damping of ground accelerations due to the incidence angle of seismic waves	200
8.4	Other triggering mechanisms	201
8.5	Topographic and geological landscape characteristics controlling slope stability	202
8.5.1	Hillslope gradient and relative relief	202
8.5.2	Elevation and upslope contributing area	203
8.5.3	Geology	204
8.6	Practical implications for landslide inventory investigations	207
8.6.1	Landslide inventory data generation and format	207
8.6.2	Approaches to landslide inventory analysis	209
8.7	Application of findings	211
8.7.1	Hazard mapping and rapid damage assessment	211
8.7.2	Earthquake dynamics	212
8.7.3	Post-seismic evolution of failures, sedimentation and carbon release	214
Chapter 9	Conclusions	216
Appendix 1		221
Appendix 2		222
References		224

List of figures

Chapter 3

3.1	Landslide density (percentage of total area affected by landsliding) plotted with distance from the projected surface break of the seismogenic fault for the Chi-Chi, Finisterre, and Northridge earthquakes.	22
3.2	Relationship between landslide concentration (%) and ground shaking intensity (Arias intensity) for the Northridge earthquake	23
3.3	Landslide Susceptibility index of geological units for the Northridge earthquake	23

Chapter 4

4.1	Stages of the Indo-Asia Collision	28
4.2	GPS tectonic surface velocities in and around the Tibetan Plateau	28
4.3	Tectonic map of Longmen Shan and Western Sichuan Basin.	31
4.4	Cross-sectional profile of topography from the Sichuan Basin to the Longmen Shan Mountains	31
4.5	Active faults and block boundaries in the Sichuan region	32
4.6	Regional geological map of the Sichuan Basin and the Longmen Shan	39
4.7	Map of Wenchuan earthquake epicentre (USGS) and coseismic fault ruptures	43
4.8	Map of the surface rupture and along-fault variation of scarp height on the Beichuan and Pengguan faults	43
4.9	Geological cross section across the epicentral region of the Wenchuan Earthquake	44
4.10	Along fault profiles of the static slip distribution, derived from the inversion of seismic waves	47
4.11	Map projected static slip distributions for the Wenchuan earthquake	48
4.12	Multi-fault coseismic slip inversion results	49
4.13	Location of strong motion observation stations in the Longmen Shan and surrounding areas	52
4.14	Wenchuan Earthquake Modified Mercalli Intensity shakemaps	53
4.15	Mapped density of aftershock epicentres	55
4.16	Locations of landslides triggered by Wenchuan earthquake	58
4.17	Relationships between earthquake magnitude, area affected by landslides and total number of landslides triggered	59
4.18	Relationship between landslide concentration and distance from coseismic surface rupture	62

4.19	Comparison of landslide concentrations in the hanging wall and footwall	62
4.20	Relationship between landslide concentration and hillslope gradient	65
4.21	Relationship between landslide concentration and elevation	65
4.22	Diagram illustrating the occurrence of river valley landslides	66
4.23	Relationship between landslide concentration and rock type	66
4.24	Locations of 12 landslides investigated in the field study of Wang et al (2009a)	67
4.25	Map showing regions of very high landslide impact	67
4.26	Aerial image of high density of landslides in Doujiangyan-Wenchuan highway region	69
4.27	Locations of landslide dams created by the Wenchuan Earthquake	69

Chapter 5

5.1	Final SPOT5 and E0-1 image coverage used for landslide mapping	81
5.2	Comparison of Landsat 5 (September 2007) and Spot 5 imagery (October 2008), using G, R and NIR bands	85
5.3	Typical spectral signatures of soils, vegetation and water relative to SPOT 5 spectral bands	85
5.4	Typical spectral signatures of soils, vegetation and water relative to E0-1 panchromatic band	86
5.5	Comparison between manual delineation of landslide and supervised classification result	89
5.6	Comparison between manual delineation of landslide and unsupervised classification result	89
5.7	Comparison between manual delineation of landslide and unsupervised classification result combined with slope filter	89
5.8	Image E1 (E0-1) panchromatic band histogram and intensity threshold	96
5.9	Final mapping coverage with areas of excessive cloud or haze, and elevation over 3500m removed.	96
5.10	Landslide classification algorithm summary	99
5.11	Mapping coverage and validation sample areas	101
5.12	Frequency-area distributions for automated and manual mapping results	105
5.13	Relationship between mapped landslide density and original image resolution	105

5.14	Relationship between original image resolution and number of mapped landslide features	106
5.15	Relationship between original image resolution and average mapped object size	106
5.16	S2-E1 and S3-E1 overlap sample areas	111
5.17	Topographic shading on image S2	112
5.18	Wenchuan earthquake landslide map	119
5.19	Matrix sample grids of different resolutions	120
5.20	Kernel-density functions for all sample grid sizes	121
5.21	Cumulative density functions for all sample grids	121

Chapter 6

6.1	Landslide density resampled using 2x2km matrix grid	125
6.2	Cumulative density function for 2x2km grid with non-mountainous areas removed	125
6.3	Across-strike sample grid	129
6.4	Across strike landslide density and mean topographic profile	129
6.5	Exponential decay functions of across-strike landslide density for the hanging wall and footwall	130
6.6	Along-strike sample grid	131
6.7	Along-strike landslide density and coseismic slip measured on the Beichuan, Penguan and Xiayudong faults	131
6.8	Multiple across strike profile, sample grid	133
6.9	Multiple along-strike landslide density profiles, plotted in along-fault projection	134
6.10	2km landslide density matrix grid and map of geological units	137
6.11	Normalised distribution of all areas and landslide areas, sampled by geological units	138
6.12	Landslide density distribution sampled by geological units	138
6.13	Landslide density by geological unit age	139
6.14	Mountain terrain only sample area	139
6.15	Normalised distribution of all areas and landslide areas, sampled by 100m elevation bins	143
6.16	Landslide density distribution sampled by 100m elevation bins	143
6.17	Normalised distribution of all areas and landslide areas, sampled by 1 degree gradient bins	144
6.18	Landslide density distribution sampled by 1 degree gradient bins	144
6.19	Normalised distribution of all areas and landslide areas, sampled by 10m relative relief bins	146

6.20	Landslide density distribution sampled by 10m relative relief bins	146
6.21	Normalised distribution of all areas and landslide areas, sampled by 100m local elevation bins	147
6.22	Landslide density distribution sampled by 100m local elevation bins	147
6.23	Normalised distribution of all areas and landslide areas, sampled by 0.1m^{-1} total curvature bins.	150
6.24	Landslide density distribution sampled by 0.1m^{-1} total curvature bins	150
6.25	Normalised distribution of all areas and landslide areas, sampled by 0.1m^{-1} profile curvature bins	151
6.26	Landslide density distribution sampled by 0.1m^{-1} profile curvature bins	151
6.27	Normalised distribution of all areas and landslide areas, sampled by 0.1m^{-1} plan curvature bins	152
6.28	Landslide density distribution sampled by 0.1m^{-1} plan curvature bins	152
6.29	Normalised distribution of all areas and landslide areas, sampled by 0.1m^{-1} total curvature bins. Graph is limited to curvature values from 1.5 to -1.5	153
6.30	Total curvature Landslide density distribution sampled by 0.1m^{-1} total curvature bins. Graph is limited to curvature values from 1.5 to -1.5	153
6.31	Normalised distribution of all areas and landslide areas, sampled by 10^0 aspect bins	155
6.32	Landslide density distribution sampled by 10^0 aspect bins	155
6.33	Normalised distribution of all areas and landslide areas, sampled by $0.1 \text{Log}10\text{m}^2$ UCA bins	156
6.34	Landslide density distribution sampled by $0.1 \text{Log}10\text{m}^2$ UCA bins	156
6.35	2km landslide density matrix grid, overlain with major river channels	158
6.36	Normalised distribution of all areas and landslide areas, sampled by 100m bins of Euclidean distance from major river channels	159
6.37	Landslide density distribution sampled by 100m bins of Euclidean distance from major river channels	159
Chapter 7		
7.1	Ordered covariance values for landslide binary and predictor variables	166

7.2	Scatter plot of logistic regression predicted landslide probabilities and actual landslide occurrence, smoothed using symmetric nearest neighbour technique	172
7.3	Non-cumulative (kernel density) distribution of landslide and non-landslide observations	173
7.4	Cumulative distribution of landslide and non-landslide observations	173
7.5	Map projected probabilities produced using all predictor variables overlain by mapped landslides	174
7.6	Sequence of model input predictors and resulting pseudo R^2 goodness-of-fit values	180
7.7	Scatter plot comparison of model probabilities produced using all predictors (1) and core predictors (4) logistic regression	180
7.8	Map projected probabilities produced using all predictor variables and core predictor variables	181
7.9	Map of probabilistic landslide occurrence for the full rupture zone of the Wenchuan earthquake	183
 Chapter 8		
8.1	Illustration of seismic moment parameters	190
8.2	Illustration of hanging wall and footwall during thrust fault earthquakes, and their proximity to the coseismic fault rupture	190
8.3	Map of Wenchuan earthquake rupture zone, showing disagreement in the location of the epicentre	196
8.4	Pattern of landslide density with distance from the epicentre within 1km concentric buffers	196
8.5	Spot imagery draped over DEM, showing landslide initiation from ridge crests	199
8.6	Pattern of landslide density by aspect, for the Finisterre, Chi Chi and Northridge earthquakes	199
8.7	Recorded Wenchuan earthquake damage by county	213
8.8	Temporal pattern of suspended sediment levels following the Chi Chi earthquake	213

List of tables

Chapter 3		
3.1	Parameters for air photo interpretation of landslides	14
Chapter 5		
5.1	Sensor systems and attributes of imagery available for remote sensing of Wenchuan earthquake triggered landslides	76
5.2	Attributes of imagery selected for landslide mapping	81
5.3	Summary of slope and geometric filters applied to unsupervised landslide classifications	91
5.4	Results of comparison between manual and automated mapping results	104
5.5	Matrix sample grid coverage attributes as a function of grid size	117
Chapter 6		
6.1	Independent variables and the geophysical processes they represent	126
Chapter 7		
7.1	Data fields used in modelling	164
7.2	Covariance matrix showing r-values for all variables	165
7.3	Logistic regression output for all variables model	169
7.4	Logistic regression output for model using statistically significant coefficients	176
7.5	Relative ranking of predictor variables	178
7.6	Subset of Table 7.2, covariance matrix for FD, G, SL, LCEL and R	179

Chapter 1

Introduction to the study

1.1 Context and justification of this thesis

Landsliding is the dominant mass wasting process in upland areas where the rate of river incision is higher than that of rock weathering of hillslopes (Burbank *et al.* 1996; Hovius *et al.* 1997, 2000; Meunier *et al.* 2008). Landslides are also one of the most destructive geological processes, being the primary cause of damage and fatalities associated with severe storms and earthquakes in mountainous regions (Swiss Re, 2000; Brabb 1993). There is now considerable evidence that the impact of landslides is increasing with time, and that in general these effects are focussed upon mountainous areas in developing countries (Alexander 2005). Data from the International Landslide Centre at Durham University shows by far the greatest death tolls affect poor, marginalised parts of society in Asia, with the majority of landslide-related deaths are caused by sudden, catastrophic first time failures (Petley *et al.* 2005).

Although progressive erosional processes can provide sufficient conditions for slope failure (Kesley 1988), the majority of landslides are induced by earthquakes (e.g., Oldham, 1899; Keefer, 1984, 1994; Harp and Jibson, 1996), rainstorms (Iverson, 2000), or a combination of these two (Dadson *et al.*, 2004). With the advent and development of GIS technologies, the last 30 years have seen increasing interest in the study of event associated landslide distributions, which affect large areas and involve high numbers of slope failures (e.g. Keefer 1984; Harp & Jibson 1996; Galli 2008; Owen 2008; Sato 2007; Khazai & Sitar 2004). Interrogation of landslide inventory databases has led to significant advancements in understanding the processes and mechanisms governing the spatial distribution of landslides. Despite this, the global database available for analysing the distributions and characteristics of earthquake induced landslides remains small, with complete or near-complete inventories for less than 0.1% of events that have occurred worldwide in the past few decades (Keefer 2009). As such, the greatest research need for this field is complete mapping of landslides triggered by many more earthquake events (Keefer 2009). In addition, many elements of earthquake-landslide systems remain poorly understood and constrained. As such, landsliding features as a major element of uncertainty for seismic hazard modelling in mountainous regions (e.g. Paterson *et al.* 2008).

On 12th May 2008, the magnitude 7.9 Wenchuan earthquake occurred along the northeast striking fault system of the Longmen Shan mountain range, on the northwest margin of the Sichuan Basin, southwest China. The earthquake resulted in over 70,000 fatalities, with direct losses to buildings and infrastructure of over US\$150 billion (Paterson *et al.*, 2008) making it China's most damaging seismic event in over 30 years (Yuan *et al.* 2008). The Wenchuan earthquake also represents the largest continent thrust earthquake recorded to date (Hubbard & Shaw 2009), and the majority of the earthquake impact zone is located in the high, steep topography of the Longmen Shan, where large numbers of landslides were triggered. Around 35% of earthquake-related deaths and much of the economic losses sustained in the event have been attributed the direct and indirect impact of these slope failures (Wang *et al.*, 2009; Paterson *et al.* 2008). As such, this event offers a considerable opportunity to both broaden the global database of earthquake induced landslides and build knowledge of a range of components of seismically triggered landslide systems.

1.2 Research aims and objectives

The principal aim of this research is to improve the understanding of controls on the distribution of earthquake-triggered landslides, through an examination of the landslide distribution triggered by the 2008 Wenchuan earthquake. The detailed objectives of the research are:

1. To develop semi-automated image classification algorithms in order to map landslides efficiently using satellite imagery over large areas of terrain
2. To produce an inventory map of landslides triggered by the Wenchuan earthquake
3. To examine spatial relationships between landslide occurrence and geophysical parameters

1.3 Organisation of the thesis

The structure of this thesis reflects a twelve month process of investigation of a contemporary natural disaster, in the immediate wake the event itself. This incorporates building an understanding of the study region, event, and the various

geophysical systems involved in earthquake-triggered landsliding, along with the generation and statistical interrogation of large geospatial databases.

Chapter 2 introduces the physical processes involved in landsliding, along with key concepts and definitions for this study.

Chapter 3 provides a context for this investigation through a review of key literature relating to the study of large scale landslide events.

Chapter 4 describes the study area and Wenchuan earthquake event. The tectonic, geological, topographic, hydrological and climatic conditions of the Longmen Shan are reviewed. Based on literature published up to the time of writing, the structural processes and mechanics of the Wenchuan earthquake are discussed, along with the findings of preliminary investigations into the landslide distribution.

Chapter 5 details the production of the landslide inventory, describing the process from initial acquisition of satellite imagery, through the development of semi-automated classification algorithms for landslide mapping, to compilation and evaluation of the final dataset.

Chapter 6 presents the results generated from the full extent of landslide mapping, relative to seismological, topographic and geological characteristics of the event and study area.

Chapter 7 explores the relative influence of different geophysical parameters on landslide occurrence through generalised linear modelling, which is then applied to estimate landslide occurrence across the full rupture zone of the earthquake.

Chapter 8 provides a further analysis and discussion of the key landslide distribution characteristics, relative to findings from other earthquake-landslide investigations. Broader implications and applications of these findings are then discussed in relation to the fields of hazard management and the geomorphological study of seismic landslide events.

Chapter 9 provides a synthesis of research findings and conclusions.

Chapter 2

Landslides: definition, causes and regional scale events

2.1 Landslide Definition

The term „landslide’ includes a broad range of ground movement types, such as rock falls, shallow translational slides and even debris flows. Due to the great diversity in type and characteristics, many different definitions seeking to unambiguously encapsulate the concept exist. As a general definition, that of Varnes (1958) is often cited:

“The term landslide denotes downward and outward movement of slopeforming materials composed of natural rock, soils, artificial fills, or combination of these materials”.

Additionally, the terms slope movement (Varnes 1978) and mass movement (Brunsden 1984) are also often used interchangeably to refer generally to landslide processes. Due to the broad nature of landslide definitions, the classification systems of Varnes (1978) and Hutchison (1968) are used to categorise different landslide types; though landslide types are not analysed as part of this investigation due to methodological constraints.

2.2 Landslide Mechanics

The stability of hillslopes can be understood in terms of the balance of forces resisting and driving downslope movement. This is often expressed in terms of a factor of safety (F) where:

$$F = \text{sum of resisting forces} \div \text{sum of driving forces}$$

Thus, where $F < 1$, the driving forces exceed resisting forces, and the slope will fail. Where $F > 1$ the slope is more likely to be stable. However, as F approaches 1 the probability of slope failure increases, so that most failures in natural hillslopes occur between $F = 1$ and $F = 1.3$ (Selby 2005). The types of forces involved in landsliding can be conceptualised simply using the infinite slope model (Skempton and De Lory 1957). The model assumes that a mobile slice of material sits on a slope of constant angle and infinite extent, thereby dispensing with the need to consider side and end effects (Selby 2005). Gravitational force acts vertically on the block, pushing it down onto the slope surface. This produces two key stress vectors. Shear stress acts in the downslope direction, while normal stress acts

perpendicular to the direction of slope, generating shear strength at the slip plane which resists downslope movement. Slope failures occur where conditions act to change the balance of these stress and strength properties in the slope, generating high shear stress and/or low shear strength. Most notably, these situations occur during seismic shaking and rainfall events.

2.2.1 Hydrological Triggering of landslides

Rainfall induced landslides rank among the most devastating natural disasters, causing billions of dollars worth of property damage and thousands of deaths every year (Hong *et al.* 2007). Hydrological triggering of landslides occurs through various mechanisms as the increasing water content in hillslope materials acts to produce conditions detrimental to slope stability. Firstly, increases in pore-water pressures at potential slip surfaces create a buoyancy effect which counteracts the normal stress and shear strength holding the material on the hillside (Selby 2005). In addition, decreases in the level of suction (negative pore pressure) due to capillary stresses, reducing the strength of many soils. Increasing the water content also decreases the aggregation of soils, reducing their frictional strength (Yee & Harr 1977). The drag of water particles moving through hillslope materials (seepage pressure) can also act to increase forces in the downslope direction (Teraghi & Peck 1948). In addition to internal processes within the hillslope, undercutting at the base of slopes by river channel erosion acts to destabilise slopes by removing mass at the toe. This mass would otherwise act to resist the downslope movement of the hillslope above (Selby 2005). Hydrological triggering conditions are mainly brought about by heavy rainfall events, though rapid snow or ice melt can have similar effects on hillslopes downstream (e.g. Cardinali *et al.* 2000).

2.2.2 Seismic triggering of landslides

Seismic triggering of landslides has been observed during earthquakes greater than $M = 4.0$ (Keefer 1984). Meunier *et al.* (2008) identify two ways in which earthquakes affect the stability of hillslopes. Firstly, seismic accelerations may cause a loss of cohesion and/or reduction in the frictional strength of substrate, through rockmass shattering or liquefaction (Meunier *et al.* 2008; Brune 2001).

Secondly, seismic accelerations cause short-lived stresses which may exceed the cohesive strength of hillslope materials (Newmark 1965). Either of these effects or a combination of the two may result in slope failure. In mountainous regions the impact of seismic acceleration is intensified as vertically incident seismic waves are diffracted by surface topography causing ground accelerations to be amplified towards ridge crests (e.g., Davis and West, 1973; Geli *et al.*, 1988; Bouchon and Baker, 1996; Meunier *et al.* 2008).

2.3 Regional scale landslide events

An important characteristic shared by both hydrological and seismic triggers is their potential for large spatial impact, producing large numbers of landslides distributed over regional scales. As such these events require an analysis approach which can both capture their regionally distributed impact, as well as providing a means for analysing controls upon both the occurrence and characteristics of large numbers of slope failures. The most commonly applied technique to this end is the use of landslide inventory maps, as discussed in the following section.

Chapter 3

Landslide inventories: data acquisition and analysis

The following section provides a preliminary review of key work with landslide inventories relevant to this investigation. The role of landslide inventories in regional landslide investigations is first discussed, before exploring techniques for landslide inventory data generation, analysis, and key findings from previous investigations into seismically triggered landslide events.

3.1 Introduction to landslide Inventories

A landslide inventory is a database containing information about landslides triggered in a particular event by seismic and/or aseismic triggering mechanisms. Inventories most often express the spatial distribution of the landslides through mapping, as well as attribute information fields on individual landslide features. The wealth of information they contain makes landslide inventories a valuable resource in both the geomorphological investigation of landslide events and hazard assessment in landslide prone regions. As such, compilation and analysis of a landslide inventory forms the basis of this investigation. This section provides an introduction to landslide inventories, their use and analysis.

Early landslide inventories took the form of large datasheets and detailed geomorphological maps compiled through a combination of field surveys, interpretation of aerial images and examination of historical archives (e.g. Carrara and Merenda 1976). However, significant technological advancements have enabled the integration of remotely sensed satellite imagery and digital elevation models, allowing for greater spatial coverage and resolution (e.g. Fruneau *et al.* 1996; Hervas *et al.* 2003; McKean and Roering 2004; Metternicht *et al.* 2005; Farina *et al.* 2006). The development of versatile GIS packages - such as ESRI's ArcGIS/Info - capable of encapsulating large attribute databases, has allowed for information collected and derived in digital databases to be directly integrated with landslide mapping (Hervas and Bobrowsky 2009).

The broad range and sample size of information produced by such databases affords landslide inventories a variety of potential applications, summarised by Galli *et al.* (2009):

1. Showing the location and type of landslides in a region (e.g. Antonini *et al.*, 1993; Cardinali *et al.*, 2001 & Antonini *et al.* 2002)
2. Examining the effects of single landslide triggering events such as earthquakes (e.g. Harp and Jibson, 1995; Owen *et al.*, 2008), intense rainfall events (e.g. Bucknam *et al.*, 2001), or rapid snow melts (e.g. Cardinali *et al.*, 2000).

3. Determining the frequency and area (or volume) statistics of slope failures (e.g. Malamud *et al.*, 2004; Hovius *et al.*, 2000)
4. Providing information for assessing landslide hazards and susceptibility (e.g. Guzzetti *et al.*, 2006; Chung and Fabbri, 2005)

This investigation seeks to utilise landslide inventory analysis for the study of an earthquake-triggered landslide event. However, understanding the natural hazard posed by landslides is inseparably linked to the other applications noted above. For example, frequency/area statistics of a landslide inventory can be used to give an idea of how complete the sample of landslides is, and knowledge of the location and type of landslides is used to gauge proximity to vulnerable populations and the damage potential of failures. Today landslide inventories play a key role in hazard assessments based on the principle of precedence: “landslides will occur where the geo-environmental conditions that led to landsliding in the past will again occur in the future” (Hervas and Bobrowsky 2009:324). Hence, identifying the spatial (and temporal) distribution of conditioning and triggering factors associated with landslide occurrence, is a central tool in attempts to determine the distribution and likelihood of future failures (e.g. Godt *et al.* 2009). In order to exploit the findings of past events to produce useful predictions of future landsliding, well constrained, quantitative relationships between landslide occurrence and relevant geo-environmental variables must be attained. Variables used in landslide inventory analysis vary depending on the nature of the event, and data availability. For the study of seismically and/or hydrologically triggered events, an ideal list of available data fields includes the following:

1. Lithology / Geology
2. Slope gradient
3. Slope curvature
4. Slope aspect
5. Elevation
6. Local slope elevation or relief

7. Distance from the epicentre
8. Distance from roads
9. Distance from river channels
10. Upslope contributing area
11. Pre-event normalised differential vegetation index (NDVI, Paruelo *et al.* 2004)
12. Peak ground acceleration
13. Distance from the co-seismic fault
14. Spatial and temporally distributed precipitation fields

Often all this information is not realistically available due to methodological constraints, and so most landslide inventories only include a subset of the required data (Hervas & Bobrowsky 2009). The application of landslide inventories may be limited by the spatial coverage and resolution of the data, as well as the variety of cartographic errors associated with the data acquisition (Malamud *et al.*, 2004). Unless a multi-temporal inventory is produced (e.g. Galli *et al.* 2008, using a time series of aerial images), a landslide inventory will also lack any temporal component. As such, single event based inventories provide a temporal snap-shot of the hillslope system, within the constraints and limitations of which analysis must be undertaken. This lack of temporal data is a particularly evident limitation when studying post-seismic landslides which may continue to occur for up to decades following a major earthquake (Dadson *et al.*, 2004), and other hillslope systems where temporal components of failure are involved (e.g. Petley *et al.*, 2008). Despite these limitations, numerous studies analysing available attributes in event based landslide inventories have produced valuable contributions towards the understanding of regional controls on landslide occurrence.

3.2 Use of remote sensing in landslide inventory mapping

Before data can be made available for analysis, the need for regional scale, digitised landslide maps affords a major challenge for any landslide inventory

based investigation. The following section examines the data and techniques available to acquire this type of data on the scale of this investigation.

Traditional mapping for landslide inventories has involved the use of air photographs to identify and delineate landslides (e.g. Cardinali 1990). The high level of detail available from these images allows for a cognitive mapping process through the recognition of characteristic landslide features such as tone, contrast, size, shape, shadow, position and direction (Liu *et al.* 2002). Detailed parameters for air photo interpretation of landslides are given in *Table 3.1*. However, the use of aerial photos has several disadvantages (adapted from Borghuis *et al.* 2007):

1. Aerial coverage is often limited, with several images necessary to cover large catchments.
2. Manual delineation of landslides is both time and labour intensive. For example, one study cited by Liu & Woing (1999) required 100 days to identify, delineate and digitise 4000 landslides into a GIS database.
3. Particularly in sub-tropical mountain areas (such as of interest in this study) clouds unavoidably obscure the ground surface.
4. Imagery is expensive to obtain with irregular recurrence intervals.

	Parameter	Likely characteristics	Operator
1	Colour	Brown, dark brown, greenish brown, light brown	Dependent on lithology/geology and may vary spatially within an image
2	Shape	Lenticular, spoon-like, tree-like pattern, rectangular or triangular	Inherent
3	Shadow	Indicates positions of valleys and ridges	Inherent
4	Position	Near ridge, cut-off slope of riverbank, road cut	Dependent of landslide triggering mechanism
5	Direction	Long axis along direction of gravity	Dependent on landslide type/character

Table 3.1: Parameters for air photo interpretation of landslides (After Nichol & Wong, 2005; Liu et al, 2002)

Given that the Wenchuan earthquake has a potential impact zone of over 75,000 km² (based on the analysis of Keefer 1984) in an area of sub-tropical monsoon activity and high levels of cloud cover, these limitations significantly reduce the potential of such methods to produce a representative data sample.

Satellite images offer several advantages over aerial photographs in their broader spatial coverage, regular recurrence interval increasing the potential of capturing cloud free images, and the potential availability of additional spectral information. Indeed it is suggested that techniques using pan-sharpened IKONOS imagery are able to obtain a data quality comparable to 1:10,000 scale aerial photographs (Nichols & Wong, 2005). The availability of satellite images in digital format holds the potential to significantly reduce the work load involved in mapping large numbers of landslides, through automated classification techniques. While few investigations have tested satellite based methods for landslide detection, recent studies are showing increasingly promising results.

A key limitation of past studies appears to be the spatial resolution of satellite imagery. Using 15m pan-sharpened Landsat ETM+, Petley *et al.* (2002) found that image classification failed to detect around 75% of landslides identified in ground mapping. Marcelino *et al.* (2003) also experienced difficulty identifying landslides only a few tens of meters wide using 20m SPOT and 15m Landsat ETM+ imagery. Here the low spatial resolution, low spectral resolution, shadowed slopes and rugged terrain are reportedly key limitations in feature classification (Petley *et al.*, 2002). However, Dadson *et al.* (2004) was able to identify ~20,000 landslides using 20m SPOT imagery following the Chi-Chi earthquake. In agreement with the finding of Petley *et al.* (2002), Dadson *et al.* (2004) state that landslides over 3 x 3 pixels (3600m²) can be mapped accurately. The omission of landslides smaller than this however, may have caused a significant under-estimation of the area disturbed by landsliding. Despite these promising results it is assumed, from the sparse methodology presented, that the mapping method for this study still primarily involved manual delineation.

More recently, Nichol and Wong (2005) have tested and validated a method in which 70% of landslides are mapped through automated change detection of 20m resolution SPOT 5 imagery, with the ability to resolve landslides to a width of 7m.

However, this method relies heavily on the fact that the areas studied undergo little seasonal anthropogenic disturbance (i.e. cultivation) so that temporal change in the image is mostly limited to landslides and subtle natural variations. The availability of the required multi-temporal „before’ and „after’ imagery is also often limited in such studies either by acquisition (cloud or a lack of available imagery per se) or financial constraints (considering a single SPOT image is priced at £2700).

Borghuis *et al.* (2007) appears to provide the most feasible solution to date. Here a combination of automated – supervised and unsupervised – and manual classification techniques, using single, 2.5m (super mode) SPOT 5 images are tested and validated. Findings suggest that, of the automated methods, unsupervised classification is capable of producing the highest aerial concordance when compared to manual mapping. This was achieved through the application of a 32 class, maximum likelihood unsupervised classification. Then, in order to filter out erroneously classified farmland, roads and houses (spectrally similar in SPOT 5 image bands) all slopes of less than 28° were removed from the classification. This fits with both local knowledge of slope thresholds for landsliding, and local planning restrictions prohibiting development on slopes steeper than 28° . However, errors of commission - attributed to roads, riverbeds and bare farmland - are still present in the classification due to the relatively low resolution of the slope model. For instance, roads smaller than 10m or areas close to steep slopes may be resolved at steeper-than-reality gradients by the 40m DEM. In addition, areas of steep slopes may be more broadly under-predicted, as is the general characteristic of DEMs. The unsupervised classification is also shown to produce significantly smaller landslide areas than the manual technique (Borghuis *et al.*, 2007). Here differential pixel values within single landslide features are shown to cause some individual landslides to be classified as multiple features. However, the unsupervised method is also shown to be more suitable in resolving small landslides ($<400\text{m}^2$) which could not be identified by eye.

Despite initial inadequacies in the data produced by satellite imagery when compared to aerial photographs, recent investigations demonstrate that the potential application of satellite imagery in landslide inventory mapping has greatly increased. Studies by Nichol and Wong (2005), Dadson *et al.* (2004) and Borghuis

(2007) demonstrate that a combination of manual and automated classification techniques can now produce useful data through which landslide distributions can be explored. Limitations of resolution and errors of commission and omission must be considered in any analysis of the output.

3.3 Techniques for landslide inventory data analysis

In order to explore relationships between earthquake-triggered landsliding and geo-environmental variables, both qualitative and quantitative analysis techniques may be utilised. Qualitative, expert knowledge based, heuristic methods are useful in providing rapid hazard assessment. However, information attained is highly subjective, it is difficult to draw comparisons between studies by different experts (Barredo *et al.*, 2000) and empirically constrained relationships cannot be attained (Hervas & Bobrowsky 2009). In order to quantitatively explore relationships, statistical analysis of landslide inventories is commonly employed in the form of bivariate and multivariate analysis techniques. A range of statistical tools are used including bivariate regression (e.g. Keefer 2000), multiple regression (e.g. Yin & Yan 1988; Carrara 1983; Garcia-Rodriguez *et al.* 2008), principal component analysis (PCA; e.g. Baeza & Corominas 2001), discriminant analysis (e.g. Carrara 1983) and susceptibility indexing (e.g. Parise and Jibson 2000). Each of these approaches has benefits, depending on the particular objectives of investigation. For example, bivariate regression analysis (e.g. Keefer 2000) allows for the independent consideration of geo-environmental variables, without the need for a priori assumptions of models or relationships (e.g. Keefer 2000; Khazai & Sitar 2003; Parise and Jibson 2000). Multiple regression and PCA approaches allow for the relative influence of numerous variables to be gauged, whilst also accounting for cross-correlation between variables (Hervas & Bobrowsky 2009). Susceptibility indexing has been used to determine the relative influence of different geological units, where geological data are unsuitable for regression analysis (e.g. Parise and Jibson 2000; Wang *et al.* 2007). As, prior to the Wenchuan earthquake, no published investigations had examined controls on earthquake-triggered landsliding in the Sichuan region, little a priori knowledge of relationships or models exists. Therefore the initial, primary focus of this study and the following review is upon bivariate analysis techniques through which the influence of different geo-environmental factors can be independently examined.

3.4 Previous seismic landslide inventory investigations

Results from statistical analysis of inventories from earthquake events have shown general correlation of landslide occurrence with 3 main factors: slope gradient, distance from the earthquake source and surface geology (e.g. Keefer, 1984, 1994, 2000; Wilson & Keefer, 1985; Parise & Jibson 2000). The total number, area and volume of landslides triggered by an earthquake is a function of earthquake magnitude (Keefer 1994; Malamud *et al.* 2004), with minimum magnitude thresholds for landslide occurrence constrained to around $M=4.0$ (Keefer, 1984; Rodriguez *et al.*, 1999).

Within a given event, the spatially distributed concentration of landslides can be expressed as either a function of distance from the epicentre or fault rupture (e.g. Keefer 2000, Meunier *et al.* 2007), or more precisely a function of ground shaking intensity (quantified as peak ground acceleration during the earthquake, or Arias (1970) intensity). Analysis of this factor is carried out through creating distance or intensity bins over the full range of the earthquake impact zone, within which landslide density is statistically examined. Meunier *et al.* (2007) have shown that landslide density (percentage area affected by landslides) from the 1999 Chi-Chi earthquake (Taiwan) can be described by an expression similar to the classical law of seismic wave attenuation. However, the 1994 Northridge and 1993 Finisterre earthquakes have a non-geometric component of landslide density, which is related to peak ground acceleration via an exponential function (Meunier *et al.*, 2007). As such, landslide density for all earthquakes studied demonstrates decay with distance from the seismic source. In addition, for earthquakes on reverse thrust faults, landslide densities are greater on the fault hanging walls than footwalls, as shown in *Figure 3.1*. This is in concordance with higher peak ground accelerations produced in these areas, due to the geometry of the fault plane (Abrahamson and Somerville 1996). While the precise nature of the relationship between landsliding and shaking intensity is not firmly constrained, these findings and others (e.g. Keefer 2000; Wang *et al.* 2007; Meunier *et al.* 2007) show that landslide density is positively correlated with, and can provide a marker for, the regional pattern of peak ground acceleration.

Despite evidence for broad scale correlations between landslide density and ground shaking, Parise & Jibson (2000) have shown that in areas of highest peak ground motion following the 1994 Northridge earthquake, landslide density shows little meaningful correlation to shaking intensity (*Figure 3.2*). They suggested that in areas of highest intensity, all motion intensity thresholds for landslide triggering have been surpassed. Therefore ground motion is no longer the dominant control on landslide occurrence. By comparing the percentage landslide coverage of different geological units, over a 160km² area of highest shaking intensities, a landslide susceptibility index for 13 geological units was created (*Figure 3.3*). This demonstrates the relative influence of rock type upon the landslide distribution, particularly evident in areas where differential ground motion can be virtually discounted. In addition, Jibson *et al.* (1994) has shown how landslide type is strongly controlled by geology through analysis of the 1991 Racha Earthquake, Republic of Georgia. For example, rockfalls in this event are mainly borne of Mesozoic limestone and Jurassic volcanic rocks, and earth slides are borne of plastically deforming claystone. Such findings have a useful application to both understanding geologic controls on landsliding and also zonation of landslide susceptibility for hazard assessment.

While these studies into geological influence present useful tools for both understanding hillslope evolution and undertaking risk assessment, the findings are specific to the particular site geological contexts within which they are set. This is highlighted in an example from Khazai and Sitar (2004) showing that the Chi-Chi earthquake produced 23% of landslides in Quaternary alluvium, while the comparable geological unit in the Northridge (Parise & Jibson 2000) and Loma Prieta (Keefer 2000) events only produced 3% and 4% of landslides respectively. This difference is thought to be an expression of Taiwan's young terrain with rapidly aggrading alluvial deposits (Khazai & Sitar 2004). Percentage areal exposures of Quaternary alluvium for Chi-Chi, Loma Prieta and Northridge are ~40%, 7.5% and 44% respectively for the areas compared by Khazai and Sitar (2004). However, Khazai & Sitar's (2004) analysis is not normalised to account for differential areal exposure or topographic features of different geologies. Despite this, considering the similar geological unit sizes but very different landslide

frequencies for Northridge and Chi-Chi, it is clear that the influence of comparable geologies in different regions should be treated as case specific.

The third major control upon landslide occurrence is slope geometry, in particular slope angle. This factor was also examined in the Northridge, Loma Prieta and Chi-Chi case studies mentioned above. Histograms of landslide frequency plotted by slope angle for the Loma Prieta event suggest that most failures occurred on slopes of around 25° (Keefer, 2000). However, the modal slope value for Northridge is $35-40^{\circ}$ (Parise & Jibson 2000), while Chi-Chi has a modal slope of 45° (Khazai & Sitar 2004). The differential role of slope geometry can be understood in terms of the geometry of the landscape as whole; those regions with steeper distributions of landslide-affected slopes are landscapes with steeper slopes geometries in general. In addition, other indices of slope geometry such as slope curvature and roughness have been shown to influence landslide occurrence (e.g. Lee *et al.* 2008).

Despite the significance of geophysical factors - associated with ground motion, geology and topography – human factors and climatic conditions have also been identified as influencing landslide occurrence. Keefer (1984), Owen *et al.* (1996), and Barnard *et al.* (2001) have suggested that human modification of the landscape through road construction is one of the most fundamental factors in the initiation of landsliding in tectonically active regions. This is supported by evidence from Owen *et al.* (2008) showing that landsliding triggered by the 8th October 2005 Kashmir earthquake was most common along roads traversing slope gradients in excess of 50° . Probably due to constraints in quantitatively coding information on anthropogenic landscape modification, little attempt has yet been made to examine the relative influence of this compared to other causal factors.

Another factor often difficult to resolve within seismic landslide inventory investigations is rainfall and its temporally dependent control on post-seismic landslide triggering. While the Chi-Chi earthquake-triggered widespread co-seismic failures, Lin *et al.* (2008) have shown that in the 5 years following the earthquake the catchment wide landslide rate remained 13 times higher than the pre-earthquake rate, and with an average landslide size even larger than for co-seismic failures. Propensity of hillslopes to fail during meteorological triggering

events (e.g. Typhoon Mindulle) was greatly increased in the post-earthquake period. Lin's analysis is clear concerning the implications of this: "*the true impact of the earthquake is reflected in post-seismic landslide statistics*" (2008: 1361). This poses a dilemma for this investigation and others which seek to assess the impact of earthquake-triggered landslides within a 1 year timescale following the event. Landslide inventories compiled during the early stages after an earthquake must be considered within their temporally limited context. However, Lin *et al.* (2008) also noted that post-seismic landsliding in Taiwan closely tracked the distribution of co-seismic landslides. Thus, inventory compilation at this stage offers a potentially useful tool in producing first order estimates of future landsliding during the post-earthquake period.

While it is useful to study the influence of factors in isolation, several investigations have demonstrated the importance of interconnectivity and cross-correlation between variables. Wang *et al.* (2007) have shown how the steepness of slopes within which landslides occur is controlled by surface geology. The role of landscape geometry in the attenuation and amplification of seismic waves has also been demonstrated (e.g. Sepulveda *et al.*, 2005; Meunier *et al.*, 2008). By undertaking multivariate analysis techniques, both cross-correlation between geophysical variables, and their relative influence on landslide occurrence can be examined (e.g. Carrara 1983; Santacana *et al.* 2003). Through this analysis, improved conceptual, statistical and deterministic models describing the multivariate nature of landslide occurrence may be achieved.

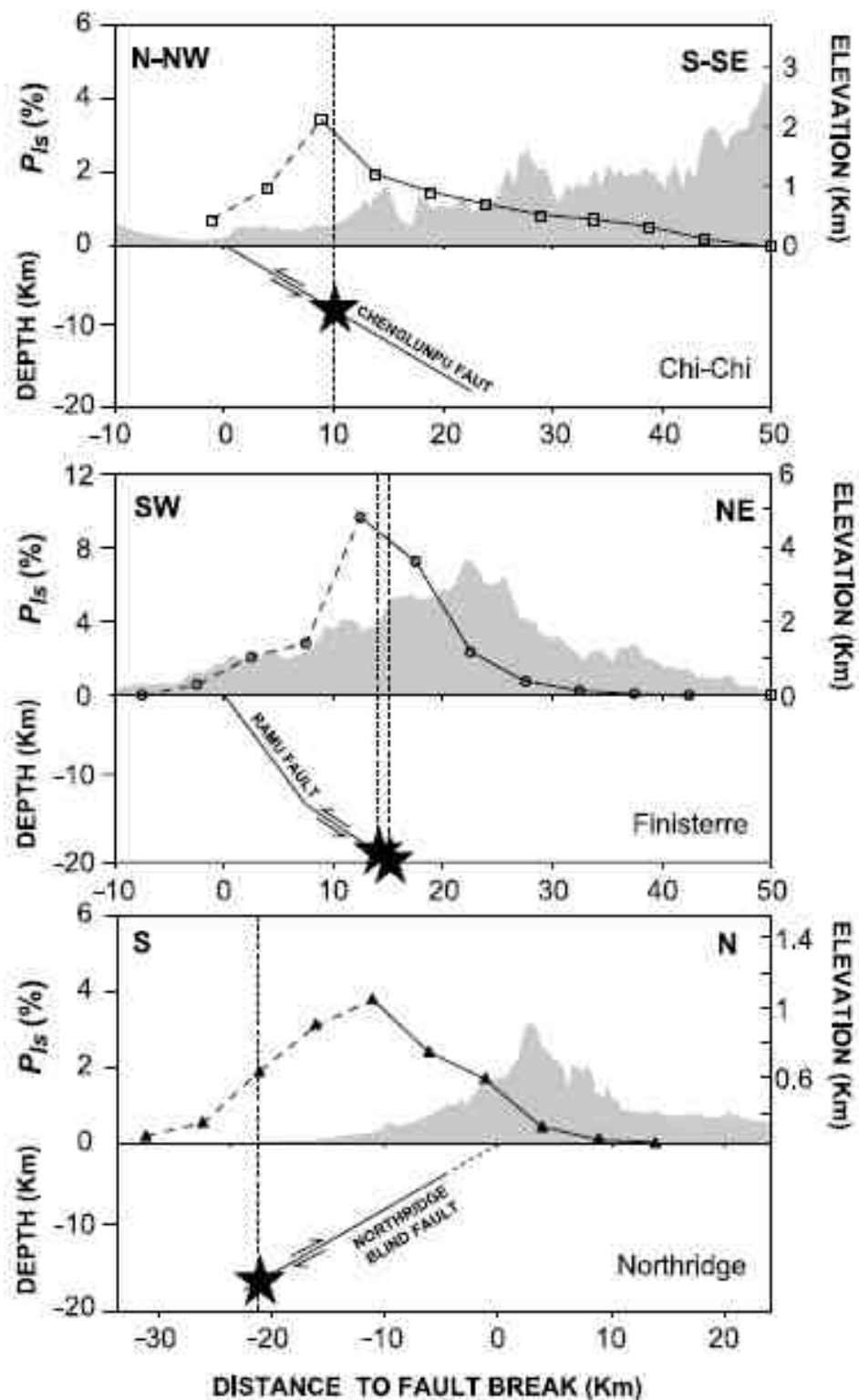


Figure 3.1: Landslide density (percentage of total area affected by landsliding) plotted with distance from the projected surface break of the seismogenic fault for the Chi-Chi, Finisterre, and Northridge earthquakes. Topographic profiles across the epicentre, perpendicular to the fault are shown in grey. (Meunier & Hovius 2007). Note the decay in landslide density with distance from the fault, and marked hanging wall and footwall effects for the Finisterre and Northridge earthquakes.

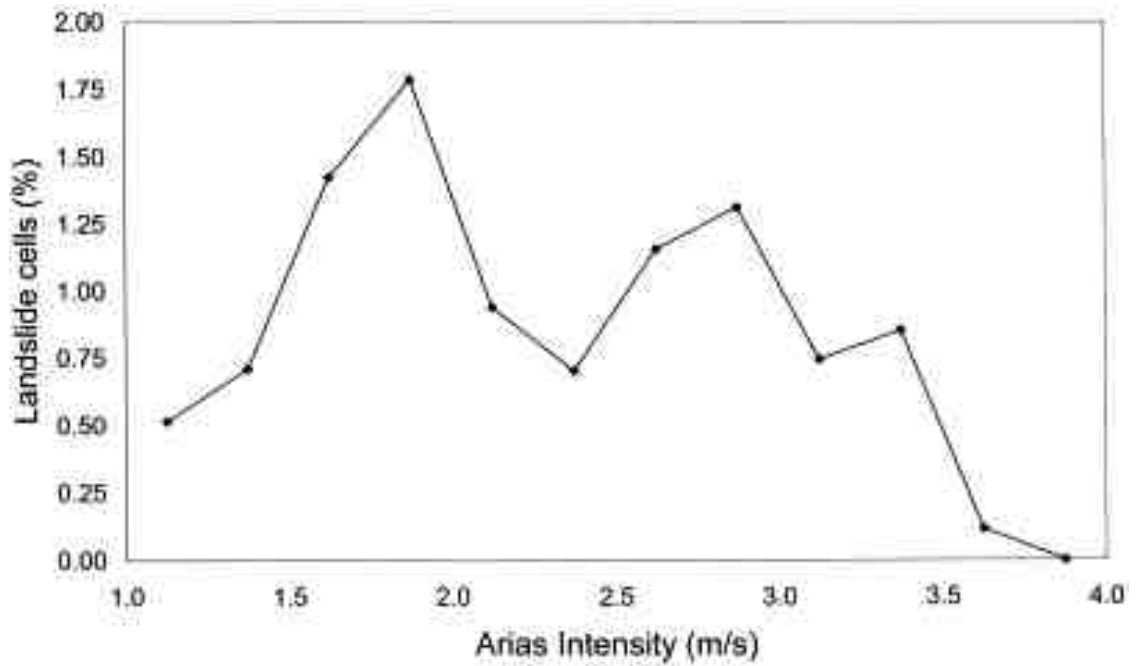


Figure 3.2: Relationship between landslide concentration (%) and ground shaking intensity (Arias intensity) for the Northridge earthquake, showing little correlation due to the overriding influence of variable geological susceptibility to landsliding (Parise & Jibson, 2000).

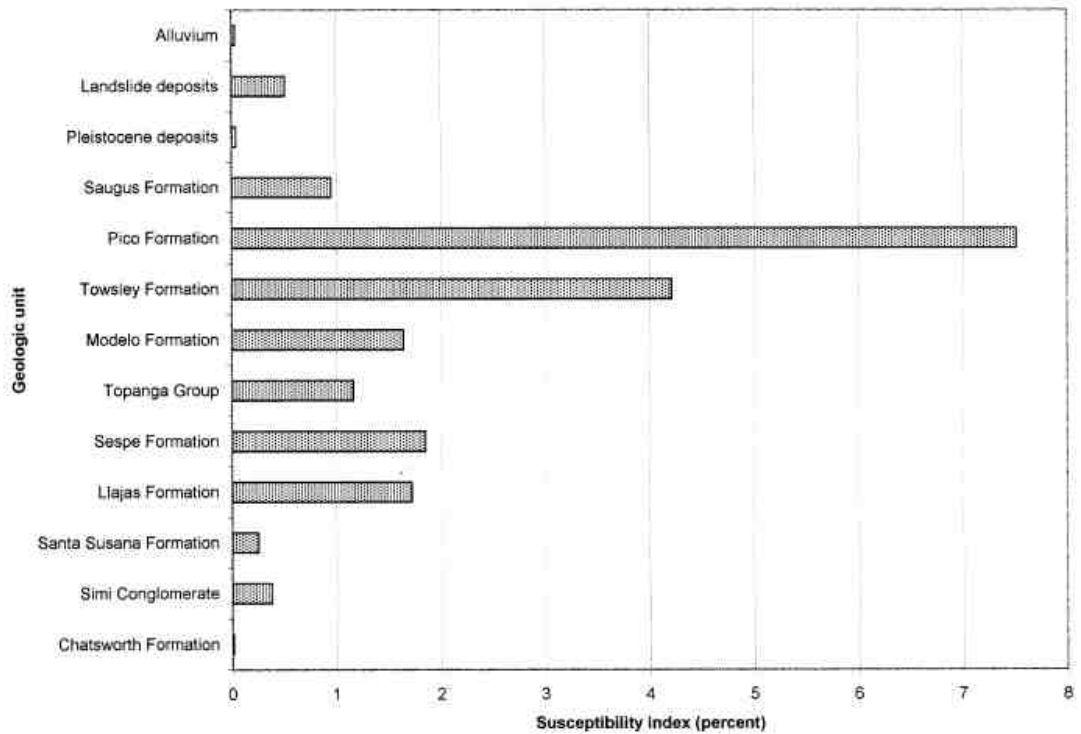


Figure 3.3: Landslide Susceptibility index of geological units for the Northridge earthquake (Parise & Jibson, 2000).

3.5 Chapter summary

This chapter has identified the core tools required to carry out this investigation, in terms of data acquisition through semi-automated landslide mapping, and dataset interrogation through bivariate and multivariate analysis of landslide occurrence and geo-physical variables. Key relationships with factors controlling the spatial distribution of seismically induced landslides have been identified. This demonstrates that, where possible, landsliding should be analysed relative to: seismological, topographic, geological and hydrological parameters, as well as features of human development within the landscape. However, it is also apparent that many datasets required for this analysis are commonly unavailable. As such, the following section provides a detailed geophysical background to the Wenchuan earthquake, which affords a basis for analysis of the landslide distribution.

Chapter 4

Geophysical background to the Wenchuan earthquake

The following chapter describes the study area and Wenchuan earthquake event. The tectonic, geological, topographic, hydrological and climatic conditions of the Longmen Shan are reviewed, based on the published literature. The structural processes, mechanics and characteristics of the Wenchuan earthquake are then described, followed by the findings of preliminary investigations into the landslide distribution. Due to the contemporary nature of this event, large amounts of literature were published throughout 2009, and following the completion of this work. Therefore the majority of this review is limited pragmatically to information available up to the time of writing (June 2009); though some more recent works of vital importance, published towards the end of the investigation period, are also referenced.

4.1 Tectonics and geology of the Longmen Shan

The Longmen Shan region forms a boundary area between the high Tibetan Plateau and the low topography of the Sichuan Basin. However, many of the region's topographic, geological and seismic characteristics result from its situation within the continental scale tectonics of the region. The following section describes the tectonic and geological setting of the Longmen Shan, beginning at a broad continental scale, before examining the Longmen Shan Thrust Belt system, its tectonic structures and geological units.

4.1.1 The India-Asia collision

In order to understand the formation, active tectonics and seismicity of the Longmen Shan region, a broader view of the regional tectonic setting is required. This begins with the collision of the Indian subcontinent and mainland Asia. Around the beginning of the Cenozoic era (~66Ma) the Indian subcontinent began to collide with and thrust beneath the Eurasian Plate (Argand, 1928). Since this time India has continued to move northwards relative to the more stable Eurasia by ~22° latitude (2420km) while rotating clockwise by ~21° (Dewey *et al.* 1988), as shown in *Figure 4.1*. A combination of crustal thickening, climatic feedbacks and isostatic rebound produced by this process has created the high topography of the Himalaya and Tibetan Plateau (Dewey *et al.*, 1988).

The main components of the collision process can be summarised in terms of 3 temporal phases (Dewey *et al.*, 1988). The first, 45-30Ma, is characterised by 1000km of convergence along the continental boundary at an average rate of 66mm a⁻¹. During this regime of almost pure thrusting, the Tibetan crust experienced north to south shortening and doubled to a thickness of around 65km. From 30-5Ma crustal shortening continued but was accompanied by little uplift and thickening. Dewey *et al.* (1988) suggested that the most recent phase of major surface uplift (~2km) has occurred from 5Ma to present day. However, more recent investigations suggests that the surface of the Tibetan Plateau may have been in excess of 4km since 35 ± 5Ma (Rowley & Currie 2006). During the second and third phases, lateral displacement of Tibet increasingly took place; a process which continues and is

manifested in both active tectonics and faulting today (e.g. Dewey *et al.*, 1988). While the dominant mechanism of Tibet's eastward displacement is disputed, the process has been shown to occur via a combination of left lateral extrusion and crustal block rotation (Armijo *et al.*, 1986, Armijo *et al.*, 1989, Avouac and Tapponnier, 1993, England and Molnar, 1990). The net result of this process is eastward movement of the upper crust of the Tibetan Plateau relative to Eurasia at rates of $\sim 15\text{-}20\text{mm a}^{-1}$ (Zhang *et al.* 2004), while the Indian subcontinent moves northward at $\sim 50\text{mm a}^{-1}$ relative to Eurasia (Burchfiel *et al.*, 2008) as shown in *Figure 4.2*.

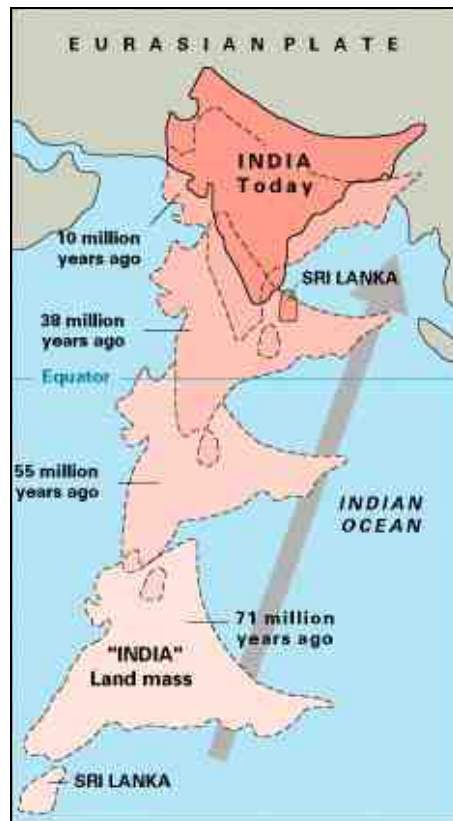


Figure 4.1: Stages of the Indo-Asia Collision. (<http://www.fas.org/irp/imint/docs/rst/Sect2/India.jpg> [last accessed 06/05/09])

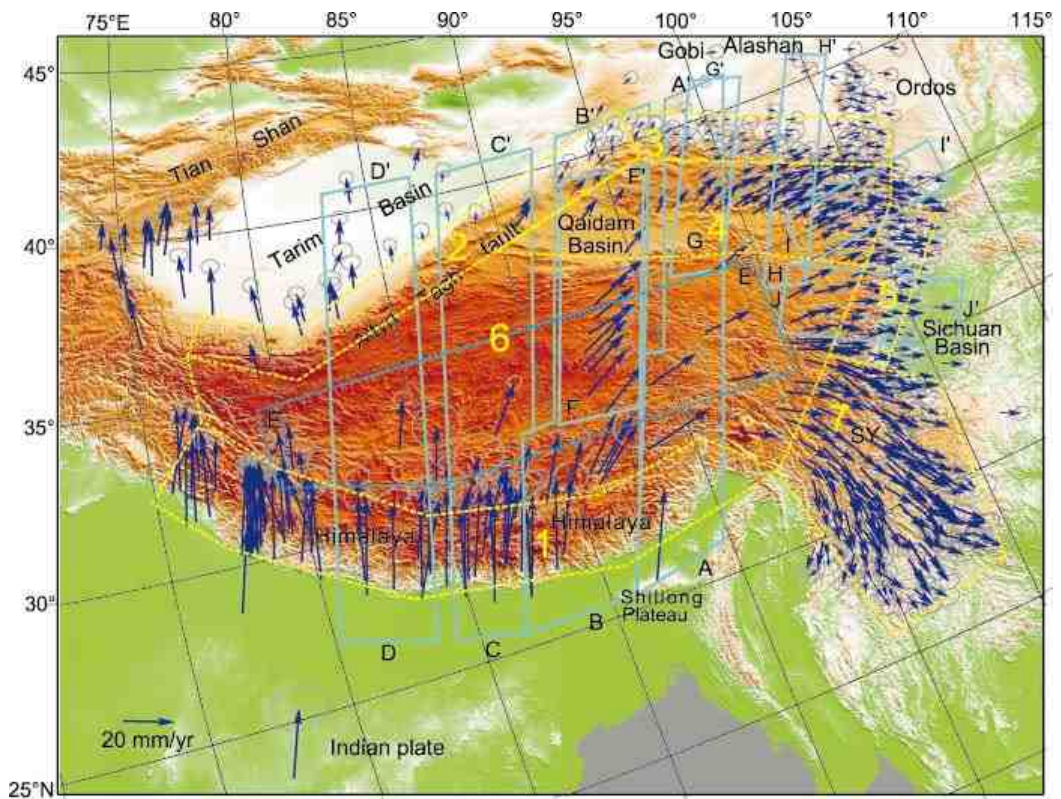


Figure 4.2: GPS tectonic surface velocities in and around the Tibetan Plateau. (Zhang et al 2004). Note large components of eastward displacement.

4.1.2 Development of the Longmen Shan

At its eastern margin the crust of the Tibetan Plateau meets the strong, stable geology of the Yangtze Craton that underlies the Sichuan Basin (Lebedev and Nolet, 2003). Here the high topography of the Longmen Shan thrust belt occurs, adjacent to the Sichuan Basin. It is characterised by elevations of up to 7500m and topographic relief of 5000m within distances of 50km (Densmore *et al.*, 2007; as shown in *Figures 4.3* and *4.4*). The process by which the topography is produced and maintained forms the topic of a contentious debate between two endmember models (Hubbard and Shaw 2009): (1) crustal faulting and shortening, with large amounts of displacement rooted in the lithosphere, causing uplift (Tapponnier *et al.* 2001); lower crustal flow, impeded by the Yangtze Craton, which inflates the crust to the north and east of the Himalayas (Clark and Royden, 2000, Clark *et al.*, 2006; Burchfiel *et al.* 2003; Bird 1991). The modern high topography of the Longmen Shan is likely to have formed between 5 and 12 Ma BP, during the late Cenozoic (Kirby *et al.*, 2002). In addition, this is the steepest margin of the Tibetan Plateau, with deeply incised river valleys, bedrock river channels and local fluvial relief of up to 3000m (Densmore *et al.* 2007). The rapid river incision apparent in the region appears to have initiated between 8 and 15 Ma BP (Clark *et al.*, 2005, Ouimet, 2007).

While the India-Asia collision now plays a dominant role in driving the active uplift of the Longmen Shan, the present mountain range shares the location of a Mesozoic collision zone which formed during the Late Triassic Indosinian Orogeny (230-200Ma) and Late Cretaceous (150-70Ma). The margin originally developed during the closure of the Paleo-Tethys Ocean and collision of the Qiangtang, North China-Kunlun-Qaidam and South China blocks. This major thrust zone was then reactivated during the India-Asia collision (e.g. (Avouac and Tapponnier, 1993, Xu and Kamp, 2000; Li et al 2003; Chen & Wilson 1994).

The Cenozoic elevation driven intensification of the East Asian Monsoon system (Zhisheng *et al.*, 2001) has undoubtedly influenced the topographic character of the Longmen Shan, in a similar fashion to its influence upon the Himalayan belt (e.g. Molnar and England 1990). Enhanced rates of denudation produced by increasing levels of precipitation at the Plateau edge have brought about deeper

valleys and steeper topographic gradients. The resulting isostatic compensation from this process in turn allows higher maximum elevation to develop, contributing to the extremely high relief of the region.

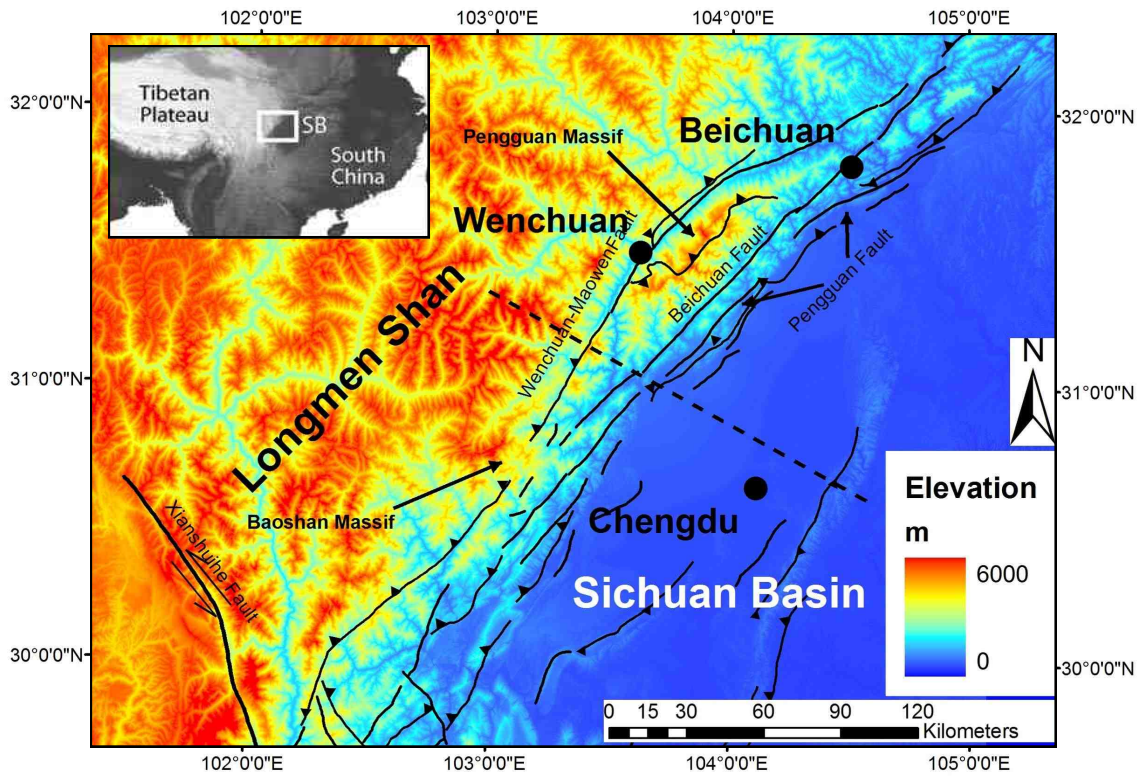


Figure 4.3: Tectonic map of Longmen Shan and Western Sichuan Basin. Topography is taken from 90m resolution SRTM data. Solid black lines are faults mapped by Densmore et al (2007) and Burchfiel et al (1995). Dashed black line indicates cross-section in Figure 4.4

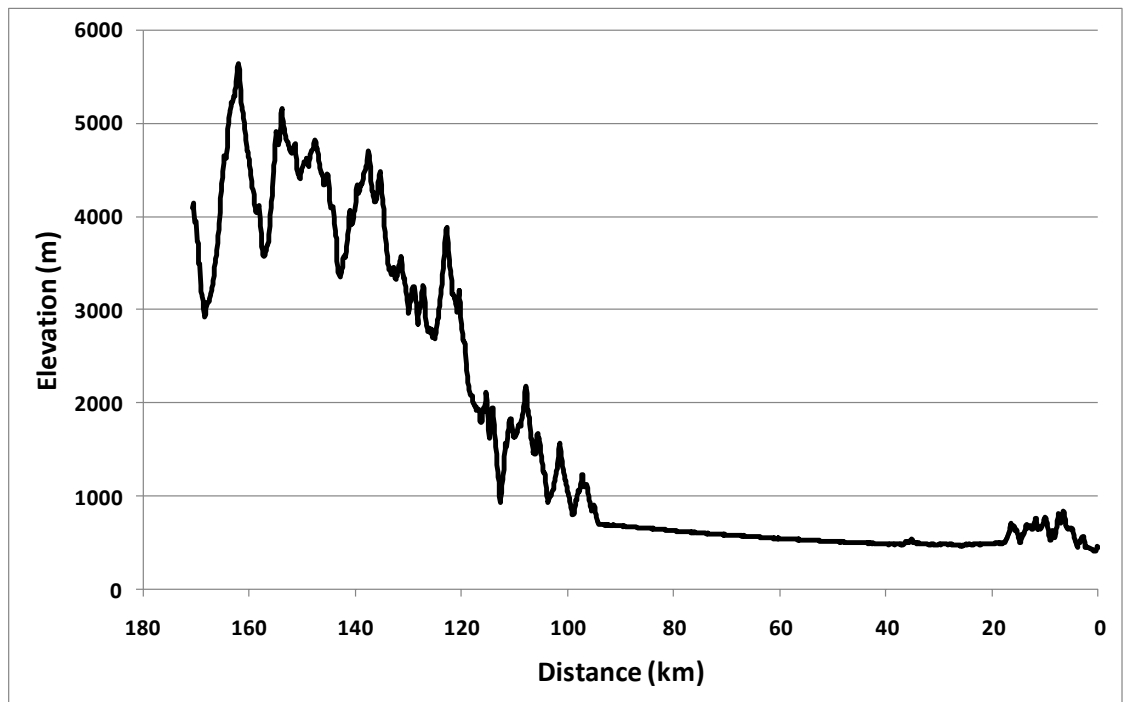


Figure 4.4: Cross-sectional profile of topography from the Sichuan Basin to the Longmen Shan Mountains. Profile trace is shown in Figure 4.3

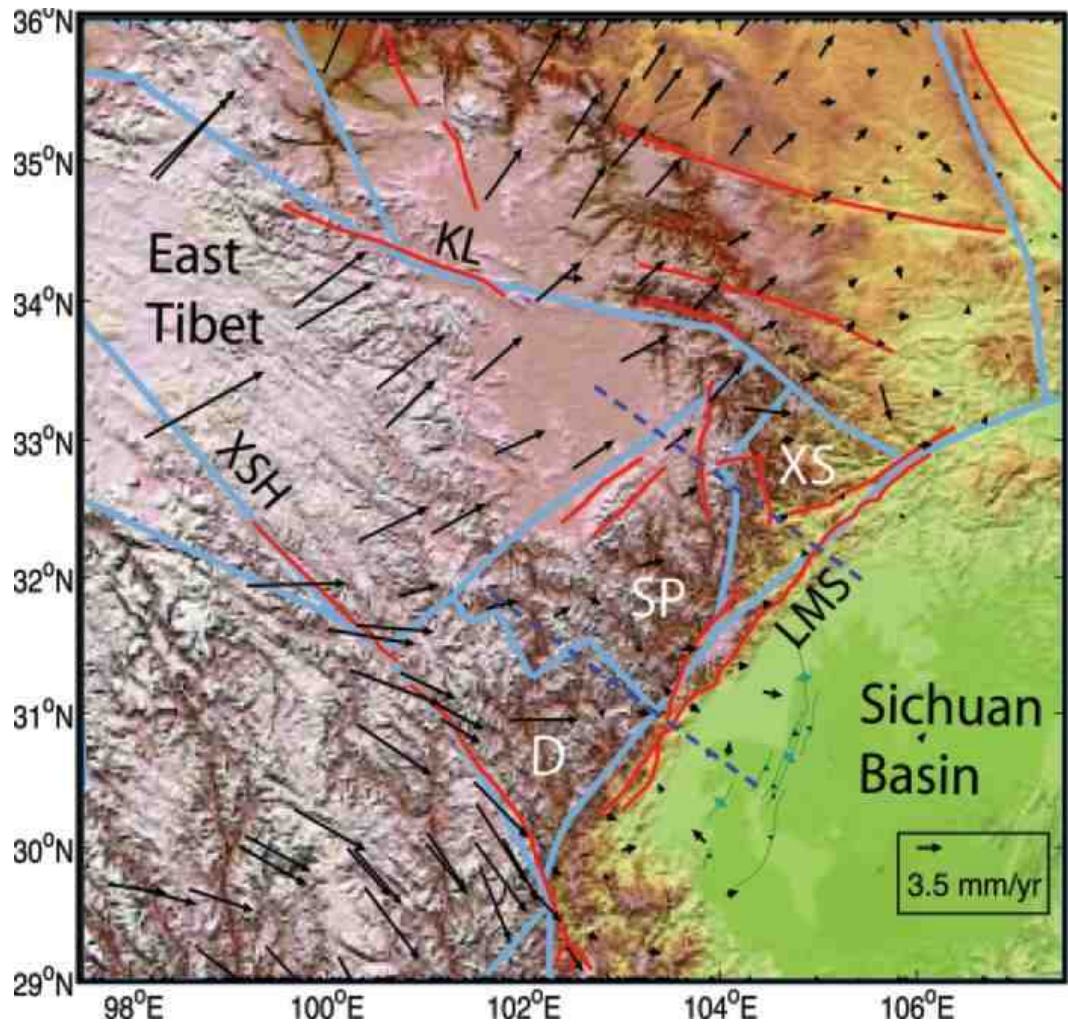


Figure 4.5: Active faults (red) and block boundaries (blue). Blocks: D = Danba; SP = Songpan; XS = Xue Shan. Fault zones: XSH = Xianshuihe fault; KL = Kun Lun fault; LMS = Longmen Shan. Black arrows are observed GPS velocities relative to the South China block. (Burchfiel et al 2008)

4.1.3 Tectonic deformation

Decadal-scale GPS measurements show that the present-day tectonics of the Longmen Shan region is dominated by clockwise rotation of upper crust around the eastern Himalayan syntaxis (*Figure. 4.2*). In the Longmen Shan, this movement is expressed as slow oblique dextral-thrust displacement (*Figure 4.5*). Total deformation rates across the faults in the Longmen Shan are $\sim 2\text{--}4 \text{ mma}^{-1}$ oblique slip, which is compatible with slip rates on individual faults over Late Quaternary time scales (Densmore et al. 2007).

In order to understand how this motion is manifest in displacement of the different tectonic blocks along the Longmen Shan, GPS-derived surface displacements provide a spatially distributed velocity field (e.g. Banerjee and Burgmann, 2002, Chen *et al.*, 2004, Gan *et al.*, 2007, King *et al.*, 1997, Paul *et al.*, 2001, Wang *et al.*, 2001, Zhang *et al.*, 2004, Zhijun *et al.*, 2005). Combining the velocity field of Zhang *et al.* (2004) with the Meade (2007) block model, Burchfiel *et al.* (2008) yielded $\sim 3\text{ mma}^{-1}$ dextral slip and $\sim 2\text{ mma}^{-1}$ convergence along the Longmen Shan boundary, relative to southern China. Furthermore, velocity data in Gan *et al.* (2007), Shen *et al.* (2000), King *et al.* (1997) and Chen *et al.* (2000) have been combined with block geometries, in order to identify 4 blocks making up the Longmen Shan boundary: the Sichuan Basin, Songpan, Xue Shan and Danba blocks (shown in *Figure 4.5*). The Songpan, Xue Shan and Danba blocks all exhibit northwest translation combined with clockwise rotation (Burchfiel et al 2008). The initial Wenchuan earthquake rupture occurred at the southwest end of the Songpan-Sichuan Basin boundary. Along this boundary, Burchfiel *et al.* (2008) estimate local slip to be roughly uniform; $1\pm 1\text{ mma}^{-1}$ dextral slip, combined with a dip-slip of $1\pm 1\text{ mma}^{-1}$ in the southwest increasing to $3\pm 1\text{ mma}^{-1}$ in the northeast (assuming a 45° west-dipping fault). Along the Xue Shan-Sichuan Basin to the northeast, the velocity field suggests subequal dextral slip and dip-slip components of $1\pm 1\text{ mma}^{-1}$, with a slight increase from southeast to northwest. The Songpan and Xue-Shan blocks are separated by the MinJiang fault system. This yields predominantly dip-slip motion of between $2\pm 1\text{ mma}^{-1}$ in the south and $3\pm 1\text{ mma}^{-1}$ in the north, with the Song-pan block thrusting over the Xue Shan block on an assumed 45° west dipping fault. Strike-slip is only observed where this fault intersects the dextral slip Qingchuan fault (Burchfiel *et al.* 2008). The northeast

limit of the Songpan block borders East Tibet. Here the boundary exhibits relatively uniform displacement along its length, of $3\pm 1\text{mm a}^{-1}$ dextral slip and $2\pm 1\text{mm a}^{-1}$ convergence. Limited and unreliable data for the Danba block means that no such velocity estimates can be yielded (Burchfiel *et al.* 2008). However, the Wenchuan earthquake occurred primarily on the Songpan-Xue and Shan-Sichuan Basin boundary fault systems, so the motion of Danba block is of less interest to this study.

4.1.4 Faults and folding

Within the Longmen Shan and Sichuan Basin thrust zone, mapping of many important active faults has been undertaken, though various characteristics of the system are still speculative. The following section provides an overview of known tectonic structures and kinematics of the region.

As discussed above, the boundary between the Longmen Shan and Sichuan Basin is formed by a series of northeast striking faults. These demonstrate components of both thrust and dextral slip (Densmore *et al.* 2007, Chen and Wilson 1996, Chen *et al.* 1994) which are reflected in the slip distribution of the Wenchuan earthquake (see *Section 4.2*). Along the eastern front of the Longmen Shan several thrust faults ramp down into the basement, indicating large displacements on the decollement which underlies this area and reaches around ~80km into the Sichuan Basin (Burchfiel *et al.* 2008). However, offsets in surface sediment strata along these faults suggest small displacements (Burchfiel *et al.* 2008). Burchfiel *et al.* (2008) suggest that is due to the near vertical displacement of lower crustal material in the Longmen Shan, resulting in the surface rate of tectonic movement differing according to depth. However, it should be noted that others argue against a purely vertical, lower crustal flow explanation for the tectonics of the Longmen Shan (e.g. Hubbard & Shaw 2009; Densmore *et al.* 2007).

Much of the Cenozoic crustal shortening and folding appears to be concentrated within the Pengguan and Baoshan massifs, on the basin side of the Longmen Shan (shown in *Figure 4.3*; Burchfiel *et al.* 2008). South of the Pengguan massif, folding of the basement is more widely distributed, resulting in shallower topographic gradients. Steep to vertical faults run southwest to northeast, parallel

to the Longmen Shan for over 100km, and interact with the Cenozoic fold and thrust structures (Burchfiel *et al.* 2008). Within this steep, active fault system, north of the Pengguan Massif these faults offset thrusts within the Mesozoic complex by around 1km, indicating little displacement (Burchfiel *et al.* 2008). West-dipping normal faults, exhibiting dextral slip components, truncate the west sides of the two massifs. These merge with the main boundary faults to the south of the Pengguan massif, where the Wenchuan-Maowen fault is exposed very close to the epicentre of the Wenchuan earthquake. Faults and folds in this area consist of Precambrian basement, Palaeozoic sedimentary strata and Jurassic-Cretaceous foredeep deposits. These are fairly shallow features descend down to the decollement at a maximum depth of around 10km. The Beichuan and Pengguan faults are the more westerly of these, and form the frontal structures of the range (Burchfiel *et al.* 2008). Continuing to the north the Beichuan fault appears to coalesce with the north-eastern reaches of the Wenchuan-Maowen fault, northeast of Beichuan (Densmore *et al.* 2007). Much of the active deformation and seismic activity of the Longmen Shan occurs on the Wenchuan-Maowen, Beichuan, Pengguan and Dayi faults (Li *et al.* 2006; Zhou *et al.* 2007; Densmore *et al.* 2007). Of these the historical activity of the Beichuan fault has been the most apparent, with the Beichuan and Pengguan faults having experienced surface rupture during the late Pleistocene and Holocene periods (Densmore *et al.* 2007).

Around 100km north of Beichuan, the Min Shan and Huya region is also heavily affected by faulting and folding (*Figure 4.5*). This area rises higher than 4000m and is bounded by the Min Jiang fault zone (in the upper reaches of the Min River) to the west, and by the Huya fault zone to the south-east. These zones consist of steep, active, west-dipping faults (Kirby *et al.* 2002), which have experienced two magnitude >7 earthquakes since 1879 (SSB 1989; Jones *et al.* 1984). These faults were not activated by the 2008 earthquake. However, deformation is relayed to the Beichuan fault via the active, east-west trending Xue Shan and Qingchuan faults, where Li *et al.* (2009) report co-seismic deformation from the 2008 earthquake.

4.1.5 Geological units and rock types

Due to the prolonged tectonic activity in the area, the Longmen Shan region comprises a diverse range of geological units. The following section describes the

geographical and lithological characteristics of the major geological units of the Longmen Shan and adjacent mountains affected by the Wenchuan earthquake. As most previous investigations into the geology of the region have focused on orogenesis and regional scale tectonics, information on lithology and hillslope materials – of interest to this investigation – is fairly limited. However, collated information from several of these studies does yield a general overview of recorded rock types within the mapped units. The geological units used in this section and during analysis are chronological units taken from Ma *et al.* (2002) and digitised as GIS shapefiles by Dr Alex Densmore (University of Durham) prior to this investigation (*Figure 4.6*).

1. Mesoproterozoic granitic basement

This is the oldest geological unit occurring within the Wenchuan earthquake rupture zone, where the Mesoproterozoic granitic basement material has been exposed following upward rotation in the thrust belt. Within the rupture zone, the main area of this unit forms a large part of the Pengguan massif, bounded by the Beichuan fault to the southeast and the Wenchuan-Maowen fault to the northwest. The basement is composed of granite, granodiorite, acidic to intermediate volcanics and various schists (Chen and Wilson 1996). Granite and granodiorite within the unit have been dated from 1017-1043 Ma (U-Pb technique) to 647-776 Ma (K-Ar whole rock) (Luo & Long 1992).

2. Neoproterozoic volcanics and dolomite

The Mesoproterozoic Granitic basement is overlain unconformably by Neoproterozoic volcanics and dolomite (Chen and Wilson 1996). These are exposed along the northern perimeter of the Pengguan massif, within the hanging wall of the Beichuan fault.

3. Palaeozoic greywacke, sandstone and shale

Regions of mapped Palaeozoic geology comprise of Cambrian-Silurian greywacke and shale disconformably overlain by Devonian to Permian sandstone and shale, and intercalated with minor limestone and basalt (Chen and Wilson 1996).

4. Mesozoic Granite

To the north-west of the rupture zone, regions of younger granite can be found, here formed by Mesozoic plutons, rather than exhumed basement.

5. *Triassic mudstone, sandstone and conglomerate*

Along the footwall side of the Beichuan fault runs the Upper Triassic Xujiahe formation. This unit is composed of alternating mudstone, sandstone and thick conglomerate, sitting disconformably on Middle Upper Triassics (Chen and Wilson 1996)

6. *Triassic (SG Fold belt) turbidites, acidic volcanic*

To the north-west of the rupture zone, units of Lower, Middle and Upper Triassic turbidites sit in the Songpan-Garze Fold Belt. These are Sinian to Triassic sediments which were folded and metamorphosed during the Indosinian orogeny (c. 227-206Ma BP). In places the sediments are unconformably overlain by the uppermost Triassic Babao Shan Formation, composed of acidic volcanics and clastics (Huang & Chen 1987; Lui *et al.* 1992)

7. *Jurassic conglomerate, sandstone, mudstone*

This unit mainly lies in the footwall of the Pengguan fault and towards lower lying topography at the edge of the Longmen Shan Foreland Basin. Here Jurassic to Lower Cretaceous deposits are composed of thickly layered to massive conglomerate, and alternating sandstone and mudstone beds (Chen & Wilson 1996).

8. *Cretaceous conglomerate*

Also located within and along the edge of the lower lying Longmen Shan Foreland Basin are large regions of Cretaceous conglomerate.

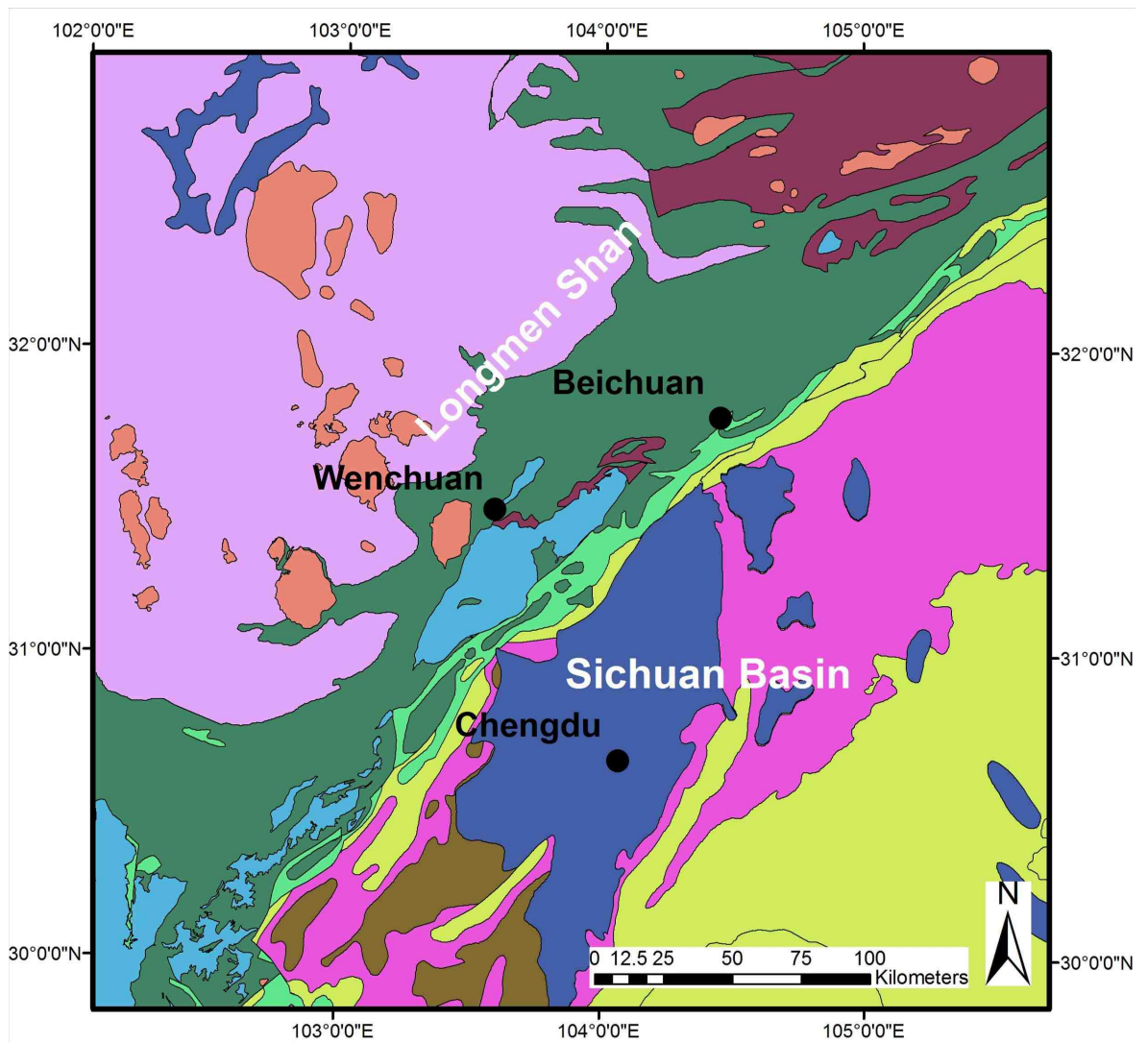
9. *Tertiary conglomerate, sandstone and mudstone*

To the south of the rupture zone, and mainly in low-lying basin areas, occur regions of conglomerate, sandstone and mudstone, interbedded with gypsum and anhydrite. These are of Cretaceous to Neogene age.

10. *Quaternary unconsolidated sediments*

A large region of thin but laterally extensive quaternary sediments lies south of the Pengguan massif, in the Longmen Shan Foreland Basin.

While all of these units fall within or adjacent to the main rupture zone of the earthquake, it should be noted that those in the footwall of the Beichuan fault underlie relatively low lying topographic features. This is in clear contrast to the large relative relief produced by units in the hanging wall to the north-west.



Legend

- Cretaceous conglomerate
- Jurassic conglomerate, sandstone, mudstone
- Mesoproterozoic Granite, Granodiorite basement
- Mesozoic Granite
- Palaeozoic greywacke and shale
- Proterozoic Volcanics and Dolomite
- Quaternary unconsolidated sediments
- Tertiary conglomerate, sandstone and mudstone
- Triassic (SG Fold Belt) turbidites, acidic volcanics
- Triassic mudstone, sandstone and conglomerate

Figure 4.6: Regional geological map of the Sichuan Basin and the Longmen Shan (After Ma et al 2002).

4.1.6 Climate

The Sichuan region has a sub-tropical monsoon climate, with a total annual rainfall of 923mm in Chengdu (Sichuan Basin), and high levels in mountain areas; around 90% of this rainfall occurs between April and September, during the monsoon period (WMO 2009). Mean monthly daytime temperatures in the Sichuan Basin range from 9 to 30°C (WMO 2009), though lower temperatures occur in the higher altitude regions of the Longmen Shan.

4.1.7 Hydrology

The Longmen Shan mountain belt is dissected by several major rivers, with catchments spanning a range of sizes and bedrock lithologies. Tectonic faults exhibit a strong structural control on the hydrological network, with most major channels affected by tectonic offsets or flowing along surface ruptures (Li *et al.* 2003; Densmore *et al.* 2007).

4.2 The Wenchuan earthquake

At 14:28:01.42 (local time) on the 12th May 2008 the Wenchuan earthquake occurred (USGS, 2008). The quake magnitude was reported as M_s 8.0 (Li 2009) and M_w 7.9 (USGS 2008), for which a millennial recurrence interval has been identified (Li *et al.* 2009). The earthquake epicentre occurred at around 31.0°N, 103.4°E, near Yingxiu Town in Wenchuan County, with a shallow focal depth of 15km similar to previous seismic events in the region (Burchfiel *et al.* 2008; USGS 2008) (*Figure 4.7*).

4.2.1 Co-seismic fault ruptures

Co-seismic surface ruptures were located on the Beichuan, Pengguan and Xiaoyudong faults, along a 280km long rupture zone. Characteristics of the surface rupture suggest a combination of thrust and dextral strike-slip occurred (Li *et al.* 2009, Densmore *et al.* in review; Liu-Zeng *et al.* 2009). The following section documents the activities of co-seismic faults activated by the earthquake, based on the field observations of Li *et al.* (2009), Densmore *et al.* (in review) and Liu-Zeng *et al.* (2009) (faults are shown in *Figure 4.7*):

Yingxiu-Beichuan (Beichuan) Fault

This was the main fault activated by the earthquake. The surface rupture is 220km long, stretching from Yingxiu (31.0°N, 103.4°E) to Shikanzi, Pingwu (32.2°N, 104.9°E), and passing through the Beichuan town (32.8°N 104.4°E). It has a steep north-west dip and strikes northeast (~N45°) parallel to the high topography of the Longmen Shan. The fault cuts a wide range of lithological units including bedrock, river terraces and alluvial fans. On this fault the earthquake produced vertical offsets of ~1.6-6.2m, and horizontal offsets of ~0.2-6.5m (Li *et al.* 2009), with two local maxima of ~5-6m and ~11m found at 35km and 140km northeast of the epicentre respectively (shown in *Figure 4.8*, Liu-Zeng *et al.* 2009). The sense of slip on the Beichuan fault was oblique with a combination of thrust and dextral strike-slip components. To the southwest and middle sections of the fault the thrust component dominates, while in the northeast (from around 135km from the epicentre) the strike-slip component is more prominent (Shen *et al.*, 2009).

Pengguan-Guanxian (Pengguan) Fault (also known as the Guanxian-Anxian fault)

Running parallel to the Beichuan fault at a distance of around 8km, the Pengguan fault surface rupture stretches for 40-50km from (31.9°N, 103.5°E) to (31.3°N, 104.1°E). Again the fault has a steep north-westerly dip and strikes northeast, with the hanging wall to the northwest. Vertical offset produced by the earthquake is ~0.4-2.7m, with a horizontal offset of ~0.2-0.7m (Li *et al.* 2009), and local maxima of ~3-3.5m (shown in *Figure 4.8*, Liu-Zeng *et al.* 2009). Here the thrust component dominates over that of dextral slip.

Xiaoyudong Fault

Running between the Beichuan and Pengguan faults, this fault was newly discovered following the earthquake, extending over a length of ~15km. While Li *et al.* (2009) identified it as a tear fault, the sense of slip is kinematically compatible with the Beichuan and Pengguan faults, demonstrating thrusting of the southwest side of the fault with a large sinistral strike-slip component (Liu-Zeng *et al.* 2009). Average offsets are reported as 1m vertical and 2.3m horizontal (Li *et al.* 2009).

Co-seismic slip partitioning

While 3 separate co-seismic faults have been identified, these crustal scale thrusts are thought to merge into a single plane around 10km below the Longmen Shan range (Hubbard and Shaw 2009), as shown in *Figure 4.9*. The diagram also shows the hanging wall of the fault system to the northwest while the footwall is situated to the southeast of the fault.

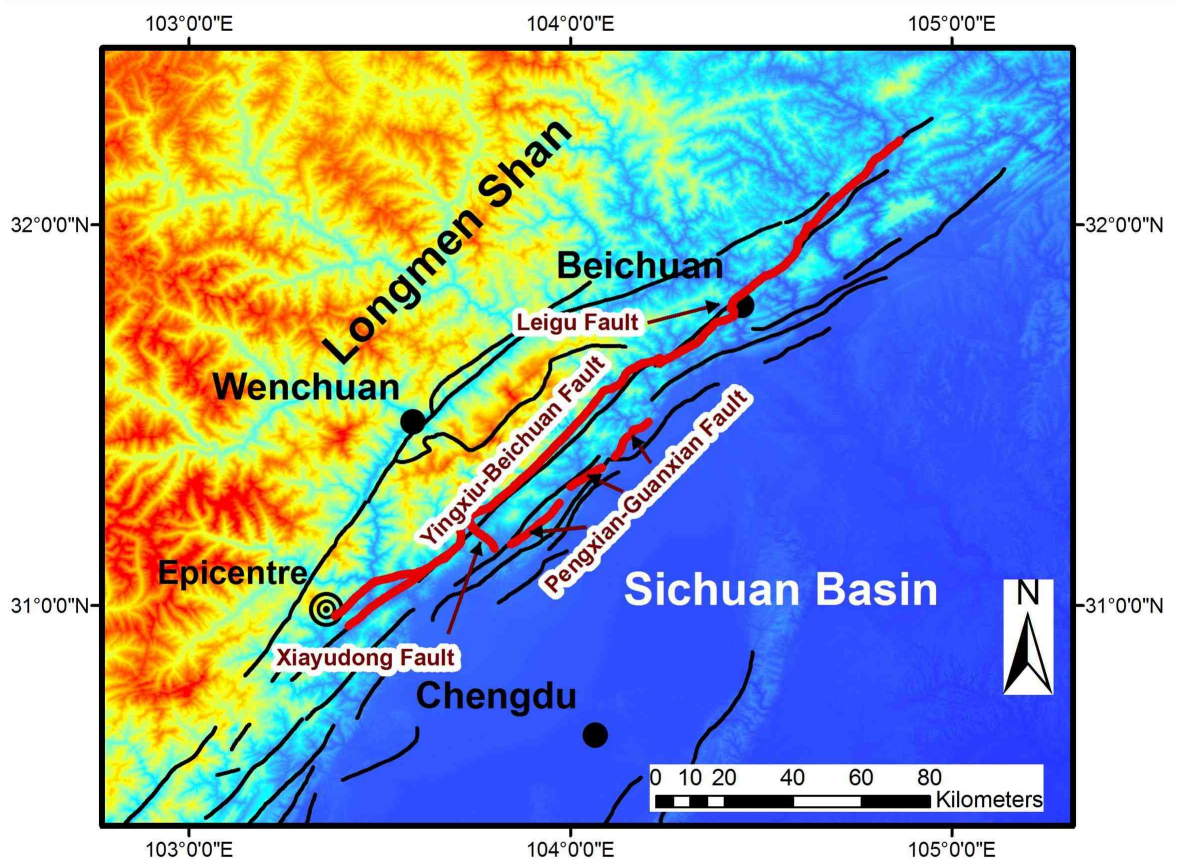


Figure 4.7: Map of Wenchuan earthquake epicentre (USGS) and coseismic fault ruptures mapped by Densmore et al (in review) (red). Other faults not activated by the earthquake are shown in black.

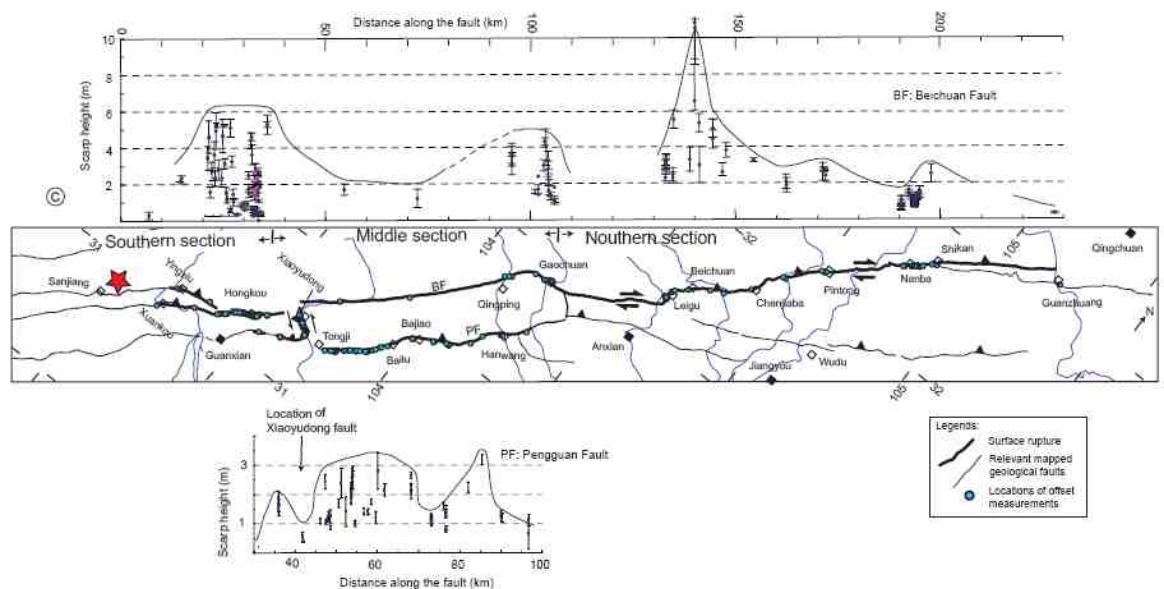


Figure 4.8 (Liu-Zeng et al 2009): Map of the surface rupture and along-fault variation of scarp height on the Beichuan and Pengguan faults. Along fault distances are relative to the location of the epicentre. Also shown are the locations of the corresponding offset measurement points.

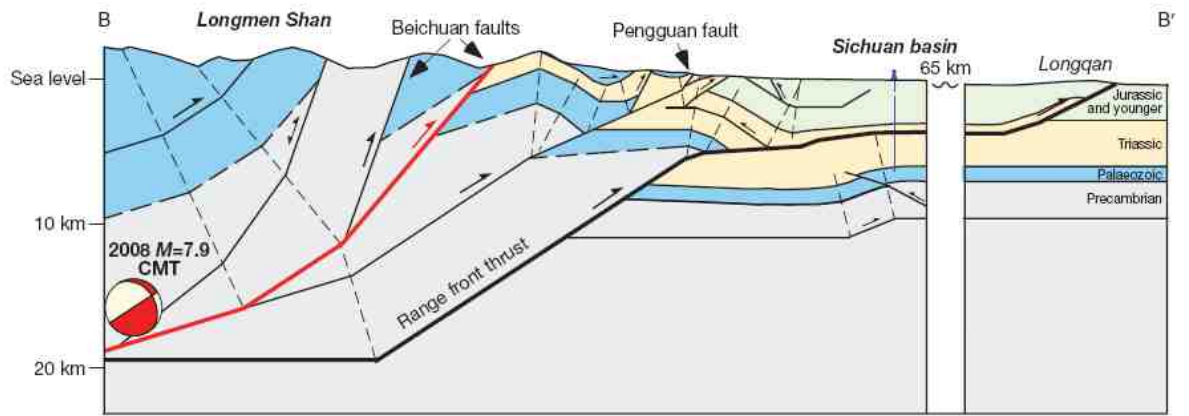


Figure 4.9 (after Hubbard and Shaw 2009): Geological cross section across the epicentral region of the Wenchuan Earthquake.

4.2.2 Distributed displacement and deformation

While field observations of fault displacements reveal important features and characteristics of the earthquake, inaccessibility of many regions and the inability to identify surface ruptures in regions of steep topography and landsliding, results in an incomplete picture of co-seismic displacements and deformation. While inversion of near-field seismographs is often used to improve the displacement model, very limited data is currently unavailable for technical and political reasons (Hao *et al.* 2009). Thus, in order to build more holistic and spatially distributed estimates of ground deformations, fault models built through inversion of global seismic waveform data and InSAR measured ground deformations have been produced.

Initial seismic wave form estimates of ground deformations were based upon a simplified, single fault model, published by Zhang *et al.* (2009), Ji and Hayes (2008), Nishimura & Yagi (2008) and Caltech (2008), shown in *Figure 4.10*. Of these, the data of Ji and Hayes, Nishimura & Yagi (2008) and Caltech (2008) were made publically available shortly after the earthquake in fault profile and map projected formats (see *Figure 4.11*). While these estimates all differ due to the model parameters used, all demonstrate a two peak distribution, with displacement maxima to the southeast and northwest. In addition, data from Nishimura & Yagi (2008) and Zhang *et al.* (2009) appear to correspond well with recorded levels of damage to urban areas. Despite this, significant inconsistencies exist in location and depth of peak displacements across all models. In addition, all these models apply a single-fault assumption which does not incorporate the slip partitioning, observed in the event as outlined in *Section 5.2*. As such, while these models provide a first order estimate of the displacement field, they are oversimplified for this earthquake (Liu-Zeng *et al.* 2009). Later during in the course of this investigation, more sophisticated reconstructions of fault displacement and crustal deformations were later published by Hao *et al.* (2009) and Shen *et al.* (2009), shown in *Figure 4.12*. These models utilise a combination of field slip measurements and InSAR (Interferometric Synthetic Aperture Radar; e.g. Massonnet *et al.* 1994; Peltzer & Rosen 1995; Wang *et al.* 2007) derived ground displacements using data from the ALOS PALSAR sensor system, to construct

multi-fault slip models. While a more complicated pattern of displacement is produced, the fundamental characteristics observed in other datasets are preserved. The vertical component of displacement is greater in the southwest, while horizontal displacement is more dominant in northeaster fault segments. Two areas of maximum displacement occur, although the northeast zone appears to combine two smaller areas of peak displacements. Wang *et al.* (2009) attributed this phenomenon to structural heterogeneities in the upper crust, suggesting that smaller displacements are apparent in regions of ductile crust. In addition, displacements mainly occur in the fault hanging wall areas to the northwest, due to the northwest dip direction of the fault.

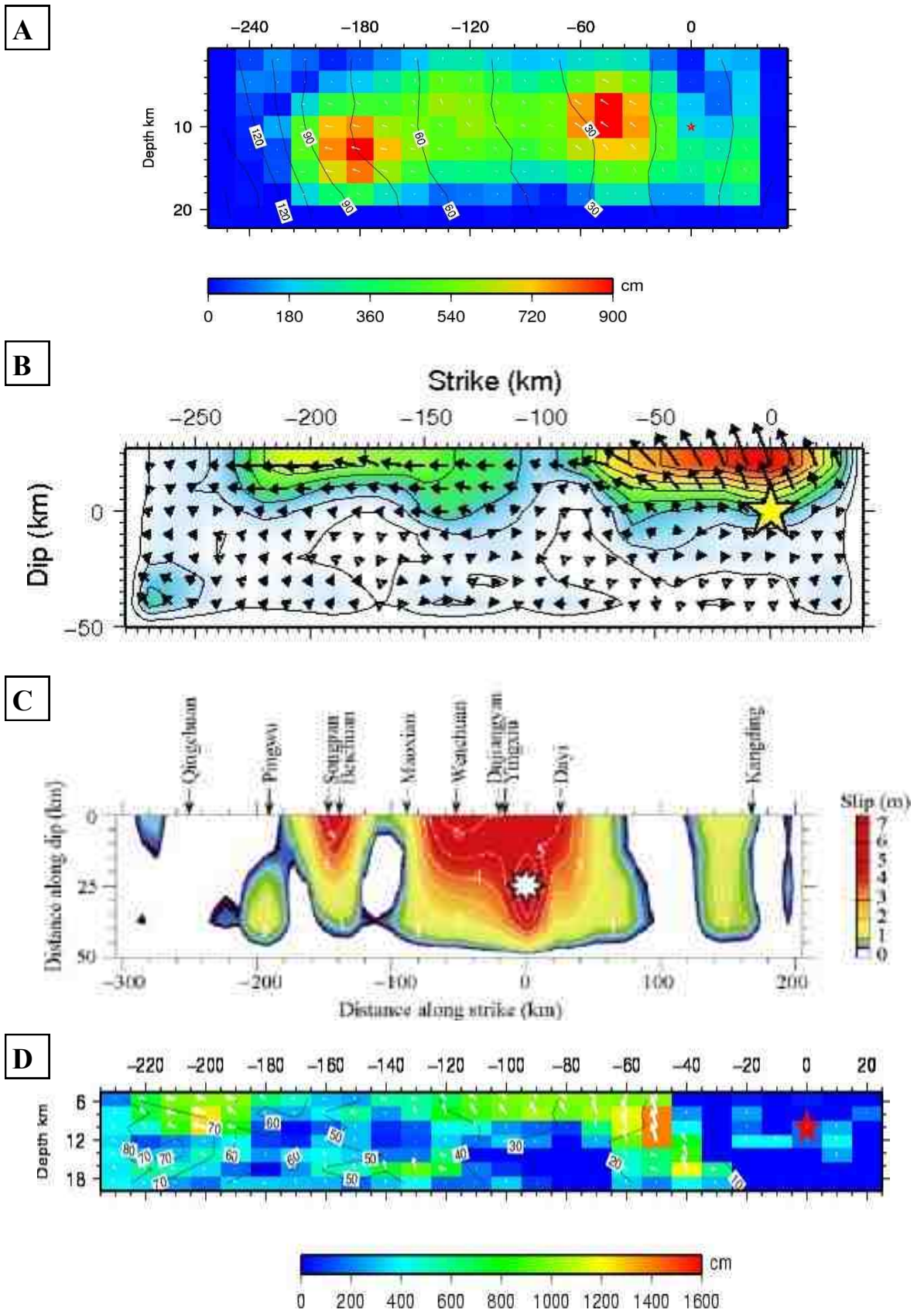


Figure 4.10: Along fault profiles of the static slip distribution, derived from the inversion of seismic waves: A - Ji and Hayes (2008); B—Nishimura & Yagi (2008) ; C - Zhang et al (2009); Caltech (2008)

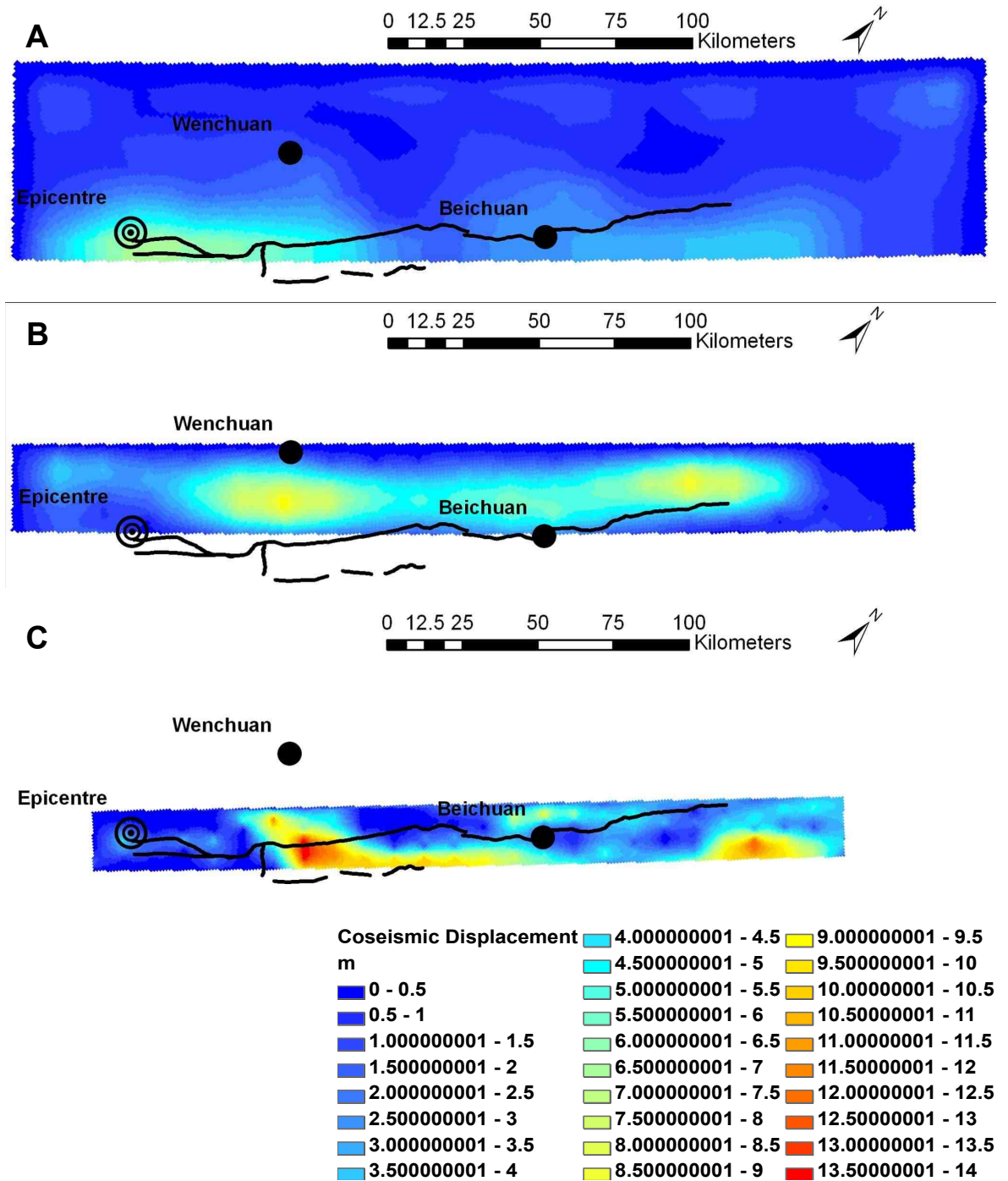


Figure 4.11: Map projected static slip distributions for the Wenchuan earthquake. Coseismic faults are shown in black: A - Nishimura & Yagi (2008); B - Ji & Hayes (2008); C - Caltech (2008).

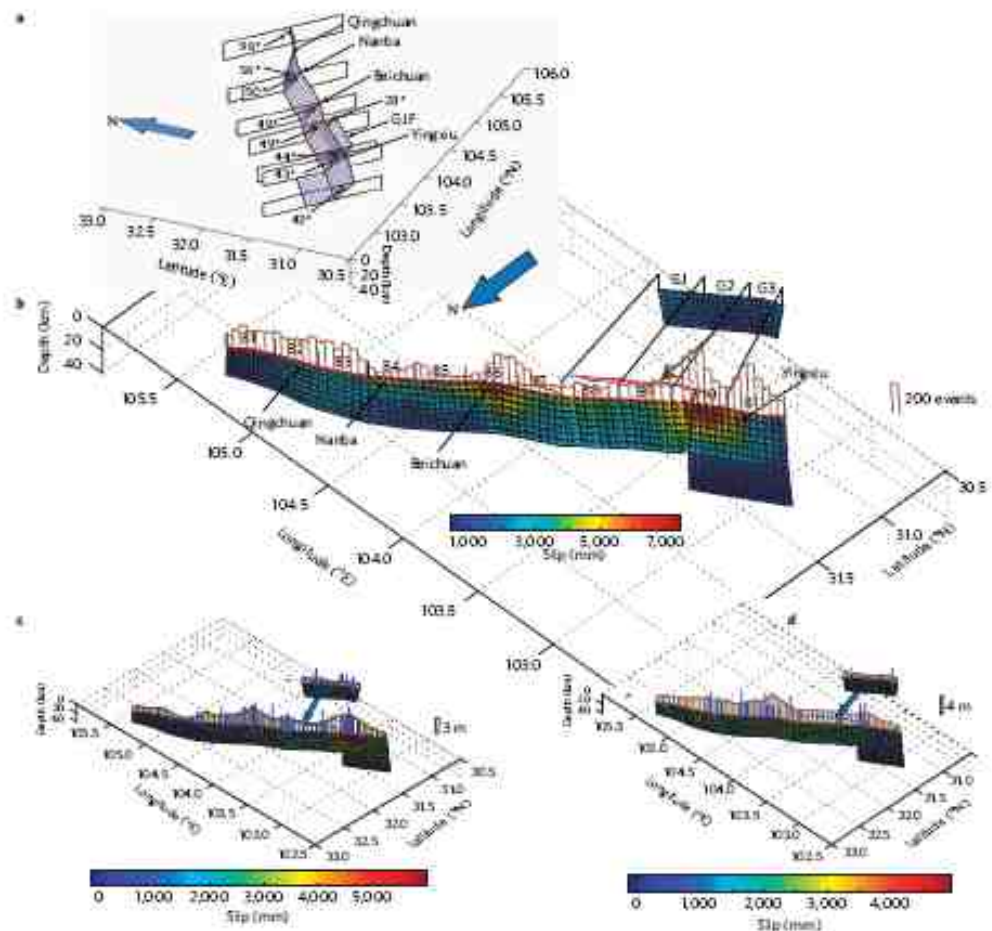
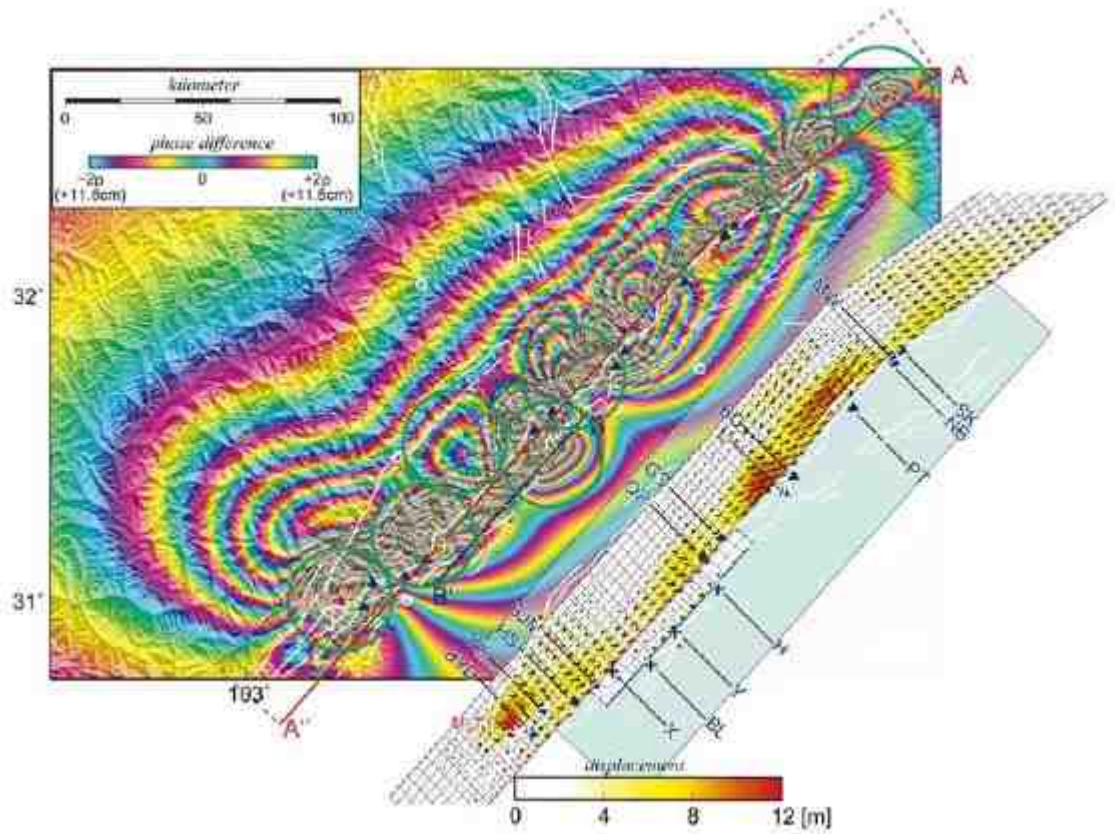


Figure 4.12: Multi-fault coseismic slip inversion results: above (Hao et al 2009); below (Shen et al 2009)

4.2.3 Seismic ground motion

Spatial variations in ground motion during earthquakes have been shown to be key factor in controlling the distribution of landslides triggered (e.g. Khazai & Sitar 2003; Meunier & Hovius 2007). Records of the Wenchuan earthquake's main shock were obtained by the National Strong Motion Observation Network System (NSMONS) for around 460 permanent free-field ground motion stations, three arrays for topographical effect and structural response observations. Additional records for aftershocks were attained from 59 mobile instruments deployed after the main shock to hardest hit areas (Li *et al.* 2008) (shown in *Figure 4.13*). A brief preliminary analysis of these data is presented in Li *et al.* (2008), however no values of intensity or peak ground acceleration are included. Unfortunately very little strong ground motion data has yet been made publically available. However, estimates derived from the data have been published by United States Geological Survey (USGS) and the China Earthquake Administration (CEA).

USGS Shakemap

In the immediate aftermath of major earthquakes, approximate maps of ground motion are produced by the USGS through the automated application „Shakemap’. Maps of Peak Horizontal Ground Acceleration (PGA), Peak Horizontal Ground Velocity (PGV), spectral bands separated PGA and Modified Mercalli Intensity (MMI), are produced and GIS contour layers made available for download. The Shakemap output is based on all available ground motion data points, interpolating based on attenuation relationships, as outlined in Wald *et al.* (2006).

While the original Wenchuan earthquake Shakemap output was generated minutes after the main earthquake event, the USGS shakemap site is continuously updated as more data and information becomes available (Wald 2009, pers comm). When this investigation began in October 2009, the available Shakemap (version 9) had been last regenerated on 18/05/2008, just six days after the earthquake (*Figure 4.14A*). Since then additional information contributed to an updated version 10 generated on 08/12/2008, almost 7 months after the earthquake (*Figure 4.14B*). In the updated model, fault dimension parameters were refined and data from local strong motion stations were added (Wald 2009,

pers comm). The modifications produced a much higher ground motion resolution, particularly in the fault rupture region. In order to generate version 10, data from 102 locations were used. Of these 32 readings were attained from strong ground motion stations, 29 readings were taken from Modified Mercalli Intensity site observations, and 41 were collected from the USGS “Did you feel it” application. The resulting Shakemap shows a continuous region of high MMI values (>8) for a distance of around 250km from the epicentre in the direction of the co-seismic rupture process. In concurrence with seismic wave attenuation properties of thrust belts, higher PGAs are present in the fault hanging wall, with lower PGAs in the footwall. It should be noted that this is still a low resolution first order estimate, though USGS intend to update the map using the full strong motion dataset, when this data becomes publically available (Wald 2009, pers comm).

China Earthquake Administration Shakemap

The CEA published a second intensity (MMI) shakemap for the Wenchuan earthquake (Li *et al.* 2008) on 29/08/08, shown in *Figure 4.14C*. Although neither raw seismic data nor GIS layers were available for this distribution, the contours from the map have been digitised for analysis. While the relative location of peaks and troughs coincide in the USGS and CEA shakemaps, in general the CEA shakemap predicts higher intensities with a less uniform attenuation pattern than either of the USGS shakemaps published. In addition, two intensity peaks can be identified in the Wenchuan and Beichuan County regions (Xiao 2008). These coincide with along fault regions of peak ground displacement identified in *Section 4.2.2*. Unfortunately no methodology data is available for how this map has been compiled. The online location of the map is a website in Chinese, was accessed via the Google translation function. Methodology documentation appears to be available in Chinese, but is inaccessible to western authors.

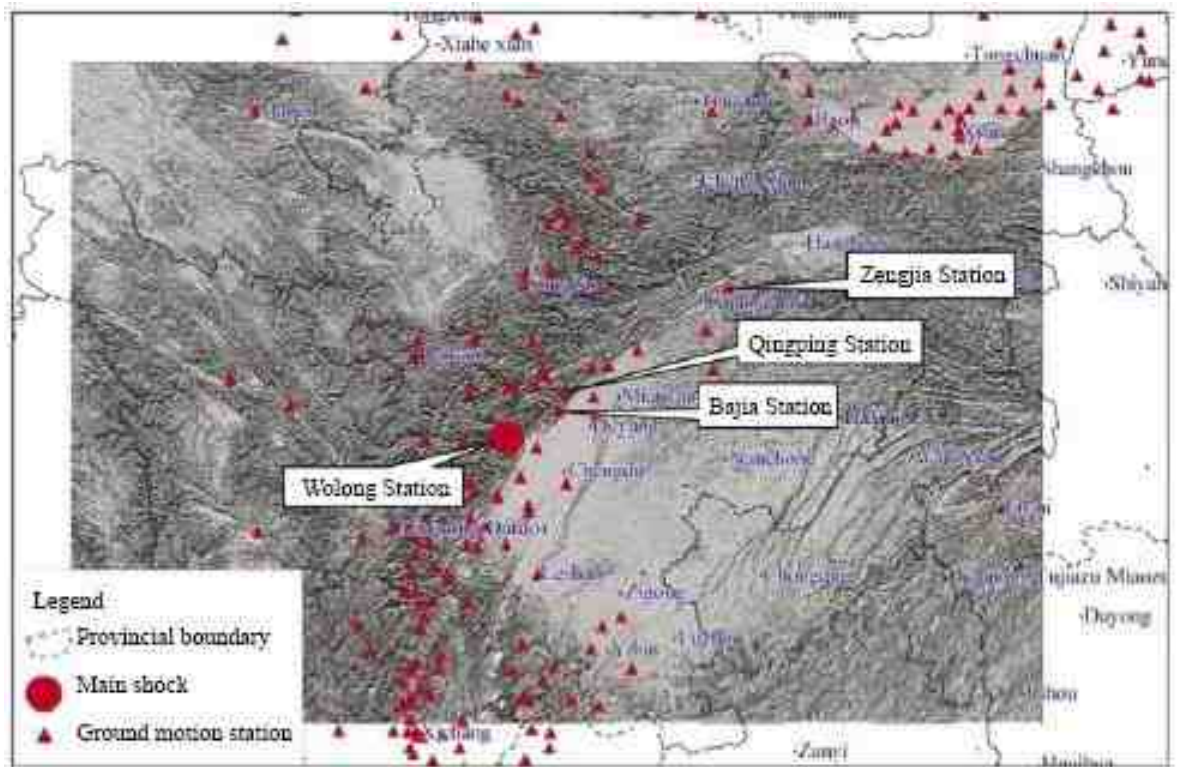


Figure 4.13: Location of strong motion observation stations in the Longmen Shan and surrounding areas (Li et al 2008)

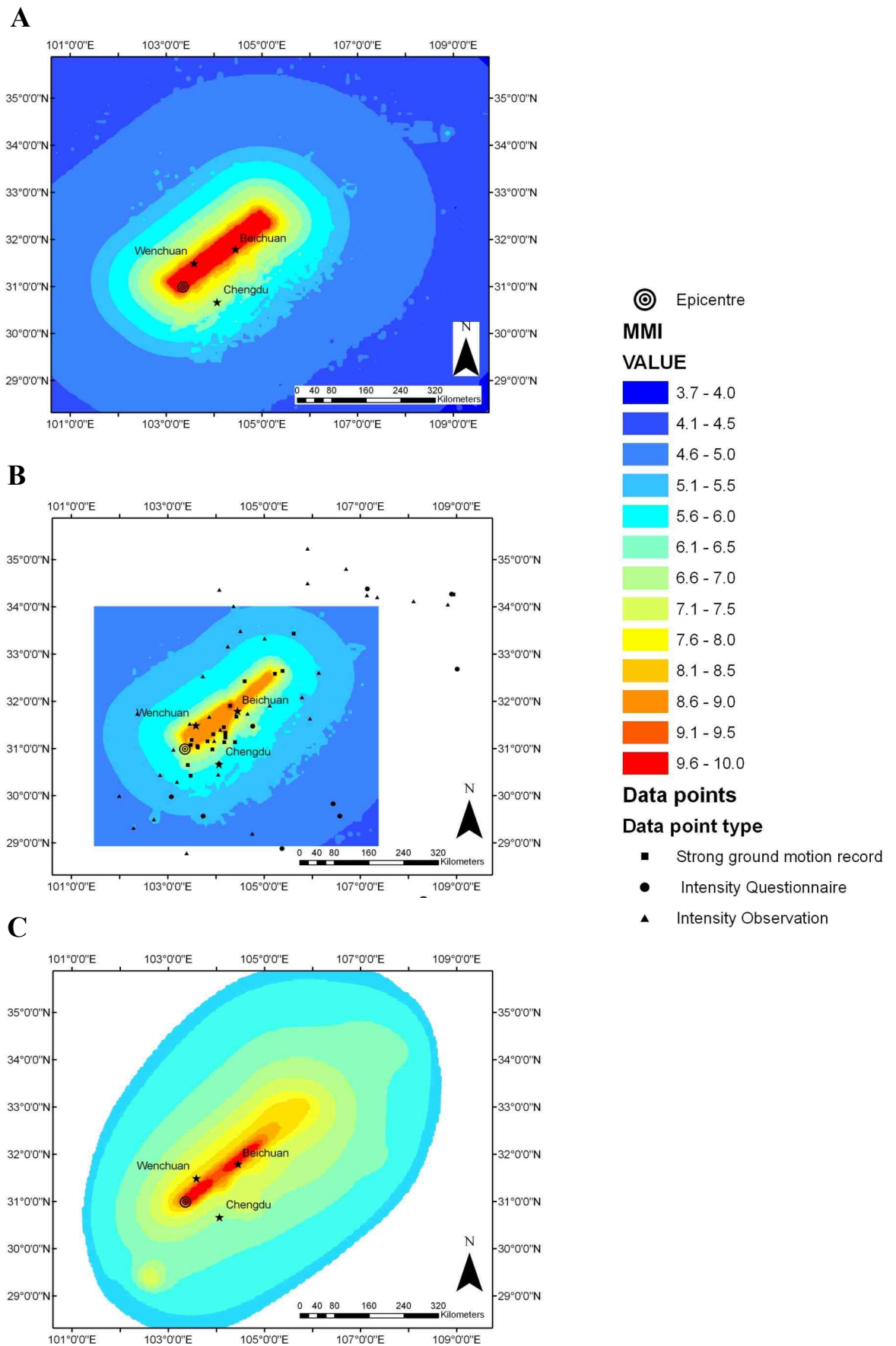


Figure 4.14: Wenchuan Earthquake Modified Mercalli Intensity shakemaps: A - USGS version 9; B - USGS version 10 (after USGS 2008); C - CEA shakemap digitised and interpolated from published map (after Li et al. 2008).

4.2.4 Aftershocks

In addition to the main magnitude 7.9 earthquake, 15 aftershocks of $M > 5.5$ were also recorded by USGS, and corresponding shakemaps for these events have been produced. These all occur along the rupture zone of the main event. Data on the location, magnitude, time and depth of an additional 1015 aftershocks epicentres occurring between 12/05/2008 and 05/09/2008, were also made available through the China Earthquake Geospatial Research Portal (CEGRP 2008). The epicentres occur a distance of around 400km along the length of the rupture zone. The areal density of epicentres $M \geq 4.0$ demonstrates two marked peaks, as show in *Figure 4.15*. These also coincide with regions of peak ground displacement (outlined in *Section 5.3*) and ground motion intensity (outlined in *Section 5.4*). Earthquakes of $M \geq 4$ are capable of triggering landslides (Keefer 1984), however these additional events are not considered in analysis of the landslide distribution at this stage, given the overriding magnitude and impact of the main shock.

4.2.5 Summary

During the 12/05/2008 Wenchuan earthquake, surface ruptures occurred over a length of ~ 280 km, along the Beichuan, Pengguan and Xiaoyudong faults, of which the length and displacements of the Beichuan fault are the most prominent. Along the rupture zone, field and modelled data suggest that two areas of peak ground displacements and ground motions occurred in the southwest and northeast. However, the precise locations of these maxima vary between datasets.

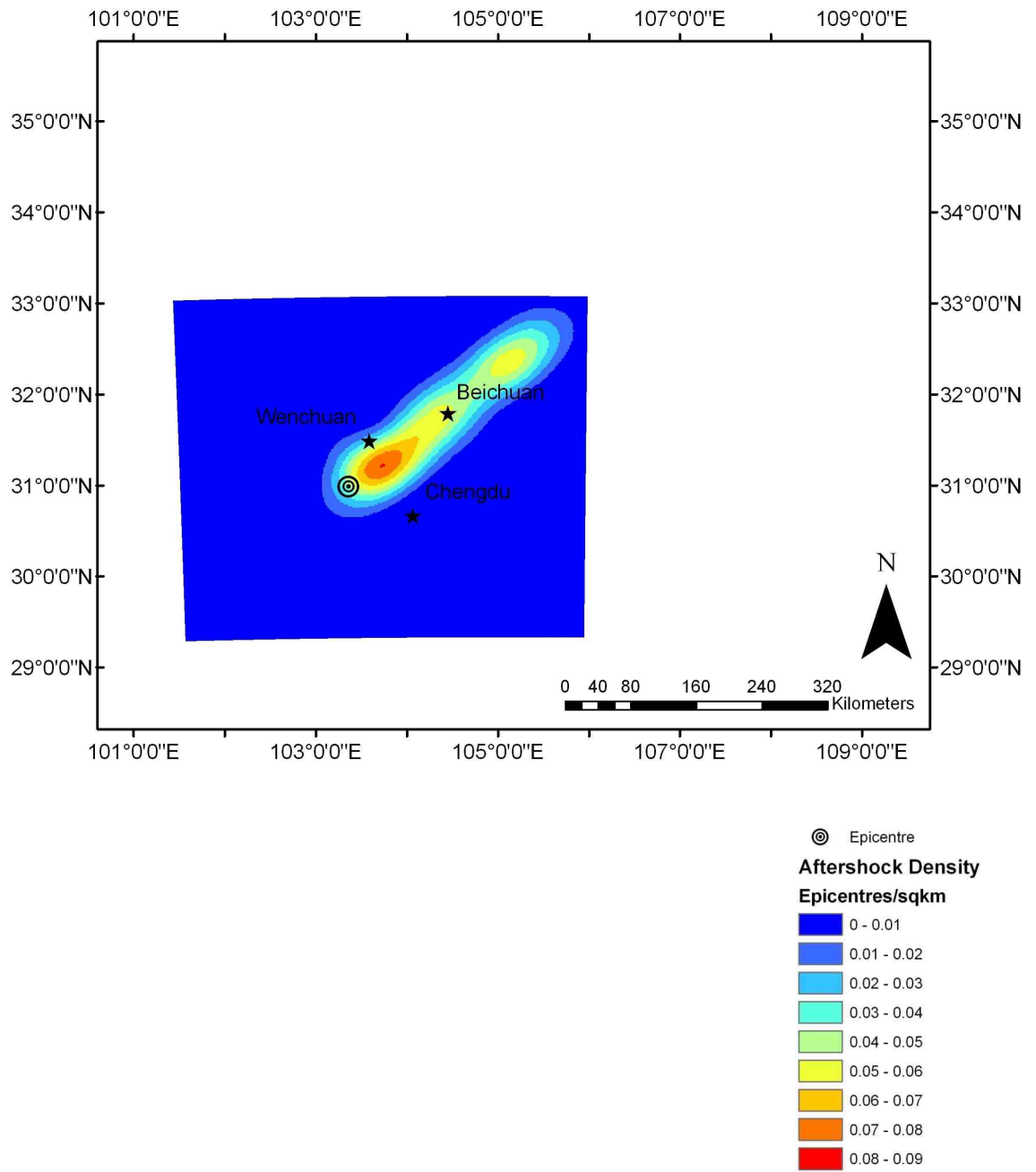


Figure 4.15: Mapped density of aftershock epicentres, $M \geq 4.0$. (Kernel density based on a 50km search radius). Raw data from CEGRP (CEGRP 2008).

4.3 Landslides triggered by the Wenchuan earthquake

During 2008 and early 2009, several preliminary studies were also published describing characteristics of landslides triggered by the Wenchuan earthquake. The following section provides a review of this literature and synopsis of the key findings and observations, in order to provide a basis for this study and further investigations into the landslide distribution. Key literature sources are first identified before the regional distribution of landslides and geophysical controls upon that distribution are addressed. The review was conducted during June 2009, so studies published after this period may not be included in this section.

4.3.1 Investigations on the regional distribution of landslides

In the time immediately following the earthquake, the Chinese Ministry of Land and Resources mobilised around 800 geologists from across China to compile an inventory of landslides triggered (Yin *et al.*, 2009). This undertaking involved a combination of ground based mapping as well as identification of landslides in aerial and satellite imagery. Because the ultimate aim was rapid information production for post-disaster management, interpretation was focused on slope failures which posed a direct threat to the human population. Thus this landslide inventory data is limited to features in this category, while numerous slope-failures in uninhabited regions or posing indirect threat to human habitat are not identified (Huang & Li 2009). Unfortunately, to date the results of this investigation have only been published in Chinese (Yin *et al.*, 2008; 2009), making it inaccessible for further review.

A second landslide inventory which claims to better describe the macro-scale landslide distribution has been compiled by Huang and Li (2009). This study utilises a combination of satellite (ALOS, SPOT, and Landsat-ETM) and aerial imagery (collected by the Air Command and China Aero Geophysical Survey, and Remote Sensing Centre for Land and Resources). Through manual interpretation, „geohazards’ – a term which appears to refer to slope failures and instabilities - are identified along the entire length of the fault rupture, as well as large areas to the north and northwest (shown in *Figure 4.16*). Although the authors are not explicit, this work also appears to combine data from the Ministry of Landslide and

Resources mapping exercise. While this investigation presents the most holistic landslide inventory coverage published to date, slope failures have been manually mapped as point features in this data, giving no consideration to their 2 or 3 dimensional geometry or magnitude. As such, any interpretation and analysis of this data can only consider the spatially distributed frequency of landslide occurrence. This is presented in the form of landslide concentration (number of landslides / km²). In addition the authors give no information regarding the criteria used to identify landslides through both remotely sensed imagery and fieldwork. This is of particular concern in regions of very high landslide density, where multiple landslides have failed side by side along river valleys, allowing them to be mapped as single or multiple features depending on the methodology. Despite these insufficiencies Huang and Li's (2009a) database was the most holistic description of the landslide distribution published at the time of this review.

A further investigation by Sato & Harp (2009) also manually identified the locations of landslides in a region 130km northeast of the epicentre, using Formosat imagery. Although only preliminary results of this investigation have been published, the study does show relationships between landslide occurrence and slope gradient, within its sample area.

The following section identifies key characteristics of the landslide distribution based predominantly around the findings of this investigation, while detailing additional landslide characteristics identified through a number of field studies.

4.3.2 Total magnitude of the landslide impact

Seismically triggered landslides extend over an area of 130 000km² (Huang & Li, 2009), involving an estimated total of 50 000 individual failures (Huang *et al.*, in press). This corresponds roughly with the predicted impact area and number constrained from previous earthquake-landslide events (Keefer 1984; Keefer 2002) (as shown in *Figure 4.17*).

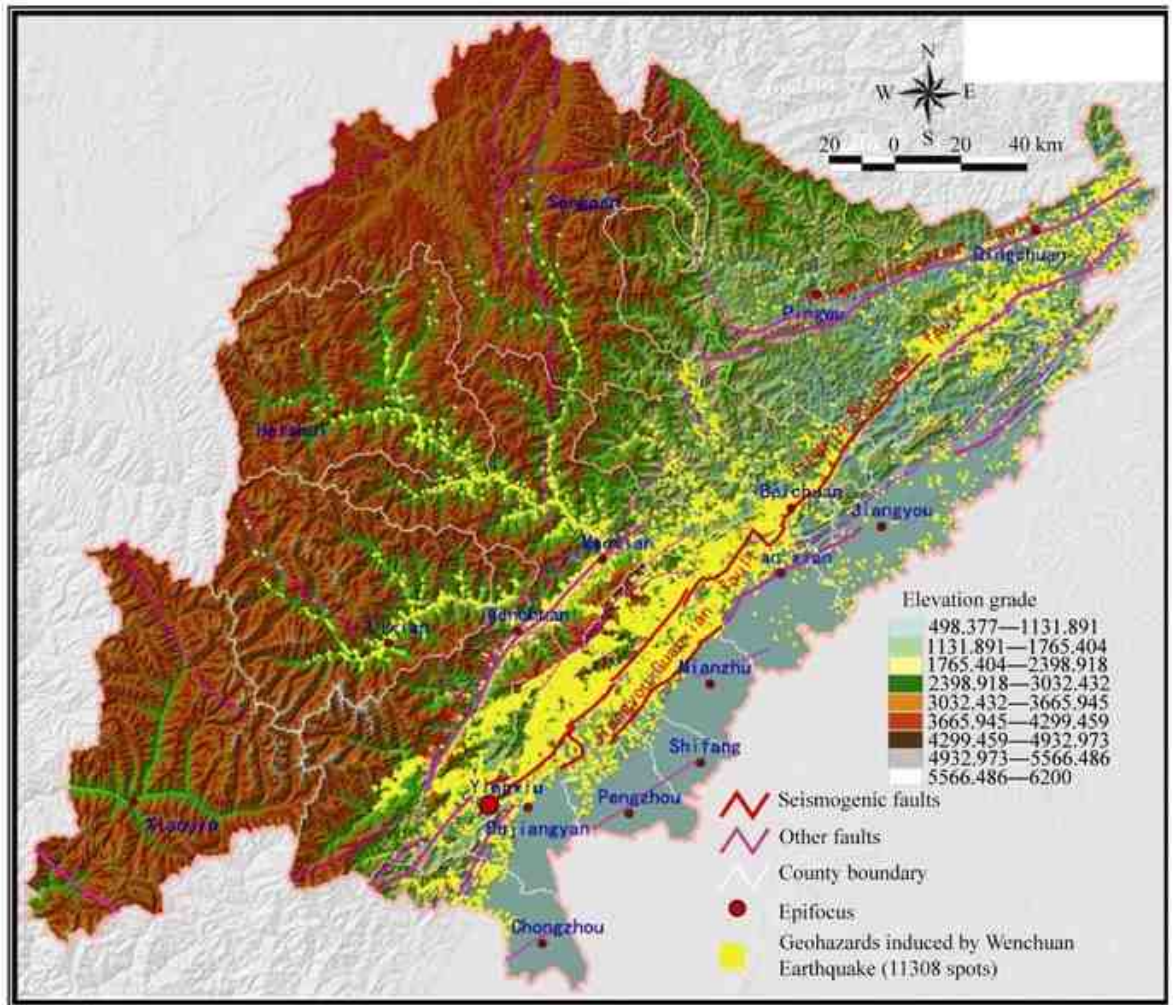


Figure 4.16: Locations of landslides triggered by Wenchuan earthquake, identified by Huang & Li (2009)

A

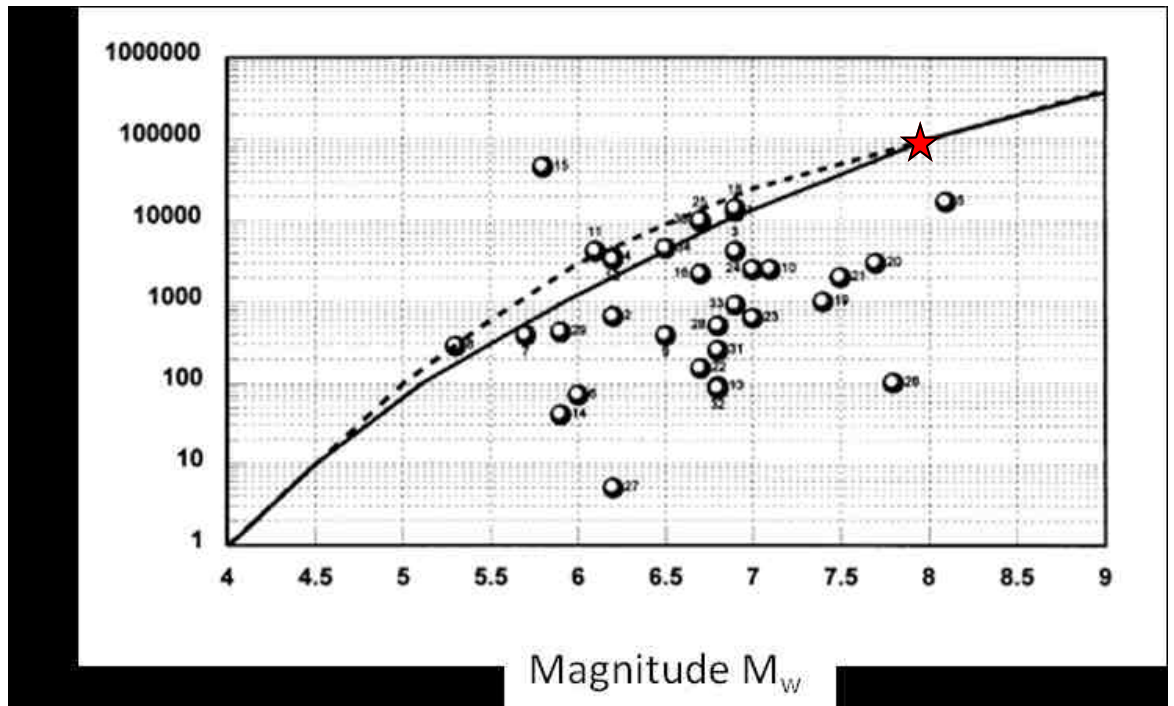
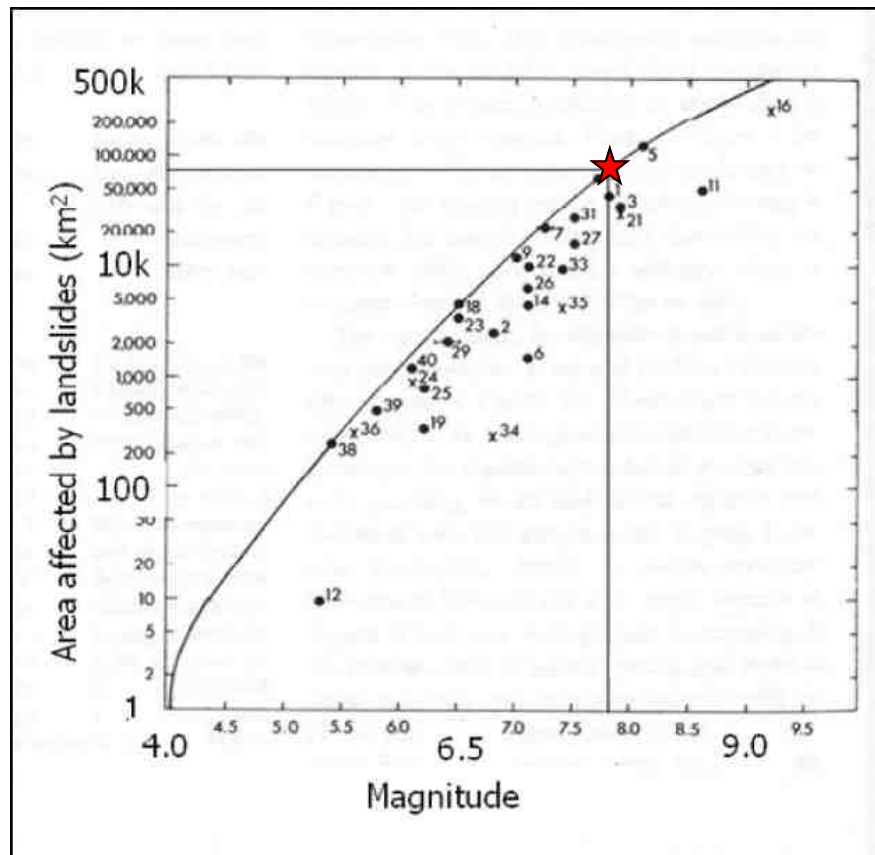


Figure 4.17: Relationships between earthquake magnitude, area affected by landslides (A, Keefer 1984) and total number of landslides triggered (B, Keefer 2002), based on results from previous earthquakes. Red stars indicate values for the Wenchuan earthquake.

4.3.3 Key characteristics of the landslide distribution

Seismic ground accelerations are expected to be a first order control on the landslide distribution (e.g. Meunier *et al.* 2007). Unfortunately, due to a lack of seismic monitoring data collected at the time of the earthquake, modelled ground acceleration estimates are of a coarse resolution. Thus at present the finer details of ground motions can only be approximated based on location relative to the co-seismic fault rupture (e.g. Meunier *et al.* 2007), relative to which the landslide distribution has been examined. These include the earthquake epicentre, surface expression of the fault rupture, magnitude of permanent ground displacements and positioning of the hanging wall and footwall.

The landslide distribution extends around 70km from the co-seismic fault, at its maximum distance, while landslide concentration exhibits an inverse relationship to distance from the fault (Huang & Li, 2009a). Higher landslide concentrations occur in the hanging wall of the fault, with peak concentrations observed within 20km of the rupture, decreasing rapidly beyond this distance (as shown in *Figures 4.18 & 4.19*). In addition Yin *et al.* (2009) observed larger failure volumes and sliding distances along the fault rupture than in other areas, with the majority of large failures occurring within 5km of the fault. From this pattern Huang and Li (2009a) identified distance from the fault as having a clear control on landslide occurrence. It is interesting to note that the high concentration of landslides does not focus around the epicentre as has been noted from the 1999 Chi-Chi earthquake, but follows the pattern of the 1994 Northridge and 2005 Kashmir earthquakes, in focussing along the length of the fault rupture (e.g. Khazai & Sitar 2004). The landslide distribution presented also appears to vary along the fault in conjunction with the co-seismic displacement pattern. For example areas of high landslide density such as Beichuan town which correspond with areas of larger co-seismic displacement (Huang & Li 2009a). This evidence suggests that ground motion has a strong control upon landslide occurrence, of which there are 3 main features.

1. A distance decay pattern as seismic waves attenuate away from the source fault

2. A hanging wall-footwall pattern of peak ground acceleration (PGA)
3. Zones of higher PGA and landslide occurrence corresponding to larger permanent ground displacements along the fault, and vice-versa.

A second conspicuous feature of the landslides is their linear distribution along major river valleys. This can be observed in *Figure 4.16*, where the landslide distribution extends along long river valleys into Heishui and Songpan counties. Huang & Li (2009a:814) stated that “the vast majority of seismogenic geohazards [slope failures] occurred along the two sides of the Minjiang River and along the deep-incised river valleys perpendicular to the Longmen Shan Mountain [range], including the Shiting River, the Mianyuan River and the Qianjiang River as well as their tributaries”.

As such, the co-seismic structures appear to control the general outline of the landslide distribution, while rivers exhibit a secondary influence upon the specific location of landslides within that general outline. However, while these dominant co-seismic and hydrological features appear to strongly control the regional spatial distribution of landslides, the occurrence of slope failures has also been explored in relation to other geophysical variables on the local scale.

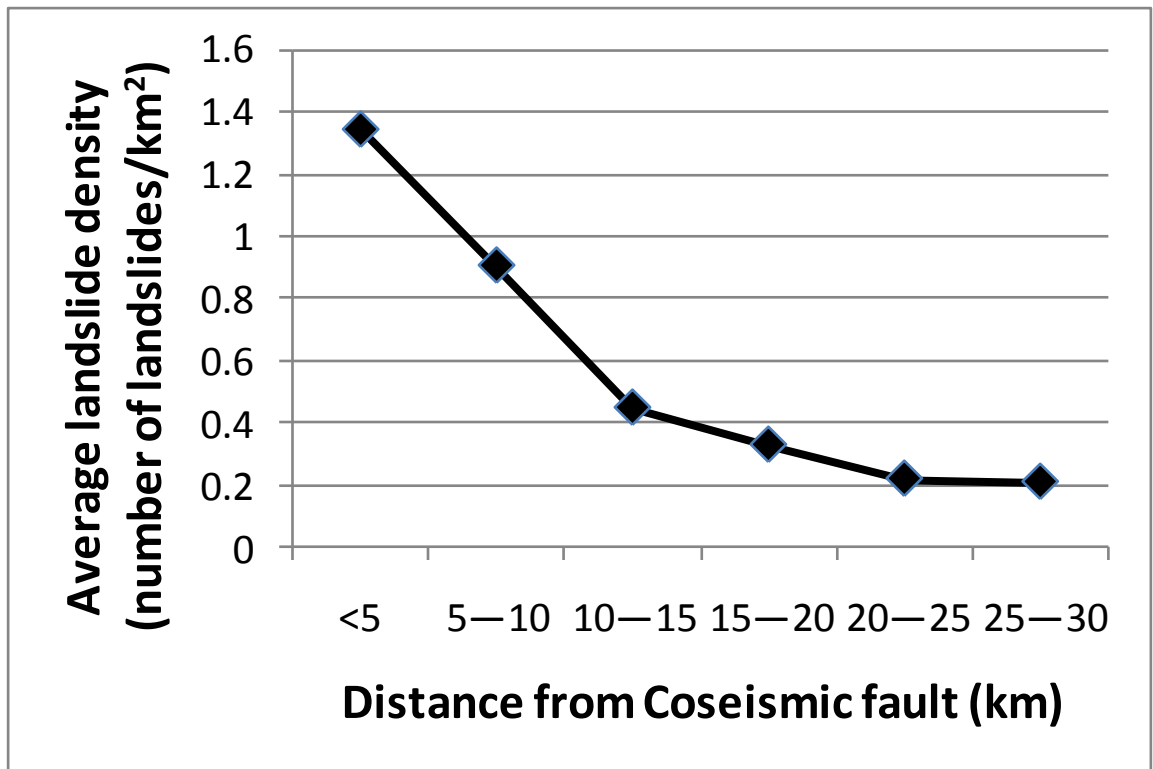


Figure 4.18: Relationship between landslide concentration and distance from coseismic surface rupture (Huang & Li, 2009).

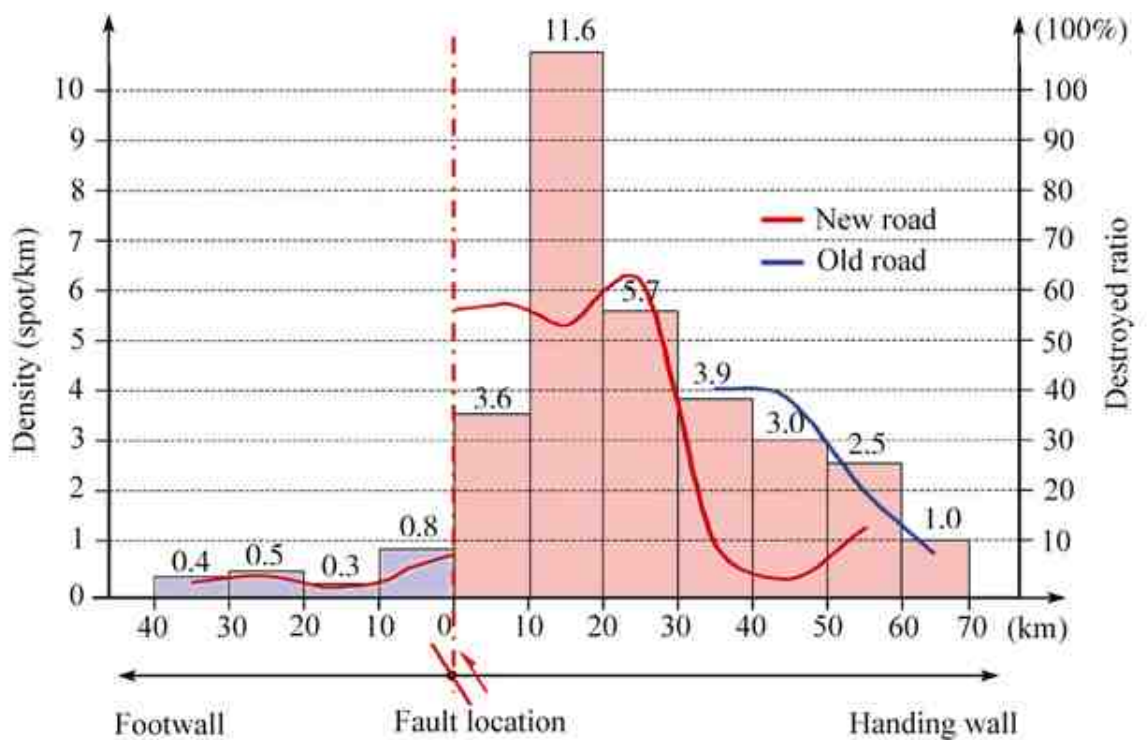


Figure 4.19 : Comparison of landslide concentrations in the hanging wall and footwall (Huang & Li, 2009).

4.3.4 Influence of hillslope gradient

Huang & Li (2009a) identified that the majority of landslides occurred on slopes with gradients between 20° and 50°, while the highest landslide concentration is found on the steepest slopes in that range from 40° to 50°, as shown in *Figure 4.20*. The authors make reference to a lower gradient threshold for landslide occurrence at around 20°. Sato & Harp (2009) report oversampling of lower gradient for the Beichuan region, with the peak landslide concentration between 30° and 35°.

4.3.5 Influence of Elevation

75% of landslides are distributed between 650-2000m in elevation, while this height range only encompasses 27% of the study area. Between 1000-1500m the highest landslide densities occur, reaching a peak of 0.63 landslides/km² (as shown in *Figure 4.21*). Above 2500m landslide density decreases rapidly (Huang & Li, 2009a). From field investigations Huang & Li (2009a) suggest that this is due to the high proportion of river valleys occurring within the peak elevation range, as illustrated in *Figure 4.22*. As noted above, large numbers of landslides are distributed along these features and thus occur at ~1500m. In addition, from field observations Huang & Li (2009a) also identified the frequent initiation of landslides along ridge crests, as expected due to the topographic amplification of seismic waves (e.g. Murphy 2002; Meunier *et al.* 2008). This adds to the apparent elevation control on landslides, initiating at similar heights along ridges and peaks.

4.3.6 Influence of lithology

Data from Huang & Li (2009a) suggest that the highest rates of landsliding occur in harder rock types, including magmatic (igneous) rock, carbonate and sandy conglomerate (*Figure 4.23*). Second to this are sand-slate, phyllite and argillites with medium level landslide densities, while soil layers exhibit relatively little landslide activity (unfortunately it is unclear what constitutes „soil layers’, in this study). In addition it is suggested that lithology exhibits a clear control on landslide type. The general observation here is that slides occur in soft rocks whereas rock falls and avalanches are more likely to occur in hard rocks (presumably based in the classification of Varnes 1978). Wang *et al.* (2009) undertook a field

investigation of 12 earthquake induced landslides distributed throughout the impact zone (locations shown in *Figure 4.24*). From this they concluded that particularly long run-out landslides occurred in slate, mudstone and shale, such as the Donghekou slide, Shibangou slide, Hongsong Hydropower Station slide, and Wangjiayan slide in Beichuan County. Large rockfalls were found to have occurred in dolomite, such as the Jingjiashan slide, also in Beichuan County. They also suggested that interactions between rock types and hydrology contributed to rapid movements and long run out distances. For example in the Hongsong Hydropower Station slide, deeply weathered granite moved as a debris-flow-like slide. Wang *et al.* (2009) suggested this is due to the saturated and undrained behaviour in the sliding zone.

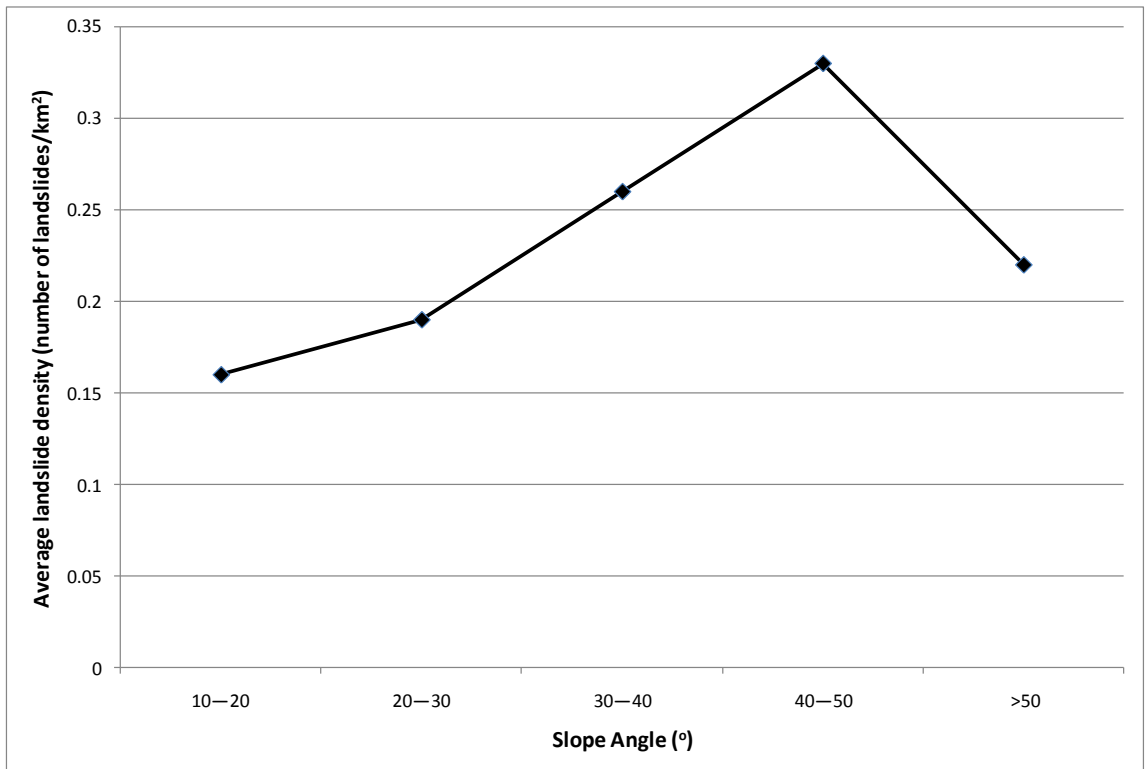


Figure 4.20: Relationship between landslide concentration and hillslope gradient (Huang & Li, 2009).

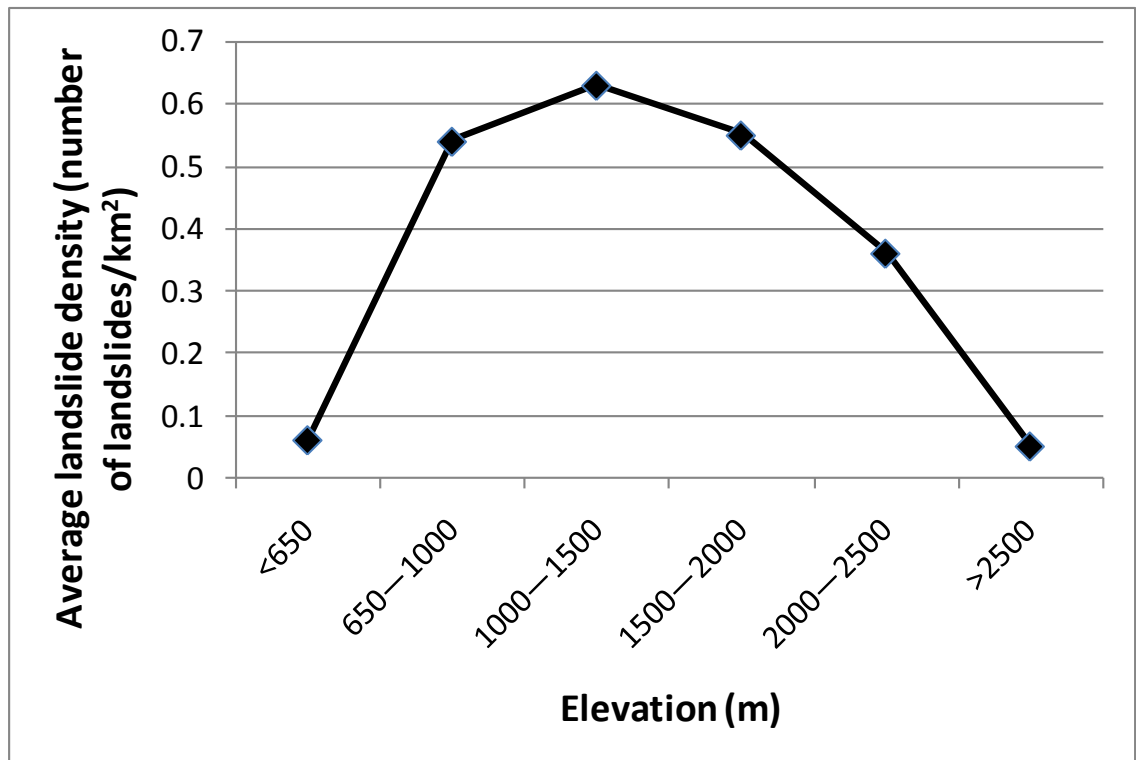


Figure 4.21: Relationship between landslide concentration and elevation (Huang & Li, 2009).

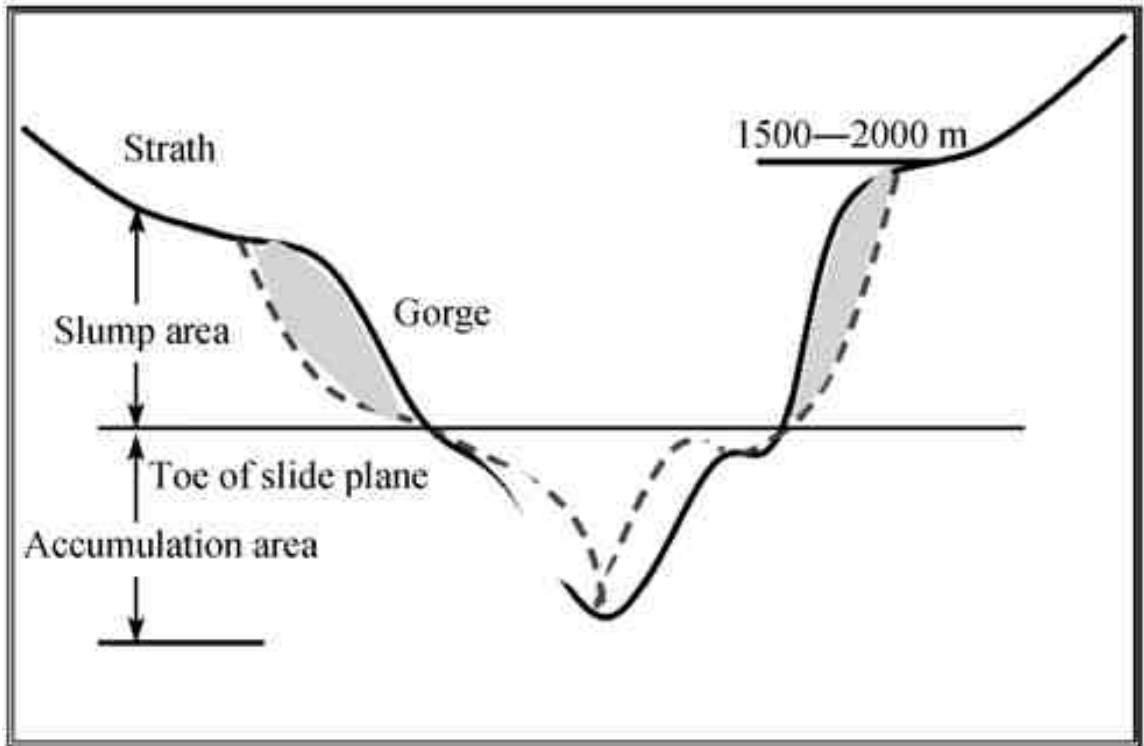


Figure 4.22: Diagram illustrating the occurrence of river valley landslides within the common height range of ~1500m (Huang & Li, 2009).

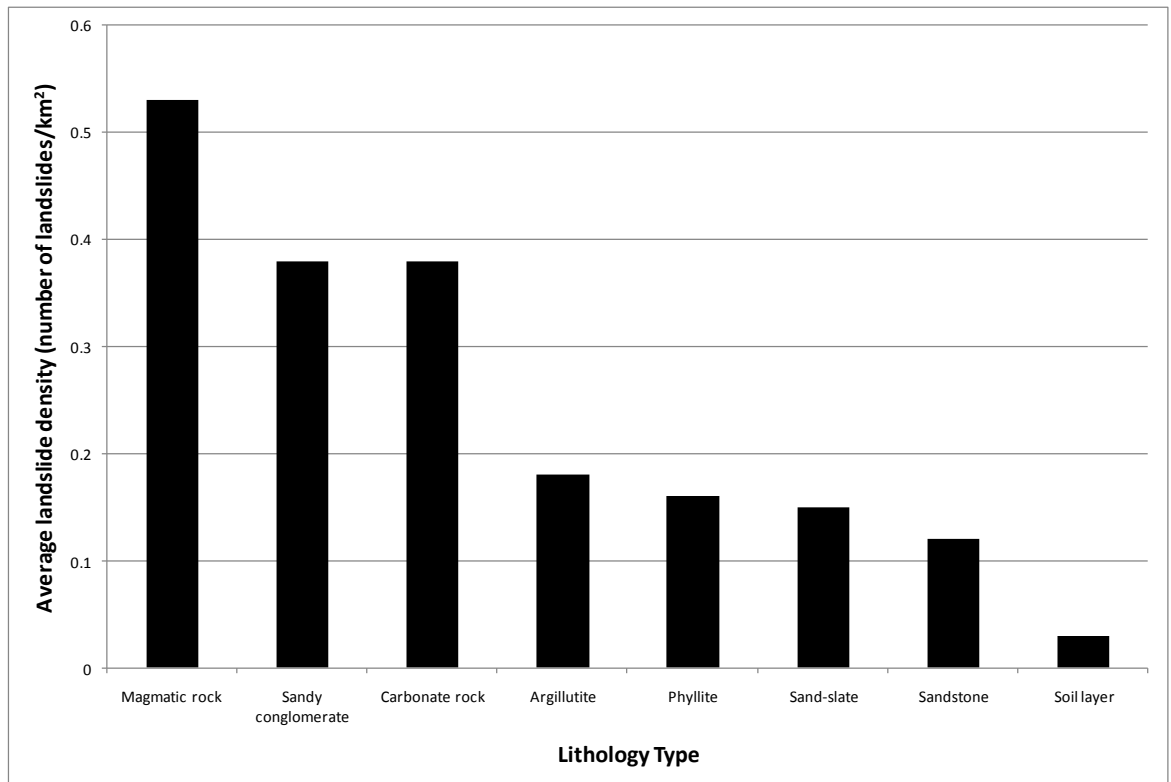


Figure 4.23: Relationship between landslide concentration and rock type (Huang & Li, 2009).

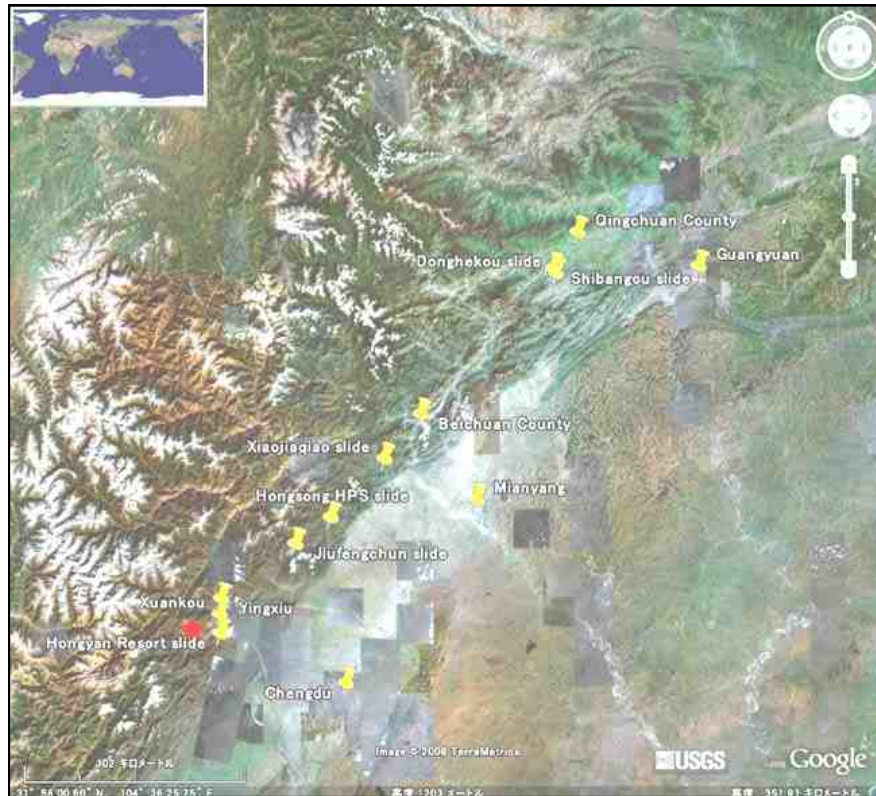


Figure 4.24: Locations of 12 landslides investigated in the field study of Wang et al (2009a).

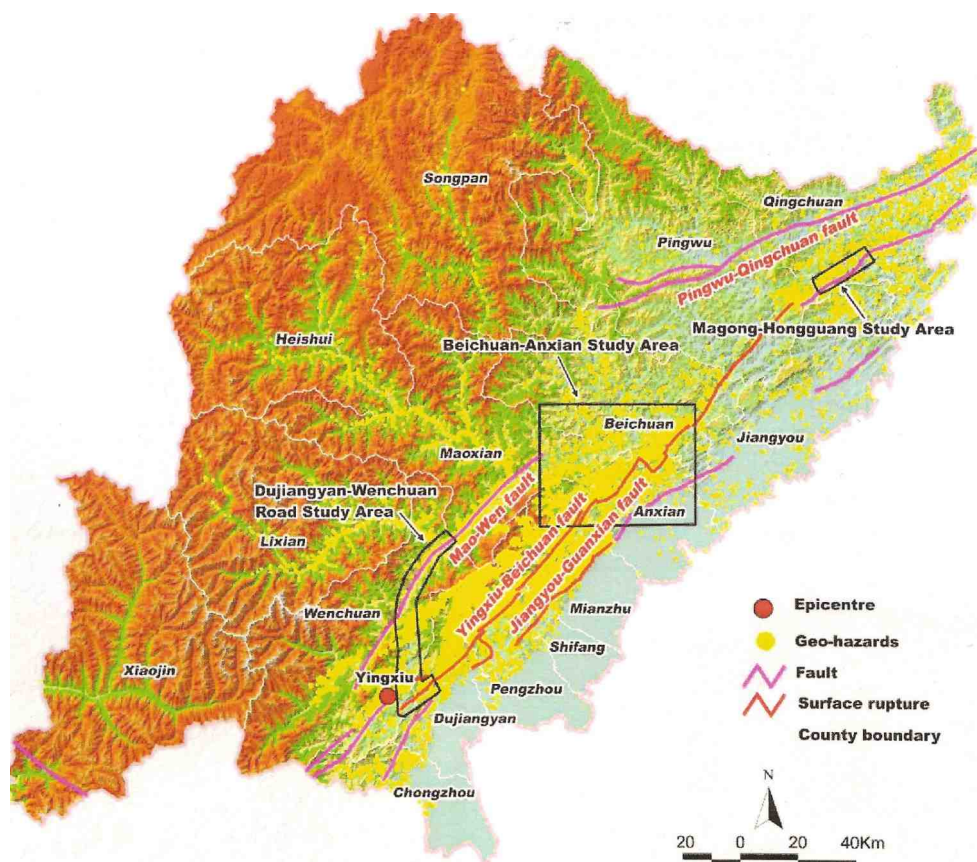


Figure 4.25: Regions of very high landslide impact: Doujiangyan-Wenchuan highway, the Beichuan-Anxian County region, Magong-Hongguang region. (marked by black polygons). (Huang & Li, in press)

4.3.7 Areas of very high landslide concentration

Huang & Li (in press) identified three areas in which the concentration of co-seismic landsliding was exceptionally high. These, shown in *Figure 4.25*, are the Dujiangyan-Wenchuan highway, the Beichuan-Anxian County region, and the Magong-Hongguang region.

Dujiangyan-Wenchuan highway region

The Dujiangyan-Wenchuan highway is a 90km long stretch of road which follows the valley of the Min River between Dujiangyan and Wenchuan. This area is close to the epicentre (ranging from ~5-40km) and to the south crosses the Yingxiu-Beichuan fault, which was active during the earthquake. Along this valley a very high density of landsliding was experienced, with several areas of continuously linked landslide scars (as shown in *Figure 4.26*). The highway here provides an important communication link connecting Wenchuan and its surrounding counties with Dujiangyan, Yingxiu and towns in the Sichuan Basin. A total of 22km of this road (24% of the road's total length) is reported to have been destroyed by landslides triggered by the earthquake (Huang & Li, in press).

Beichuan-Anxian County region

This was reportedly the most severely damaged area during the earthquake, through which the co-seismic Yingxiu-Beichuan fault passes. Despite this region being between 80 and 150km from the epicentre, large fault displacements were recorded (e.g. Liu-Zeng *et al.* 2009; Densmore *et al.* in review; Shen *et al.* 2009) which appear to correlate with the high density of landsliding. Huang & Li (in press) estimate that 5% of the area is covered by landslides, with high densities of up to 0.8 landslides/km². Also in this area are the Daguangbao and Wenjiahou landslides, which are the first and second largest slope failures that occurred in this event, respectively. Beichuan Town in the northwest of this region was also the most damaged urban area, where several large landslides descended into the town. Upstream from Beichuan the Jian River valley, the large Tangjiashan landslide dammed lake also formed, which severely threatened the town's survivors for a time after the earthquake until it was drained through intensive excavation of a drainage channel (Liu *et al.*, 2009)

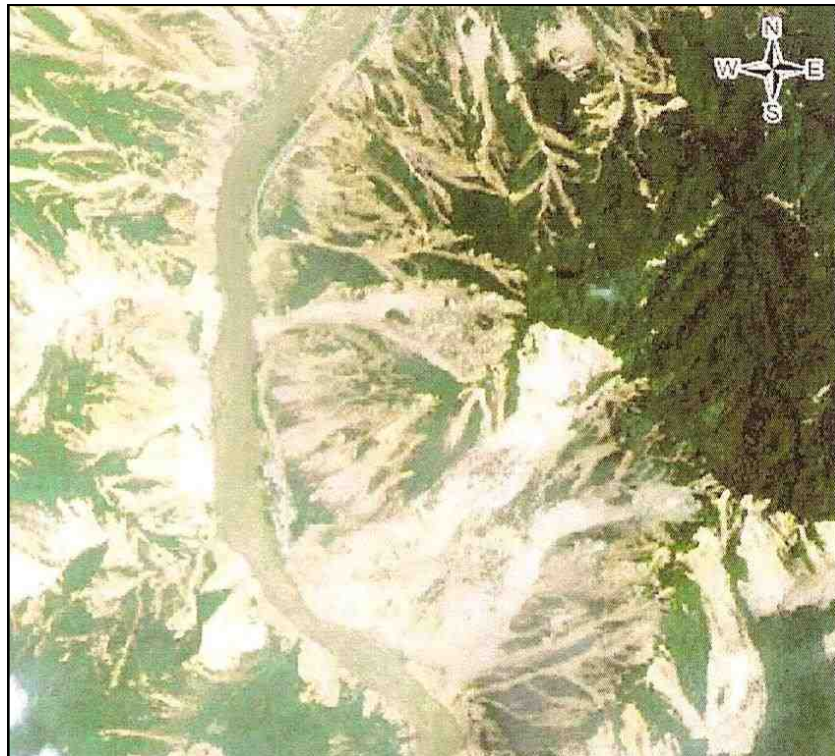


Figure 4.26: Aerial image of high density of landslides in Doujiangyan-Wenchuan highway region (Huang & Li, in press)

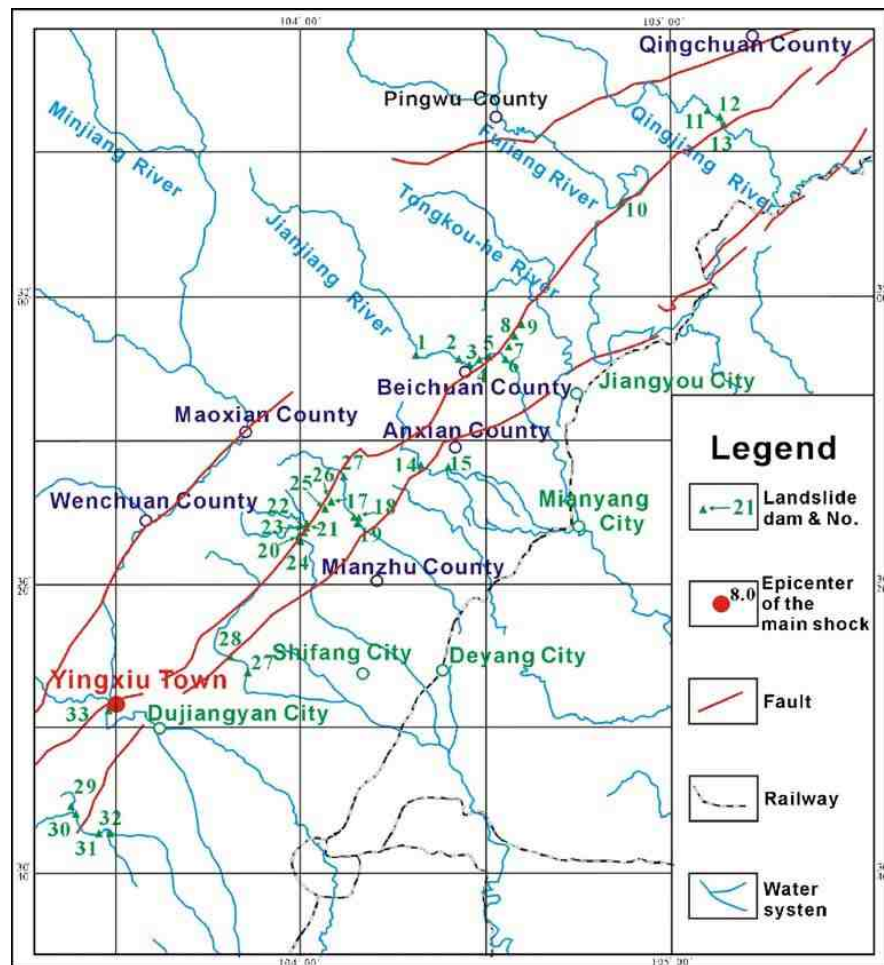


Figure 4.27: Locations of landslide dams created by the Wenchuan Earthquake. (Yin et al, 2009)

Magong-Hongguang region

Around 200km northeast of the epicentre, a third region severely affected by landsliding is the area between Magong Town and Hongguang Town. Again the Yingxiu-Beichuan fault passes through this region, where landslides of “comparatively high concentration and large scale” are recorded (Huang & Li, in press: 4). According to Huang & Li’s analysis of aerial images for this region, nearly 10% of the area is covered by landsliding, with 35 landslides of area larger than 50 000m². Here the main rock types are phyllites and carbonates.

4.3.8 Landslide dammed lakes

Numerous landslide dams also formed along major river valleys. These features blocked several rivers allowing large lakes to form on the upstream side of the dam. Listed from northeast to southwest, the following rivers were blocked: the Qing River, the upper stream of the Fu River, the Tongkou River, the Jian River, the Xiushui River, the Baishui River, the Mianyuan River, the Shiting River, the Min River, and the Xi River (Yin *et al.* 2009), shown in *Figure 4.27*. Of the lakes formed, eight had water volumes greater than 5 million m³, and 11 were of between 1 and 5 million m³ (Cheng *et al.* 2008). Landslide dammed lakes are of particular concern as the valley blocking deposits are likely to collapse resulting in catastrophic outburst floods downstream of the dam (e.g. Hancox *et al.* 2005). The hazard posed by these features depends on a combination of dam height, dam deposit structure, total lake capacity, probability of flash flooding and duration before the dam is filled to capacity. As such those dams of greatest height, blocking rivers with the largest catchment areas pose the largest potential hazard.

In order to manage the hazard posed by valley blocking landslides, two main strategies were utilised. If the landslide mass was sufficiently stable the lake was preserved, while allowing water to flow out through a spillway. Spillways were dug and stabilised using large boulders, with a system of stepped pools constructed in the channel in order to reduce the force of discharge (Wang in press). For example, this strategy was applied in the management of dams along the Jian (Tongkou) and Min Rivers. A second method was to drain the lake before it has chance to fill to capacity. This was carried out by digging spillways which the

outflow of water then eroded, until the lake has emptied. This technique was applied in order to manage the Tangjiashan landslide dam.

Following preparation of this review, a more holistic, up-to-date review of landslide dammed lakes created in the Wenchuan earthquake is now available (Ciu & Sombatpanit 2009).

4.3.9 Summary

As of April 2009, several key studies had been published regarding landslides triggered by the Wenchuan Earthquake. Whilst no holistic 2 or 3 dimensional regional mapping of landslide features has yet been undertaken, these studies still reveal several important characteristics of the distribution. The magnitude of seismic ground motion, inferred through the earthquake's co-seismic structures, is a first order distance control on the spatial distribution of landslides. Of secondary importance is the location of major river valleys which determine more precisely where in the landscape many of the landslides occur. At the local scale landslides occur on slopes with gradients between 20° and 50°, with higher frequencies on steeper slopes within that range. A logical link can be inferred between the spatial distribution of steep slopes and the steep sides of major river valleys. As such the combination of river undercutting and over-steepening of slopes by fluvial erosion conceptually explains the hydrological control on the density of landslide occurrence. Lithology is identified as influencing both the distribution and type of slope failures. Higher landslide densities appear to occur in harder rocks, whereas fewer failures occur in soft rocks and soil. Slide-type failures were also found to occur in softer, more plastically deforming rocks such as slate, mudstone and shale, whereas rock falls and avalanches occurred in harder rocks such as dolomite. In addition, saturation of certain rock types is presented as contributing to high failure velocities and long run out distances.

In terms of the spatially distributed magnitude of the landslide impact, the following 3 main areas of landslide concentration have been identified: Dujiangyan-Wenchuan highway, the Beichuan-Anxian County region and the Magong-Hongguang region. These areas demonstrate a culmination of factors contributing to high landslide density, exhibiting close proximity to the surface expression of the

co-seismic Beichuan fault as well as being situated on major rivers. In addition to the hazard posed by landslides themselves, the additional secondary hazard of landslide dammed lakes and resultant outburst flooding was also present, with several large landslide dams formed by the earthquake.

While studies conducted to date appear to reveal a first order estimate of the distribution of earthquake-triggered slope failures, this analysis is predominantly based upon point locations of landslides, while little consideration is given to the size or geometry of failures. In addition, analysis of controls on the spatial distribution of landslides has been carried out using slope, elevation, lithology type, and location relative to co-seismic and hydrological features. However, this is a very limited range of geophysical variables known to influence the distribution of landslides (see *Section 3.1*). The analysis techniques applied are also relatively simplistic, with no multivariate analysis, or consideration of interactions between geophysical parameters. As such, holistic regional scale mapping of landslides combined with consideration of a wider range of seismic, topographic, hydrological and geological factors, and more sophisticated analysis techniques, are required to further understand the landslide distribution and controls upon it.

4.4 Chapter Summary

A detailed background to the Wenchuan earthquake along with review of current knowledge and understanding of the landslide distribution has been provided. Key areas for further investigation have also been identified, and as such this study is now well placed to further explore the landslide distribution. A key requirement of this is the production better landslide inventory data for the event, as conducted in the following section.

Chapter 5

Production of a landslide inventory map

The following chapter details the production of a landslide inventory map for the Wenchuan earthquake. The identification and acquisition of suitable imagery for mapping is first described. Then the process of semi-automated landslide detection algorithm development and evaluation is discussed.

5.1 Acquisition of imagery for landslide mapping

As outlined in *Section 3.2*, high resolution optical satellite imagery affords spatial and spectral data appropriate for landslide mapping, at lower cost than aerial surveys. In this section the characteristics of imagery captured by seven optical satellite remote sensing systems in the aftermath of the Wenchuan earthquake are examined. The suitability of the imagery for landslide mapping is reviewed in order to identify imagery appropriate for use in this investigation.

5.2 Available satellite imagery

A broad range of satellite imagery types are now available, captured by numerous different sensor systems. This investigation required imagery captured from within a specific spatial and temporal window, covering the rupture zone during aftermath of the Wenchuan earthquake. In addition, imagery of spatial and spectral resolution appropriate for landslide identification and delineation was also required. In general it has been shown that both higher spatial and spectral resolution is favourable for the identification and delineation of landslide scars (Petley *et al.* 2002). A key consideration for acquisition of imagery in the Sichuan region is climate. The region is affected by both the Southeast Pacific Ocean monsoon, and the Southwest Indian Ocean monsoon. The Longmen Shan's location at the edge of the high Tibetan Plateau results in high levels of orographic rainfall. For these reasons cloud and haze free imagery of the region is very difficult to obtain. As such it was necessary to review data from a range of different image types, in order to compile the most complete coverage of the study area possible. Exemptions from this review were data from aerial and active (radar) systems. While it was reported that aerial imagery of the rupture zone was captured following the earthquake, no aerial imagery has yet been made available for public acquisition or preview. Though radar data can be acquired independent of cloud cover, their use in landslide remote sensing is still in its infancy and little work into automated landslide classification has yet to be undertaken. In addition, geometric layover effects in Side Looking Radar (SLR) imagery make it difficult to use in areas of steep terrain. As such, only imagery from optical satellite systems was reviewed, from the following sensors:

1. Quickbird
2. IKONOS
3. ALOS (Advanced Land Observing Satellite), PRISM sensor
4. SPOT 5
5. EO-1 (Earth Observing 1)
6. Landsat 7 EMT+
7. UK-DMC (Disaster Monitoring Constellation)

Sensor and imagery specifications are given in *Table 5.1*

Here characteristics of available imagery from the above systems are discussed in order to assess their suitability for use in this type of investigation.

Sensor system	Imagery source	Spatial resolution	Band Colour	Wavelength (μm)
Quickbird	http://www.digitalglobe.com/	0.61m	Panchromatic	0.45 - 0.9 μm
		2.44m	Blue	0.45 - 0.52 μm
		2.44m	Green	0.52 - 0.6 μm
		2.44m	Red	0.63 - 0.69 μm
		2.44m	Near Infrared	0.76 - 0.9 μm
IKONOS	http://geofuse.geoeye.com	0.8m	Panchromatic	0.45-0.90 μm
		4m / 1m pan-sharpened	Blue	0.445-0.516 μm
		4m / 1m pan-sharpened	Green	0.506-0.595 μm
		4m / 1m pan-sharpened	Red	0.632-0.698 μm
		4m / 1m pan-sharpened	Near Infrared	0.757-0.853 μm
ALOS - Prism	http://www.eorc.jaxa.jp/ALOS/obs/palsar_strat.html	2.5m	Panchromatic	0.52 - 0.77 μm
SPOT 5	http://www.spotimage.fr/	5m	Panchromatic	0.50 - 0.89 μm
		10m / 5m pan-sharpened	Green	0.50 - 0.59 μm
		10m / 5m pan-sharpened	Red	0.61 - 0.68 μm
		10m / 5m pan-sharpened	Near Infrared	0.78 - 0.89 μm
		10m	Mid Infrared	1.58 - 1.75 μm
EO-1	http://glovis.usgs.gov/	10m	Panchromatic	0.48 - 0.69 μm
		30m / 10m pan-sharpened		0.433 - 0.453 μm
		30m / 10m pan-sharpened	Blue	0.45 - 0.515 μm
		30m / 10m pan-sharpened	Green	0.525 - 0.605 μm
		30m / 10m pan-sharpened	Red	0.63 - 0.69 μm
		30m / 10m pan-sharpened	Near Infrared	0.775 - 0.805 μm
		30m / 10m pan-sharpened	Near Infrared	0.845 - 0.89 μm
		30m / 10m pan-sharpened		1.2 - 1.3 μm
		30m / 10m pan-sharpened	Mid Infrared	1.55 - 1.75 μm
		30m / 10m pan-sharpened	Short Wave Infrared	2.08 - 2.35 μm
		30m / 10m pan-sharpened	Short Wave Infrared	2.08 - 2.35 μm
Landsat 7 ETM+	http://glovis.usgs.gov/	15m	Panchromatic	0.52 - 0.90 μm
		30m / 15m pan-sharpened	Blue	0.45 - 0.515 μm
		30m / 15m pan-sharpened	Green	0.525 - 0.605 μm
		30m / 15m pan-sharpened	Red	0.63 - 0.690 μm
		30m / 15m pan-sharpened	Near Infrared	0.75 - 0.90 μm
		30m / 15m pan-sharpened	Mid Infrared	1.55 - 1.75 μm
		30m / 15m pan-sharpened	Thermal Infrared	10.40 - 12.5 μm
		30m / 15m pan-sharpened	Short Wave Infrared	2.09 - 2.35 μm
UK-DMC	http://www.dmcii.com/	32m	Near Infrared	0.77 - 0.90 μm
		32m	Near Infrared	0.77 - 0.90 μm
		32m	Red	0.63 - 0.69 μm
		32m	Red	0.63 - 0.69 μm
		32m	Green	0.52 - 0.60 μm
		32m	Green	0.52 - 0.60 μm

Table 5.1: Sensor systems and attributes of imagery available for remote sensing of Wenchuan earthquake triggered landslides.

5.2.1 Quickbird and IKONOS

Quickbird and IKONOS systems provide the highest spatial resolution imagery examined, between 0.61m and 1m pan-sharpened multispectral products. Even within 10m resampled preview images, landslides areas are clearly visible using these data types. As in all imagery obtained, areas of bare soil produce strong contrast to surrounding vegetated areas. Thus landslide scars are distinct. However, the coverage offered by Quickbird and IKONOS imagery is limited for a number of reasons. IKONOS imagery is available in relatively small 11x11km individual scenes, of which very limited cloud free coverage was available for the study area. Similarly, Quickbird is limited to small 16x16km squares, or 16x165km strips. The flight path of these strips runs north to south, crossing the rupture zone at around a 45° angle. While many scenes would therefore be needed to cover the area of interest, very little cloud free imagery was available for time following the earthquake. In addition, both imagery types are very expensive to purchase at between \$16 – 20/km².

5.2.2 ALOS-PRISM

ALOS imagery was provided for use in this study by the USGS, purchased at \$0.3/km². The spatial resolution of the imagery is still high at 2.5m, however only a single panchromatic band is available via the PRISM instrument. Although landslides can be visually identified in cloud free areas of the imagery, the images again suffer from very high levels of cloud cover and additional haze in cloud free regions. The contrast between landslides and surrounding regions is not as sharp as in other panchromatic images reviewed. Haze acts to further reduce the contrast. The result is that, while landslides may be visually identified, few histogram features exist with which information may be extracted from the image. Cloud cover and limited image availability also result in fairly poor coverage of the study area.

5.2.3 SPOT 5

SPOT 5 imagery was available for the study area in 5 – 10m panchromatic and multispectral formats. While smaller features are masked by the relatively lower resolution of SPOT, landslides are still clearly visible in the imagery. Landslides

are visible in the panchromatic imagery, but can be more clearly distinguished in multispectral scenes. Here landslides appear very brightly in red (2) and NIR (3) bands, in contrast with darker green surrounding vegetated areas. Through a combination of scenes captured during September and November 2008, and January 2009, around 24 000km² of cloud free imagery was available covering a length of 300km along the rupture zone. In addition to fortunate data capture conditions, the south-west to north-east flight path of the SPOT 5 satellite helped achieve such a good coverage, with scenes closely aligned to the SW-NE rupture trend. While imagery costs for SPOT 5 data are still relatively high at \$1.05–2.1/km², these are nonetheless far more accessible than Quickbird and IKONOS for regional scale investigations.

5.2.4 EO-1 ALI

The EO-1 ALI satellite does not continuously acquire imagery, but responds to data acquisition requests. On 7th July 2008 a single 4000km² scene was captured in the south-west of the rupture zone, at the time costing around \$0.085 / km². These data have since been made freely available via USGS Glovis (<http://glovis.usgs.gov/>). The along fault flight path again helps create a suitable image coverage. Landslides are visible in sharp contrast in this 10m panchromatic imagery. Landslides appear much brighter and lighter than surrounding dark areas of vegetation. However, landslides are more visible on east facing valley sides, as the image is lit from the east by a sun azimuth of 105° and elevation of 66°. Landslides on west facing slopes are much darker and more difficult to identify with the limited spectral information. While 30m pixel, nine-band multispectral imagery is also available from the ALI system, this was not available until after landslide mapping for this investigation was completed.

5.2.5 Landsat 7 ETM+

Data from the Landsat 7 archive and new acquisitions are now available to be freely downloaded via USGS Glovis (<http://glovis.usgs.gov/>). The large scene area of around 31000km² allowed data for the study area to be easily obtained. The spectral information available in Landsat 7 bands can be used to produce a range of false colour composite and principal component analysis combinations, through which different landslide features can be identified (Petley *et al.* 2002). However,

the low (30 - 15m) spatial resolution of Landsat means that many smaller features are not resolved, and only larger landslide features triggered by the earthquake were visible. In addition, the scan line corrector (SLC) which compensates for the forward motion of the satellite stopped working in 2003. The result is a zigzag geometric distortion effect across the image. As such, only a small central portion of the data acquired over the rupture zone was suitable for landslide identification, and extensive processing of the imagery would be required before mapping could be undertaken.

5.2.6 UK-DMC

Under an activation of the International Charter for Space and Major Disasters, imagery was acquired from the Disaster Monitoring Constellation UK-DMC satellite. These data were made freely available to those undertaking research in the area. Similar to the Landsat 7 data, the suitability of the imagery is limited by its low spatial resolution of 32m. Despite this, the six spectral bands allow areas of bare soil to be clearly identified. The imagery was also available over the entire rupture zone, though significant areas were obscured by cloud. However, the major limitation of the DMC imagery was that excessive cloud cover meant that automated georectification and orthorectification processes had not been carried out (Stephens 2009, pers comm), resulting in offsets of up to 30km.

5.2.7 Summary

While landslides may be best resolved by high spatial resolution multispectral sensors such as Quickbird and IKONOS, the limited scene coverage and cost of imagery reduce their suitability for regional scale investigation. Data freely available from coarser resolution Landsat 7 and UK-DMC satellites certainly reduce the cost and coverage related problems associated with Quickbird and IKONOS. Even with their coarser spatial resolution, these images can still provide a regional first order estimate of landslide coverage. However, geometric image errors significantly reduce their suitability to cartographic functions. A balance between coverage, cost and resolution is achieved through the medium-high resolution imagery of SPOT 5, EO-1 and ALOS. However, the key consideration and challenge for acquisition of appropriate data was finding cloud- and haze-free imagery. Ultimately this is controlled by favourable weather conditions as the

satellite passes over the region. Cloud free imagery was available from SPOT 5 and EO-1 systems. Subsequently, four SPOT 5 scenes and one EO-1 scene were acquired to achieve a total image coverage of around 21000km² (*Figure 5.1*). Details of final imagery acquired are given in *Table 5.2*, along with imagery codes used to refer to particular scenes throughout this chapter. Note that SPOT 5 data was obtained in a combination of 5m resolution in G, R and NIR bands (provided under an agreement with USGS), and additional 5m scenes and lower cost 10m scenes in G, R, NIR and MIR bands purchased separately.

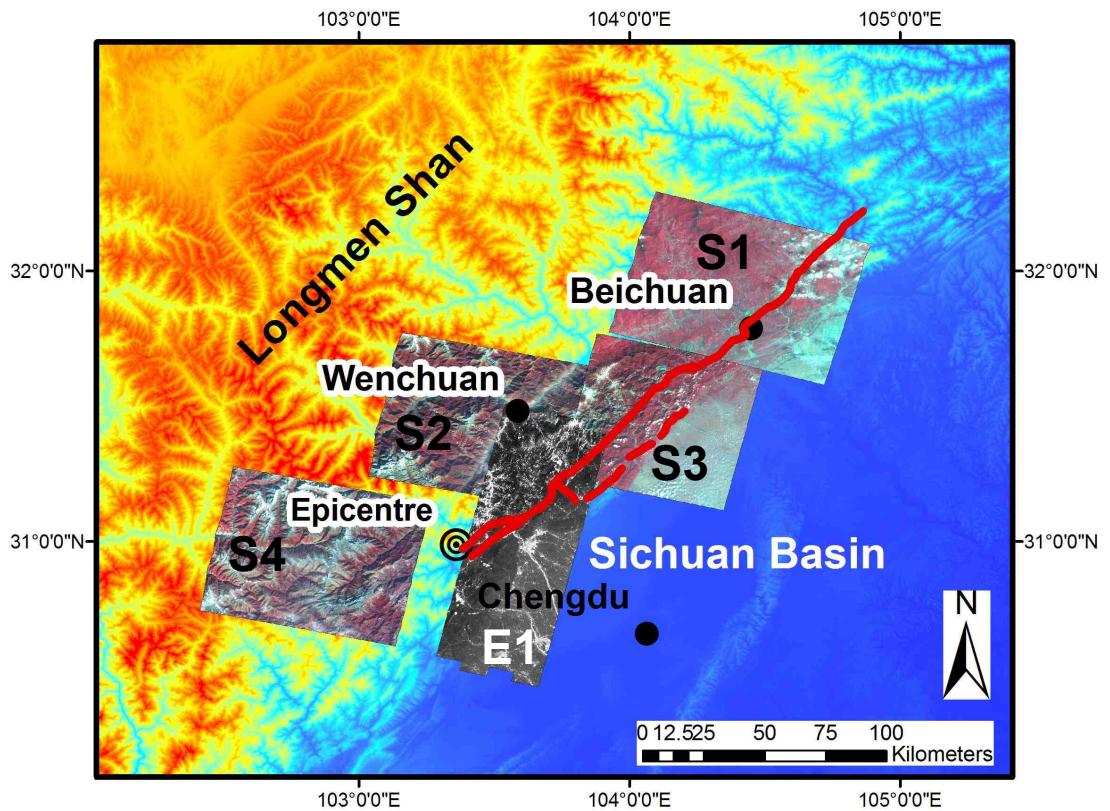


Figure 5.1: Final SPOT5 and E0-1 image coverage used for landslide mapping. Image labels correspond to those in Figure 5.2.

Image Type	Image ID	Image coordinates				Image area (km ²)
		NW	NE	SW	SE	
SPOT 5	S1	104°55.434"E 32°17'31.648"N	104°53'26.747"E 32°5'53.424"N	103°55'30.771"E 31°46'29.857"N	104°43'0.588"E 31°34'51.464"N	4676
SPOT 5	S2	103°9'47.608"E 31°46'13.285"N	103°55'52.923"E 31°38'0.9"N	103°2'0.091"E 31°14'48.295"N	103°47'30.59"E 31°6'35.91"N	4458
SPOT 5	S3	103°52'58.336"E 31°46'8.014"N	104°29'38.795"E 31°38'38.355"N	103°44'16.922"E 31°14'33.706"N	104°20'52.598"E 31°7'13.614"N	3592
SPOT 5	S4	102°32'19.099"E 31°16'30.09"N	103°16'1.612"E 31°8'38.627"N	102°24'52.192"E 30°44'59.327"N	103°8'10.149"E 30°36'58.042"N	4260
EO-1 ALI	E1	103°32'36.988"E 31°30'22.788"N	103°55'14.72"E 31°23'35.469"N	103°17'24.291"E 30°34'48.803"N	103°39'46.937"E 30°27'53.94"N	4043

Image Type	Image ID	Acquisition date	Pixel resolution	Available spectral bands	Cloud cover	Look angle	Sun azimuth	Sun elevation
SPOT 5	S1	04/06/2008	5m	G R NIR	8%	29.85	122.78	74.03
SPOT 5	S2	15/12/2008	10m	G R NIR MIR	10%	27.91	155.04	31.04
SPOT 5	S3	13/10/2008	10m	G R NIR MIR	10%	3.67	150.95	32.32
SPOT 5	S4	15/01/2009	10m	G R NIR MIR	0%	25.17	154.54	47.30
EO-1 ALI	E1	07/07/2008	10m	Panchromatic	9%	11.13	104.73	66.28

Table 5.2: Attributes of imagery selected for landslide mapping

5.3 Landslide mapping methodology

In order to examine the regional distribution of landslides visible in the acquired satellite imagery, a landslide inventory map delineating seismically triggered landslide areas is required as a basis for analysis. However, the large number of landslide features triggered by the earthquake presents a significant challenge to producing a holistic landslide map. In order to avoid long working periods associated with manual delineation of landslides, semi-automated techniques for the identification and delineation of landslides have been produced. The following section describes the series of stages through which a satisfactory method was developed, and presents an evaluation of the algorithm based on comparison to manually delineated landslide samples.

5.3.1 Image processing software and coordinate system

Image processing and GIS analysis in this section of the investigation was carried out using the following computer packages and add-on tool-packs:

- ERDAS Imagine 9.3
- ENVI 4.6.1
- ArcMap
 - Spatial analysis tools and Spatial analyst toolbar
 - 3D analysis tools
 - ETGeowizards (http://www.ian-o.com/ET_GeoWizards/gw_main.htm)

All analysis was carried out in the WGS 1984 UTM (zone 48) coordinate system.

5.3.2 Temporal control: pre- and post- Wenchuan earthquake landslides

In order to capture the landslide impact of the earthquake from satellite imagery taken after the event, temporal control on the occurrence of mapped landslides is required. This allows for an awareness of whether landslides were triggered by the earthquake, or were present in the region prior to the event. In order to achieve this, addition imagery captured prior to the earthquake was also acquired. Landsat

5 imagery of the region captured until the end of 2007 is freely available through USGS Glovis (<http://glovis.usgs.gov>). Two images were downloaded from June and September 2007, providing almost complete cloud free coverage of the study area. Landsat 5 bands 2, 3 and 4 are comparable to Spot 5 bands 1, 2 and 3 (respectively). In addition, multispectral bands for the post-earthquake EO-1 image were obtained towards the end the investigation, which also provide similar radiometric bands for direct visual comparison.

Visual comparison of pre- and post-earthquake imagery demonstrates that the study area was barely affected by landsliding prior to the event. From this period imagery show virtually no landslides, compared with large numbers of landslides visible in post-earthquake imagery (for example see *Figure 5.2*). In addition, this finding is back up by very few reports of landslides in literature on the region, and observations from field investigations (Densmore 2009, pers comm). Therefore, mapping of landslides visible in post-seismic imagery will record predominantly seismically induced landslides (co- or immediately post-seismic failures), with minimal contribution from pre-earthquake events. Based on this finding, mapping of the landslide distribution is undertaken using a single image approach, without the need for multi-temporal change detection.

5.3.3 Pre-processing enhancements

Prior to image classification and extraction of landslide features, a number of textural and spectral image enhancement techniques were applied to the imagery in an attempt to improve their suitability for landslide mapping. While some of these processes would have improved the condition of imagery for manual landslide classification, no processes were found to improve the suitability of imagery to the automated mapping techniques. In fact, both the Spot 5 and EO-1 images were already well suited to the application of automated classification algorithms, due to the high levels of intensity and colour contrast with which landslide features are depicted.

5.3.4 Automated classification of landslides

Classification is the process whereby pixels in an image are sorted into categories, based on certain sets of criteria. These criteria are analysed by means of spectral

and/or spatial pattern recognition techniques. In the case of this investigation it was required that pixels were classified into two discrete groups: landslide and non-landslide. As such, a binary approach to image classification was adopted, with the aim of generating a binary classification dataset of landslide (=1) and non-landslide (=0) areas.

The data available for landslide classification are the pixel values of available radiometric bands for each region of imagery, as well as elevation from the SRTM DEM dataset. As the spatial characteristics of landslides vary in size over several orders of magnitude, as well as in shape and orientation, spatial pattern recognition is difficult to achieve. However, the spectral properties of landslide scars are much more homogenous and easily recognised using computer programmable techniques. This is due to the fact that landslide scars produce areas of bare soil, which exhibit a highly contrasting spectral and intensity signature in comparison to surrounding vegetated areas. As shown in *Figures 5.3 and 5.4*, bare soils exhibit higher reflectance than vegetation in SPOT G, R and MIR bands, and lower reflectance than vegetation in the NIR; in the EO-1 panchromatic band, bare soils predominantly exhibit higher reflectance than vegetation. Thus systems of spectral classification are applied to extract landslide features. In order to categorise pixels, the computer system must first be trained to recognise spectral patterns in the data (e.g. Lillesand *et al.* 2004; Drury 1987). Two main techniques exist for training and classifying imagery: supervised classification and unsupervised classification. The following section describes each of these techniques, and their applicability and performance in the classification of landslides.

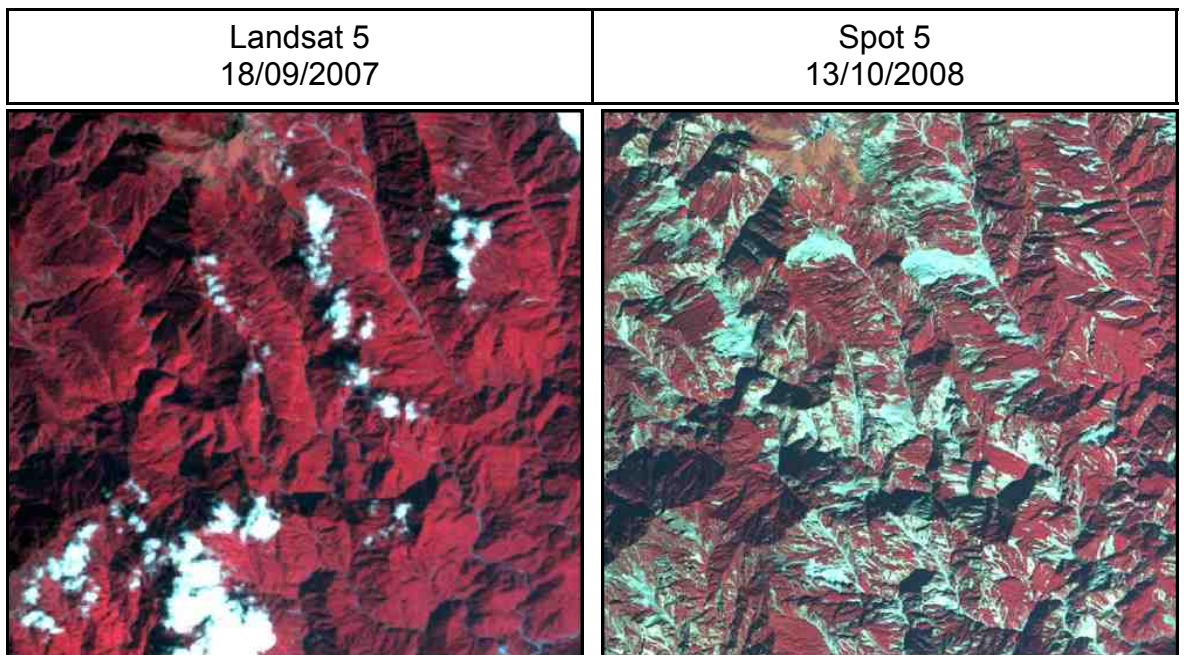


Figure 5.2: Comparison of Landsat 5 (September 2007) and Spot 5 imagery (October 2008), using G, R and NIR bands. Landslides appear as bright turquoise areas (bare rock and soil). In imagery from 2007 virtually no landslide features are visible (note that white areas are clouds), while a high density of landsliding is visible in imagery from 2008.

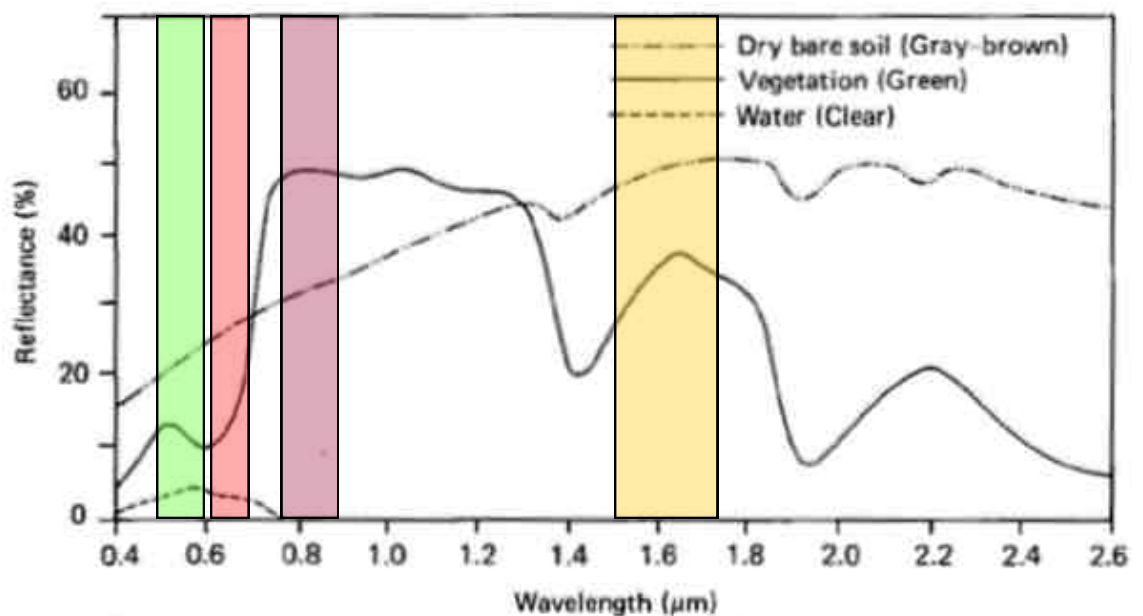


Figure 5.3: Typical spectral signatures of soils (gray-brown), vegetation (green) and water (clear). Spot 5 multispectral bands are shown in colours. Green = Green, Red = Red, Purple = NIR, Yellow = MIR. (After http://geog.hkbu.edu.hk/virtuallabs/rs/env_backgr_refl.htm).

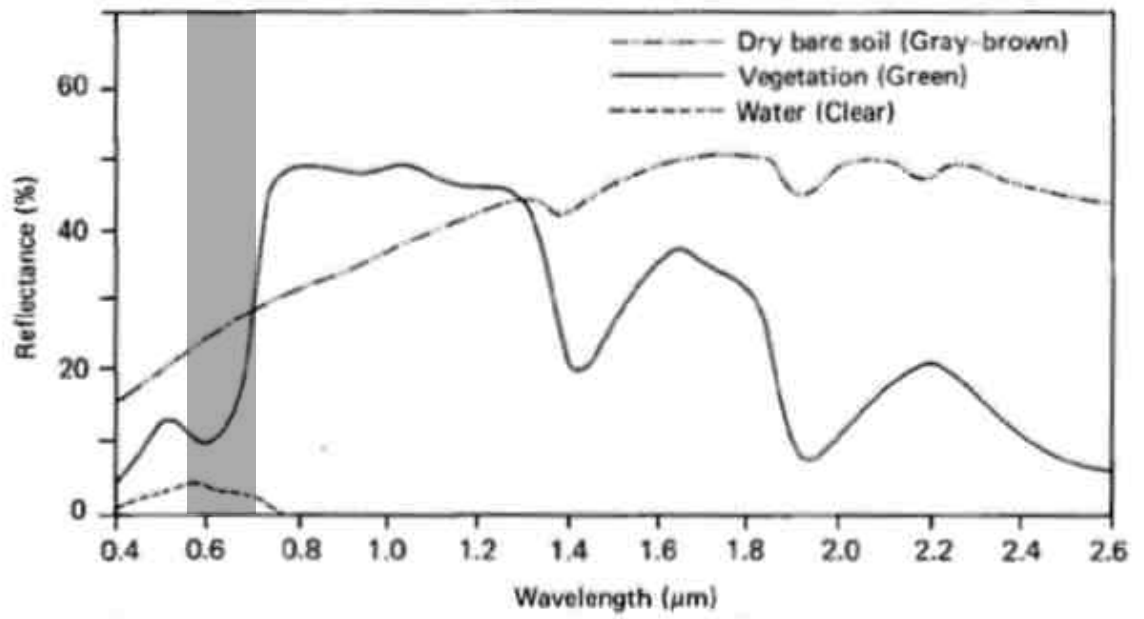


Figure 5.4: Typical spectral signatures of soils (gray-brown), vegetation (green) and water (clear). E0-1 panchromatic band is shown in gray. (After http://geog.hkbu.edu.hk/virtuallabs/rs/env_backgr_refl.htm).

5.3.5 Supervised classification

Through this technique the analyst selects sample areas in an image, which are identifiable as certain features. A maximum likelihood classification model is then used to identify pixels with similar spectral characteristics, and finally assign all regions in the image to a given class (Leica-Geosystems 2002). To apply the technique to this investigation, characteristic landslide and non-landslide training areas were selected in SPOT 5 imagery, and image pixels output into two corresponding classes. This was carried out using the *supervised classification tool* in ERDAS Imagine 9.2. Despite attempting a number of different training sample sizes and combinations, the technique was found to produce highly fragmented landslide features. The major issue here is that landslides produce messy features with highly variable pixel values. This is expected, given the unconsolidated mixture of debris contained within scars and deposits. In addition, many urban areas, arable fields, roads and river channels were wrongly commissioned as landslides, due to their similar spectral properties (as shown in *Figure 5.5*).

In an attempt to improve upon this result supervised classification was also carried out using a stack of spectrally enhanced images (principal component and ratio images), which all exhibit high contrast between landslide and non-landslide areas. Unfortunately this produced similar results.

5.3.6 Unsupervised classification

Unsupervised classification consists of a more computer-automated approach to identifying spectral signatures. A user-defined number of classes are determined based on spectral distinctions in the n-dimensional feature space. The technique is used to output a given number of classes, which can then be interpreted to assign meaning by the user. Despite the final binary output required for this investigation, it is possible to first produce a number large number of output classes, which can then be reclassified into those characterising landslide and non-landslide regions. Unsupervised classification images were produced for all multispectral SPOT 5 scenes using the ERDAS Imagine 9.2 *unsupervised classification tool*. Default maximum likelihood settings for the process were used.

Borghuis *et al.* (2007) found that 32 classes were appropriate to satisfactorily separate landslide and non-landslide areas in SPOT 5 images of southern Taiwan (Section 3.2). However, 32 classes proved inadequate across many areas of the Sichuan imagery. In order to provide a conservative increase in class resolution and produce a diverse platform for reclassification, 100 unsupervised classes were used. The resultant image was then reclassified into a binary mask based on visual identification of landslide and non-landslide areas. This was most straightforwardly achieved by importing both the original and classification images into ArcMap for visual overlay analysis. The problem of feature fragmentation is avoided as signature classes were selected to encapsulate full landslide areas. Final binary reclassification was performed using the *reclassify* function, within the ArcMap *Spatial Analysis toolpack*.

A very clean delineation of landslide features with no identifiable errors of omission was achieved. However, like the supervised classification result, large errors of commission were produced, where urban areas, arable fields, roads and rivers were wrongly classified as landslides (as shown in *Figure 5.6*).

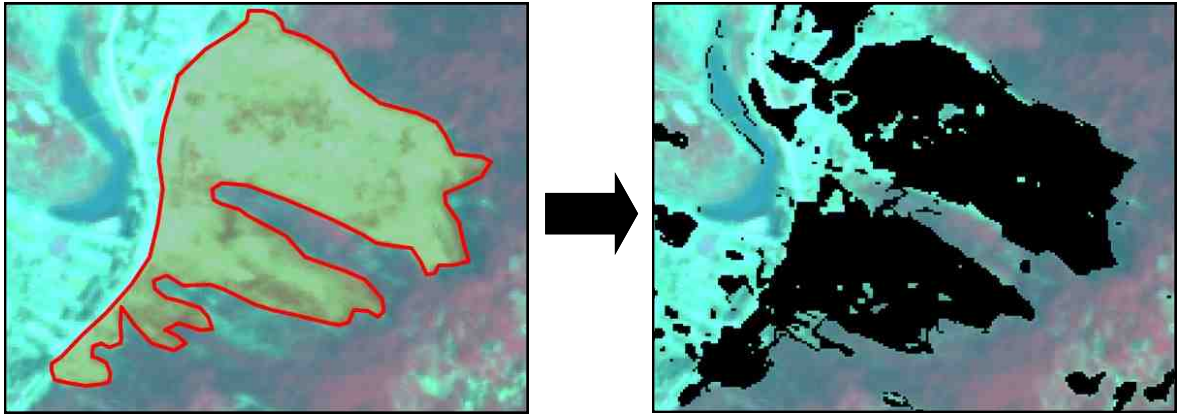


Figure 5.5: Comparison between manual delineation of landslide (left) and supervised classification result (right)

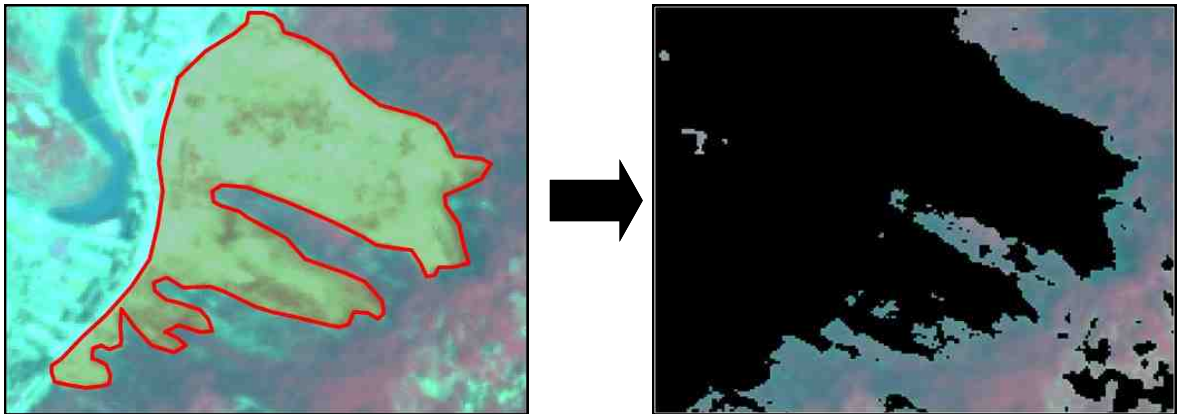


Figure 5.6: Comparison between manual delineation of landslide (left) and unsupervised classification result (right).

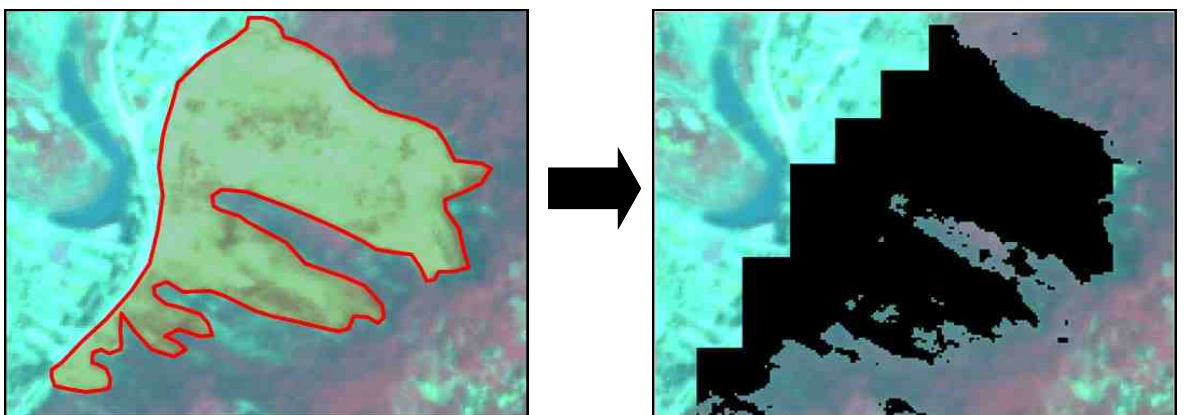


Figure 5.7: Comparison between manual delineation of landslide (left) and unsupervised classification result combined with slope filter (right).

5.3.7 Classification filtering

In order to filter out errors of commission whilst not obscuring true landslide areas, a combination of filters based on the slope, aspect and geometry of features were applied to the classification result.

I. Slope Mask

Borghuis *et al.* (2007) developed a method of filtering errors of commission based on slope derived from 40x40m elevation data. It was identified that most wrongly commissioned urban areas, roads, farmland and riverbeds occur on shallow slopes, whilst landslides have much steeper slope angles (e.g. Chang and Slaymaker 2002). Through experimentation with different slope masks Borghuis *et al.* (2007) concluded that a threshold of 28° was appropriate to effectively remove the majority of false positives whilst not excluding true landslide areas.

In order to apply the technique to this investigation, a DEM with the maximum available resolution of 90m (USGS SRTM) was used. A raster of slope gradient (assessed on a 270x270m window) was derived from this data using the ArcMap Spatial Analyst toolbar. A series of binary rasters were generated using the spatial analyst reclassify function, classifying pixels above a given slope threshold as 1, and those below the threshold as 0. These were generated at intervals of 1° for all slopes between 10° and 40° . In order to erase regions with lower than threshold slope values from the landslide classification, binary slope-mask and classification rasters were multiplied together at the highest input resolution using the ArcMap *3D analysis>raster math tool*. The resultant image is a binary raster of landslide and non-landslide areas, with regions shallower than the defined slope threshold removed from the classification (*Figure 5.7*). Optimum slope thresholds were identified through experimentation, based on those which produced the best visual coherence with visually identifiable landslide areas in the original imagery. Slope thresholds applied to each image are given in *Table 5.3*. Appropriate thresholds for different images vary, perhaps due to different lithological material properties, which allow landslides to occur at variable slope gradients. As such a 20° slope threshold was used for images S2, S3, S4, & E1, while 17° was used from S1. Despite the low DEM resolution, this method successfully reduces errors of commission, while additional errors incurred by the pixelization of landslide edges

are of little significance over the large spatial scale at which the study is conducted.

Image	Slope	Noise filter	Circularity ratio	Circularity ratio	Length-width ratio	Orientation-aspect difference
S1	Slope < 17°	Area < 300m ²	Circularity > 0.7	Circularity > 0.6 AND Area < 2000m ²	Length-width ratio > 7	Area < 15000 AND Length-width ratio < 1.5 AND Difference > 40
S2	Slope < 20°	Area < 300m ³	None	None	None	None
S3	Slope < 20°	Area < 300m ⁴	None	None	None	None
S4	Slope < 20°	Area < 300m ⁵	None	None	None	None
E1	Slope < 20°	Area < 300m ⁶	None	None	None	None

Table 5.3: Summary of slope and geometric filters (conditions for object removal) applied to unsupervised landslide classifications

II. Feature oriented filters

Following use of the slope filter, some additional commission errors remained within the S1 image, despite more successful classifications of other images. Numerous fields and roads occur on slopes greater than 20°, and slivers of urban areas and river channels were generated by the coarse slope mask resolution. Arable fields were particularly prominent in S1, primarily due to their higher incidence in the region, but also because of the season of image capture when the ground would still be relatively bare following the harvest period. To further remove this error, landslide classification masks were converted to polygon features (using ArcMap *spatial analyst toolbar*) and a series of feature oriented filters were applied (summarised in *Table 5.3*).

a. Noise filter

A „noise filter’ was applied to all images to remove small, isolated pixel clusters or individual pixels too small to be classified as landslides. Borghius *et al.* (2007) applied a threshold of three adjacent pixels to achieve this, thus enforcing a minimum landslide mapping unit. In order that this unit be constant across all

mapped areas of varying image resolutions, a threshold of three pixels was used for 10m imagery (S2, S3, S4 & E1) while a threshold of six pixels was applied to 5m imagery (S1). Therefore the minimum landslide mapping unit is 300m² for all regions.

b. Geometric filters

While images S2, S3, S4, & E1 produced an accurate classification at this stage in the algorithm, arable fields remained a significant problem in the image S1. However, landslide and non-landslide features can be separated through a number of their geometric characteristics. Key parameters are the 2 dimensional shape at nadir view, and the 3 dimensional direction of the long axis, when combined with a DEM. Thus a series of 2 and 3 dimensional filters were applied to the dataset as described below. Optimum filter parameters were all defined through experimentation based on their best visual result.

i. Circularity Ratio

Circularity ratio was calculated for all S1 polygons using the ArcMap *ETGeowizards > Polygon characteristics* tool. This generates a value between 0 and 1, as a measure of the polygon's circularity. For example, a perfect circle would be 1, while thinner, more elongated polygons would produce lower values. This field is useful in separating small landslides from small arable fields. Small landslides generally produce small but elongated features, perhaps as few as seven pixels in size, whereas small arable fields produce more square or circular features. Hence polygons with the following characteristics were removed:

Circularity > 0.7: All features with circularity greater than this appeared to be non-landslide, field features.

Circularity > 0.6 AND Area < 2000m²: This filter removed small objects which have very limited elongation characteristics. While not all features with circularity > 0.6 are non-landslides, most small features with area < 2000m² do fit this category.

ii. Length-width ratio

Length and width fields were also generated using the *ETGeowizards > Polygon characteristics* tool, from which their ratio was then calculated. While landslide

features can be identified by their higher length-width ratio, objects with very high ratios were generally found to be roads, stream channels or valley bottom slivers created by the slope masking process. Therefore, these were removed using the following filter:

Length-width ratio > 7

iii. Primary axis alignment

When combined with a DEM, landslides may also be identified by the alignment of their long axis in the down-slope direction (Liu *et al.* 2002). Filtering based on this principle was achieved by comparing object orientation with slope aspect. Object orientation was calculated using *ArcMap>Spatial analyst toolbox>zonal geometry*. This generates a value range of 0-180°, which correspond to grid bearing values of 90-270°. Note that all orientations are normalised to a single hemisphere. These were converted to grid bearing orientation values by:

Orientation + 90 = Grid Orientation

Aspect was derived from the DEM (*ArcMap>Spatial Analyst>Surface Analysis>Aspect*) and mean aspect sampled for each polygon (*ArcMap>Spatial Analyst>Zonal Statistics*). Mean aspects were then normalised to one hemisphere (90-270°) through the following logic equation:

If Aspect > 270° then -180

If Aspect < 90° then +180

Orientation and mean aspect fields could then be directly compared to assess the alignment of objects relative to the direction of slope. An orientation-aspect difference (*OAD*) field was generated using *Equation 5.1*:

$$OAD = \sqrt{(Orientation - Aspect)^2}$$

Equation 5.1

As a general principal, objects are unlikely to be landslides where *OAD* is large, and likely to be landslides where *OAD* is small. However, single polygons delineating large multiple landslide clusters are problematic in this analysis, as

they may cover a broad range of different aspects including opposing valley sides and may be elongated in the along-valley direction. As such, a size threshold of 15000m² was set for orientation based filtering. It was also observed that the low DEM resolution did not resolve gully features, making landslides appear to elongate perpendicular to the direction of slope, where they failed into gullies. In order to minimise removal of landslide features, a length-width ratio condition threshold of 1.5 was also applied. Combining these conditions the following filter was applied to remove objects with over 40° difference between long axis alignment and aspect.

Area < 15000 AND Length-width ratio < 1.5 AND Difference > 40

5.3.8 Panchromatic band thresholding

In order to classify panchromatic image E1 a technique of gray-level histogram thresholding was used. As noted above, within EO-1 imagery landslides appear much brighter than surrounding vegetated regions. The optimum pixel intensity (PI) threshold level to delineate full landslide areas was identified through visual experimentation with different levels. The final threshold applied was:

PI ≥ 105 (for a 255 radiometric level, unsigned-8-bit image, see Figure 5.8)

Following thresholding, a 20° slope mask was applied to remove wrongly commissioned areas, as described in Section 5.3.7. While minimal object filtering was required, the 300m² object area noise filter was also applied.

5.3.9 Exemptions

During classification a number of regions were identified in which accurate classification of landslide features could not be achieved. These regions occur under 2 conditions:

1. Regions obscured by cloud or significantly strong haze, such that features on the ground could not be identified
2. Regions above 3500m elevation. While landslides could be clearly identified where a strong contrast was produced between landslide scars and

surrounding vegetated areas, in regions above 3500m the terrain appears to be predominantly rock and scree covered. Here it is very difficult to delineate landslide scars, as no vegetation cover exists with which to delimit newly generated features.

Due to these limitations, areas of cloud were removed from the classification by manual delineation in ArcMap, and areas above 3500m were removed using a mask based in the SRTM DEM. The resulting total mapping coverage is shown in *Figure 5.9*.

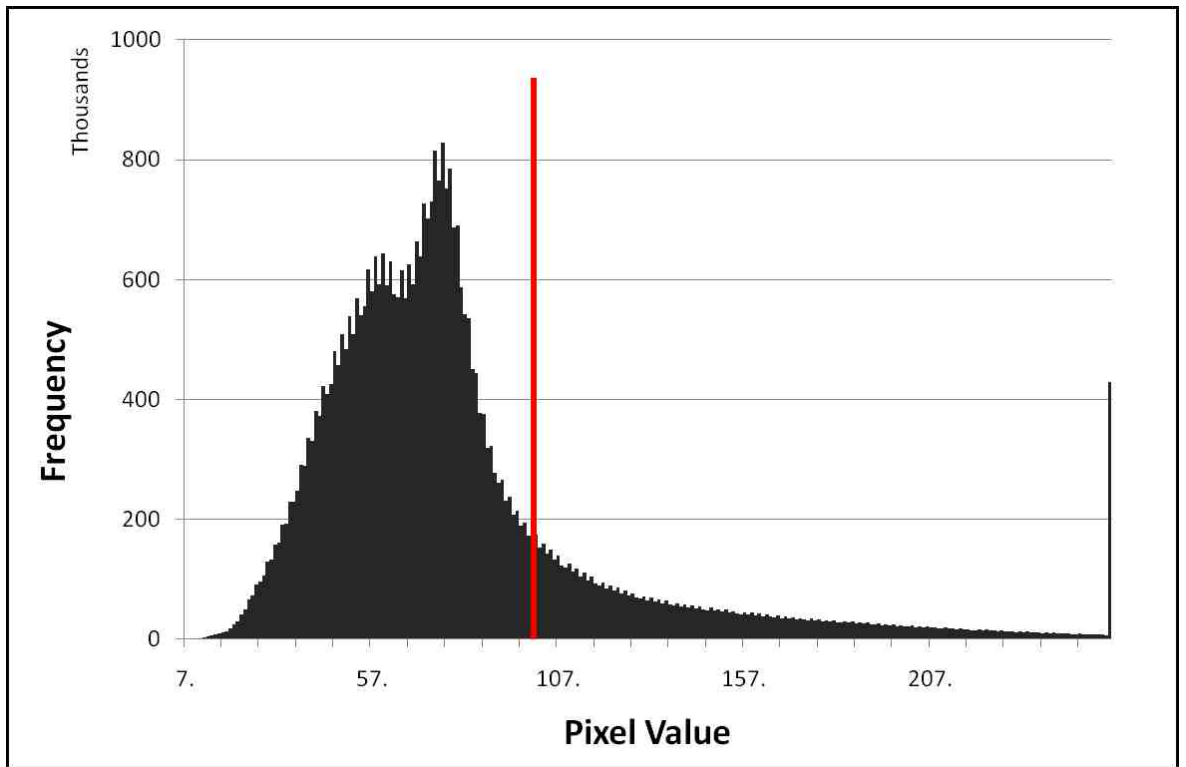


Figure 5.8: Image E1 (E0-1) panchromatic band histogram (black) and intensity threshold (105, red).

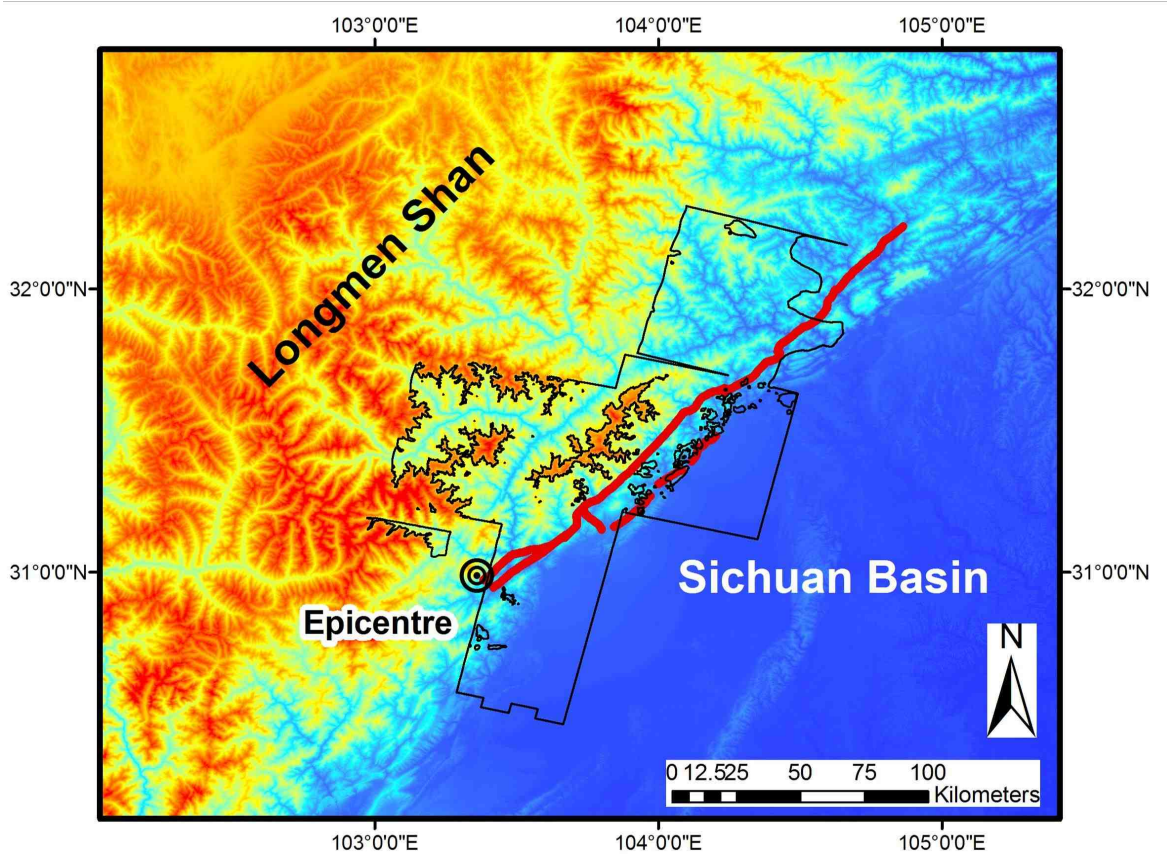


Figure 5.9: Final mapping coverage with areas of excessive cloud or haze, and elevation over 3500m removed.

5.3.10 Full map compilation

To compile classification outputs coverage areas from all images were mosaiced with overlap dominance appropriate to give the maximum cloud free mapping area. The order of overlap dominance was:

1. E1
2. S3
3. S2
4. S1
5. S4

For example, in areas where E1 and S3 coverage areas overlap only the classification result from E1 is retained.

5.3.11 Manual editing

Despite improvements made by application of filters, errors of commission were visible in the final compiled dataset. For this reason an overview of the entire mapped output was undertaken, in order to manually remove obvious visible errors. Editing was particularly focused on image S1, where large, visually identifiable areas of arable fields remained to be removed from the classification. In addition a manual reclassification of valley bottom areas in image S2 was undertaken, where light-haze-covered ground appeared to suffer from relatively frequent errors. Here the visual identification and classification of landslide scars was based upon the parameters outlined in *Table 3.1*.

5.3.12 Final classification algorithm summary

The final image classification process applied to classify imagery in this investigation can be summarised in seven stages, as shown in *Figure 5.10*:

1. Production of a single image band as a basis for classification
2. User definition of landslide classes or band threshold
3. Application of slope filter

4. Application of noise filter
5. Application of object orient filters (where required)
6. Full map compilation
7. Manual editing and correction of final mapping result

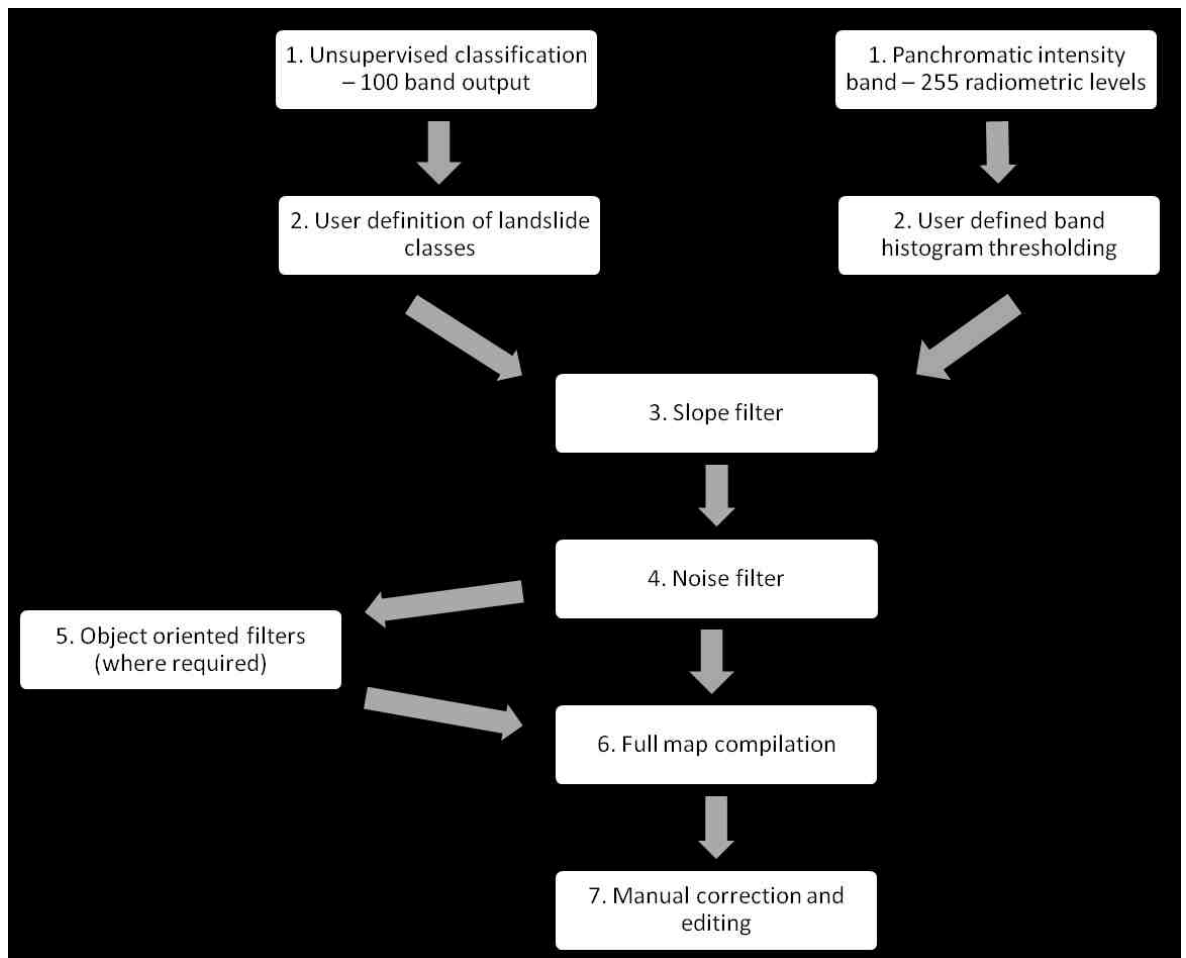


Figure 5.10: Landslide classification algorithm summary.

5.4 Validation and evaluation of automated landslide mapping

Before the mapping result is used in analysis of the landslide distribution, it is important that the result be validated and potential sources of error identified. This was carried out through comparison of manual and automated landslide mapping results (e.g. Borghuis *et al.* 2007). Automated classification results from the three different image types (SPOT 5 -3 band, SPOT 5 – 4 band, EO-1 – Panchromatic) are also compared in areas of image overlap, along with testing the impact of original image resolution upon derived landslide mapping. Finally, sources of mapping error are summarised and evaluated. While this dataset evaluation would have been most accurately achieved through comparison of the automated result with ground surveyed landslide mapping, the opportunity for fieldwork was not available for this investigation.

5.4.1 Comparison of classified and manually mapped landslides

In order to examine the relative accuracy of the automated classification techniques, 36km² sample areas (*Figure 5.11*) of classified landslides were compared with the same landslides manually delineated, in images S1, S3 and E1 (all three image types). Landslides were visually identified and manually delineated as polygon features based on their geometric, textural and spectral characteristics (see *Section 3.2, Table 3.1*) in the raw imagery. Where landslides could be identified as individual features they were mapped as such. Otherwise multiple landslides were mapped as single features, bounded by their combined perimeter area. Both manual and automated datasets were analysed in polygon feature format. Using ETGeowizards to clip and erase overlap areas, errors of commission and omission were extracted for analysis. Landslide density (percentage area affected by landsliding) is adopted as a primary unit for analysis and evaluation of the dataset. This reflects the primary analysis method applied in exploring regional patterns in the landslide distribution (e.g. Meunier *et al.* 2007), thus testing the accuracy of mapping for this application.

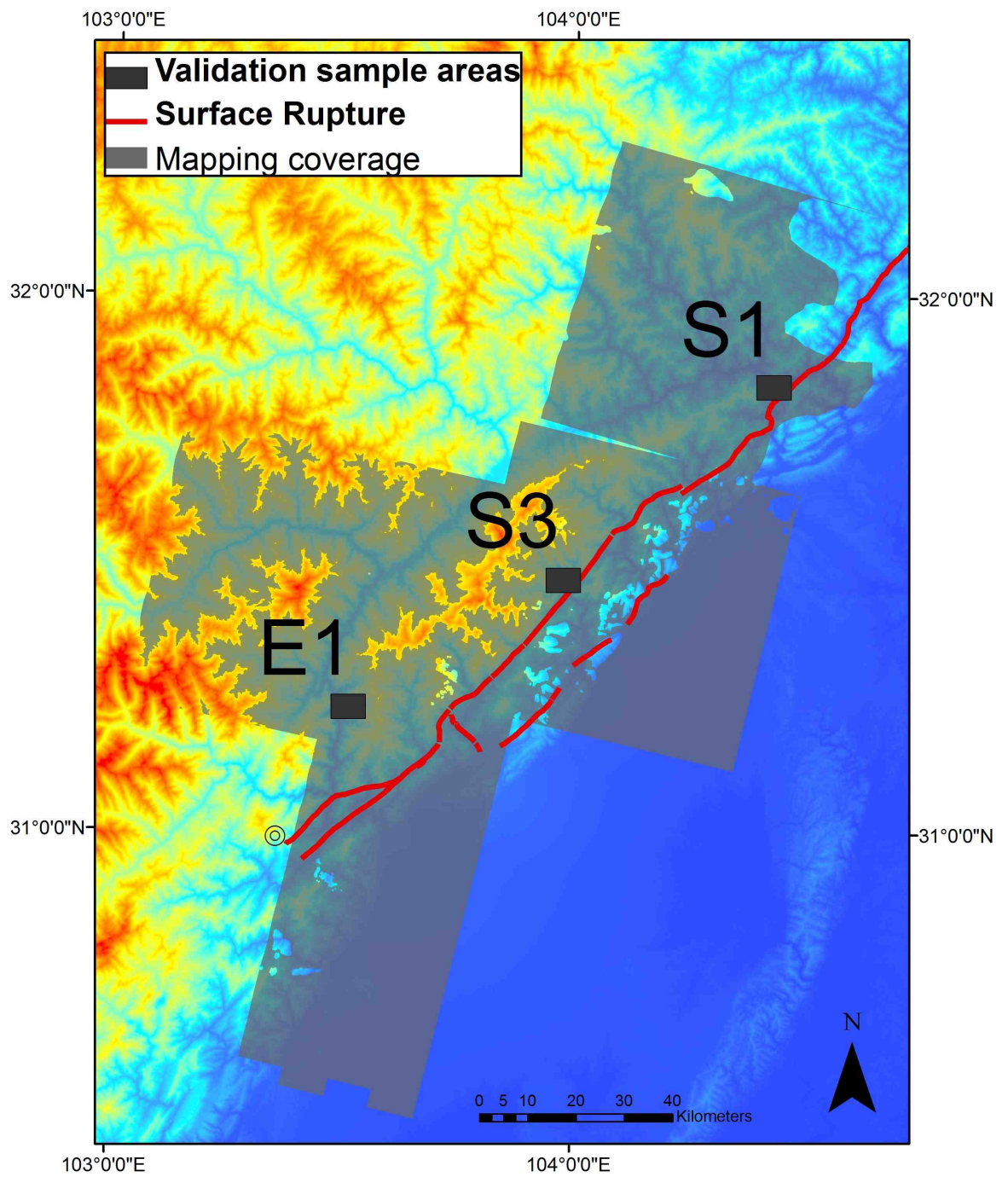


Figure 5.11: Mapping coverage and validation sample areas

Results

Table 5.4 lists results of comparison tests carried out on manual and automated mapping results for all three images. Automated mapping techniques produce a net underestimation of landslide areas, relative to manually mapped results, of between 6.2 and 22.7%. This underestimation is produced through the combination of errors of commission (areas falsely classified as landslides) and errors of omission (areas of landslides not classified as such). Areas commissioned by automated but not manual techniques equate to between 3.2% and 5.6% of the total sample area. Areas omitted by automated mapping equate to between 7.4 and 12.5 % of the total manually mapped area. These errors result in a net areal automated-manual overlap of between 58.7 and 66.2%, similar to those achieved through application of the same method by Borghius *et al.* (2007), of between 53 and 66%. As a percentage of the total sample area mapped, these results indicate an overall landslide density underestimation of between 1.8 and 9.3%.

Manual and automated techniques also generate data with very different magnitude and frequency statistics. The total number of objects generated is higher for the automated result in all cases. This is particularly evident in data from image S3, where many small pixel scale features are omitted from the manual mapping, but included in the automated result. Plotting the frequency-area distribution of the datasets using the kernel density method shows that all automated datasets are positively skewed relative to manually derived data (Figure 5.12).

Discussion

The general underestimation generated by automated mapping appears to be due to a combination of omission of landslides on slopes below threshold values, and also inaccuracies in manual delineation. When manual mapping was undertaken the technique was to draw around the edge of landslide features, so that all landslide pixels are enclosed within the polygon. However, automated delineation generates exact lines along pixels edges, creating apparent omission errors around polygon perimeters. In addition automated mapping often fragments landslide areas, particularly where vegetation covered ground is present within a

landslide feature. Here the analyst can manually delineate the whole landslide as a single polygon, while the automated technique delineates areas of bare ground separately. This error is in part masked by errors of commission, which mainly occur due to inaccuracies in the DEM derived slope mask, and incorrect commission of features in valley bottoms.

Much interest in landslide inventory analysis concerns the frequency-magnitude (area) statistics of these datasets (e.g. Malamud *et al.* 2005, Hovius *et al.* 2000). Given the significant differences in the object frequency-areas distributions for manual and automated results, the dataset does not appear to be suitable for this form of analysis. The dataset provides a first order measure of area affected by landsliding, rather than the number and characteristics of individual failures. Investigations in which frequency-area analysis has been applied have been produced using much higher resolution aerial imagery or ground based mapping, techniques much better suited to object oriented study of landslides.

While correlations between manual and automated mapping datasets have been explored, it is clear that the accuracy of manually mapped results relies heavily on the role of the analyst. As such, this experiment does not compare automated mapping with a necessarily „correct’ result, but rather compares two methods of first order data extraction, both prone to a series of (presumably independent) errors. In order to provide a test of the true accuracy of both these techniques, comparison with landslides mapped in higher resolution aerial imagery or through ground based studies is necessary. As yet no such data is available, though this further level of validation should be undertaken when it is. Nevertheless, both manual and automated mapping have been shown to extract similar landslide areas and relative landslide densities, with accuracy levels comparable to similar studies of this type.

Image	S1		S3		E1	
Image Type	SPOT5		SPOT5		EO-1	
Pixel size	5m		10m		10m	
Number of spectral bands	3		4		1	
Total sample area (km ²)	36		36		36	
Classification technique	<i>Automated</i>	<i>Manual</i>	<i>Automated</i>	<i>Manual</i>	<i>Automated</i>	<i>Manual</i>
Mapped landslide area (km ²)	9.88	10.54	8.57	11.08	12.26	15.61
Landslide density (%)	27.45	29.27	23.80	30.77	34.06	43.35
Number of separate mapped objects	725	465	1027	433	579	200
Landslide area difference (%)	6.23		22.65		21.44	
Landslide density difference (%)	1.82		6.97		9.29	
Landslide density error of commission (%)	5.57		3.61		3.23	
Landslide density error of omission (%)	7.40		10.58		12.52	
Areal Overlap (%)	62.76		58.72		66.18	

Table 5.4: Results of comparison between manual and automated mapping results. Note that landslide density refers to the percentage area affected by landslides.

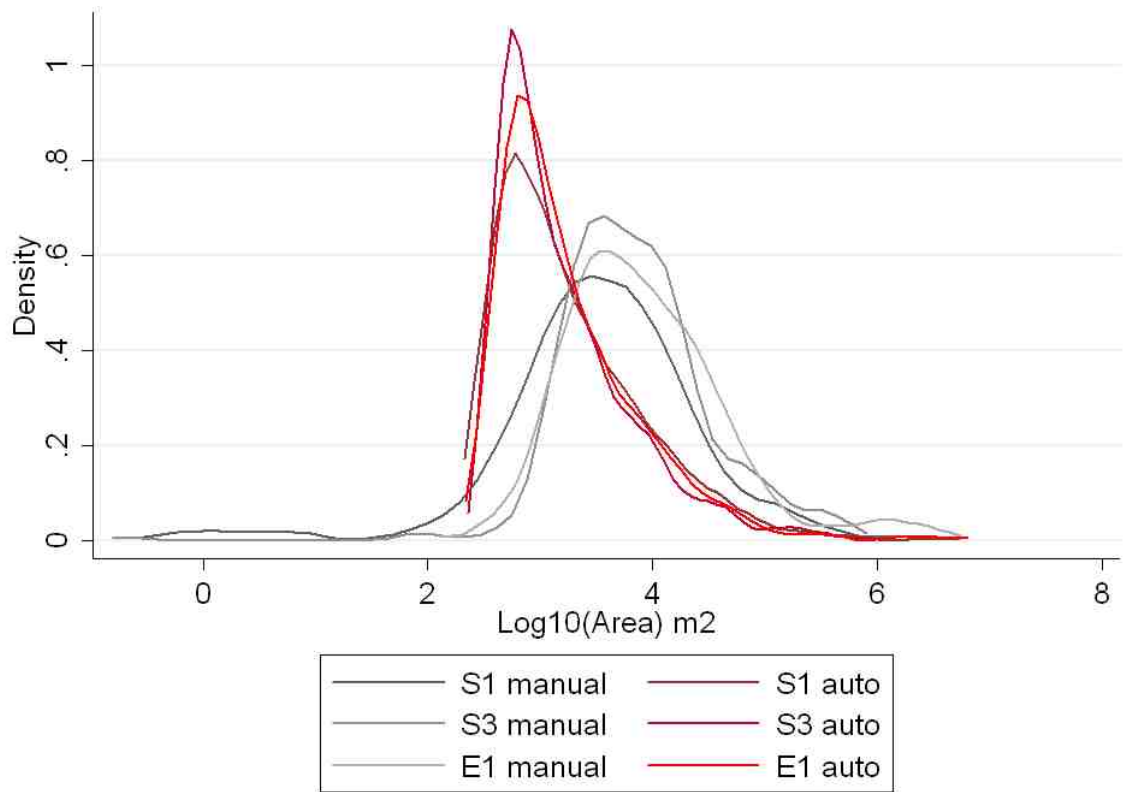


Figure 5.12: Frequency-area distributions for automated and manual mapping results. Note that landslides mapped through the automated technique are positively skewed relative to manually mapped landslides.

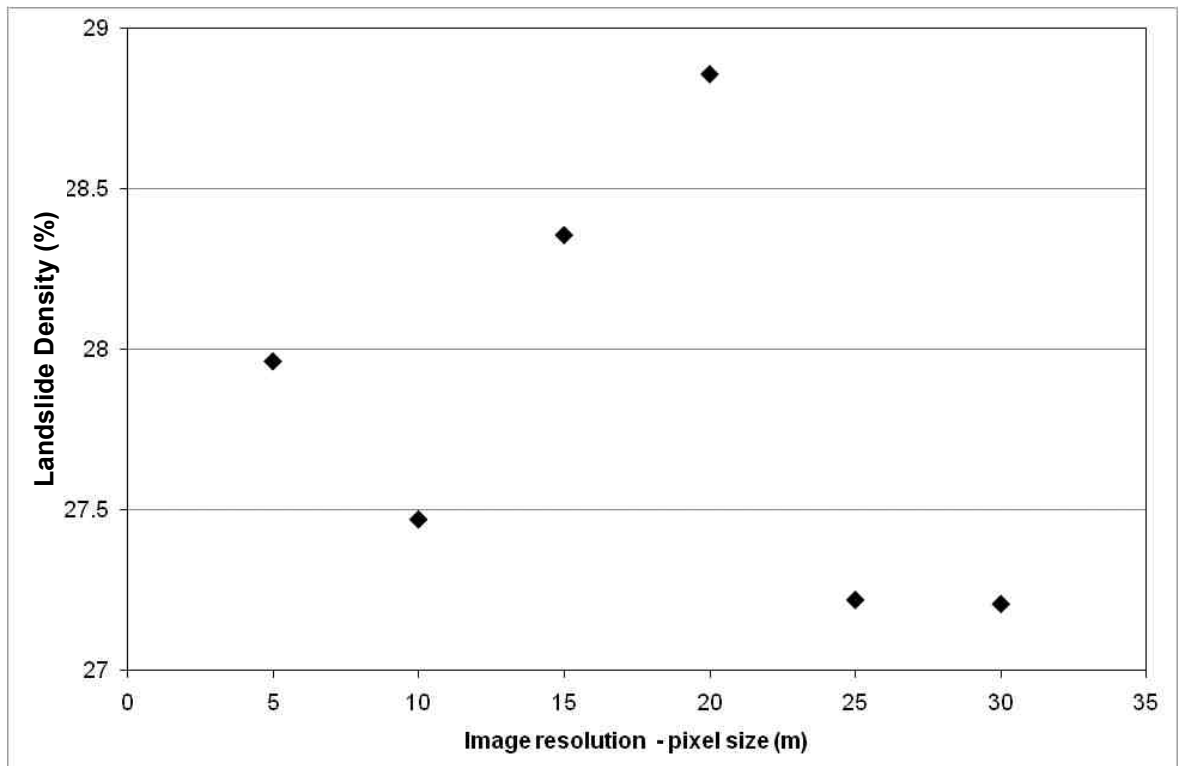


Figure 5.13: Relationship between mapped landslide density and original image resolution

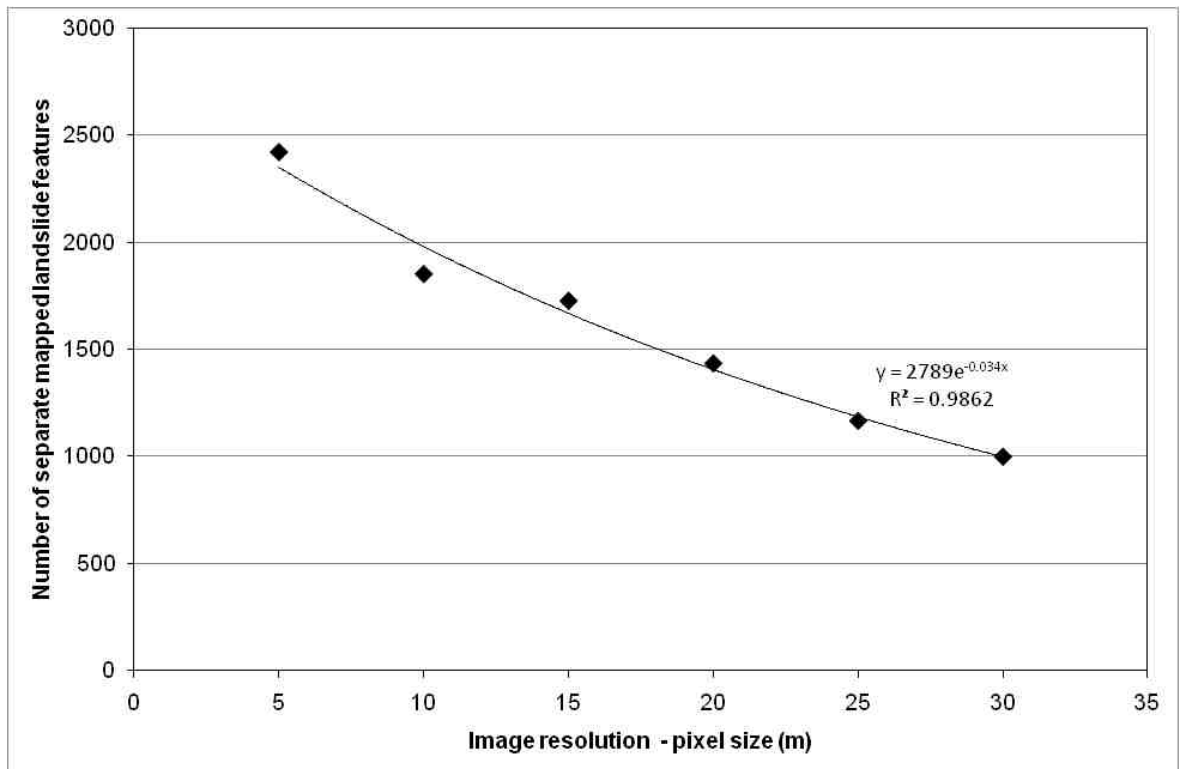


Figure 5.14: Relationship between original image resolution and number of mapped landslide features

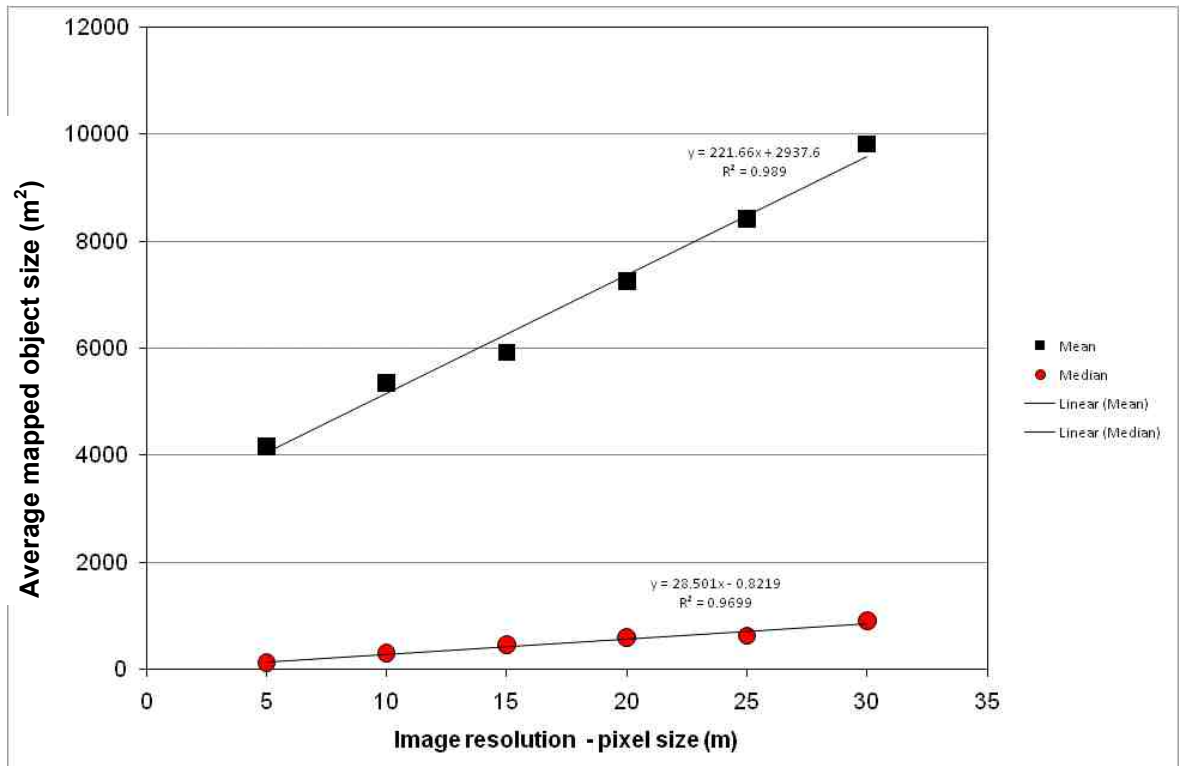


Figure 5.15: Relationship between original image resolution and average (mean and median) mapped object size

5.4.2 Comparison of landslide maps derived from different resolution images

As a number of different image types were used to create the overall landslide map, due consideration must be given to the impact of varying spectral and spatial resolution upon the data extracted. The following section compares mapped landslide areas from SPOT 5 imagery of varying spatial resolutions, and overlapping areas of EO-1 and SPOT 5 imagery of varying spectral resolution and conditions of image capture.

I. Impact of spatial resolution on mapped landslide areas

In order to examine the effect of varying spatial resolution upon landslide mapping outputs, the S1 sample image was used. Due to the low level of agricultural activity in the sample area, a relatively clean binary classification was produced through stages 1-4 of the classification algorithm alone (see *Figure 5.10*). Hence, this provided a suitable area to test the impact of resolution on landslide classification, without introducing object size constraints. The sample image was resampled to pixel resolutions of 5m, 10m, 15m, 20m, 25m and 30m. The images were then classified through classification stages 1-4, each time selecting the same unsupervised signature classes (*5.10*, stage 2), in order to produce binary landslide classification masks at 5m, 10m, 15m, 20m, 25m and 30m resolution.

Results

No systematic relationship appears to exist between image resolution and landslide density over the whole sample, for this range of values, as shown in *Figure 5.13*. In addition, the maximum variability in total mapped landslide area is low, at 3.2% from the mean. Of particular interest to this investigation, classification based on a 10m raster generates a total landslide area 1.8% lower than that derived from a 5m raster. Despite small variations in the overall landslide area, the areal pattern of mapped landslide areas is maintained for all resolutions.

In terms of object characteristics, a clear negative relationship is shown between the number of separate features generated and raster resolution. As shown in *Figure 5.14* this relationship appears to be best approximated as an exponential function ($r=0.98$). Since no polygon based filtering was undertaken here, the

minimum mapping unit is defined by the raster pixel resolution, which produced the modal object size in each case. As raster resolution increases, the mean and median feature areas increase as linear functions (*Figure 5.15*).

Discussion

The findings from this section suggest there is no systematic relationship between mapped landslide area and pixel size, with very little effect on mapped landslide areas using different image resolutions. The spatially distributed pattern of landslides is also maintained using all image resolutions. This suggests that the combined use of 5m and 10m imagery to generate the regional landslide map is a valid approach for this investigation. While the 10m resolution sample produced a landslide area 1.8% lower than the 5m sample, this finding is specific to the sample area used with no evidence of a systematic relationship between pixel size and mapped landslide area. Thus it is not applicable, based on this evidence, to apply a constant error band across all areas mapped from 10m imagery.

The frequency-area statistics of the dataset are highly sensitive to raster resolution, primarily due to changes in the minimum mapping unit. This finding suggests that, while 5m+ satellite imagery is suitable for the regional study of landslide distributions, the applicability of the data to object oriented analysis is limited by increasing pixel size. Frequency-area density distributions for landslides derived from different image resolutions demonstrate how the minimum mapping unit and peak frequency are controlled by the image resolution.

II. Impact of image type and spectral resolution

In order to validate the combined use of SPOT 5 and EO-1 image types, corresponding classifications in cloud free areas of image overlap were also compared (*Figure 5.16*). Sample areas were used for areas of S2-E1 overlap and S3-E1 overlap, in order to examine the impact of image acquisition conditions, as well as spectral attributes. Classification masks for overlapping images were clipped to the exact overlap extent and converted to polygon features for analysis.

Results

In areas of S3-E1 overlap, S3 based classification yields an average landslide density that is 2.5% less than that derived from E1. This is mainly brought about by the low sun angle (47°), causing a significant topographic shading effect and obscuring landslide features. In addition, E1 imagery presents a sharper contrast at landslide edges, which allows the algorithm to map right up to the vegetation line. In contrast, landslide edges appear more gradual in the SPOT 5 imagery, allowing for a thin unclassified halo to surround the features and creating generally smaller landslide objects. Despite these limitations, the general spatial pattern of landslides is preserved.

Where S2 and E1 images overlap, the contrast in classification results is much more striking. The S2 classification generates a much smaller average landslide ratio, 10.1% less than that mapped using E1. This is again due to a combination of topographic shading, much more severe in this image with a very low morning sun angle of 31° , and the edge pixel effect described above. Topographic shading is of particular significance as very few landslides on north to west facing slopes can be identified (shown in *Figure 5.17*). In addition, the image overlap region suffers from significant haze in river valleys, which further obscures features in this region of high landslide density. Once again, despite the relative differences in landslide area, the overall pattern of landslides is preserved in both classifications.

It is also important to note that the images compared in this section were also captured after different periods following the earthquake. E1 was captured in July 2008, S2 in December 2008 and S3 in October 2008. As such, the extent to which mapping is influenced by post-seismic landsliding and vegetation re-growth may vary between image scenes.

Discussion

Areas of overlapping classifications based on EO-1 and SPOT 5 imagery generate the same overall distribution of mapped landslide areas. However, while the relative pattern is similar, the total landslide areas extracted vary, as shown with particular significance in the comparison of images S2 and E1. This effect appears to be primarily due to the conditions of image acquisition (topographic shading and valley haze) as opposed to the image type and spectral resolution, although misclassification of edge pixels may add in part to this effect. While these findings

suggest that classification of SPOT 5 imagery yields an underestimation of landslide area relative to EO-1, the effect may not be quite as acute as the S2-E1 comparison suggests. Valley haze conditions which affect a significant proportion of landslide areas in the S2 sample image are not as severe across all imagery. As in *Part I* of this section, it is not appropriate to apply a constant error rating, both due to uncertainties in the distributed error value, and the fact that significant raster resampling is undertaken in further analysis.

Despite variation in acquisition dates, errors generated by post-seismic landsliding and vegetation regrowth are not expected to be significant at this level of regional scale, first order landslide mapping.

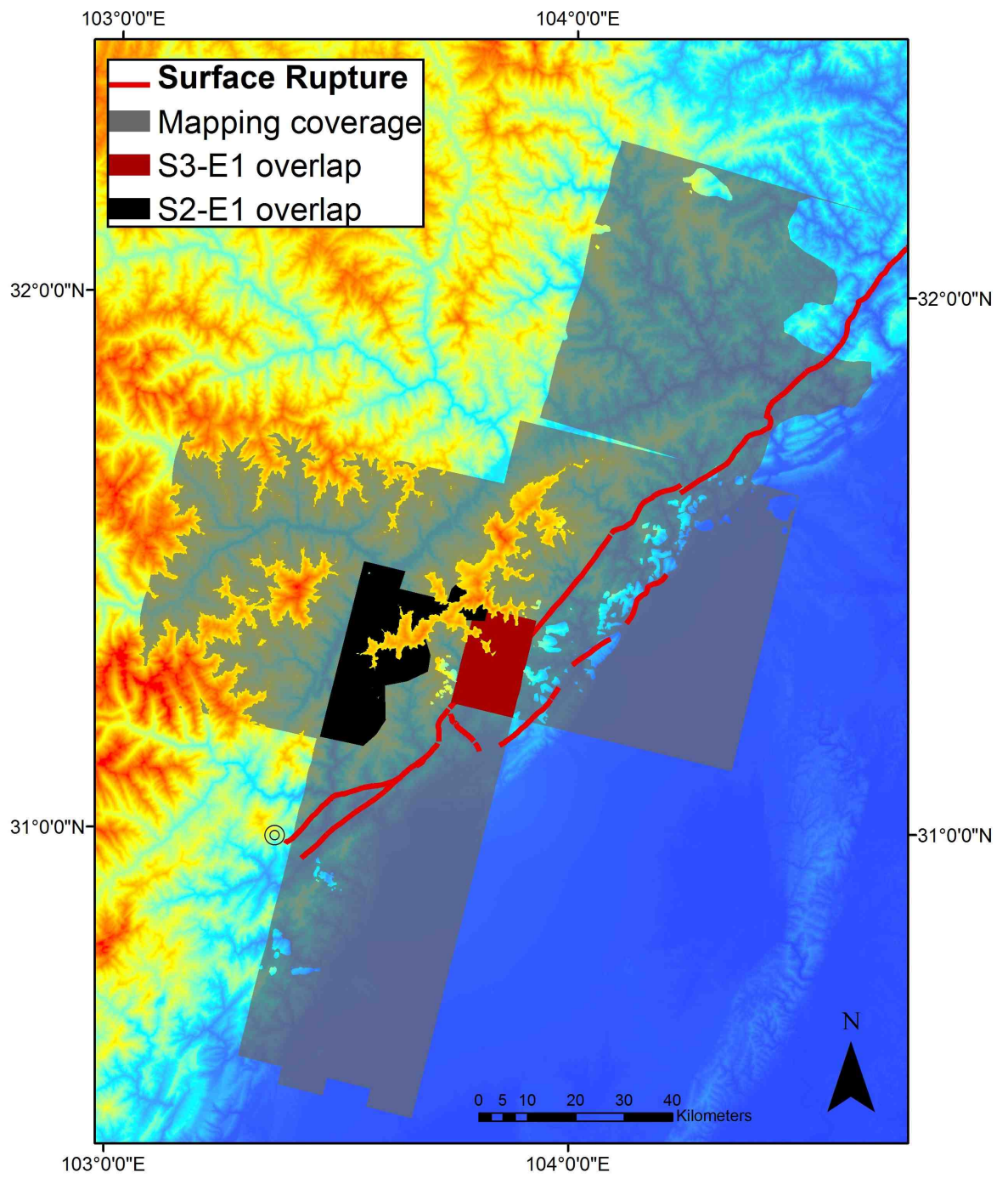


Figure 5.16: S2-E1 and S3-E1 overlap sample areas



Figure 5.17: Area of image S2. Low sun angle and significant topographic shading makes mapping landslides on northwest facing slopes problematic.

5.4.3 Image condition limitations

Based on findings from the above section, limitations of the mapping process produced by conditions of the imagery used are now summarised.

I. Hillshading

While manual and automated mapping techniques can both be applied to extract landslide areas, the extent to which newly triggered landslides can be identified is limited by spatial and temporal characteristics of the imagery. For landslides to be identified by either method they must be visually distinct. As discussed above, this is true for most areas where failures occur on vegetated slopes. However, all images are affected to varying degrees by topographic shading. In image S1 the effect is very mild due to the relatively high sun angle (74°) and landslides are classifiable on all slopes. In image E1 the sun angle is lower. This, combined with the lack of spectral information, makes landslides on shaded, northwest facing slopes very difficult to differentiate from surrounding areas. Images S2, S3 and S4 suffer from very low sun angles between 31° and 47° . Despite the availability of spectral information in these images, shading is so severe that almost no features could be identified or mapped on northwest facing slopes.

II. Variable vegetation coverage

Areas to the west of the study area required relatively intensive manual reclassification due to their thin vegetation cover. In these regions landslides become increasingly difficult to identify as conditions become more arid, and contrast between landslides and surrounding areas decreases. For this reason it is likely that mapping in this region generates an underestimate of the area affected by landsliding.

III. Valley haze

While areas of severe cloud and haze were removed from the final mapping result, some valley bottom areas suffered from light haze. While this did not completely obscure landslides, changes in their spectral signature meant that the automated classification was prone to error. In these regions (mainly in image S2) significant manual correction was required.

5.4.4 Summary

Comparison of automated and manual landslide mapping techniques demonstrate that the automated landslide classification system can be used to delineate landslide areas where they are visibly identifiable in high contrast SPOT 5 and EO-1 imagery. The resulting total landslide areas produced are similar, with a maximum difference between landslide areas mapped using manual and automated techniques of 23%, due to a combination of errors of commission and omission.

Several sources of error have been identified. Topographic shading results in an underestimation of landslide density, particularly in images S2, S3 and S4. Underestimation of landslide areas appears to be most acute on hillslopes facing northwest in image S2, where a low sun angle combined with sparse vegetation cover makes even the visual identification of landslide scars particularly problematic. The effect of mild, variable haze acts to alter spectral signatures differentially across the imagery. While this is problematic for automated classification, accurate manual delineation is still possible, so little error should be produced by this effect. Image resolution does not appear to have a significant effect on total mapped landslide areas, but the frequency-area characteristics of the dataset are very sensitive to this, with a clear inverse relationship between pixel size and landslide frequency.

5.5 Data format and resampling

As landslide inventory datasets may take variety of different data formats and must be analysed relative to various other data types, a variety of resampling techniques may be employed to both describe and analyse the dataset. Prior to presenting the dataset itself, this section describes the main data formatting technique used in analysis, as well as the impact of variations in format on data characteristics.

The landslide inventory map can be presented in its raw-data format as landslide area polygons (as shown in *Figure 5.18*). These polygons represent areas mapped as “landslide”, using the automated mapping technique described in *Section 5.3*. It is important to note that, while these provide a useful measure of areas affected by landsliding, individual polygon features do not necessarily represent individual landslides, and likely delineate and encompass multiple coalesced landslide scars, particularly in areas with high levels of landslide occurrence. This data artefact is due in part to the methodological limitation where the mapping technique is unable to automatically separate conjoined landslide features. However, linked with this is the practical problem of separating conjoined landslides, particularly in areas where large reaches of valley wall have collapsed in a seemingly continuous landslide feature; linked with this is a conceptual problem of how individual landslides should be defined in these scenarios.

While the raw data format can reveal many key aspects of the landslide distribution, in order to both describe and analyse the dataset it is useful to spatially resample the landslide-affected area over a variety of scales, which are reflective of different geophysical controls upon the landslide distribution. This is achieved by calculating the landslide density, P_{ls} , as a percentage of the total area, within desired sample zones (after Meunier *et al.* 2007; *Equation 5.2*):

$$P_{ls} = A_{ls}/A_t$$

Equation 5.2.

where A_{ls} is the area affected by landsliding, and A_t is the total area within a given sample zone. This is calculated by converting the landslide shapefiles into a 5m pixel resolution binary raster of landslide (pixel value = 1) and non-landslide (pixel

value = 0) areas. The ratio of landslide to non-landslide pixels is then extracted using ArcGIS zonal statistics, and converted to a percentage value. Throughout Chapter 6, the landslide data are resampled in this way using a variety of sample grids, the resolution of which are intended to be reflective of different geophysical parameters controlling landslide occurrence over a range of spatial scales. To ensure clarity and continuity, the sample grid used to resample landslide occurrence will be presented in a figure each time this operation has been carried out.

5.5.1 Matrix grid sampling

The most straightforward mode of spatial resampling, and a useful tool in visualising the macro-scale pattern of landslide occurrence, is to produce a landslide density grid for the full areal mapping coverage. This is generated through sampling P_{ls} using a matrix grid of constant cell size covering the full mapping region. The data layers produced provide both a useful visual tool for exploring general patterns of landslide occurrence, and can be used to reduce the size of the dataset for more time efficient computer processing.

However, the sample grid resolution used has an effect on both the level of spatial detail of the data produced, and the extent to which the non-uniformly shaped mapping area can be covered using non-truncated cells. In order to examine the impact of the sample resolution upon the data distribution, landslide density was resampled using regular square matrix grids of 0.5km, 1km, 2km, 5km and 10km cell size (shown in *Figure 5.19*). The lower limit is set by the software package, which was unable to sample landslide density for finer matrix grids. In order to maintain a uniform cell size, only whole cells which fitted within the borders of the coverage area were used. The resultant grid areas and the coverage produced as a function of grid size are shown in *Table 5.5*. It is clear that, due to the shape of the mapped area, only grid sizes $\leq 2\text{km}$ are suitable to give a majority sample of the data, whereas grid sizes $\geq 5\text{km}$ omit large proportions (over 40%) of the mapped area.

Matrix grid size (km)	Number of cells	Total cell covered area (m ²)	Percentage total mapping coverage
0.5	44598	11150000000	93.62329071
1	10466	10468000000	87.89673606
2	2336	9352000000	78.52601029
5	263	6625000000	55.62818842
10	38	3700000000	31.06781844

Table 5.5: Matrix sample grid coverage attributes as a function of grid size

5.5.2 Non-cumulative and cumulative distributions

In order to examine the distribution of data values produced for each grid cell size, the kernel density estimation method was applied. This method estimates the non-cumulative density function of a variable using a symmetric kernel convolution, thus avoiding any discontinuities imposed by setting arbitrary bin sizes for a histogram (Cox 2004). In order to examine the cumulative distributions, quantile plots were also produced.

The kernel density functions for all sample grids are shown in *Figure 5.20*. Each density function observes the same overall, positively skewed distribution. However, as the cell size increases, maximum landslide densities decrease. In addition, the proportion of lower P_{ls} pixels also decreases, with grids of 2km, 5km and 10km exhibiting a slight roll-over as P_{ls} approaches 0. Plotting the cumulative density functions of these distributions (*Figure 5.21*) again yields similar overall patterns produced by all grid sizes. However, while 0.5km, 1km and 2km grid distributions are very similar, those for 5km and 10km stray significantly from the distribution for finer resolutions.

5.5.3 Discussion

The first issue brought about by sampling P_{Is} using a variety of grid sizes is that larger grids produce very limited coverage of the total mapped area. As such, only grid sizes $\leq 2\text{km}$ are suitable for achieving coverage over the whole area.

The non-cumulative and cumulative distributions produced for 0.5km, 1km and 2km grids show that, within this range, the sampling resolution has little impact on the overall data distribution. However, the effect of varying sample resolution is mainly seen at the high P_{Is} end of the distribution. As resolution decreases the maximum P_{Is} becomes lower as this is averaged over a larger area. This means that larger grid sizes are less able to resolve areas of more localised landslide impact, and subsequently provide a coarser overall representation of the dataset.

In further analysis of the data in this way, it is appropriate to use a range of sampling scales. However, it is important to recognise the effect of sample area, particularly with regard to the high P_{Is} tail of the distribution. The main impact of this is that each sampling of P_{Is} provides a relative index of landslide impact within the sample zones used, which is not directly comparable to P_{Is} sampled at different scales and using different grid sizes.

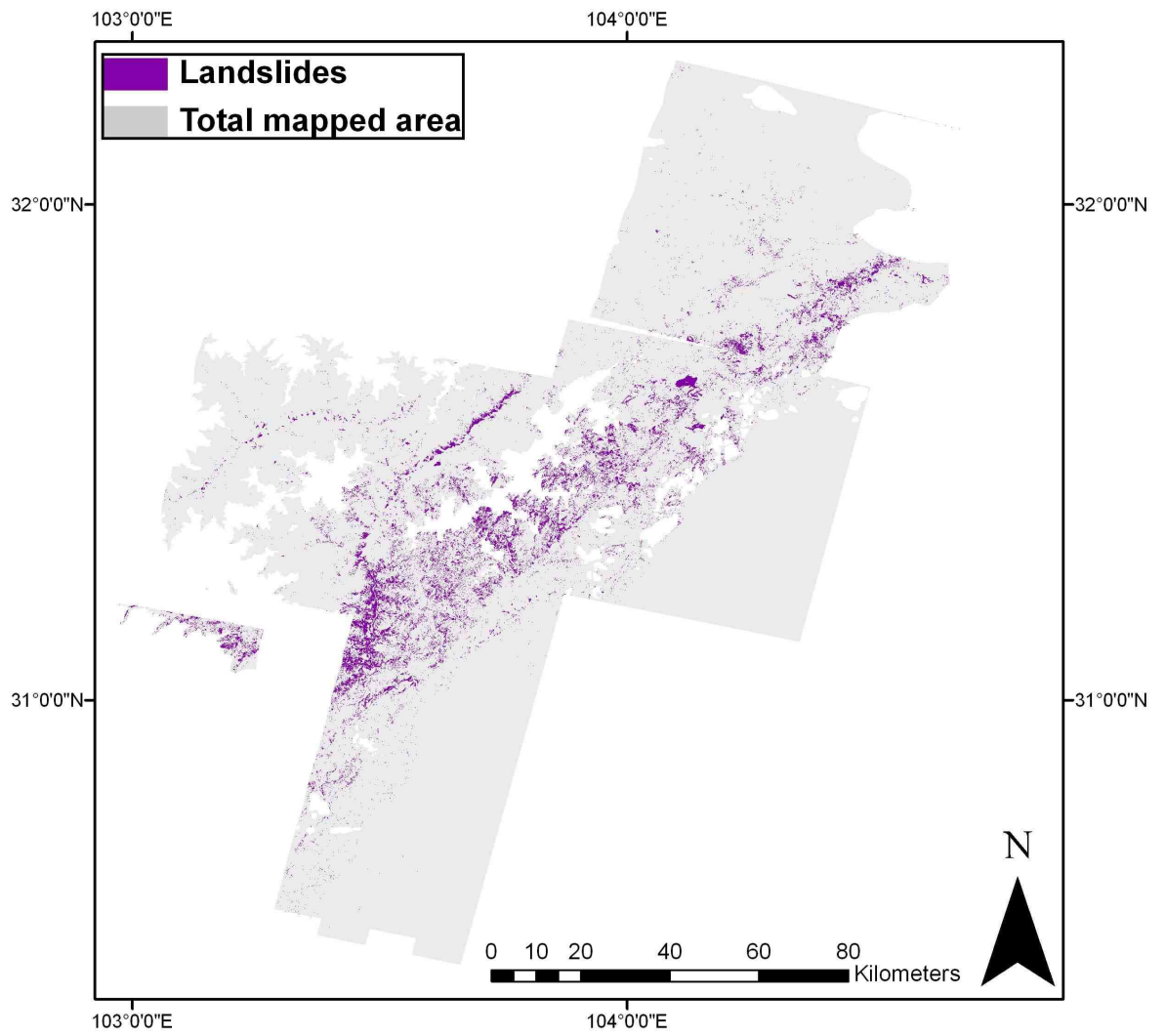
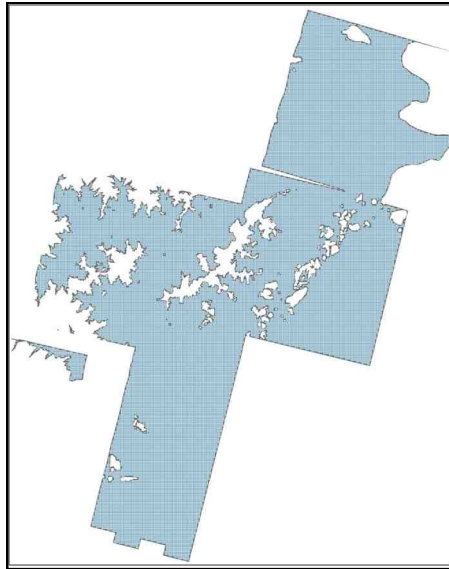
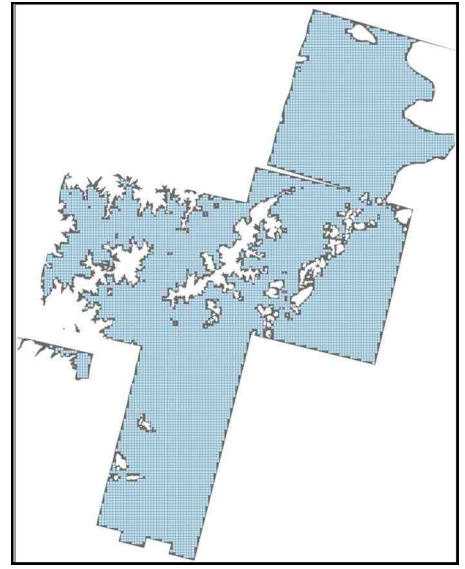


Figure 5.18: Wenchuan earthquake landslide map

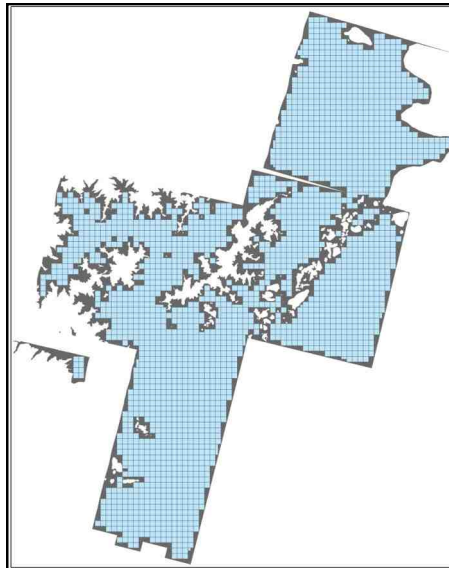
0.5km



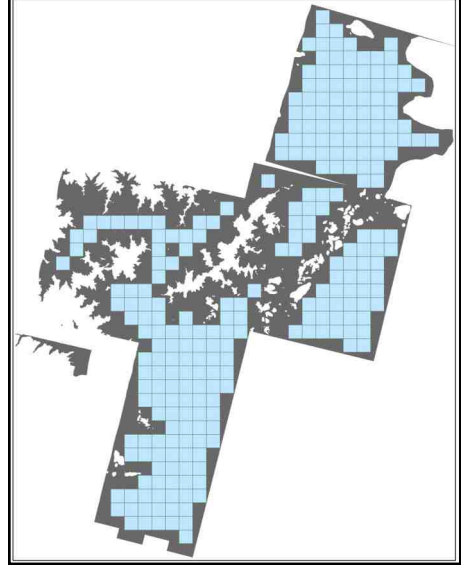
1km



2km



5km



10km

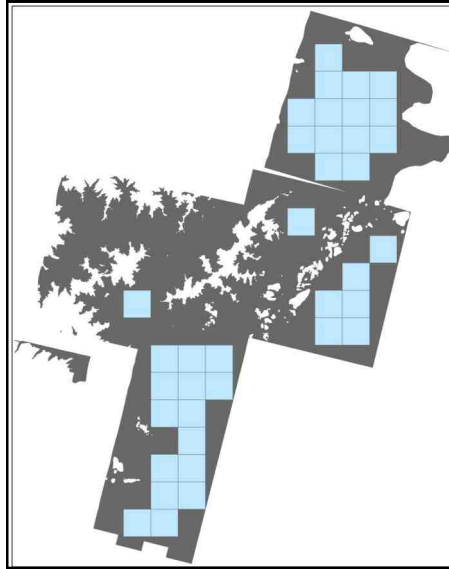


Figure 5.19: Matrix sample grids of different resolutions

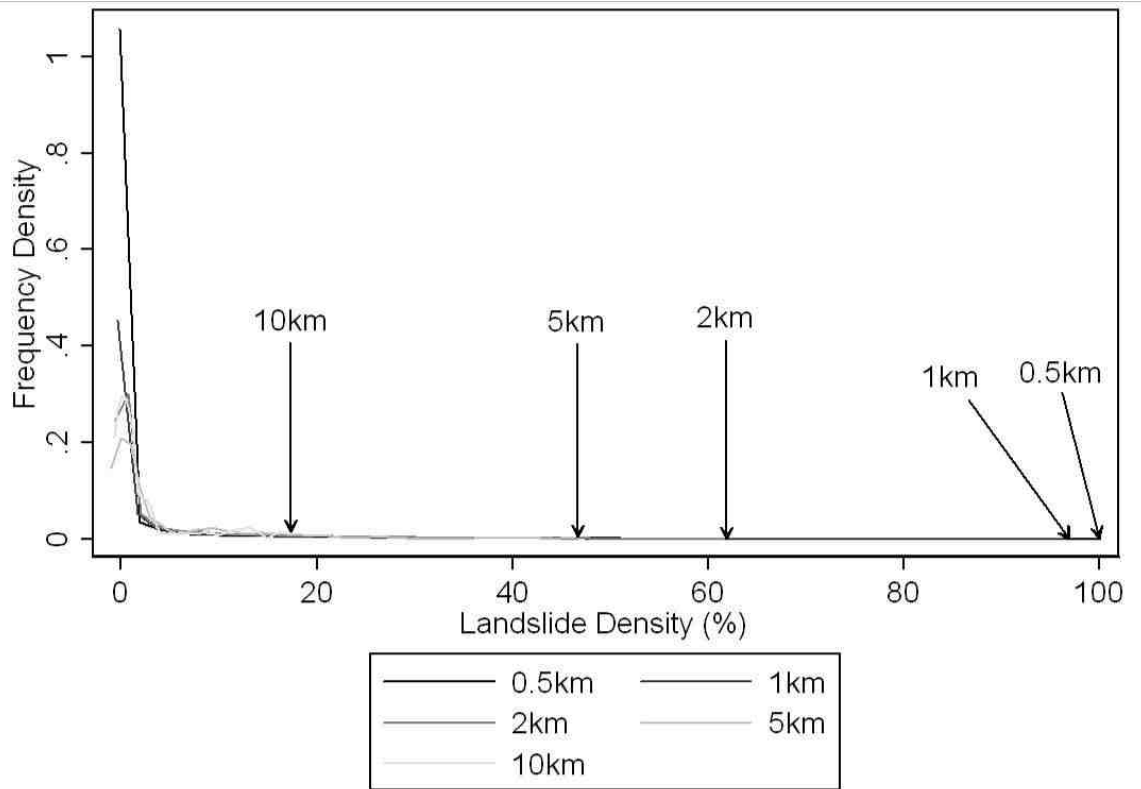


Figure 5.20: Kernel-density functions for all sample grid sizes. Labelled arrows indicate maximum landslide densities by grid size.

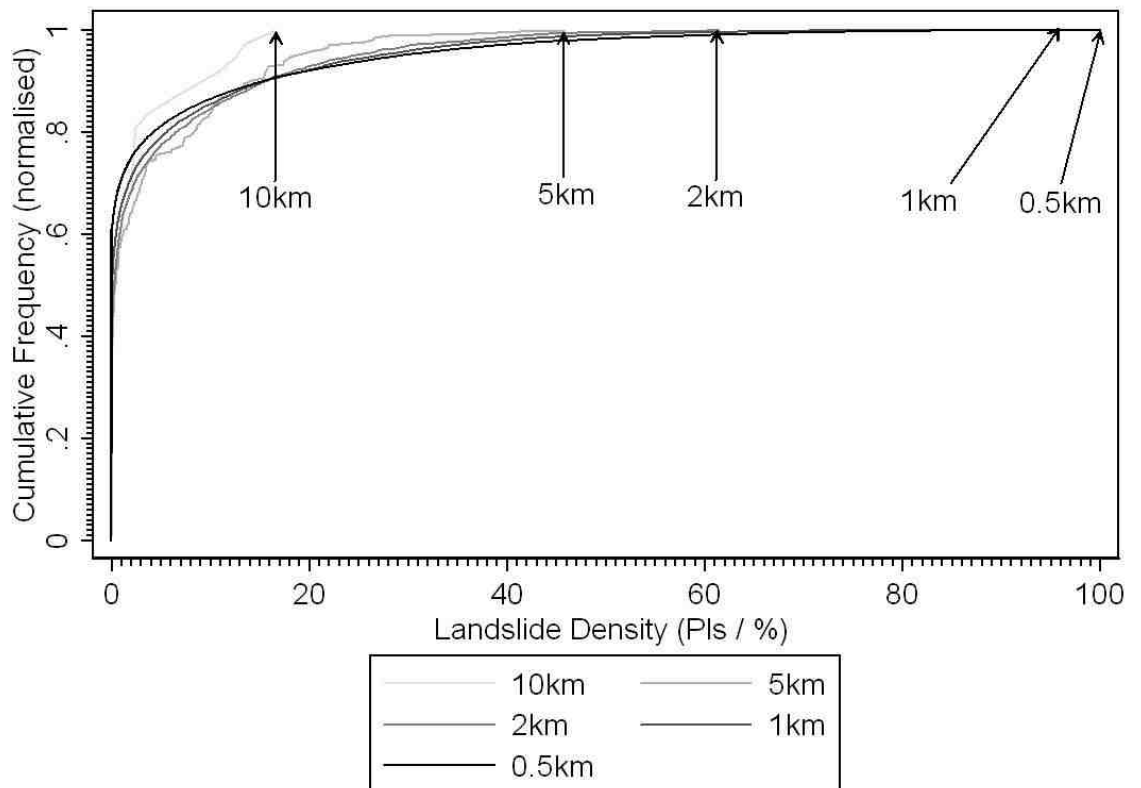


Figure 5.21: Cumulative density functions for all sample grids. Labelled arrows indicate maximum landslide densities by grid size.

Chapter 6

Results:

The landslide distribution

This chapter presents data generated from the application of the methodology developed and validated in Chapter 5. This landslide inventory dataset provides a widely applicable resource which may be utilised in many different areas of study. For the purposes of this investigation, use of the data is limited to examining controls on the spatial distribution of landslides.

6.1 Overall landslide inventory map

The completed landslide inventory map is presented in *Figure 5.18*. Mapping has been carried out over a total coverage area (A_T) of 11,909km². Around 5% of this zone (557km²) has been mapped as landslide areas. As discussed in *Section 5.3.9*, mapping coverage is not continuous, due to the inability to map areas of significant cloud and haze, or dry regions >3500m in altitude. The coverage area equates to ~12% of the maximum area (100 000km²) predicted to be affected by landsliding in an earthquake of this magnitude (Keefer 2002). The map covers 150km of the 200km surface rupture (Densmore *et al.*, in review), or 280km total co-seismic fault length suggested by the most recent, comprehensive fault model (Shen *et al.*, 2009). Fault models suggests that the majority of co-seismic slip occurred within the mapped area (Shen *et al.*, 2009; Nishimura & Yagi 2008; Ji and Hayes *et al.* 2008), as do most regions of high ground acceleration, with 65% of areas >0.5g covered by the map (USGS 2008). As such, despite the limited total coverage, the mapped area represents a significant sample of the main impact zone of the earthquake.

The majority of the mapped area covers the steep topography of the Longmen Shan mountains, where most landsliding has occurred; however within this an area of around 3,000km² covers regions of relatively flat topography in the Sichuan Basin. The area is dissected by several large rivers including the Min River and Jin River, and exposures of all of the main geological units of the region are also covered in the sample zone.

6.2 Data characteristics of the landslide distribution

In order to examine macro-scale patterns in the landslide distribution while removing local noise, the 2x2km landslide density grid matrix (introduced in *Section 5.5*) is used (*Figure 6.1*). Truncated edge pixels have not been removed from the map, in order to improve the visual result; however the scale range is limited to samples from full 4km² pixels only. The cumulative distribution function for this data is shown in *Figure 6.2*. The maximum P_{Is} sampled within a 4km² grid cell is 64.3%. The majority of the region experiences lower landslide impacts, with 35% of total mapped area (A_T) showing $P_{Is} = 0\%$, and 62% showing $P_{Is} < 1\%$. However, this distribution is strongly skewed by the influence of large areas of the

Sichuan Basin included in the data, which are relatively flat, low lying, and hence have not and could not generate landslides. By removing these areas and considering data from within the mountain range alone, a better representation of controls on the landslide distribution can be achieved. These areas were removed by manually delineating the break in slope along the mountain front, to leave the mountain range only coverage area A_{MT} . The cumulative distribution function for this data is shown in *Figure 6.2*. In the resulting dataset, 13% of A_{MT} shows $P_{IS} = 0\%$, and 45% shows $P_{IS} < 1\%$. Areas of significant $P_{IS} > 20\%$ are limited to around 10% of A_{MT} .

6.3 Landslides relative to geophysical variables

Characteristics of landslide distributions can be described and examined using available thematic datasets, from which independent variables are produced, corresponding to various geophysical processes which harbour a conceptual link to the occurrence of landslides (e.g. Lee *et al.* 2008, Keefer 2000; Khazia 2004), summarised in *Table 6.1*. These factors can be split into two categories based on the mechanism by which they influence landsliding:

1. Ground acceleration triggering of hillslope failures
2. Geophysical causes of hillslope instability

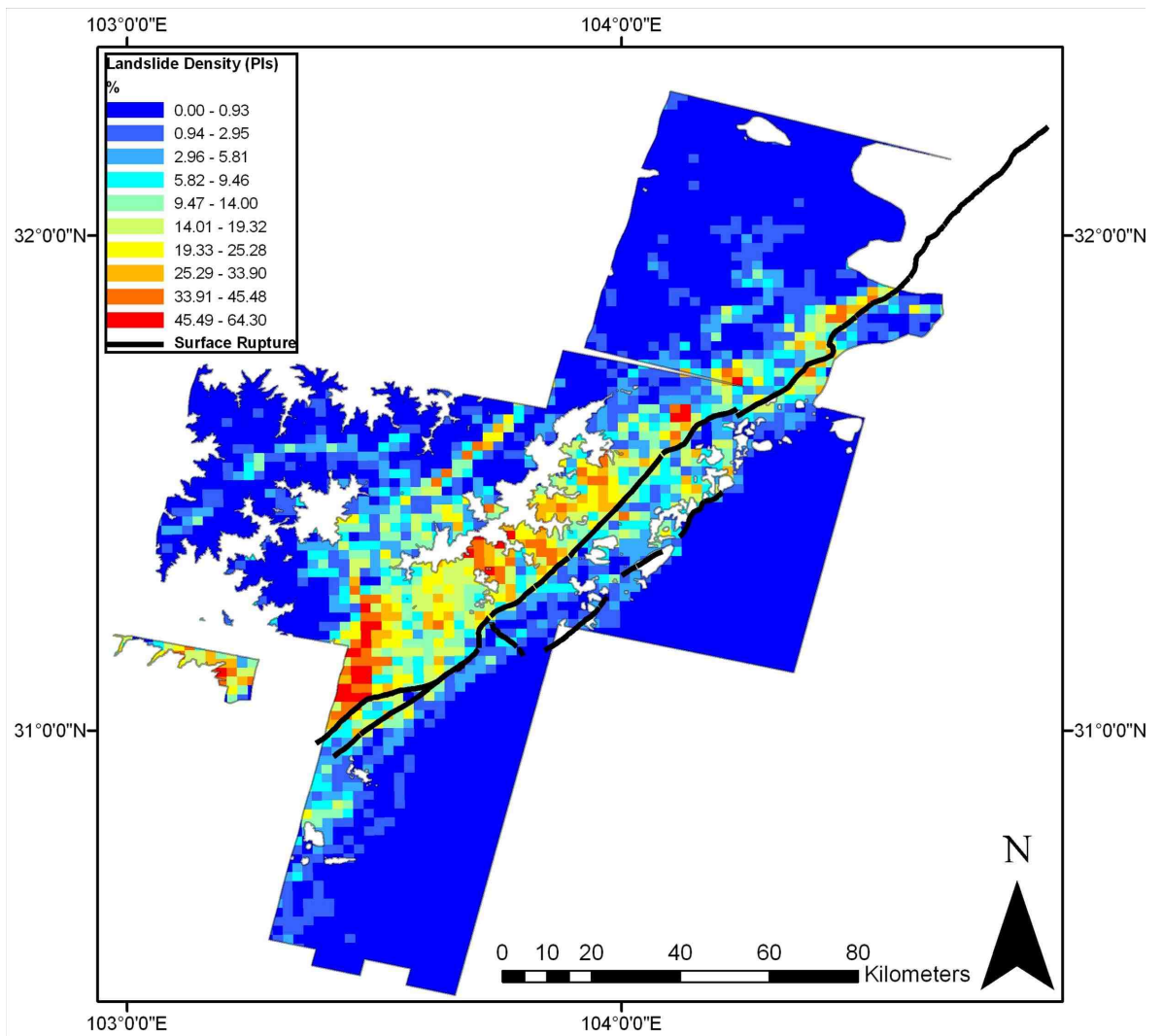


Figure 6.1: Landslide density (PIs) resampled using 2x2km matrix grid

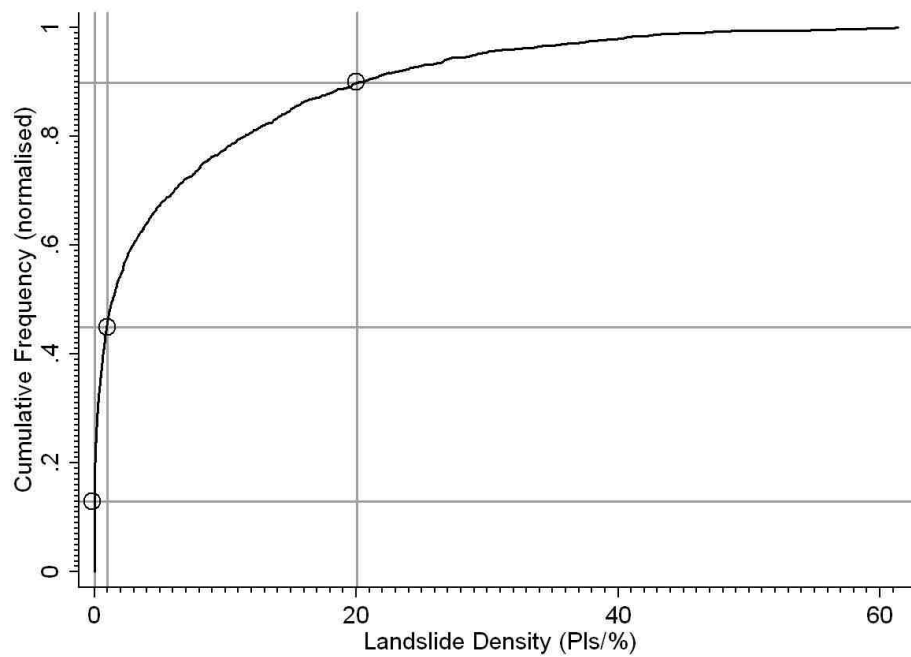


Figure 6.2 Cumulative density function for 2x2km grid with non-mountainous areas removed. Reference lines and markers refer to values quoted in Section 6.2.

Independent variable	Geophysical process
Distance from co-seismic fault rupture	Attenuation pattern of peak ground accelerations (Meunier <i>et al.</i> 2007)
Co-seismic slip distribution	Seismic moment release relating to magnitude of ground accelerations (Campbell 1981)
Hanging wall or footwall	Position relative to the northwest dipping fault plane
Geological unit	Material properties of soils and rocks
Slope gradient	Balance of normal and shear forces within hillslopes, soil water content and flow velocities (Wilson & Gallant 2000)
Elevation	Subaerial processes, potential energy and topographic amplification of seismic waves
Local elevation	Potential energy (Wilson & Gallant 2000), topographic amplification of seismic waves (Meunier <i>et al.</i> 2008), vertical distance from river channels
Relative relief	Potential energy (Wilson & Gallant 2000), balance of normal and shear forces across larger spatial scales (Schmidt & Montgomery 1995)
Plan curvature	Converging / diverging flow, soil water content, soil characteristics (Wilson & Gallant 2000)
Profile curvature	Flow acceleration, erosion / deposition rate, balance of normal and shear forces (Wilson & Gallant 2000)
Total curvature	Topographic amplification at convex knick-points in the landscape (Meunier <i>et al.</i> 2008)
Aspect	Subaerial processes - energy available for erosion. Mode of erosion. Incidence angle dependent topographic site effect on peak ground acceleration (Meunier <i>et al.</i> 2000)
Distance from major river channels	Ground water content, slope steepening due to fluvial erosion.
Upslope contributing area	Runoff volume, soil water content (Wilson & Gallant 2000)

Table 6.1: Independent variables and the geophysical processes they represent

6.4 Ground acceleration triggering of hillslope failures

The first order macro-scale pattern of seismic landslide occurrence in past earthquakes has been related to the regional distribution of ground motions which trigger co-seismic landsliding (Meunier *et al.* 2007; Lee *et al.* 2001; Lin *et al.* 2000). However, ground motion data for the Wenchuan earthquake is very limited, with shakemaps largely based on reports of experienced ground motion, post-

seismic building damage observations and very few strong ground motion records. However, the distribution of co-seismic ground deformation may be used to infer spatial variations in seismic energy released by the earthquake (Wald *et al.* 1999), with the amplitude of seismic waves being expressed as a function of distance from the earthquake source (e.g. Taylor *et al.* 1986; Trifunac 1994; Ambraseys & Douglas 2003). Thus, in the following section, landslide occurrence is described relative to the distance to mapped co-seismic fault ruptures and to the distribution of slip on the co-seismic fault. To achieve this, the pattern of landslide occurrence is generalised in the across-strike and along-strike directions, through a directional sampling of P_{ls} .

6.4.1 Across-strike pattern of landslide occurrence

In order to examine the general across-strike pattern of landsliding for the Chi-Chi, Finisterre and Northridge earthquakes, Meunier *et al.* (2007) sampled P_{ls} within 5km spaced distance buffers along 50km across-strike corridors. Here, in an extension of this method, P_{ls} has been by distance from the main trace of the Beichuan fault, using 1km spaced distance buffers (*Figure 6.3*). Sample areas in the hanging wall and footwall were assigned positive and negative distance values respectively, in order to produce a constant across fault profile from southeast to northwest, shown in *Figure 6.4*. The mean topographic profile is also shown, extracted using the same sample grid.

The data show a clear hanging wall effect, with much higher landslide density on the hanging wall and much lower landslide density on the footwall, even in the immediate vicinity of the fault. Superimposed on this there is a general pattern of decay in landslide density with increasing distance from the surface rupture trace. The decay patterns for both the hanging wall and footwall are best described by exponential functions (*Figure 6.5*). In the hanging wall this decay pattern begins ~10km from the co-seismic fault rupture and continues to the maximum sample fault-distance of 79km. The decay also features two minor peaks that vary from the overall trend, both of which coincide with major river tributaries parallel to the fault. The decay length in the footwall is much shorter, exhibiting $P_{ls} \approx 0$ from the break in slope at the mountain front. This rapid decay coincides with a rapid drop in both mean elevation and slope gradient east of the Pengguan fault. Here the

topographic relief is much lower, with shallow slopes unlikely to sustain landsliding. Hence, in the decay functions plotted in *Figure 6.5*, the footwall data are truncated at the mountain front, 18km from the Beichuan fault. The footwall decay is also relatively smooth, with only slight fluctuations in decay rate between the Beichuan and Pengguan fault ruptures.

6.4.2 Along-strike pattern of landslide occurrence

The pattern of landsliding may also be generalised and examined in the along-strike direction. However, this method of analysis is not seen in the literature as most continental earthquakes have much shorter rupture lengths. In order to extract the general pattern of along-strike landsliding, the sample area was reduced to a 20km buffer either side of the Beichuan fault main trace. This was intended to produce an along-strike sample of roughly constant width, whilst sampling over a large enough across-strike length as not to be skewed by localised noise in the near-field area. The buffer was segmented into 10km slices along a N45°, roughly fault-perpendicular bearing (*Figure 6.6*). P_{IS} was sampled in each of these segments and reprojected into an along-fault coordinate system (x-axis aligned to N45°). As shown in *Figure 6.7*, the intensity of landslide occurrence varies significantly in the along-strike direction. Higher landslide densities are seen to the southwest, in the near epicentre region, with generally lower densities moving northeast. This overall pattern is punctuated by between three and four peaks which occur at along-strike distances of around 20, 40-60, and 120km from the epicentre.

This along-strike pattern of landslide occurrence appears to coincide with features of the co-seismic slip distribution. As also indicated in *Figure 6.7*, the three main peak areas of landslide occurrence coincide with peak regions of permanent co-seismic ground displacements along the Beichuan fault (20-40km and 130-150km) and Pengguan fault (40 to 90km). While the sample mapping area breaks down towards the north-eastern limit of the rupture zone, field observations and preliminary mapping carried out by Li & He (2009) do suggest continued high levels of landslide occurrence in these areas and further along the fault. However, despite this apparently clear pattern, it should be noted that P_{IS} sample areas do vary due to the non-continuous mapping coverage.

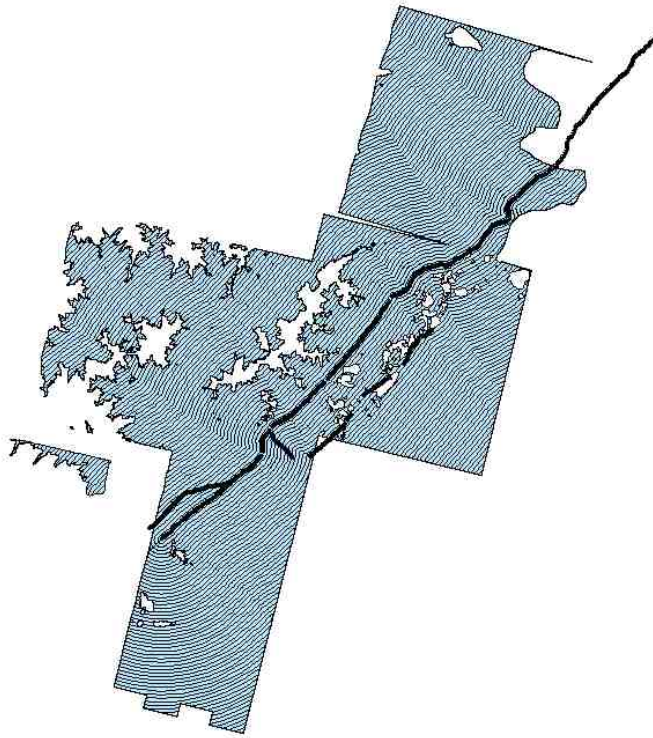


Figure 6.3: Across-strike sample grid—1km distance buffers from the Beichuan fault surface rupture.

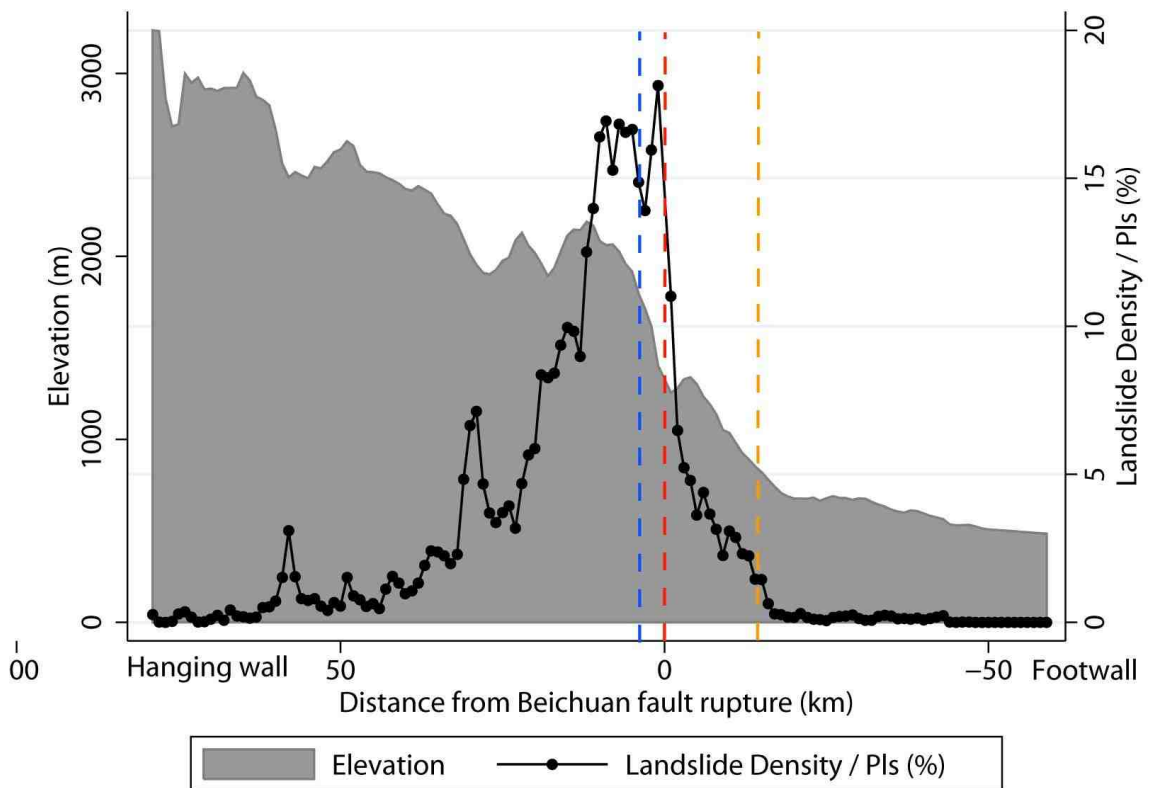


Figure 6.4: Across strike landslide density (black line) and mean topographic profile (grey area; sampled using sample grid in Figure 6.3). Surface fault rupture locations: Beichuan fault main trace (red), Beichuan fault southwest limb (blue), Penguin fault (orange).

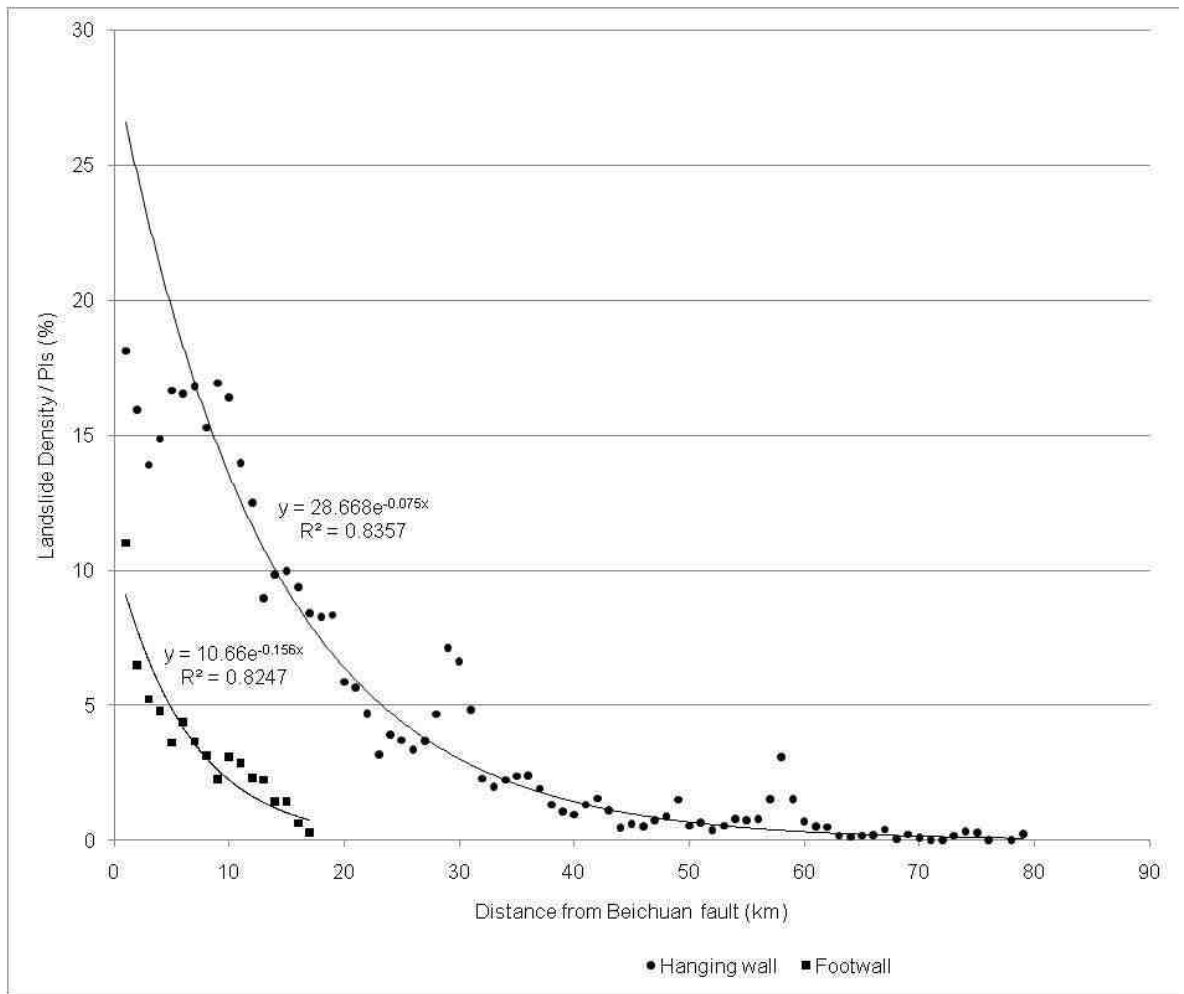


Figure 6.5. Exponential decay functions of across-strike landslide density for the hanging wall and footwall

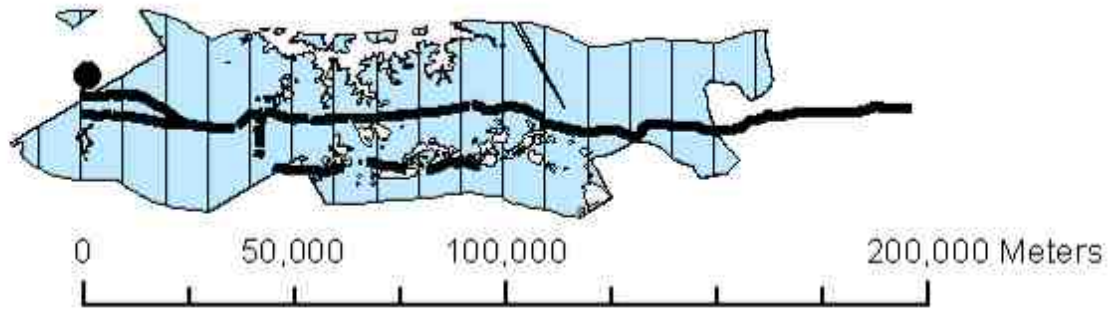


Figure 6.6: Along-strike sample grid. 10km segments along a 20km buffer from the Beichuan fault main trace.

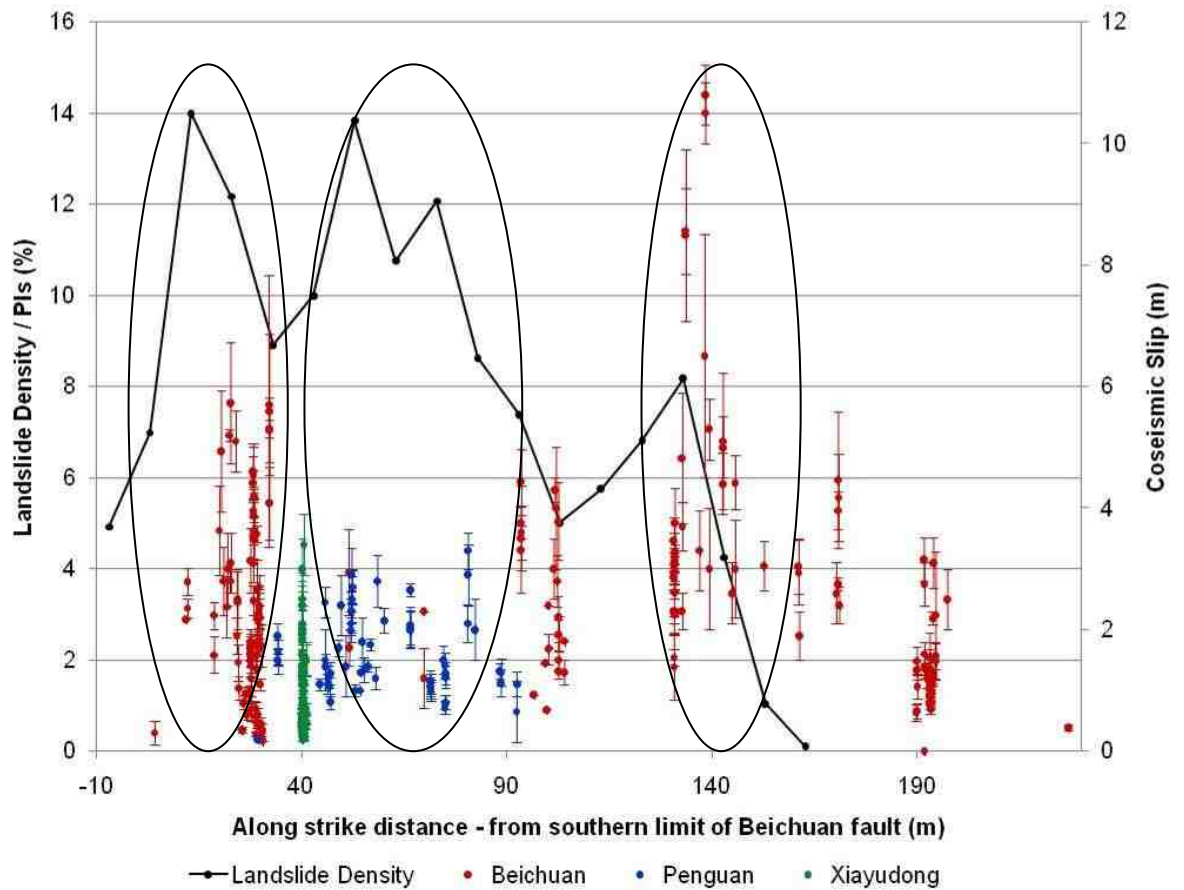


Figure 6.7: Along-strike landslide density and coseismic slip measured on the Beichuan, Penguan and Xiayudong faults. Slip data from Densmore et al (in review). Distance scale refers to along-strike distance to the northeast, from the southern limit of the Beichuan fault.

6.4.3 Two dimensional spatial variations in landslide occurrence

The above approaches present the landslide distribution relative to a single dimension, relating to ground motion patterns in the across or along-strike directions. This is a useful approach for generalising the pattern of landslide occurrence (e.g. Meunier *et al.* 2007). However, it presents a very limited perspective when investigating large earthquakes with long rupture lengths, where the evolution of ground motions is dependent on the fault-relative perspective. A more holistic spatial overview of the pattern of landslide occurrence is achieved by sampling P_{Is} over multiple across-strike cross-sections, spaced evenly in the along-strike direction. As opposed to the matrix sample grid shown in *Figure 6.1*, this approach is better suited for articulating the relative change in landslide density between contiguous and proximal areas, as expressed in the dominant directions of influence of fault normal impact decay and along fault rupture variability. The sample grid used for this is shown in *Figure 6.8*. Note that the spacing across-strike is 1km, while the spacing along-strike is 10km. This is intended to reflect the different scales over which influences on seismic ground motions vary in these two dimensions.

Using a 3D surface plot (*Figure 6.9*) the pattern of landslide occurrence is visualised in across- and along-strike directions simultaneously. Again the hanging wall effect is evident, particularly in areas to the southwest (lower values on the long axis), where landslides occur almost exclusively in the hanging wall of the Beichuan and Pengguan faults. However, further along-strike from the Pengguan fault, several profiles reveal increasing landslide occurrence in the footwall. To the southwest landslides are also distributed at greater distances from the fault rupture, however P_{Is} values decay much more rapidly with distance from the fault in the northeast.

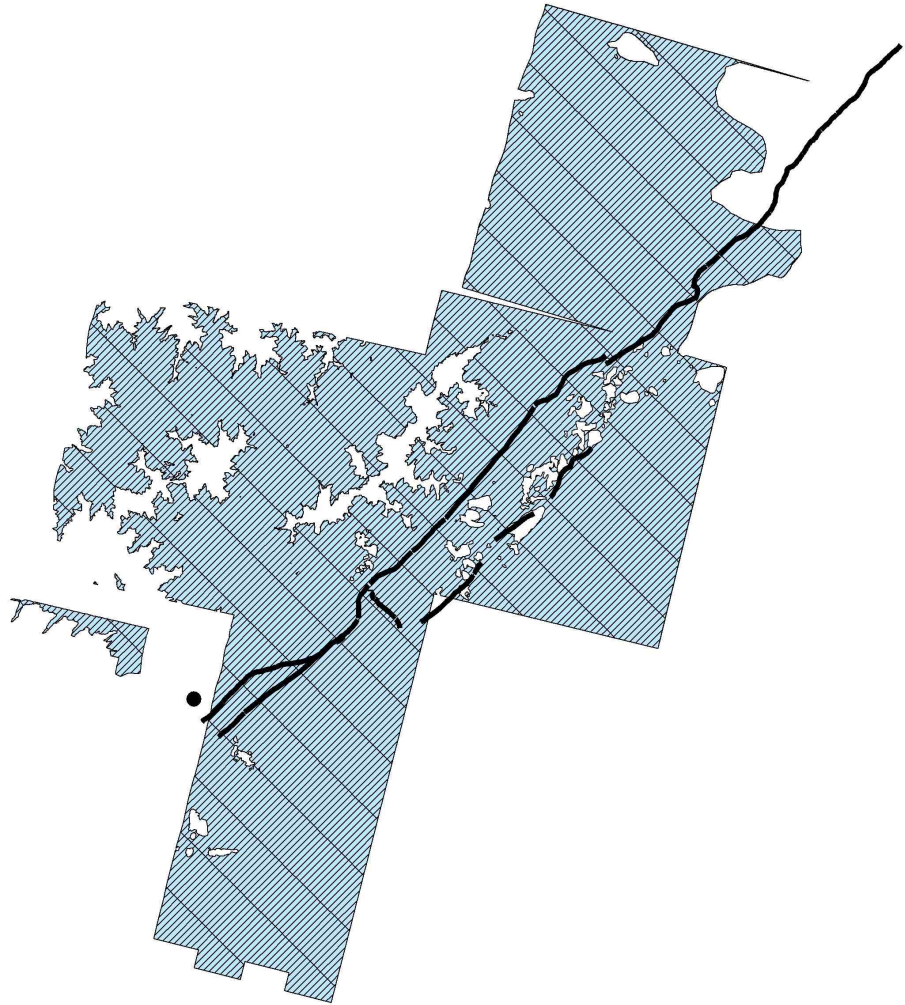


Figure 6.8: Multiple across strike profile, sample grid.

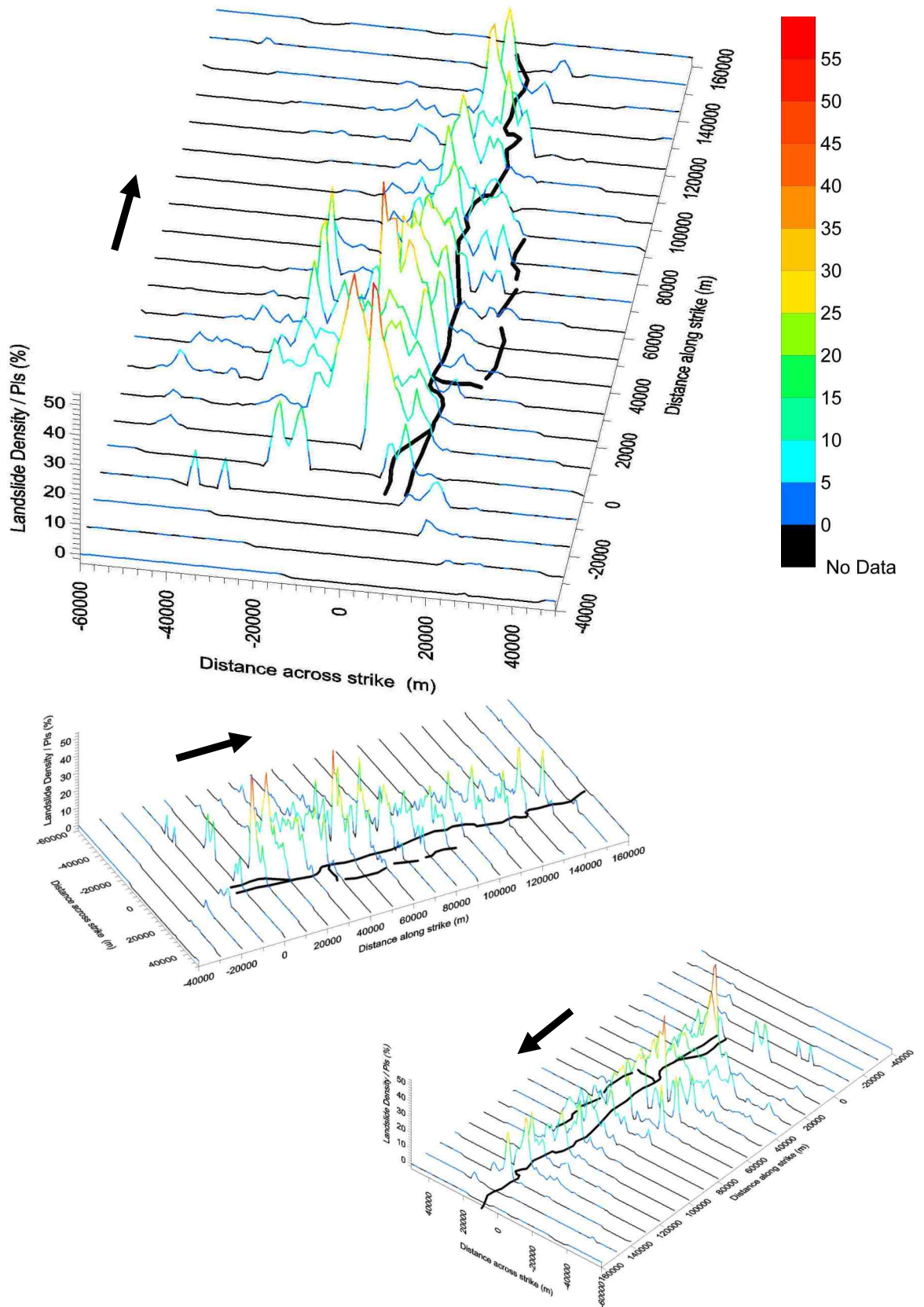


Figure 6.9: Multiple along-strike landslide density profiles, plotted in along-fault projection. Long axis trends at 45° (northeast). Thick black lines show surface ruptures. Black arrows indicate north direction.

6.5 Landslide occurrence relative to geophysical causes of hillslope instability

While proximity to the earthquake source and the evolution of ground motion magnitude defines the area affected by seismic landsliding, a number of geophysical causal factors act to make areas of the landscape inherently unstable, with the potential for failure when seismic shaking occurs. Here landslide occurrence is described relative to two datasets reflective of these causes: the regional map of geological units, and the digital elevation model through which various characteristics of the topography are derived.

6.5.1 Landslide occurrence relative to geological units

This section is based around *Figures 6.10 to 6.13*, which illustrate the pattern of landslide occurrence relative to geological units. In *Figure 6.10*, geological controls may be linked to the macro-scale distribution of landslides, through visual comparison of geological and landslide density maps. *Figure 6.11* presents the normalised area distribution for the full mapped area (A_{MT}) and the landslide covered area (A_{ML}), within different mapped geological units, while *Figure 6.12* shows the landslide density (P_{Is}). Finally *Figure 6.13* is used to highlight the pattern of landslide occurrence relative to age of geological units.

Mesoproterozoic granitic basement yields the highest landslide density of 18% (*Figure 6.12*), however the unit has an aerial coverage (A_{Tc}) of only $A_T = 0.12$ (*Figure 6.11*). Field reports suggest that landslides in this unit were predominately shallow surface failures, which stripped off thin top soils to expose bedrock (Petley 2009 pers comm, Densmore 2009 pers comm). Also exhibiting high landslide occurrence are Proterozoic volcanics and dolomite, with $P_{Is} = 11\%$, and $A_{Tc} = 0.02$. Both these units compose the high, steep terrain of the Pengguan massif area, in the hanging wall of the co-seismic fault rupture.

Next are Palaeozoic greywacke and shale, and Triassic mudstone, sandstone and conglomerate. Both these units exhibit $P_{Is} = 4\%$. The Palaeozoic unit is extensively distributed throughout the hanging wall of the Beichuan fault, with only small areas mapped to the southeast of the co-seismic ruptures. However, Triassic mudstone occurs entirely in the proximal footwall of the Beichuan fault, and between the

Beichuan and Pengguan faults. In addition, the Palaeozoic unit is the most common geology type covering $A_T = 0.43$, while the Triassic unit covers only $A_T = 0.09$.

The Triassic (SGF fold belt) turbidites and acidic volcanics unit has the next highest P_{ls} of 2%. A relatively small area of this unit is mapped ($A_T = 0.05$), beginning at a distance of around 50km from the fault rupture in the hanging wall. All other units exhibit $P_{ls} < 1\%$, including Jurassic conglomerate, sandstone and mudstone; Cretaceous conglomerate; Mesozoic granite; Quaternary unconsolidated sediments; and Tertiary conglomerate, sandstone and mudstone. Notably the Quaternary unit is the second most common ($A_T = 0.18$), yet exhibits the lowest overall landslide density, $P_{ls} = 0.003\%$, with the majority of the unit's area falling within the low slope filter used in mapping.

With the exception of Mesozoic granite, all units with $P_{ls} < 1\%$ occur in footwall areas and exhibit low gradients and relief. However, the Mesozoic granite plutons occur between 30 and 50km into the hanging wall. The dominant spatial pattern of landslide occurrence by geological units reflects the overall macro-scale pattern presented in *Figure 6.1*, of higher P_{ls} in the hanging wall units, lower P_{ls} in footwall units, and overall decay with distance from the fault rupture.

Figure 6.13 shows landslide density plotted against the approximate age (with uncertainty margins) of geological units. This shows a pattern of increasing landslide occurrence with rock age, which is best expressed by the Tan function:

$$P_{ls} = a \tan(bG_a)$$

Equation 6.1

$$R^2 = 0.91$$

where G_a is the geological unit age in years B.P., and a and b are constants: $a = 21.6$ and $b = 3.95 \times 10^{-4}$.

While the dataset produced in this investigation is not appropriate for detailed landslide size analysis, the two largest landslides lie in Proterozoic volcanics and dolomite, and Palaeozoic greywacke and shale; the largest landslide bridges both units, while the second largest occurs solely in the Palaeozoic unit.

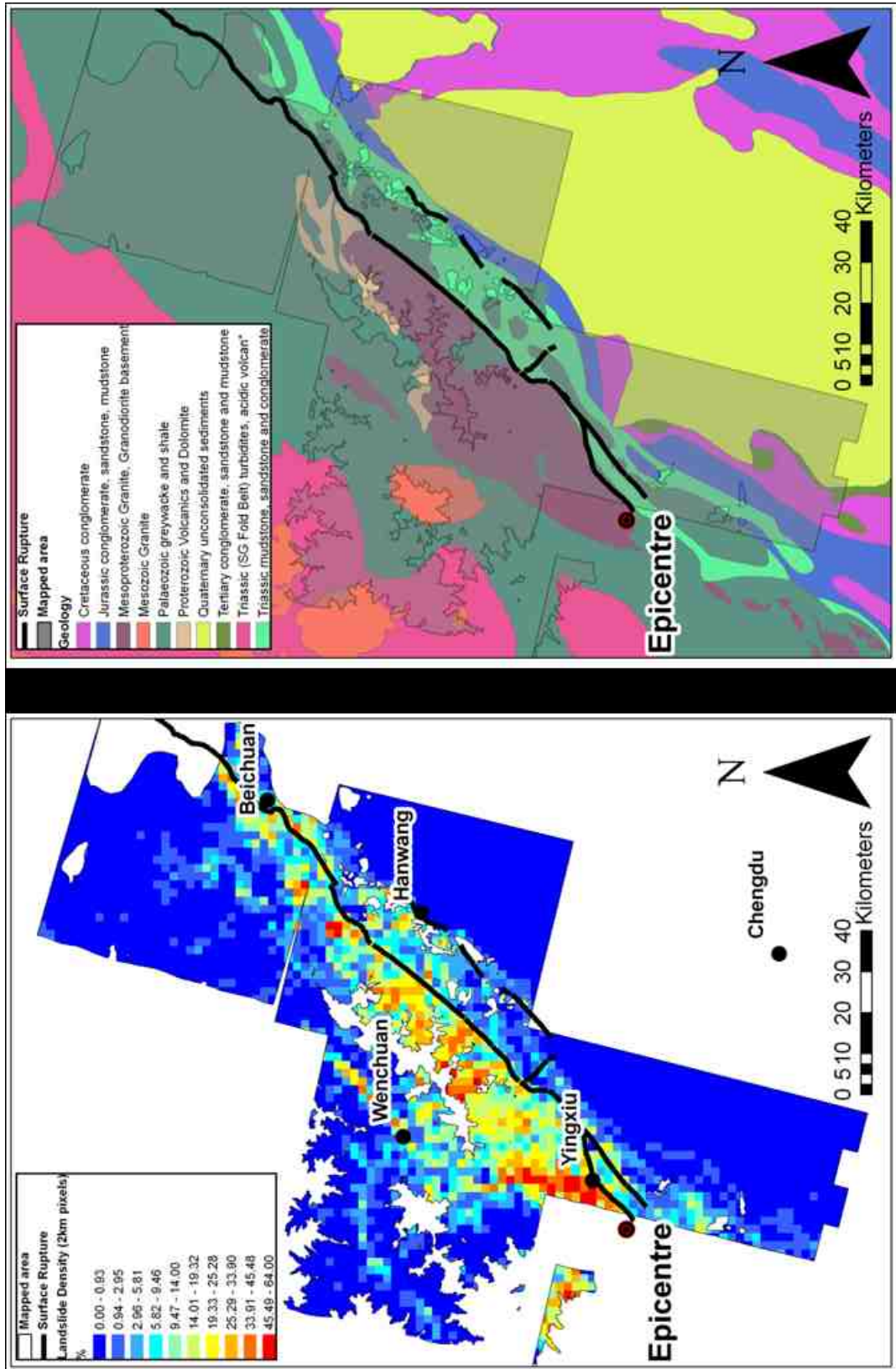


Figure: 6.10: Left - 2km landslide density matrix grid; Right - Map of geological units (Ma *et al* 2002)

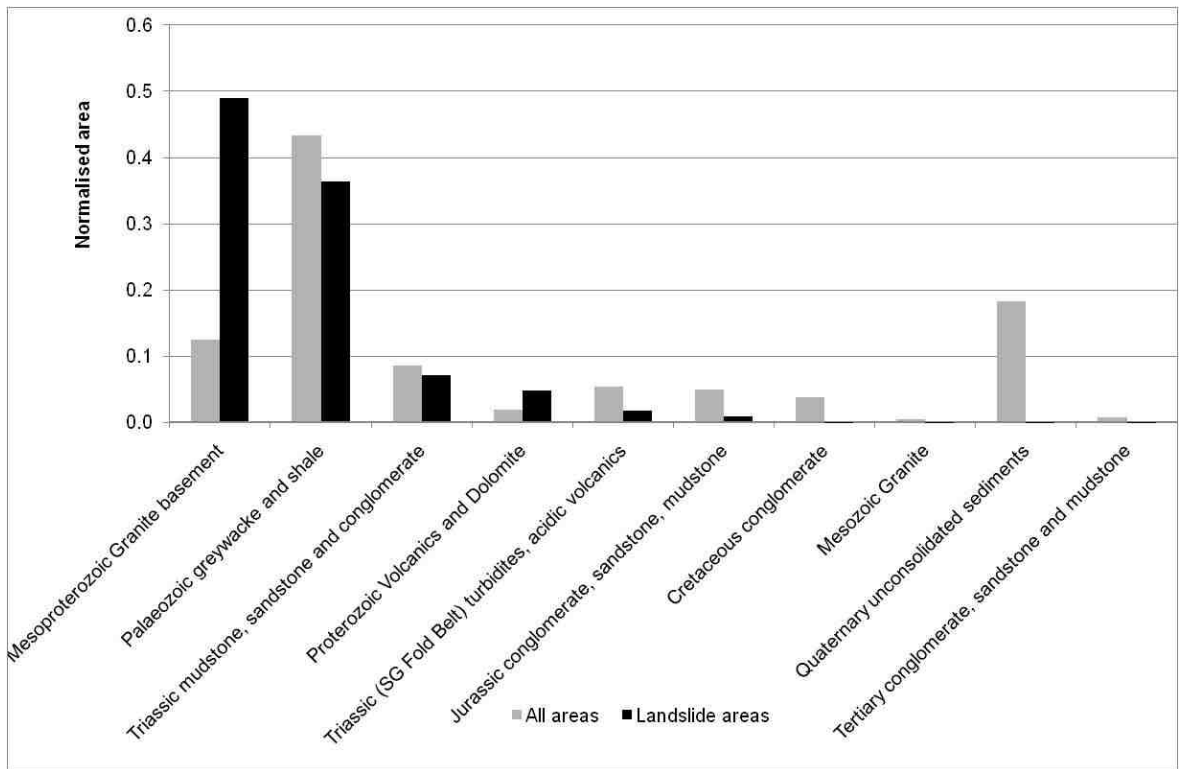


Figure 6.11: Normalised distribution of all areas and landslide areas, sampled by geological units.

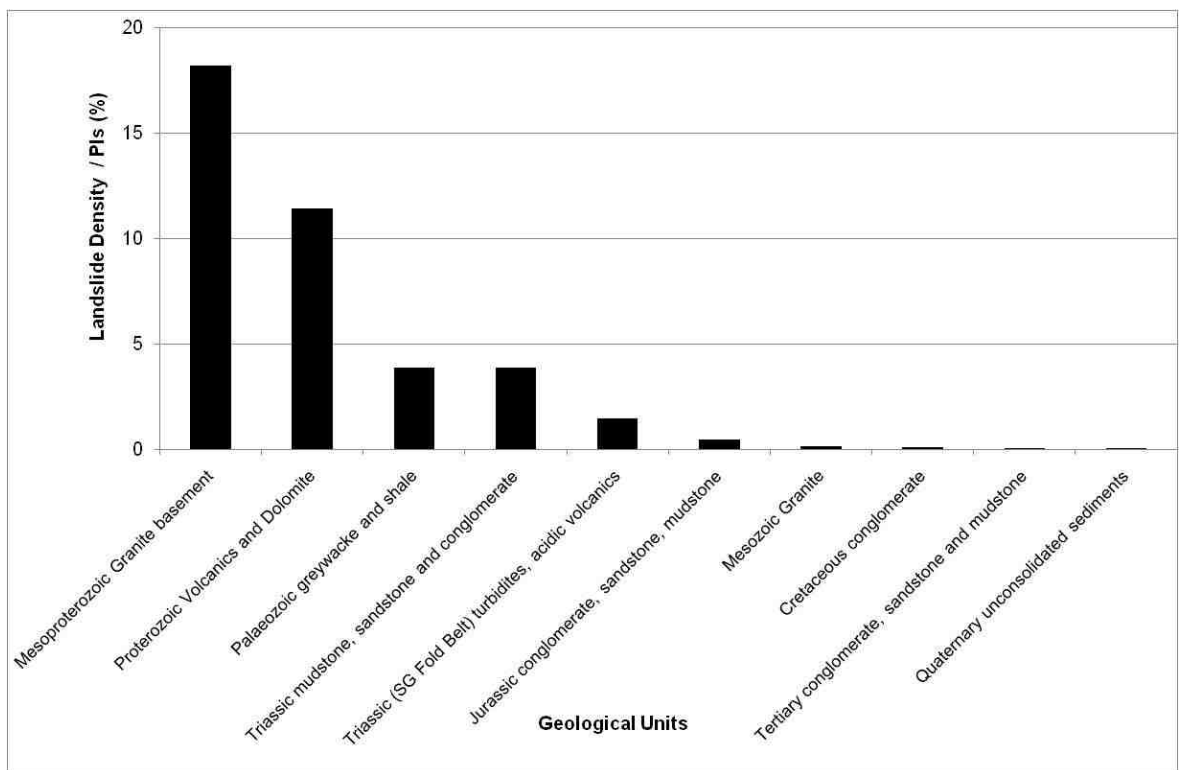


Figure 6.12: Landslide density distribution sampled by geological units.

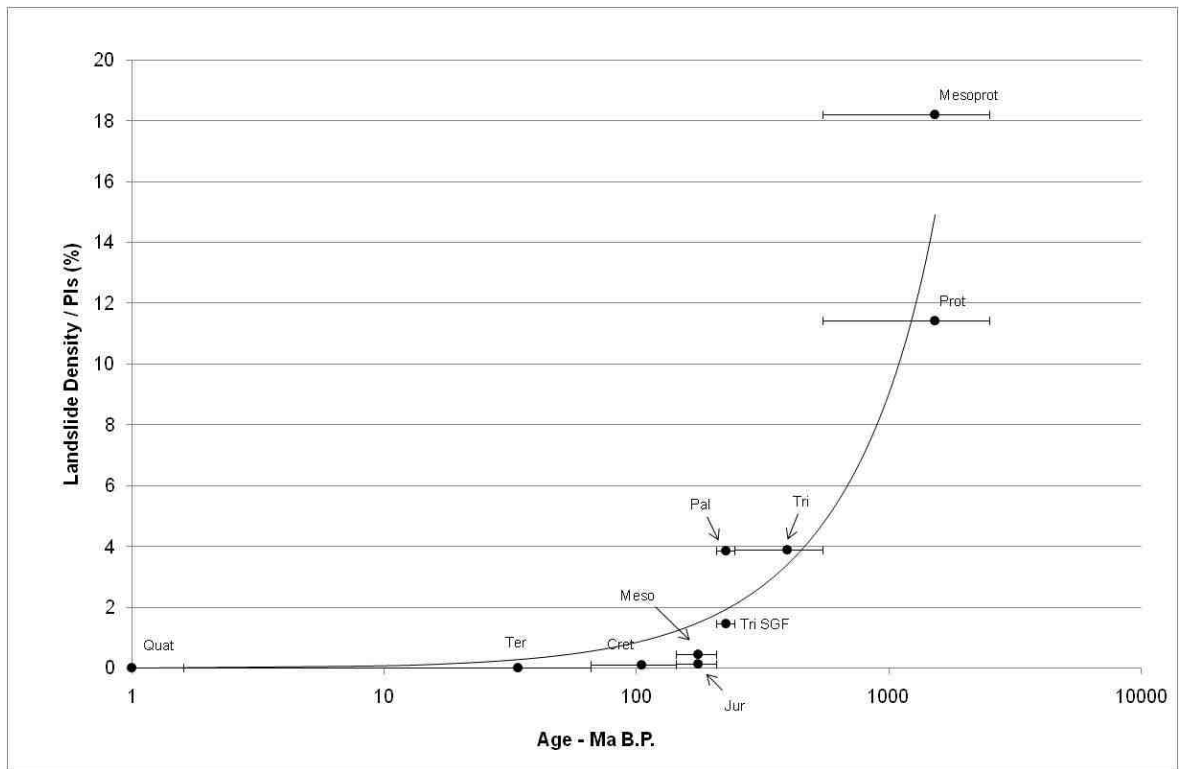


Figure 6.13: Landslide density by geological unit age.

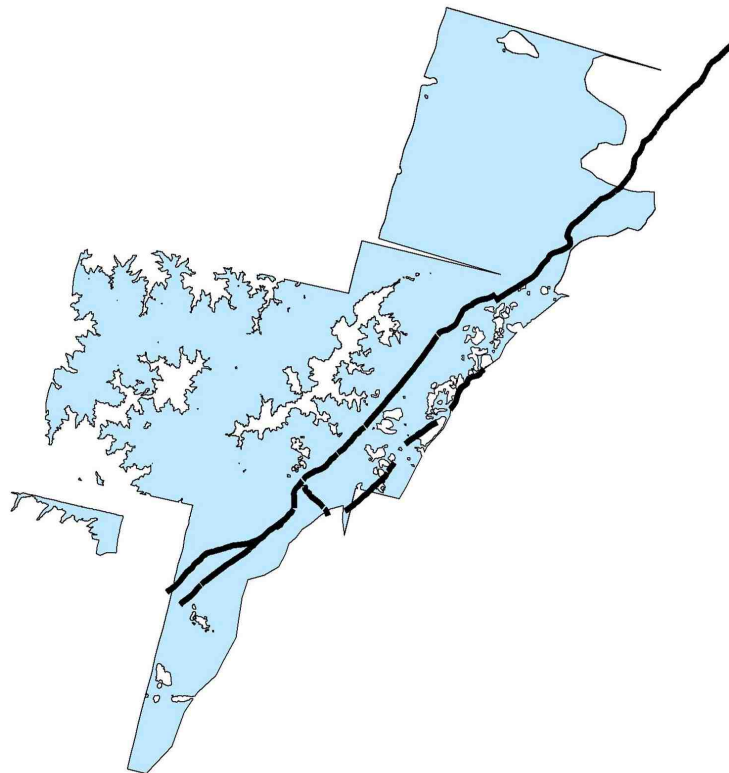


Figure 6.14: Mountain terrain only sample area (A_{MT}). Fault ruptures shown by thick black lines.

6.5.2 Landslide occurrence relative to topographic attributes

The SRTM DEM dataset provides topographic elevation data across the full coverage of the study area (A_T) at 90m pixel resolution. Using the DEM, the topography of the area can be described through a range of attributes (Wilson and Gallant 2000). The spatial distributions of topographic attributes are commonly used as an indirect measure of the spatial variability of Earth surface processes (Moore *et al.* 1991), and thus provide a useful series of base layer data with which to describe and analyse landslide inventories (e.g. Lee *et al.* 2008). In this section the following primary topographic attributes (Moore *et al.* 1991) are used to explore topographic characteristics of the landslide inventory:

- Elevation
- Slope gradient
- Local-elevation
- Relative relief
- Profile curvature
- Plan curvature
- Total curvature
- Aspect
- Upslope contributing area
- Distance from major river channels

Derivatives of the raw elevation data were produced using the appropriate surface functions in ArcGIS spatial analyst. Compound topographic attributes, such as topographic wetness indices, have also been applied to landslide distributions (e.g. Lee *et al.* 2008). However, these are not used at this stage in order to avoid the complicating affects and cross-correlations which results from combining multiple primary attributes.

As in the above sections, P_{ls} was sampled within zones reflective of variations in geophysical factors. Unlike the regular spatial sample grids and geological unit areas, topographic data is spatially continuous and must therefore be divided into evenly spaced bins in order to create zones of near-constant value within which P_{ls} is sampled. For each topographic attribute, bin ranges were user defined, based on spatial variability of the thematic layer and the range of values, in order to reflect the overall relationship between P_{ls} and the independent variable. In order to suppress the influence of non-uniformly distributed, inherently stable terrain, the sampled area used in this section of the analysis is limited to the mountain range coverage area A_{MT} , as described in *Section 6.2*. For each topographic attribute the normalised area distribution functions are presented for the full mapped area (A_{MT}) and the landslide covered area (A_{ML}), and on a separate plot landslide density distribution is given. Due to the relatively small 90m zone fragment size (produced by the DEM raster resolution) it is not possible to generate figures showing individual zone areas in full detail. However, the sample area (A_{MT}) is shown in *Figure 6.14*.

6.5.2.1 Elevation

Using the original SRTM elevation data, P_{ls} was sampled in binned zones at 100m elevation intervals. The normalised area distribution in *Figure 6.15* shows that the distribution of landslide-affected hillslopes tracks closely with the distribution of all elevations in the area. However, landslides are oversampled on lower slopes between 1000 and 2500m, and undersampled in areas between 2500 and 3500m. This is reflected in the landslide density curve (*Figure 6.16*), showing generally higher P_{ls} at lower elevations and lower P_{ls} at higher elevations. Very low areas also experience relatively low landslide density.

6.5.2.2 Hillslope gradient

Figures 6.17 and 6.18 were produced by sampling P_{ls} within 1° gradient bins. In *Figure 6.17* both datasets produce a roughly symmetrical normal distribution; however the distribution of landslide-affected hillslopes is negatively skewed by $\sim 6^\circ$ relative to all hillslopes in the sample area. This shows that landslides oversample steeper hillslopes, whilst undersampling hillslopes of shallower gradient. The resulting landslide density curve (*Figure 6.18*) shows an increase in

landslide density with gradient, which can be expressed as the exponential function:

$$P_{Is} = 1.6652e^{0.0536\beta}$$

Equation 6.2

$$R^2 = 0.97$$

where β is gradient in degrees. However, despite the strength of the fit, significant noise and a slight rollover occurs between 62 and 67°. At these high values the sample area is very small, increasing the likelihood of outlying data points – note that the outlier at 67° was excluded when fitting the trendline. Greater deviation from the trend is also seen at lower values of gradient less than 20°. Whilst the sample size is also smaller for these values, this is likely to be an artefact of using slope gradient masks of 17° and 20° in the mapping process. *Figure 6.18* also shows a linear relationship between gradient and the standard deviation of landslide density ($^{\circ}P_{Is}$):

$$^{\circ}P_{Is} = 0.6564\beta + 9.6331$$

Equation 6.3

$$R^2 = 0.98$$

This appears to fit well for low and mid-range gradient values. Again, poorer correlation and a change in trend is evident for values of gradient >61°, and greater deviation from the trend at gradients <20°, due to the small sample size at the extremes of the range. This shows that, while P_{Is} increases with gradient, variability in P_{Is} also increases. Thus, even at steeper gradients, many hillslopes did not fail.

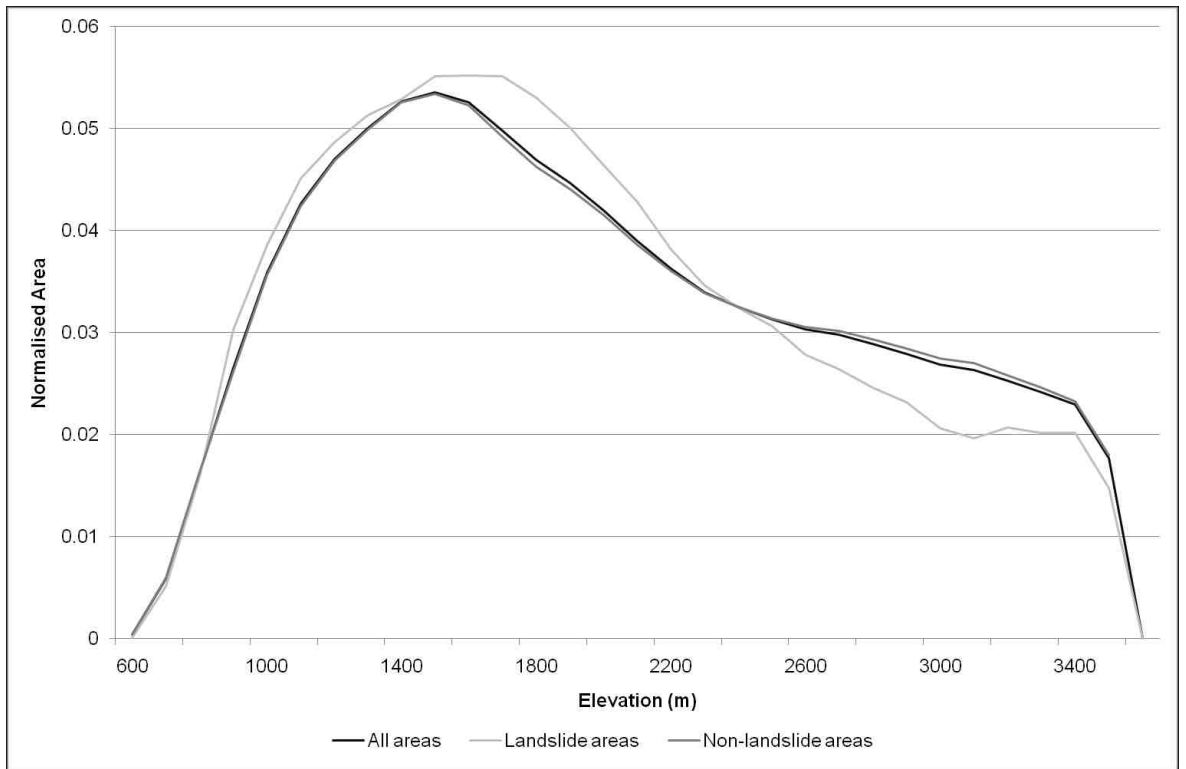


Figure 6.15: Normalised distribution of all areas and landslide areas, sampled by 100m elevation bins.

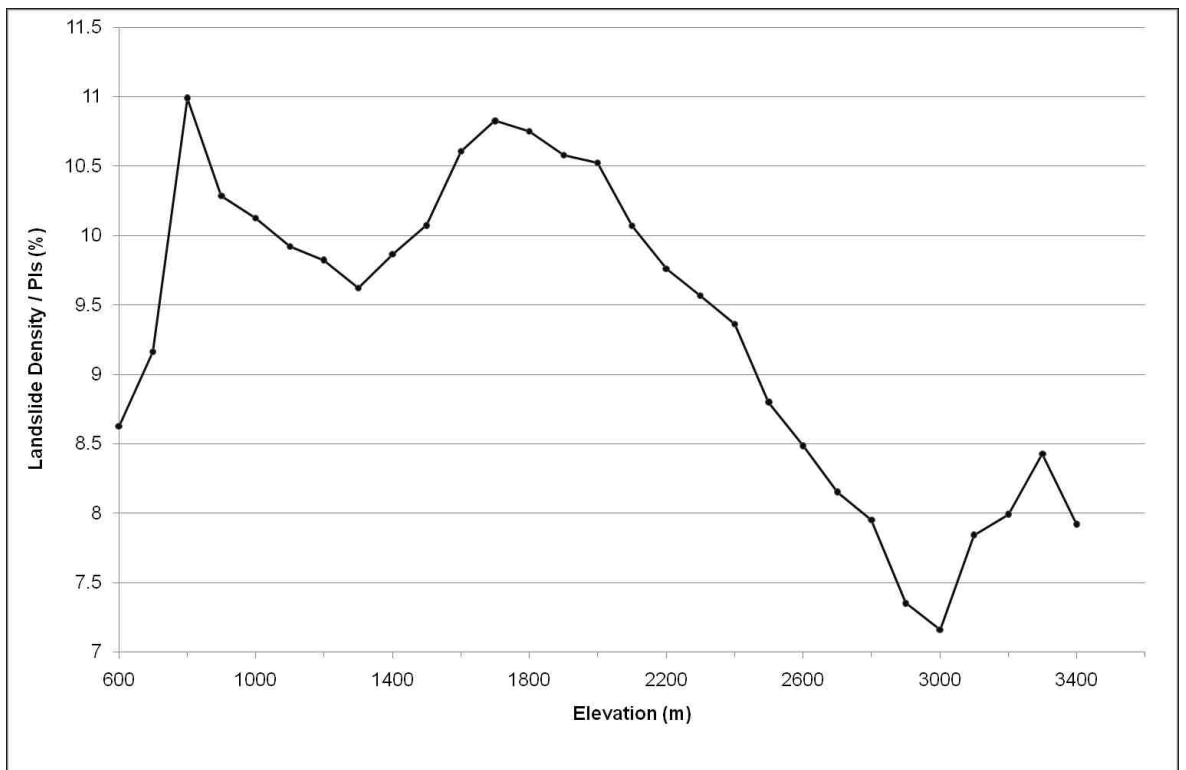


Figure 6.16: Landslide density distribution sampled by 100m elevation bins.

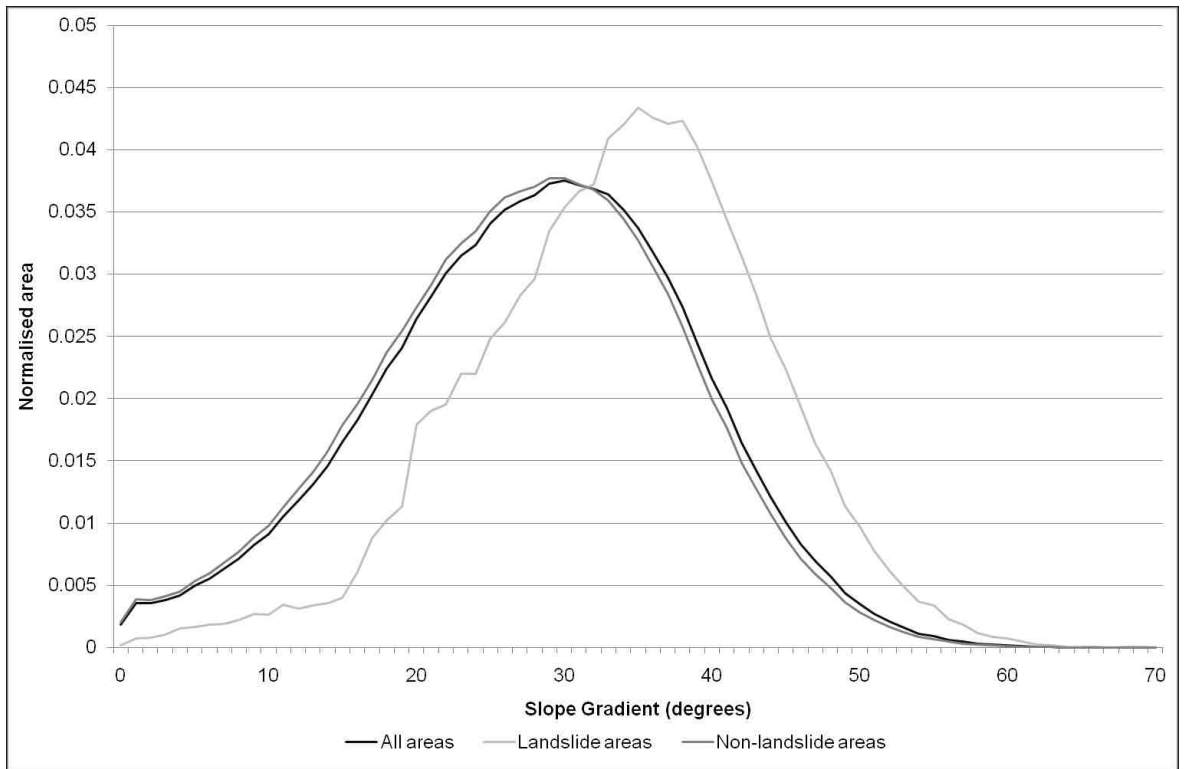


Figure 6.17: Normalised distribution of all areas and landslide areas, sampled by 1° gradient bins.

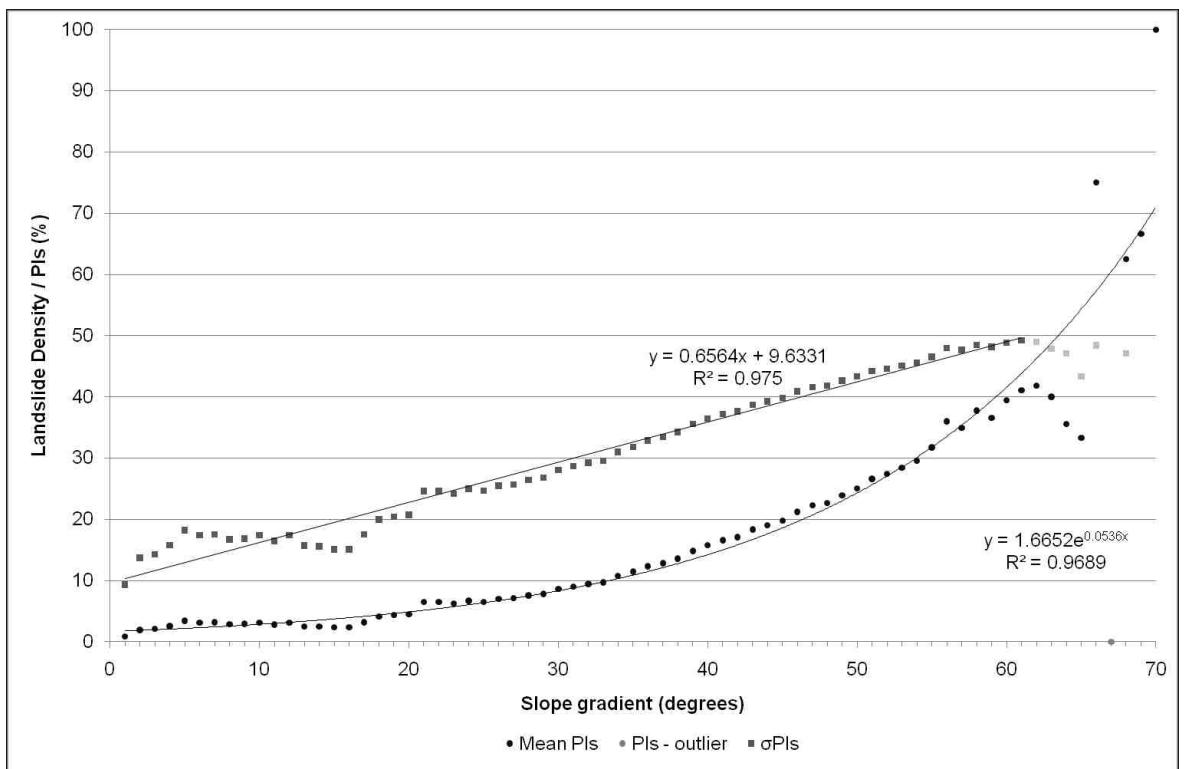


Figure 6.18: Landslide density distribution sampled by 1° gradient bins.

6.5.2.3 Relative relief

Relative relief (R) is calculated from the change in elevation over a given search radius, providing an index not only for overall hillslope gradients, but also the length of steep slopes and potential energy available for slope failure. In order to reflect river to peak horizontal distances of most landslide inducing valleys, a search radius of 2km was used, and the data divided into 10m bins. The normalized area distribution (*Figure 6.19*) shows a similar pattern to that of gradient. Landslides undersample on lower relief hillslopes and oversample on hillslopes with higher relief. This is reflected in the landslide density distribution (*Figure 6.20*), which shows an increase in landslide density with relative relief, which is best described by the following curve:

$$P_{Is} = a \text{Cosh}(bR)$$

Equation 6.4

$$R^2 = 0.90$$

where a and b are constants: $a = 0.5160$ and $b = 2.119 \times 10^{-3}$

6.5.2.4 Local elevation

While the raw elevation values in the DEM give absolute height, landslide processes occur at the hillslope scale, not the scale of the mountain range as a whole. To reflect this P_{Is} was sampled using a raster of elevation within a 4km search radius. Again, this convolution size was used to reflect stream to peak horizontal distances of most landslide inducing valleys, while allowing for a large enough elevation range that longer slopes did not become saturated with peak values. In *Figure 6.21*, the normalised values for A_{MT} and A_{ML} both track closely to one another in a positively skewed distribution. This creates fairly constant P_{Is} at local elevation values between 100m and 2400m (*Figure 6.22*). At high local elevations there is greater variation in P_{Is} and a peak at the highest elevation value. Here the sample size is very small, with the peak P_{Is} value based on a sample of only 4 raster pixels, compared to >95000 pixels in the 500m bin.

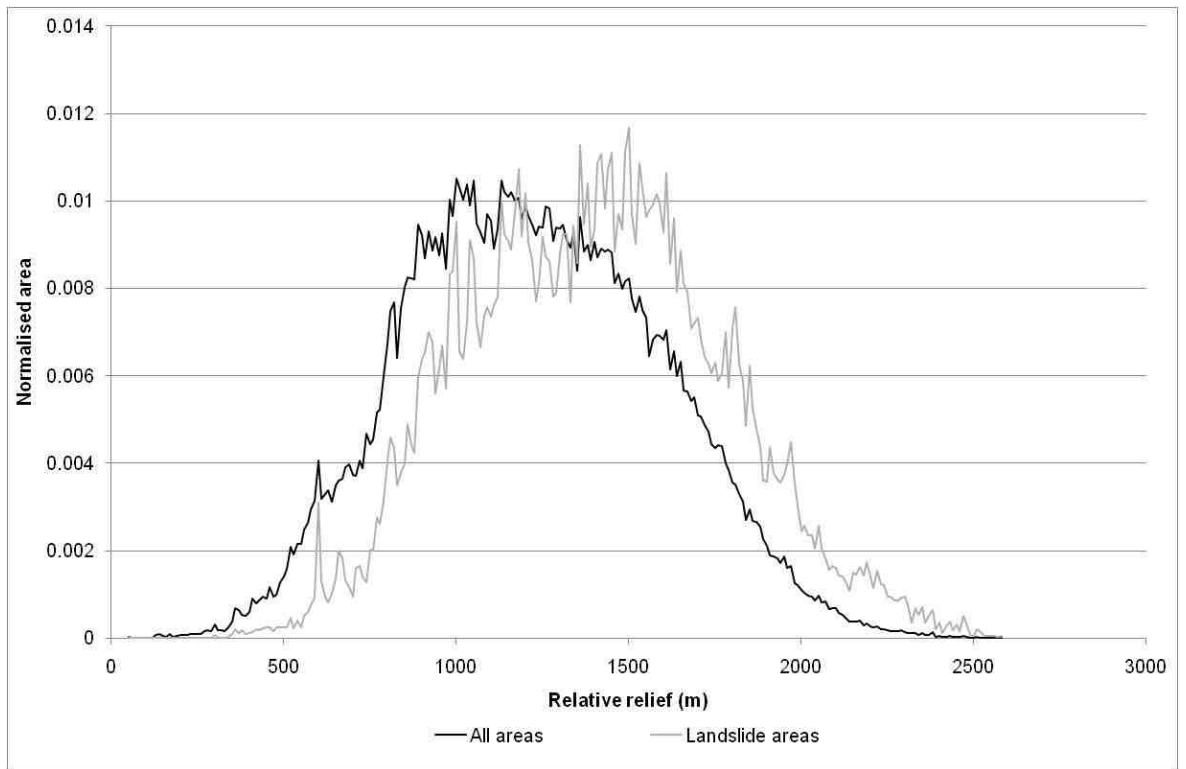


Figure 6.19: Normalised distribution of all areas and landslide areas, sampled by 10m relative relief bins.

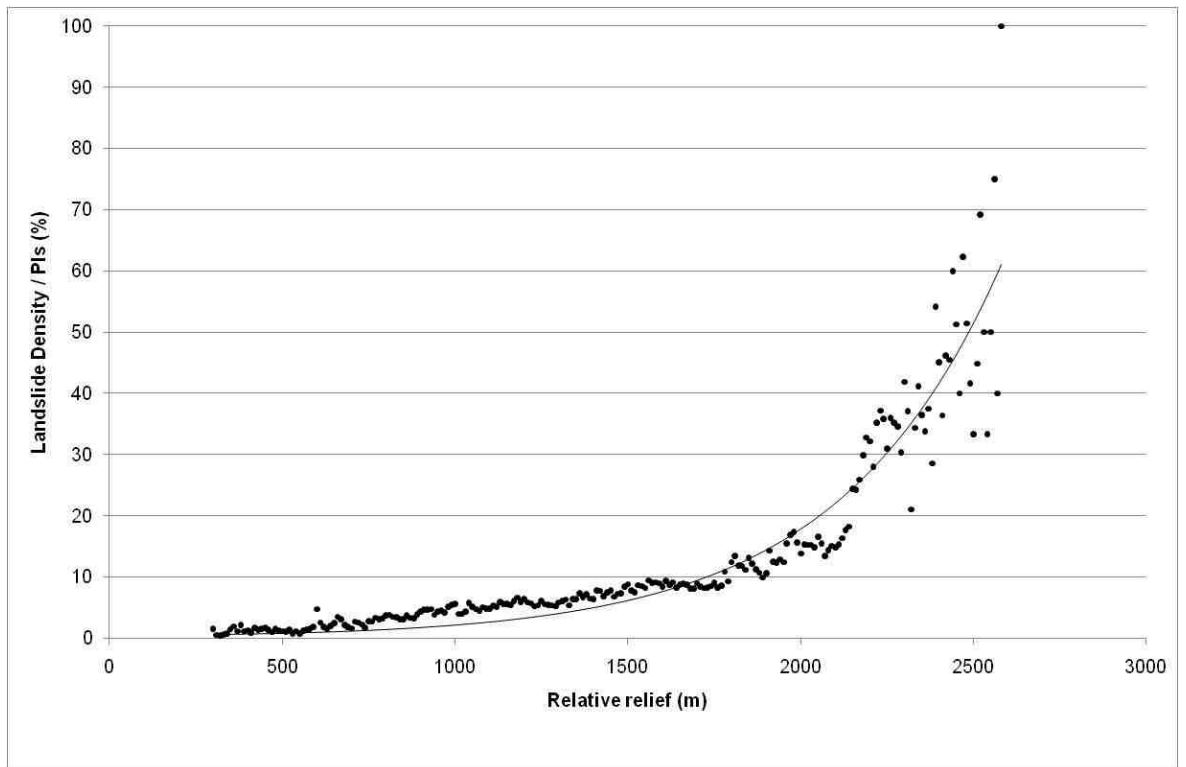


Figure 6.20: Landslide density distribution sampled by 10m relative relief bins.

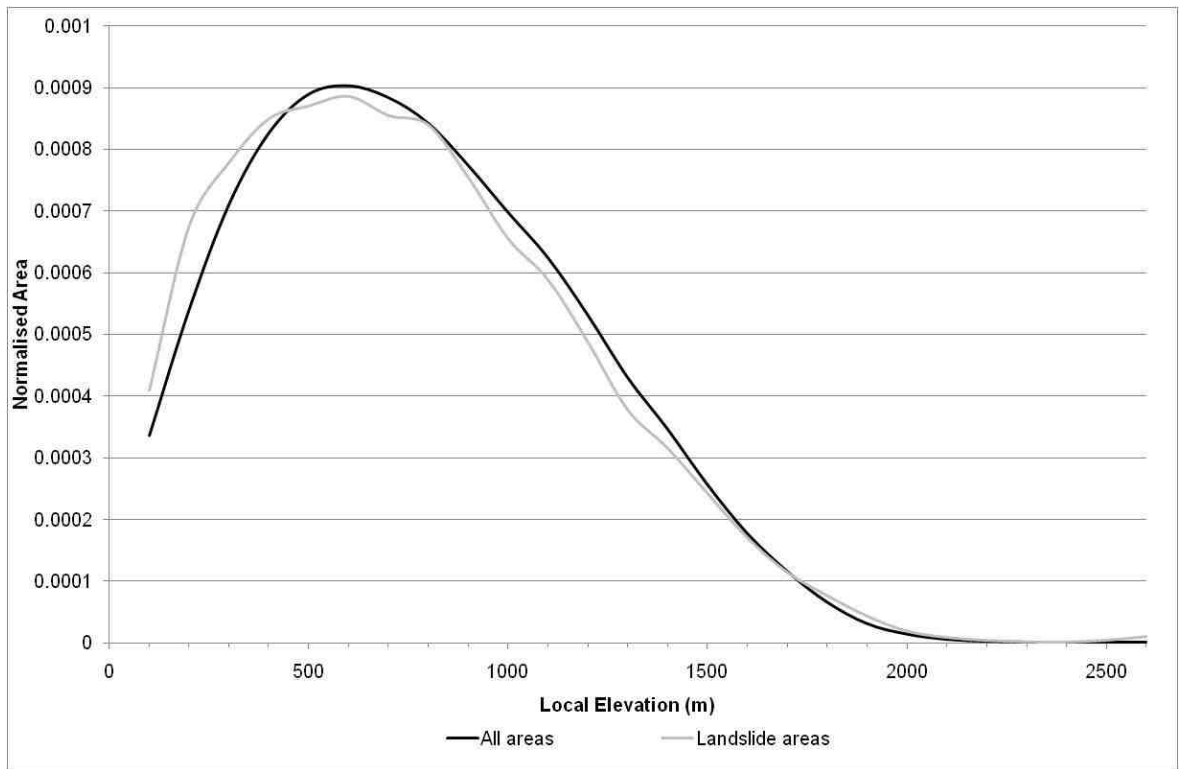


Figure 6.21: Normalised distribution of all areas and landslide areas, sampled by 100m local elevation bins.

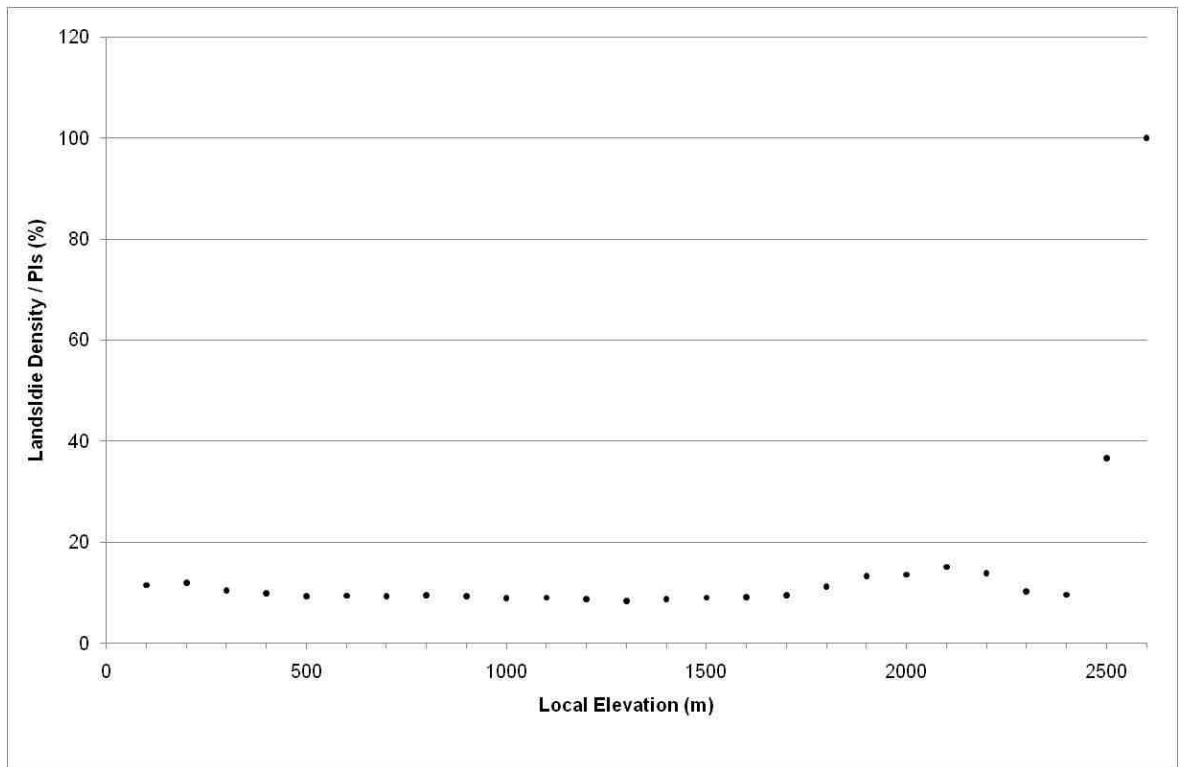


Figure 6.22: Landslide density distribution sampled by 100m local elevation bins.

6.5.2.5 Slope curvature

Curvature is a measure of the spatial change in gradient on a pixel to pixel basis, indicating whether a surface is concave or convex. Three forms of curvature measurement are commonly used in geomorphological investigation:

- Profile curvature, relating to flow acceleration, and the rate of erosion or deposition
- Plan curvature, signifying convergence or divergence of flow, along with soil water content
- Total curvature, calculated from the sum of the profile and plan curvatures, indicating whether the overall shape of a surface is curves inward or outward.

Curvature units were divided into 0.1m^{-1} bins for analysis. In all normalised area distributions, mid-values of curvature $\sim 0\text{m}^{-1}$ make up the majority of the sample. This is demonstrated in the full range of values plotted for total curvature in *Figures 6.23 and 6.24*. Thus, while the distributions are spread over a range of over $\pm 10\text{m}^{-1}$, the majority of pixels range between $\pm 1.5\text{m}^{-1}$ (plan and profile curvature) to $\pm 3\text{m}^{-1}$ (total curvature), with significant noise in the landslide density distribution beyond these limits. In order to remove outlying data-points and better visualise the majority of the data, plots for curvature are truncated where the sample size becomes close to 0; this occurs roughly at a distance of 5 standard deviations from the mean.

The frequency distribution for profile curvature (*Figure 6.25*) shows a slight undersampling of concave-up slopes (curvature $< 0\text{m}^{-1}$), and a slight oversampling of convex-up slopes (curvature $> 0\text{m}^{-1}$). Planar hillslopes (curvature $\approx 0\text{m}^{-1}$) are also undersampled. This is reflected in the landslide density distribution (*Figure 6.26*), which shows higher landslide densities on convex than concave surfaces. Considering the whole dataset, this produces an average P_{ls} of 25% for profile concave surfaces and 28% for profile convex surfaces.

Contrary to the pattern observed for profile curvature, the frequency distribution for plan curvature (*Figure 6.27*) shows a slight oversampling of concave hillslopes

(hollows, curvature $< 0\text{m}^{-1}$), and a slight undersampling of convex hillslopes (noses). This results in higher landslide densities on concave than convex surfaces (*Figure 6.28*). Considering the whole dataset, this produces an average P_{ls} of 32% for plan concave surfaces and 18% for plan convex surfaces.

For total curvature, the frequency distribution (*Figure 6.29*) shows an oversampling of concave hillslopes and an undersampling of convex hillslopes. Like the landslide density distribution for plan curvature, this produces higher landslide densities on concave than convex surfaces (*Figure 6.30*). Considering the whole dataset, this produces an average P_{ls} of 29% for overall concave surfaces and 18% for overall convex surfaces.

In summary, examining the landslide distribution using curvature measures shows that the majority of landslide affected areas occur on hillslopes with low curvature values close to 0. In other words, on hillslopes which are neither excessively concave nor convex. However, at these mid-values, landslides occur preferentially on hillslopes with concave plan and total curvatures, and convex profile curvatures.

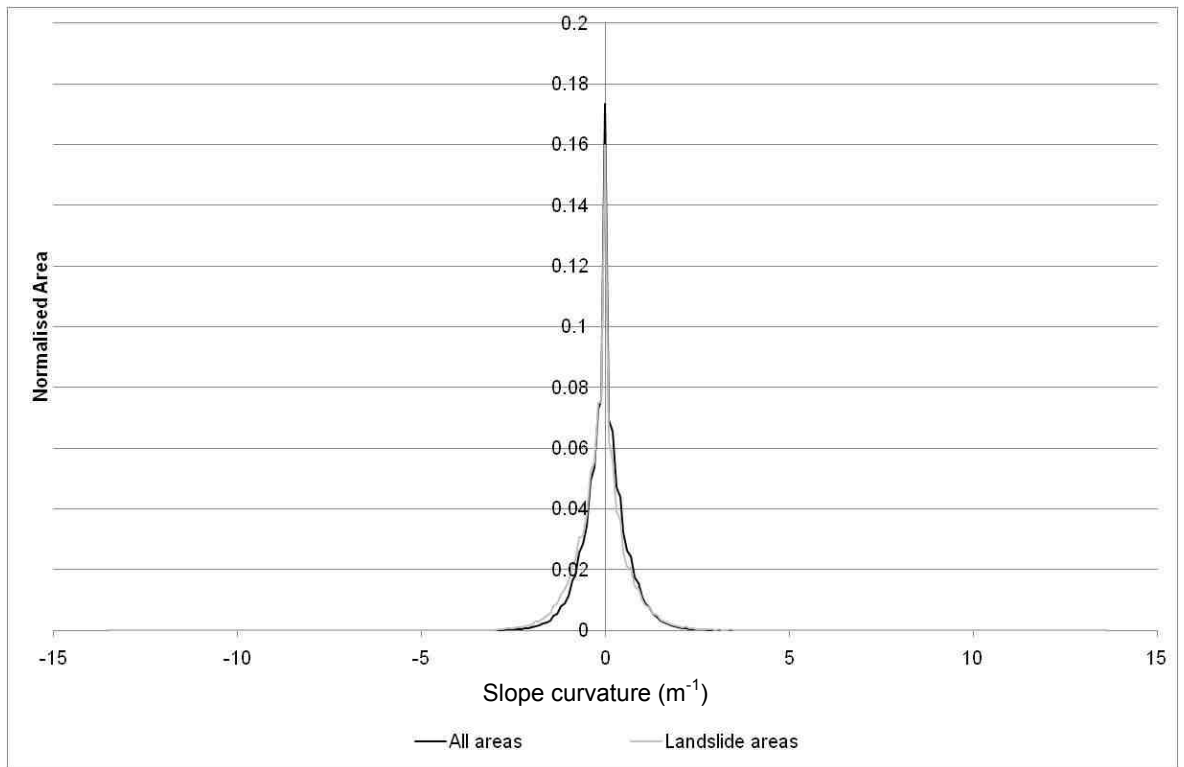


Figure 6.23: Normalised distribution of all areas and landslide areas, sampled by 0.1m^{-1} total curvature bins.

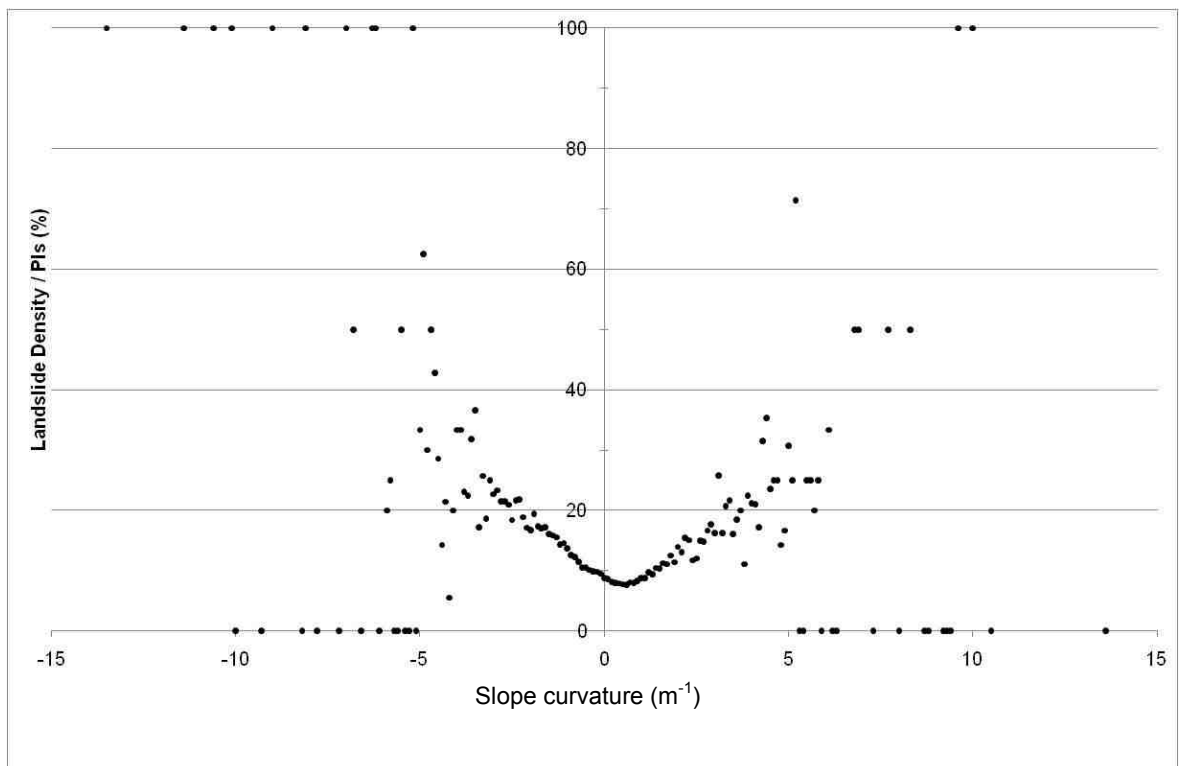


Figure 6.24: Landslide density distribution sampled by 0.1m^{-1} total curvature bins.

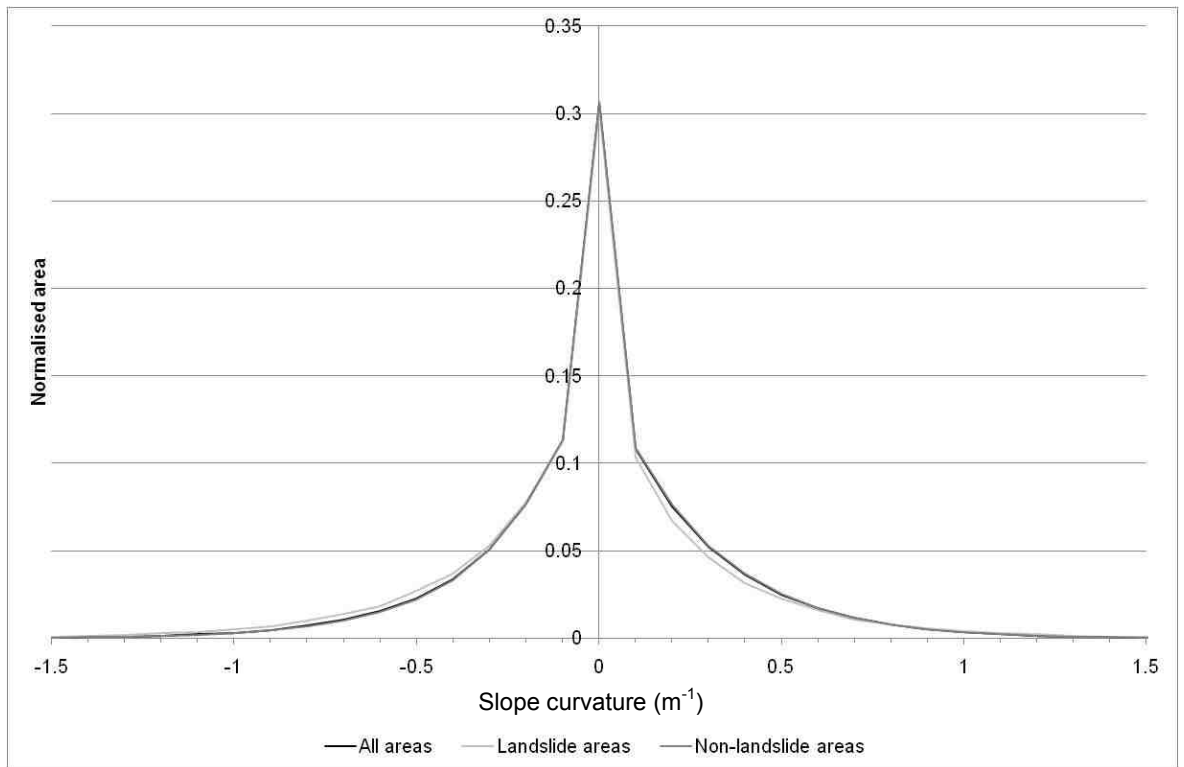


Figure 6.25: Normalised distribution of all areas and landslide areas, sampled by $0.1m^{-1}$ profile curvature bins. Graph is limited to curvature values from 1.5 to -1.5 .

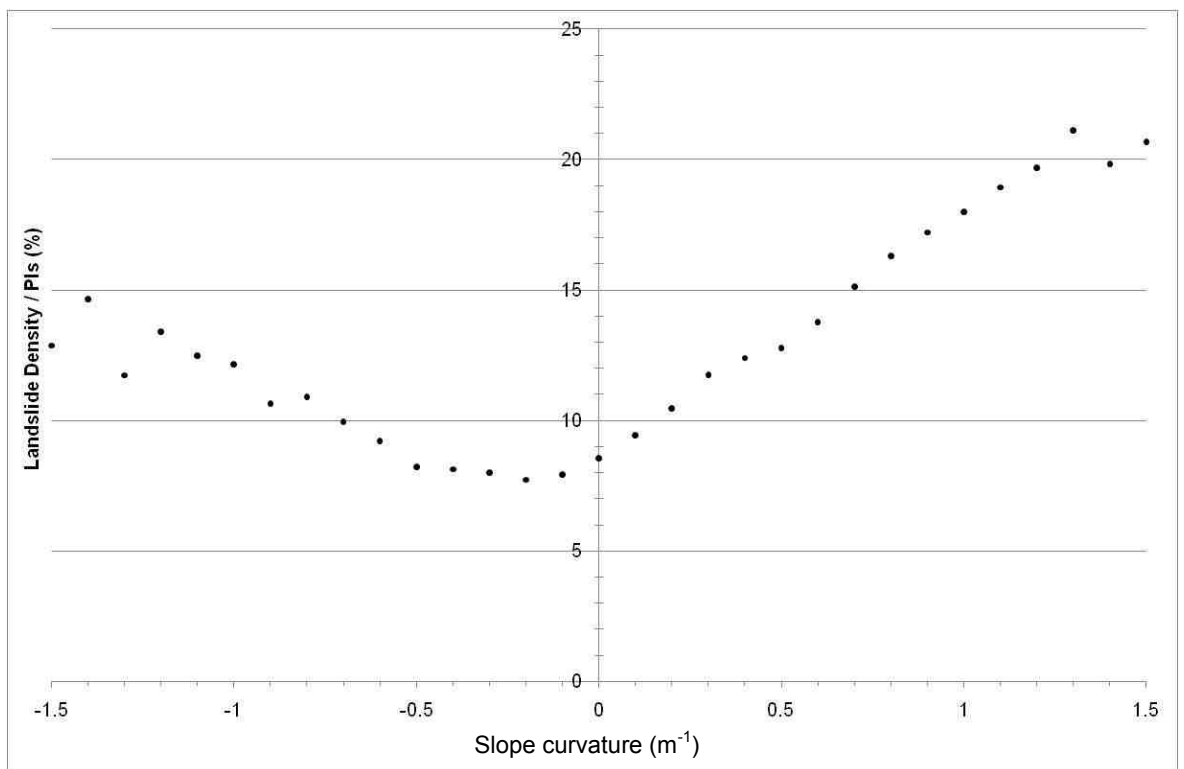


Figure 6.26 Landslide density distribution sampled by $0.1m^{-1}$ profile curvature bins. Graph is limited to curvature values from 1.5 to -1.5 .

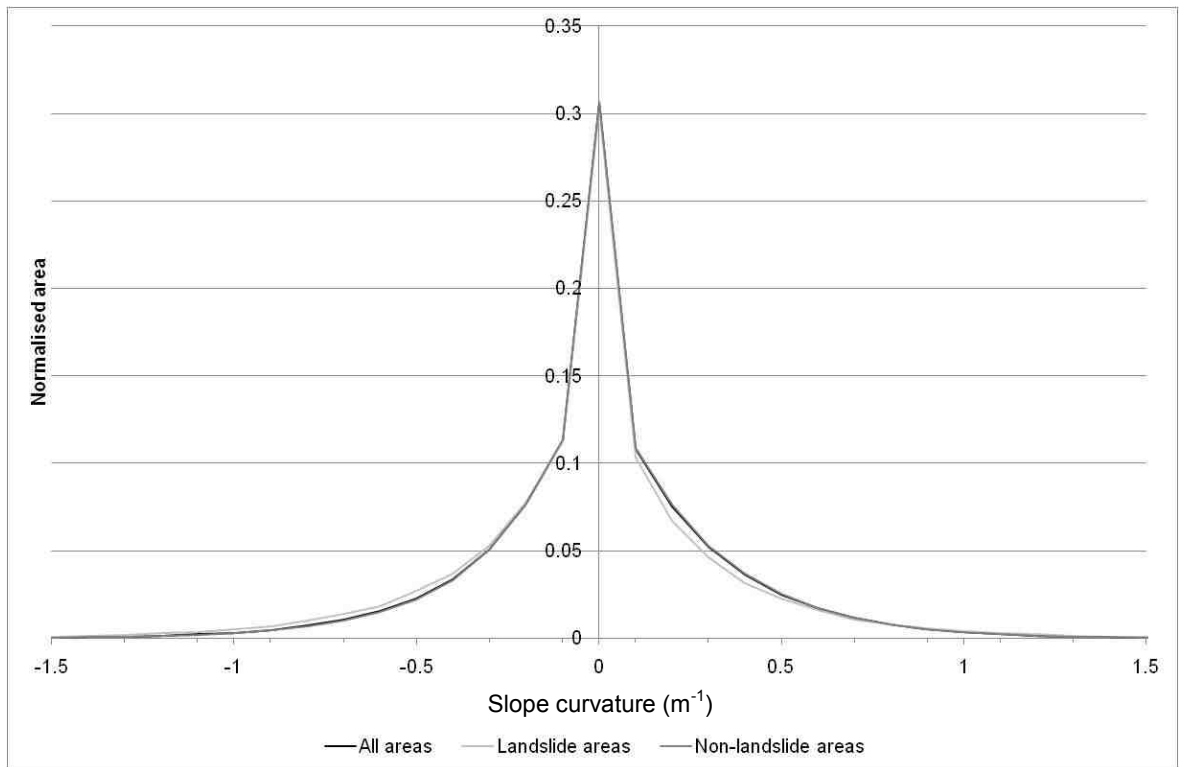


Figure 6.27: Normalised distribution of all areas and landslide areas, sampled by 0.1m^{-1} plan curvature bins. Graph is limited to curvature values from 1.5 to -1.5 .

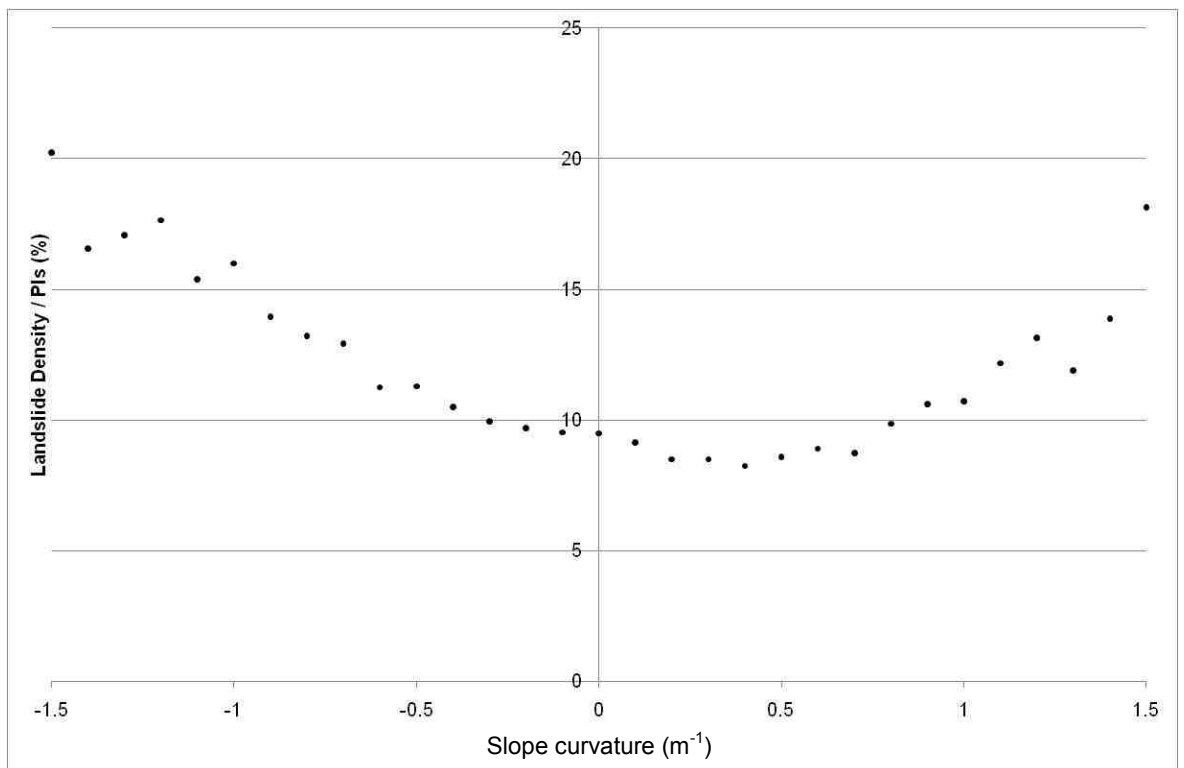


Figure 6.28: Landslide density distribution sampled by 0.1m^{-1} plan curvature bins. Graph is limited to curvature values from 1.5 to -1.5 .

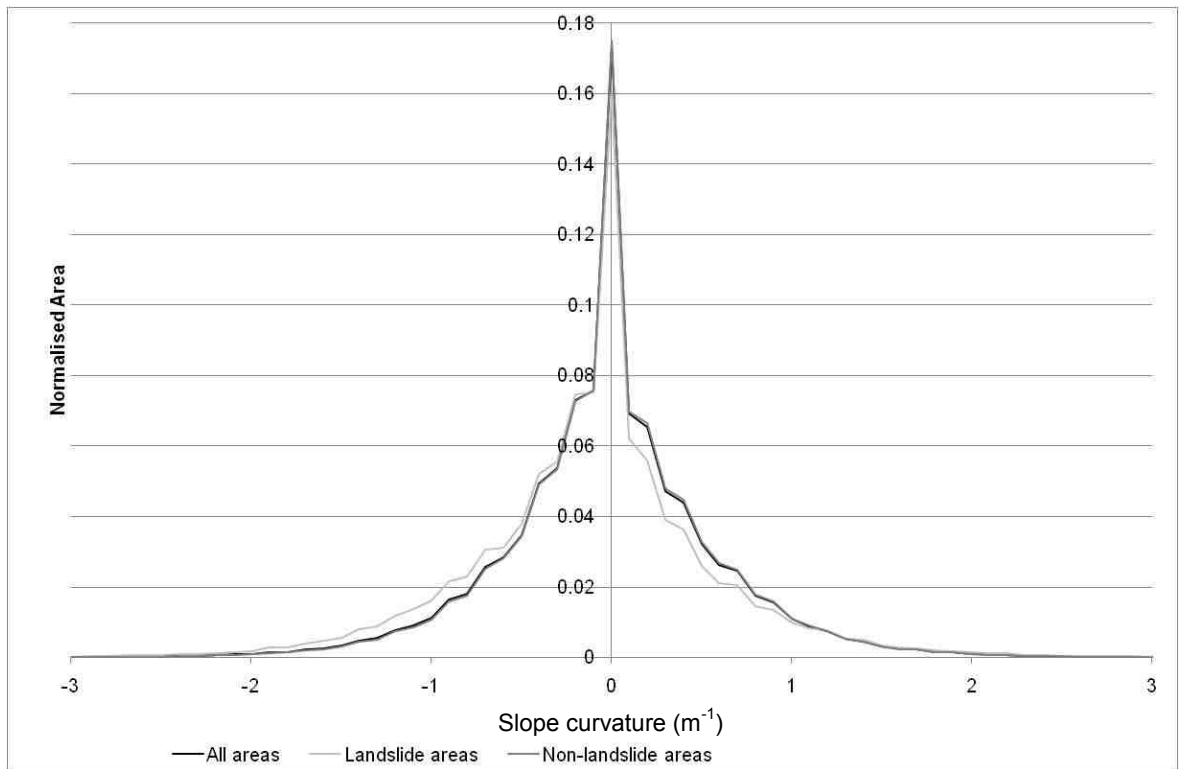


Figure 6.29: Normalised distribution of all areas and landslide areas, sampled by $0.1m^{-1}$ total curvature bins. Graph is limited to curvature values from 1.5 to -1.5 .

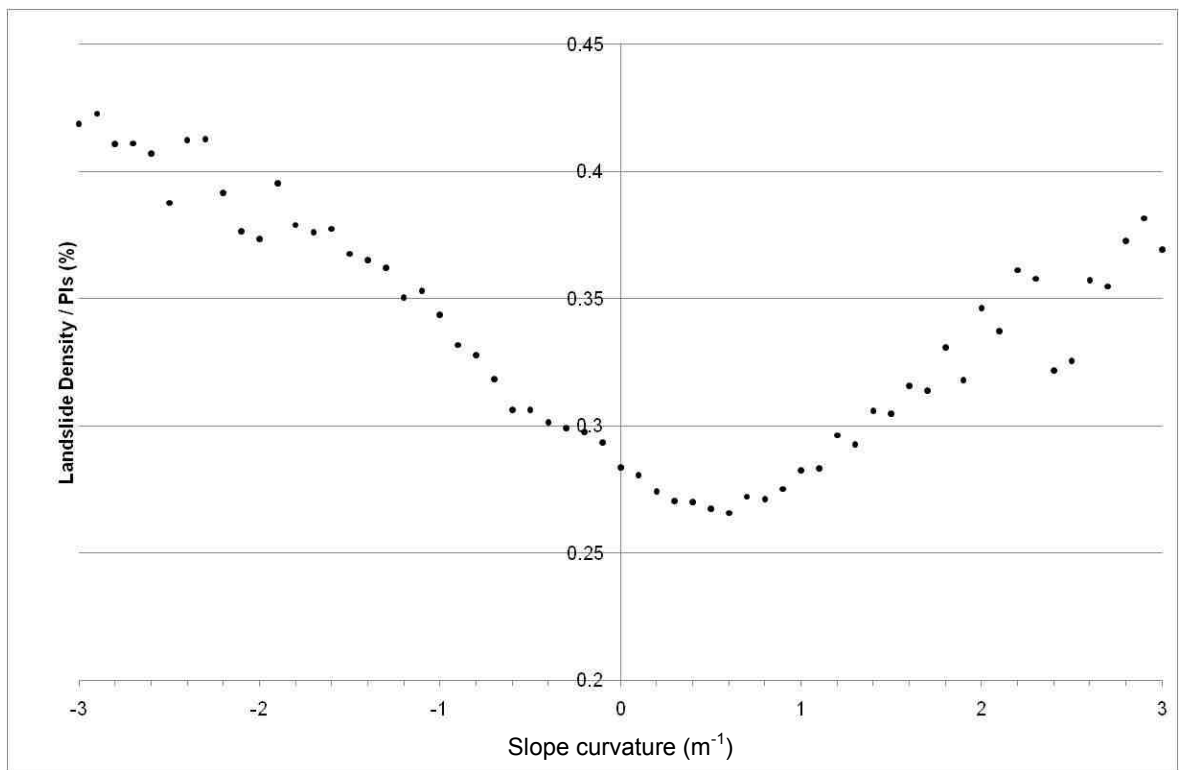


Figure 6.30: Total curvature Landslide density distribution sampled by $0.1m^{-1}$ total curvature bins. Graph is limited to curvature values from 1.5 to -1.5 .

6.5.2.6 Aspect

In order to examine the aspect distribution of P_{Is} , topographic aspects was divided into 10° bins, from 0 to 350° N. In order to reflect the directional nature of the datatype, both frequency and probability distributions are plotted using polar coordinates. The normalised area distribution (*Figure 6.31*) shows an oversampling of landslide areas between 60° and 200° (clockwise), and an undersampling of landslide areas between 210° and 40° (clockwise). This results in a pattern of higher landslide densities on slopes facing southeast, falling to lower landslide densities on slopes facing northwest (*Figure 6.32*).

As shown in *Figure 6.4*, landsliding took place in the hanging wall of the Beichuan and Pengguan faults, almost exclusively. Therefore, this suggests oversampling and higher landslide densities on slopes facing towards the co-seismic fault rupture.

6.5.2.7 Upslope contributing area

The upslope contributing area (UCA in m^2) of a given point in the landscape provides an index for the runoff volume passing through that location. As upslope contributing area values are distributed over several orders of magnitude, bins were selected at regular intervals of $0.1 \log_{10}UCA$.

The normalised area distribution (*Figure 6.33*) shows an inverse relationship between UCA and the sample size. Landslides undersample on slopes with $\log_{10}UCA < 4.4$, but oversample for those with values between 4.5 and 5.9. Beyond this point the sample size becomes very small (beyond the 99th percentile). In terms of the landslide density distribution (*Figure 6.34*), P_{Is} increases between values of 3.9 and 4.8, but the decreases beyond this point, with increasing variability. Peak landslide densities are seen at very high levels of UCA, however the sample size is very small for these areas.

This data shows that the majority of landsliding occurs on slopes with low UCA, however the probability of landsliding increases within the first order of magnitude increase in UCA. Thereafter the probability of landsliding and the overall occurrence of landslides decrease. However, minority areas with very high UCA appear to experience much high rates of landslide occurrence.

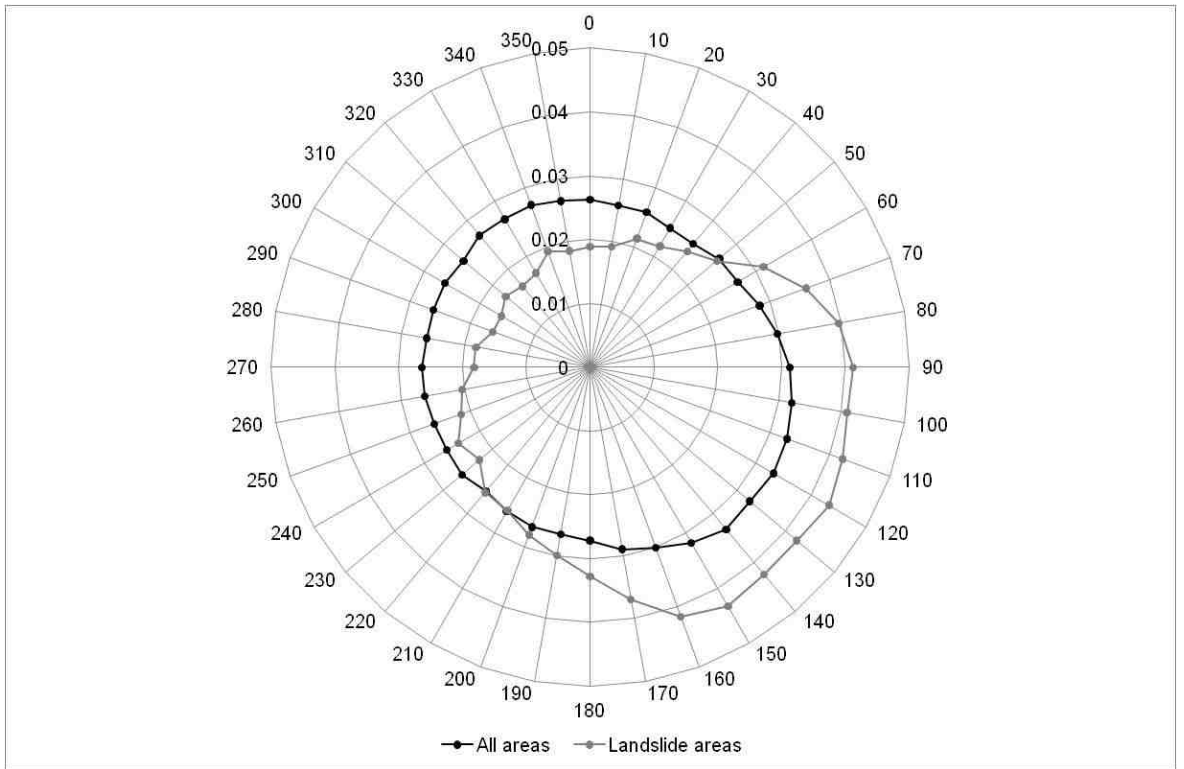


Figure 6.31: Normalised distribution of all areas and landslide areas, sampled by 10° aspect bins.

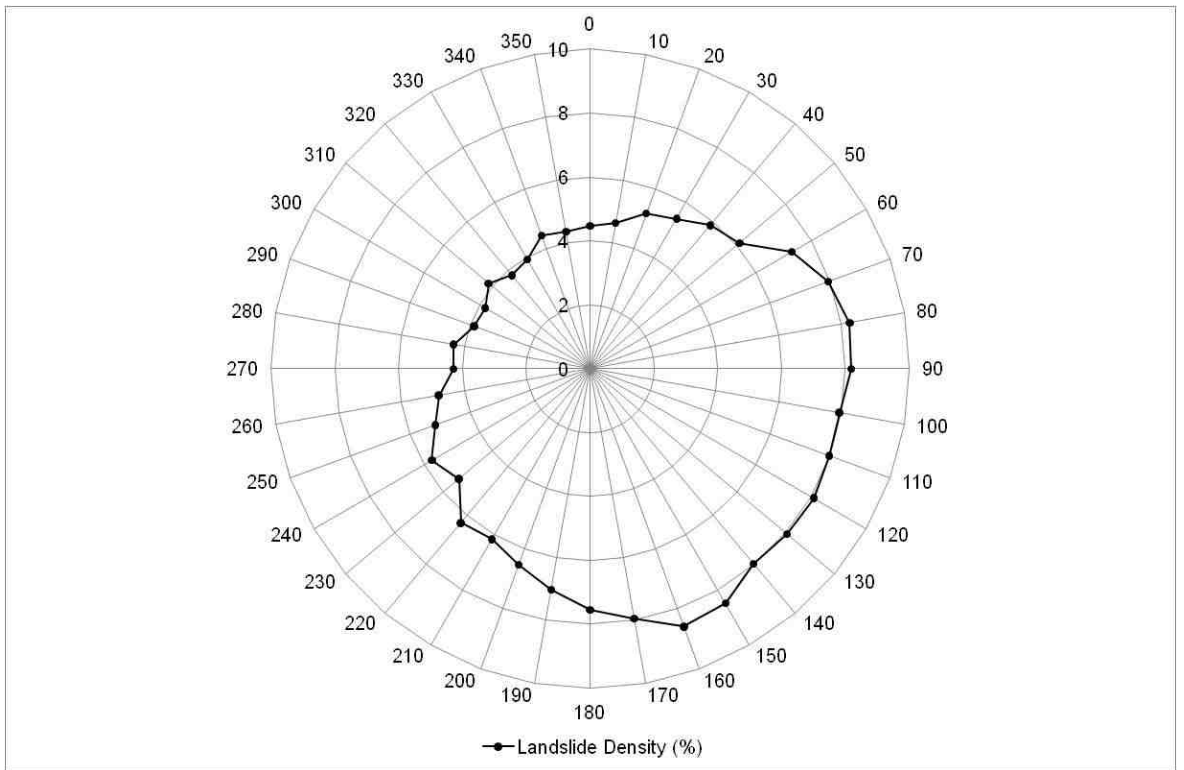


Figure 6.32: Landslide density distribution sampled by 10° aspect bins.

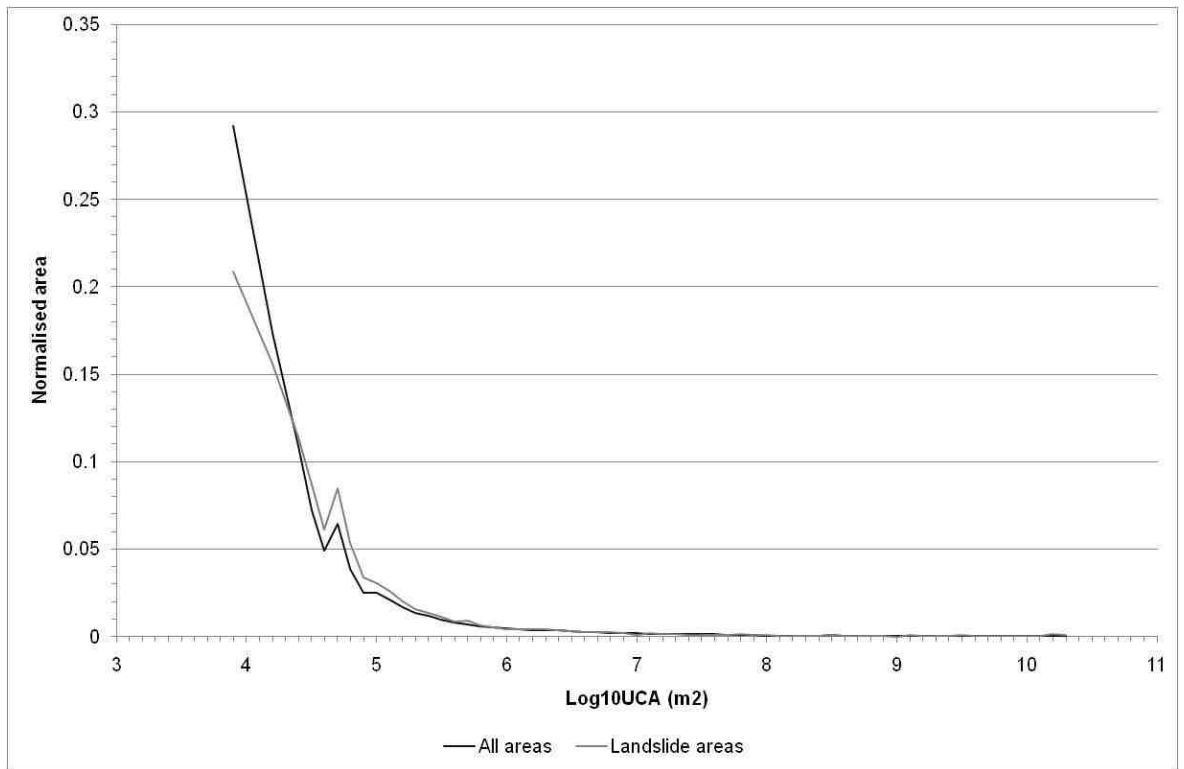


Figure 6.33: Normalised distribution of all areas and landslide areas, sampled by 0.1 Log10m² bins.

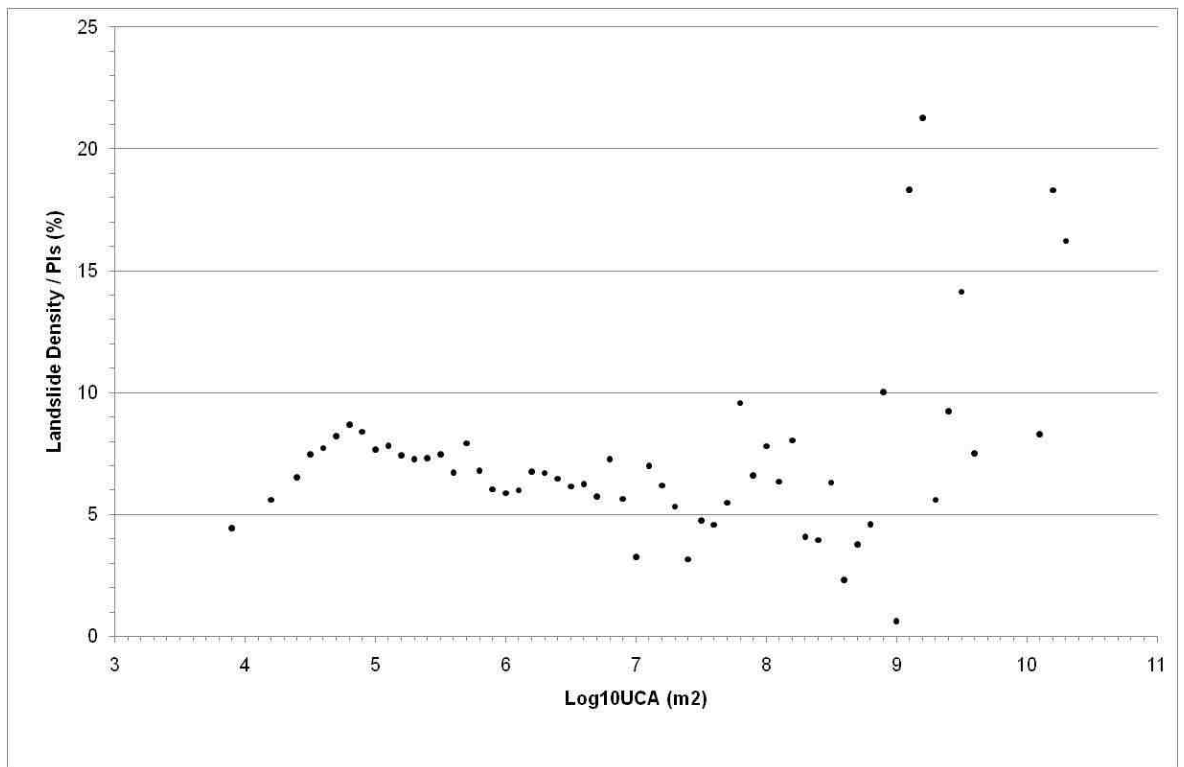


Figure 6.34: Landslide density distribution sampled by 0.1 Log10m² bins.

6.5.2.8 Distance from major river channels

Figure 6.35, shows the macro-scale pattern of landslide occurrence in relation to major river channels extracted from the DEM. For this, a UCA threshold of 44km^2 was used to define the channels as this was found to reflect the major rivers in the mountain range, along which high density areas of landsliding appear to occur (*Figure 6.35*). While the UCA is used to describe landslide occurrence in relation to local runoff patterns throughout the landscape, the macro-scale pattern of landsliding may be described in relation to larger scale features of the hydrological system. To achieve this, P_{Is} was sampled within 0.1km bins of Euclidean distance from these major river channels.

The normalised area distribution (*Figure 6.36*), shows an oversampling of landslide areas within 1km of the river channels. Thereafter landslide areas undersample, until a slight oversampling between 7km and 8km. In the landslide density distribution (*Figure 6.37*), this results in the highest landslide densities close to the river channels at 0.1km, followed by a decay with distance to $\sim 2\text{km}$. While P_{Is} peaks at 0.1km, at 0km P_{Is} drops by almost 2%; this is likely due to the removal of landslide masses in river channels from the mapping, through the use of a slope gradient filter. Between 2km and 5km P_{Is} increases slightly, before decreasing again at $\sim 6\text{km}$. Between 6km and 8km a second peak in P_{Is} occurs. This appears to be related to the very large landslides in the distribution, which occur in higher catchments away from these major channels.

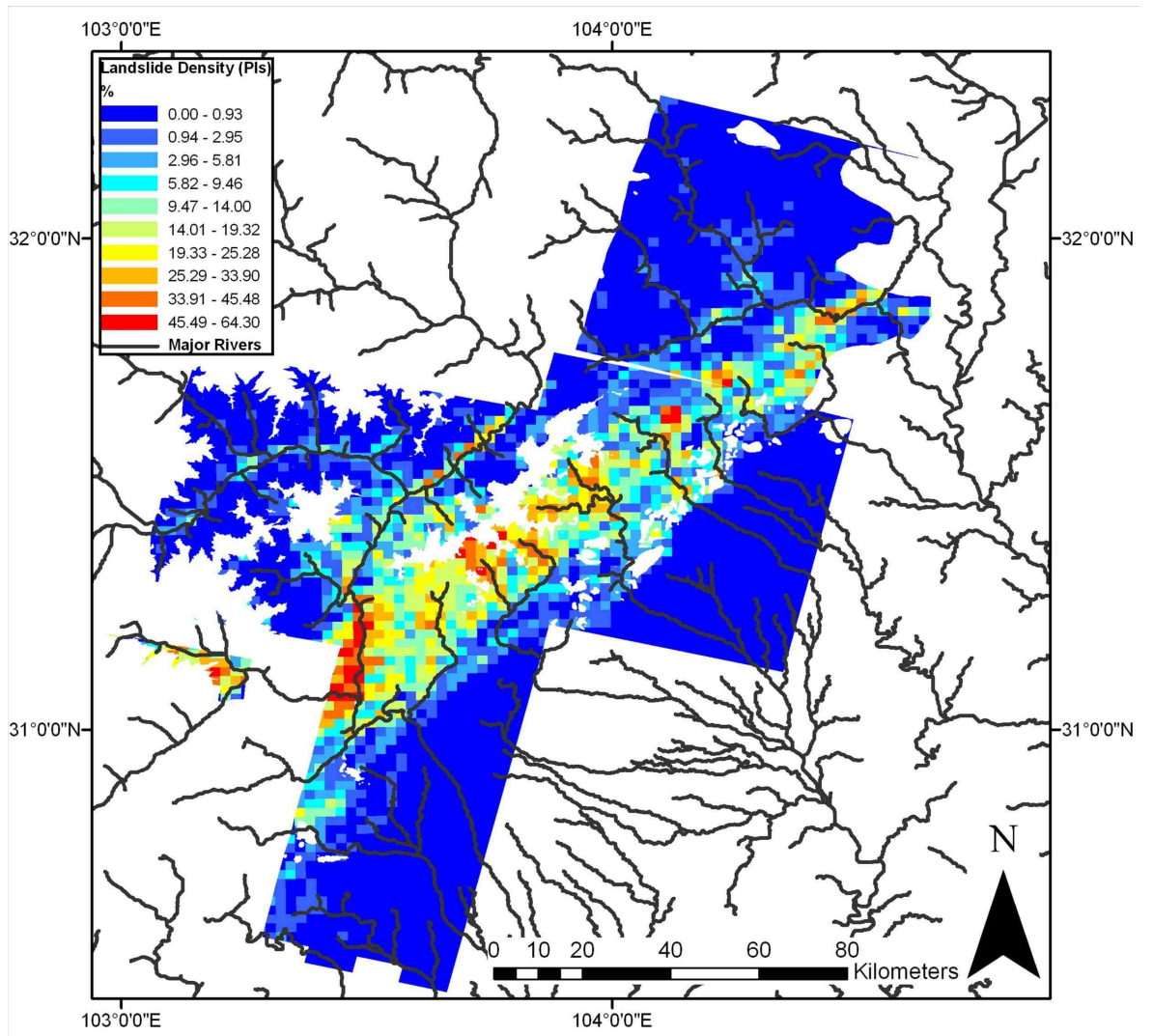


Figure 6.35: 2km landslide density matrix grid, overlain with major river channels (UCA > 44km²)

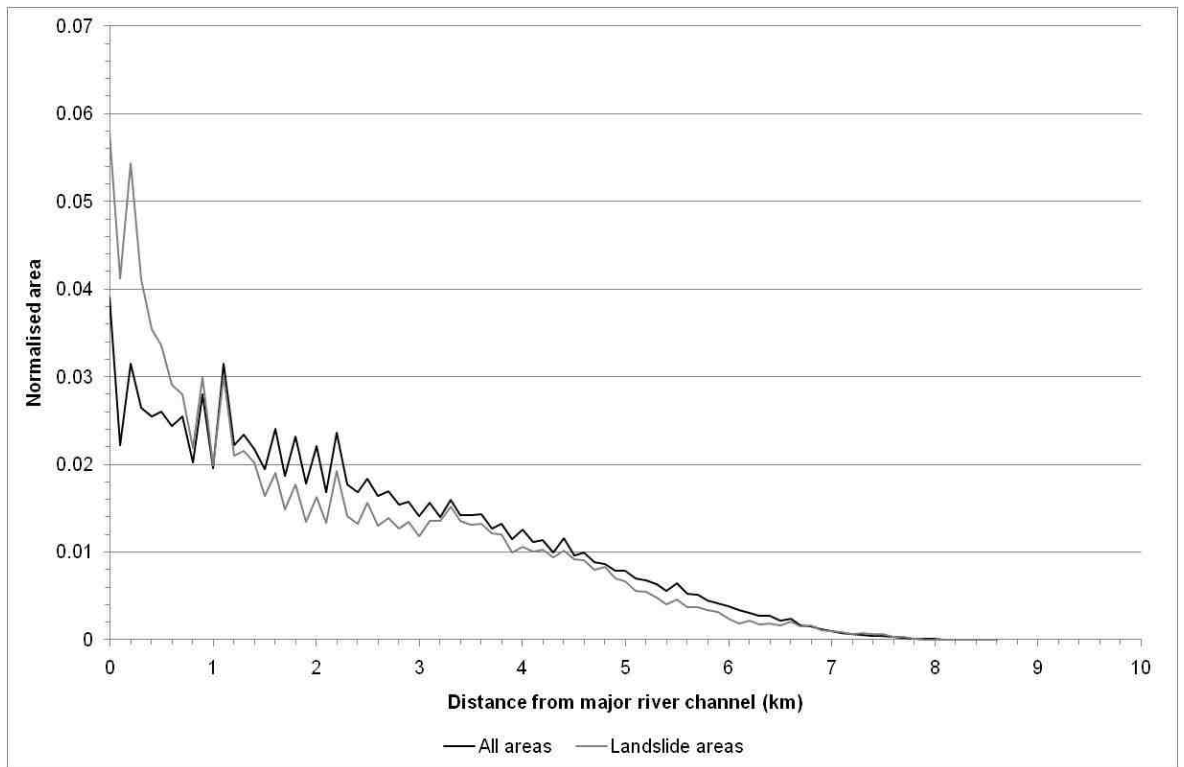


Figure 6.36: Normalised distribution of all areas and landslide areas, sampled by 100m bins of Euclidean distance from major river channels ($UCA > 44 \text{ km}^2$)

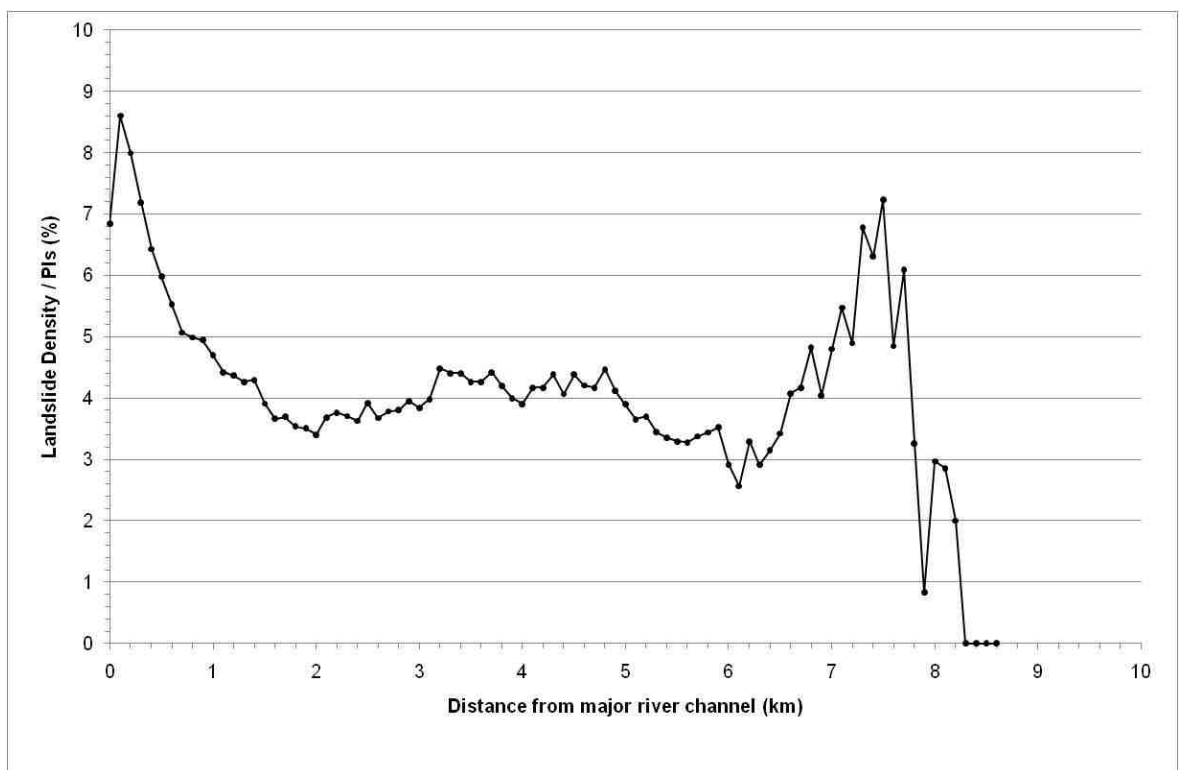


Figure 6.37: Landslide density distribution sampled by 100m bins of Euclidean distance from major river channels ($UCA > 44 \text{ km}^2$)

6.6 Chapter summary

Associations of landslide density and seismic, topographic and geological attributes have been considered individually using bivariate techniques. An exponential decay in landslide density is observed with across-strike distance from co-seismic surface ruptures. However, the pattern of this decay varies with along-strike distance, with landslides confined to areas closer to the fault in the northeast, and distributed further from the fault in the southwest. This is superimposed over a marked hanging-wall effect, which is most pronounced in the southwest where landslides occur almost exclusively in the hanging wall and landslide density remains high for greater distances from the co-seismic fault rupture. Regions of peak landslide occurrence in the along-strike direction also appear to coincide with peak areas of co-seismic slip on the Beichuan and Pengguan faults.

Older geological units in hanging wall areas exhibit a strong oversampling of landslides, most notably Mesoproterozoic granitic and Palaeozoic greywacke and shale, where the majority of the landslide impact is focussed. In addition, Triassic mudstone, sandstone and conglomerate, as well as Triassic (SGF fold belt) turbidites and acidic volcanics, both exhibit significant landslide densities. Landslide density demonstrates strong positive correlation with topographic attributes of hillslope gradient and relative relief. Landslide densities are near constant across the range of local elevations. Higher landslide densities are found in areas close to major river channels and on hillslopes with southeast aspects. Hillslopes with concave plan and total curvatures, and convex profile curvatures also exhibit higher landslide densities. Finally, there appears to be overall positive correlation between landslide density and upslope contributing area, however the precise nature of the relationship is unclear.

The data demonstrate the complex nature of seismological, geological, topographic and hydrological variables controlling the spatial distribution of earthquake-triggered landslides. Following on from this the importance of different spatial scales over which the influence of different variables acts is apparent. To better understand the processes which govern seismic landslide occurrence, the

following chapter explores the relative influence and interrelationship of the geophysical variables examined in this section.

Chapter 7

Statistical modelling of landslide occurrence

Chapter 6 presented bivariate relationships between landslide occurrence and the available thematic datasets reflecting different components of seismicity, topography, geology and hydrology. In order to further understand the relative influence of these predictor variables, the following section applies a generalised linear modelling approach to build logistic regression models for landslide probability, based on the available parameters. This is achieved by first modelling landslide probability using all predictor variables, before sequentially removing the least significant predictors, in order to identify fundamental controls on landslide occurrence. As a final exercise the logistic model for landslide probability is applied across the entire rupture zone of the Wenchuan earthquake, in order to produce a probabilistic landslide distribution incorporating areas not covered by the sample data from the available imagery.

7.1 Data format

In order to carry out this analysis, GIS data layers for both dependent and predictor variables were converted to raster format and resampled to the SRTM DEM resolution (90m) using a nearest neighbour method. Data values from all rasters were then sampled to a point at each pixel centroid location, to produce a data table of 1,042,754 observations covering the fields shown in *Table 7.1*. Within the database, the landslide variable was preserved as a binary field, while categorical predictor variables „*geology*’ and „*hanging wall or footwall of Beichuan fault*’ were given integer values in order of ascending landslide density. Slope aspect (A_s) has been related to characteristics of seismic wave evolution dependent on slope direction relative to the fault rupture (Meunier *et al.* 2008). In order to reflect this, new aspect values were generated as a function of the actual aspect rotated clockwise 135° (A_r), centring the mid value of aspect (180°) at the $N45^\circ$ trending direction of the fault rupture. Where:

$$A_s = 45^\circ, A_r = 180^\circ$$

$$A_s = 135^\circ, A_r = 0^\circ$$

The normalised sine and cosine of A_r were then calculated to reflect fault parallel and fault perpendicular aspect influences, so that:

$$\text{Sin}(A_r) = 1 = \text{fault perpendicular to the northwest}$$

$$\text{Sin}(A_r) = -1 = \text{fault perpendicular to the southeast}$$

$$\text{Cos}(A_r) = 1 = \text{fault parallel to the northeast}$$

$$\text{Cos}(A_r) = -1 = \text{fault parallel to the southwest}$$

7.2 Bivariate relationships

Chapter 6 explored the nature of bivariate relationships between the occurrence of landslides and the independent variables. These relationships are summarised, in terms of r-value, in the covariance matrix for the dataset (*Table 7.2*) and plotted for relationships with landslide occurrence in *Figure 7.1*.

Dependent variable	ID Code	Units or values
Landslide binary	<i>LS</i>	0 = non-landslide 1 = landslide
Predictor variables		
Distance from co-seismic fault ruptures	<i>FD</i>	Metres
Co-seismic slip distribution	<i>DS</i>	10^{-3} Metres
Hanging wall or footwall of Beichuan fault	<i>HF</i>	0 = footwall 1 = hanging wall
Geology	<i>G</i>	Ranked integer values from 1 to 9, in order of ascending landslide density
Slope gradient	<i>SL</i>	Degrees
Elevation	<i>DEM</i>	Metres
Local elevation	<i>LCEL</i>	Metres
Relative relief	<i>R</i>	Metres
Total curvature	<i>CT</i>	m^{-1}
Plan curvature	<i>CPL</i>	m^{-1}
Profile curvature	<i>CPR</i>	m^{-1}
Aspect	A_s	Degrees from North
	A_r	Degrees rotated 135° from North
	$\sin(A_r)$	1 = fault perpendicular to the northwest -1 = fault perpendicular to the southeast
	$\cos(A_r)$	1 = fault parallel to the northeast -1 = fault parallel to the southwest
Distance from major river channels	<i>RD</i>	Metres
Upslope contributing area	<i>UCA</i>	$\log_{10}(m^2)$

Table 7.1: Data fields used in modelling

Variables	LS	FD	DS	HF	G	SL	DEM	LCEL
LS	1							
FD	-0.2173	1						
DS	-0.0487	0.062	1					
HF	0.0311	0.4492	0.2111	1				
G	0.2724	-0.5294	0.0146	0.0841	1			
SL	0.1809	0.1997	0.0184	0.3296	0.0806	1		
DEM	-0.0264	0.4789	-0.056	0.5358	-0.0069	0.3566	1	
LCEL	-0.0185	0.1908	-0.0264	0.3716	0.1371	0.3148	0.8152	1
R	0.1732	0.3016	-0.0036	0.491	0.1437	0.5835	0.6143	0.5444
CT	-0.044	-0.0109	0.0032	-0.0059	0.0044	0.037	0.0642	0.1506
CPL	-0.0254	-0.0095	0.0027	-0.0098	0.0022	0.0362	0.02	0.0661
CPR	0.0506	0.0094	-0.0029	0.0007	-0.0054	-0.0283	-0.0901	-0.1931
RD	-0.0717	-0.0704	-0.0679	0.0035	0.0456	-0.0307	0.313	0.4161
UCA	0.0427	0.0307	-0.0046	0.0303	0.0015	-0.2211	-0.0839	-0.2212
sin(A _r)	-0.084	0.0313	0.0116	0.0531	-0.0066	-0.0162	0.0449	0.0335
cos(A _r)	0.0036	0.0118	0.0138	-0.0025	0.0025	0.006	-0.0009	0.0007
	R	CT	CPL	CPR	RD	UCA	sin(A _r)	cos(A _r)
R	1							
CT	0.0037	1						
CPL	-0.0149	0.8631	1					
CPR	-0.0206	-0.8751	-0.5109	1				
RD	-0.0128	0.0062	-0.0298	-0.0391	1			
UCA	-0.0054	-0.512	-0.5122	0.3807	-0.0835	1		
sin(A _r)	-0.0108	0.0035	0.0001	-0.0059	-0.0372	-0.0058	1	
cos(A _r)	0.0008	0.0004	0.0007	0	-0.0136	0.0017	0.0142	1

Table 7.2: Covariance matrix showing r-values for all variables

These results generally concur with the conceptual relationships demonstrated in Chapter 6. However, the covariance value for LS (landslide occurrence) and DS (co-seismic slip distribution) suggests a negative relationship. While a positive relationship was suggested in Section 6.4.2, this is not demonstrated by direct spatial correlation; likely due to the high level of local scale variation in ground motions between contiguous fault segment zones. A negative relationship does not fit conceptually with the association of seismic moment, PGA and landslide occurrence. As such DS was not used in logistic regression and modelling.

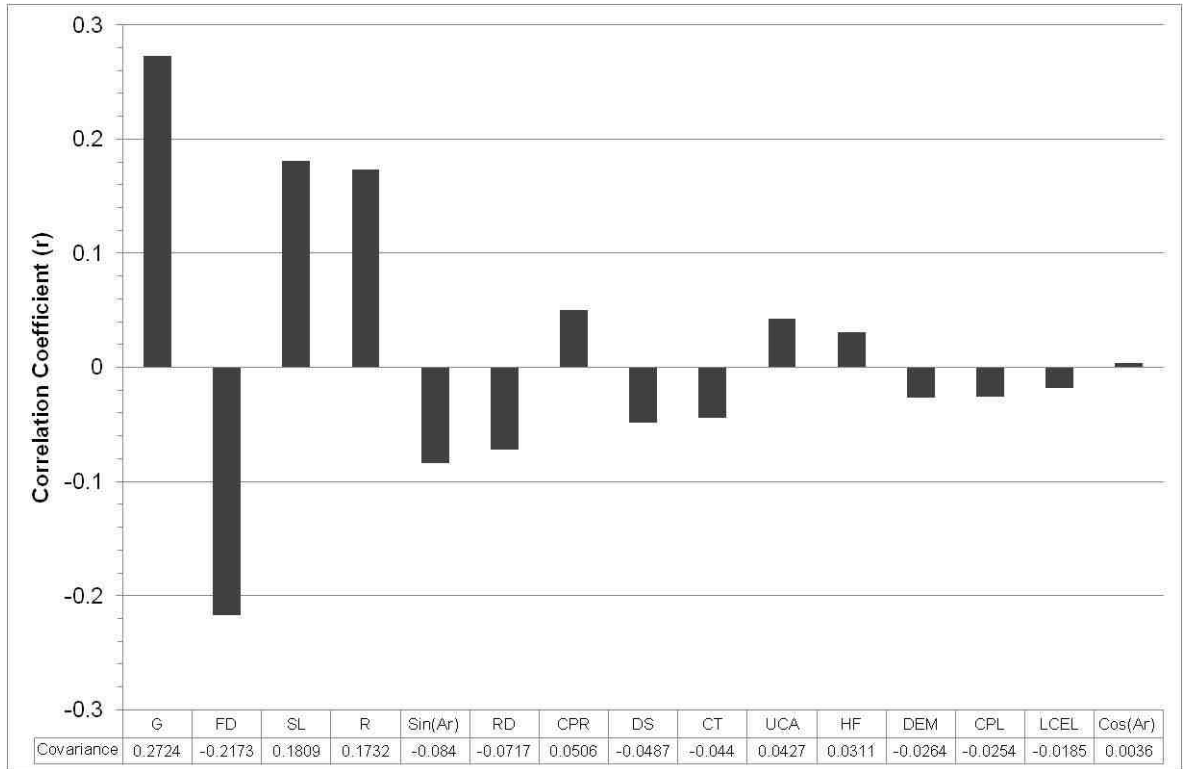


Figure 7.1: Ordered covariance values for landslide binary and predictor variables

7.3 Introduction to generalised linear modelling of landslide probability: logistic regression

Linear regression is the most commonly used model in both social and physical sciences to explore relationships between continuous dependent and controlling variables. However, in order to handle a binary, categorical dependent variable (such as “landslide” and “non-landslide”) a special type of regression model is required. For this logistic regression is used, which carries assumptions reflecting the non-linear (S-curve) nature of relationships between binary dependent and independent variables (Long 1997; Agresti 2007). As with linear regression, logistic regression can be used with a single or several predictor variables. The primary objective of logistic regression is to model the probability that a given situation is true, i.e. that the dependent variable is 1, based on the following equation:

$$\text{Log}(P_r \div 1-P_r) = b_0 + b_1x_1 + b_2x_2 + b_3x_3 \dots b_nx_n$$

Or

$$P_r = 1 \div (1 + e^{-(b_0 + b_1x_1 + b_2x_2 + b_3x_3 \dots b_nx_n)})$$

Equation 7.1

Where P_r is the probability of the binary qualifier being 1, x_n are the predictor variables, b_n are the coefficients of the predictor variables, and e is the exponential function.

As such, logistic regression is a commonly applied method used to model relationships between landslide occurrence and geophysical variables (e.g. Ayalew & Yamagishi 2005; Dai & Lee 2003; Gorsevski *et al.* 2006; Garcia-Rodriguez *et al.* 2008; Kincal *et al.* 2009). The majority of these studies have focused on the use of the output probability values for mapping of landslide susceptibility in future events, based on the assumption that the past occurrence of landslides in a specific site is indicative of the potential for future landslides to occur in sites with similar characteristics. However, the application in this investigation focuses on hind-casting landslide occurrence, to understand the extent to which the spatial distribution of landslides is explained by the available predictor variables.

In order to gauge the strength of correlation and degree of explained variability produced by regression models, R^2 values generated in ordinary least squares (OLS) regression are conventionally used. In order to incorporate the non-linear nature of logistic relationships, several pseudo or alternative R^2 measurements have been proposed as an equivalent statistic to evaluate the goodness-of-fit of logistic models (see Long 1997). However these vary in both methodology and derived values, and cannot be interpreted as one would interpret OLS R^2 values. Despite the binary nature of the observed landslide data, the use of conventional R^2 values does provide a meaningful measure of goodness-of-fit (Cox 2009 pers comm); a perfect model will generate an R^2 of 1, whilst a poor model will produce results closer to 0. Thus, conventional OLS R^2 is provided for reference throughout the modelling process, while pseudo R^2 values are also quoted to allow comparison to previous investigations. These are calculated automatically by the data analysis suite Stata using McFadden's R^2 (http://www.ats.ucla.edu/stat/mult_pkg/faq/general/Psuedo_RSquareds.htm, Appendix 1), and follow the general principle that pseudo R^2 values > 0.2 are evidence of a relatively good fit (Clark & Hosking 1986).

7.4 Landslide probability modelling

Initially, logistic modelling was carried out using all predictor variables bar DS. The model coefficients and correlation statistics are shown in *Table 7.3*. Model output fields given are: Number of observations; „LR χ^2 (x)‘ (Likelihood ratio chi-square with x degrees of freedom); „Prob> χ^2 (p)‘ (p-value associated with the chi-square, with a p-value less than 0.001 indicating the model as a whole is statistically significant); Pseudo R^2 (McFadden's R^2 ; Appendix 1); R^2 (OLS R^2); Predictor (predictor variables); Coefficient (values for logistic regression); Standard error; z (z-statistic, calculated by dividing the coefficient by the standard error); p (two tailed p-value for the z-test); 95% confidence interval.

Number of observations		1042754				
LR chi²(14)		178875.33				
Prob > chi² (p)		0.0000				
Pseudo R²		0.2640				
R²		0.215				
Predictor	Coefficient	Standard error	z	p	95% confidence interval	
<i>FD</i>	-0.0000749	0.00	-170.79	0	-0.0000757	-0.000074
<i>HF</i>	0.2785568	0.01	24.34	0	0.2561306	0.300983
<i>G</i>	0.2663283	0.00	83.55	0	0.2600804	0.272576
<i>SL</i>	0.0549285	0.00	119.37	0	0.0540266	0.055830
<i>DEM</i>	0.0004006	0.00	34.06	0	0.0003776	0.000423
<i>LCEL</i>	-0.0020913	0.00	-100.97	0	-0.0021319	-
<i>R</i>	0.0026965	0.00	113.77	0	0.0026501	0.002743
<i>CT</i>	-5.808673	4.66	-1.25	0.213	-14.94515	3.327808
<i>CPL</i>	5.894954	4.66	1.26	0.206	-3.241575	15.03148
<i>CPR</i>	-5.632926	4.66	-1.21	0.227	-14.76939	3.503534
<i>RD</i>	-0.0000314	0.00	-11.91	0	-0.0000366	-
<i>UCA</i>	0.2238308	0.01	39.02	0	0.2125883	0.235073
<i>Sin(A_r)</i>	-0.3227096	0.01	-60.65	0	-0.3331382	-
<i>Cos(A_r)</i>	0.0030124	0.01	0.56	0.577	-0.0075709	0.013595
<i>_cons</i>	-7.240535	0.04	-196.34	0	-7.312814	-7.168255

Table 7.3: Logistic regression output for all variables model (1). Key for variable codes is given in Table 7.1.

A p value less than 0.001 indicates that the model is statistically significant. Based on the correlation coefficients, the following model for probability of landsliding (P_r) is produced:

$$P_r = 1 / (1 + e^{-([-7.240535] + [-0.0000749*FD] + [0.2785568*HF] + [0.2663283*G] + [0.0549285*SL] + [0.0004006*DEM] + [-0.0020913*LCEL] + [0.0026965*R] + [-5.808673*CT] + [5.894954*CPL] + [-5.632926*CPR] + [-0.0000314*RD] + [0.2238308*UCA] + [-0.3227096*Sin(A_r)] + [0.0030124 * Cos(A_r)]))})$$

Equation 7.2

R^2 and pseudo R^2 values indicate that between 22 and 26% of variation in the spatial occurrence of landslides is explained by the predictor variables, and conversely, between 78 and 74% of the variation is not explained by the datasets available. Despite the low pseudo R^2 value, this represents a relatively good fit, based on the analysis of Clark & Hosking (1986).

7.5 Comparison of landslide occurrence and modelled probabilities

In order to understand how actual landslide occurrence corresponds with modelled probabilities, P_r and LS may be compared both graphically and spatially. While a scatter plot of LS against P_r is difficult to interpret due to the binary nature of LS, the overall relationship can be visualised by applying a smoothing line (symmetric nearest neighbour smoothing), shown in *Figure 7.2*. Here the smoothing line can be understood as the ratio of landslide to non-landslide samples (landslide density) plotted against modelled landslide probability. In addition, the relationship between landslide and non-landslide samples across the probability scale may be further understood through both their non-cumulative (kernel density) and cumulative distributions (*Figures 7.3 and 7.4*).

Figure 7.2 shows a gradual increase in the proportion of landslide (LS = 1) samples with P_r . The relationship exhibits a slight S-curve, with a greater rate of increase in landslide occurrence between probability values of 0.1 and 0.4, and a tailing off either side of this range. However, this effect is slight and as such there is no defined probability threshold above which landsliding becomes abundant. The reason for this is clear from *Figure 7.3*. Here the non-cumulative kernel density distributions of landslide and non-landslide areas demonstrate significant overlap, with the modes of both landslide and non-landslide observations occurring at low landslide probability values of 0.104 and 0.002 respectively. While the proportion of samples affected by landsliding increases with probability, the available thematic data cannot discriminate LS at mid to low probability values, which are high in frequency. Although the probability of landsliding becomes greater than that of non-landsliding at $P_r = 0.5$, over 70% of landslide samples actually occur at $P_r < 0.4$, as shown in *Figure 7.4*. In other words, within the landscape there are large areas with medium to low probabilities of landsliding, and it is upon hillslopes within these probability bounds that the majority of landsliding occurs.

This issue is particularly apparent when comparing the spatial distribution of actual landslides and landslide probabilities. By projecting modelled probabilities (P_r) for each observation into the mapping coordinate system, the spatial distribution of probabilities can be visualised relative to mapped landslide areas (*Figure 7.5*).

Areas of higher probability generally concur with the distribution of mapped landslides. However, there are also significant regions with high landslide probabilities which did not actually result in failure and landsliding, and conversely regions with low landslide probabilities which did fail. Particularly notable are the locations of very large landslides at the north-eastern limit of the Pengguan massif, which exhibit relatively low probability values. Nevertheless, the modelled probabilities appear to provide a reasonable macro-scale estimate of the distribution of actual landslides, as the geophysical parameters used in modelling are representative of key processes and mechanisms causing landsliding in the majority of cases.

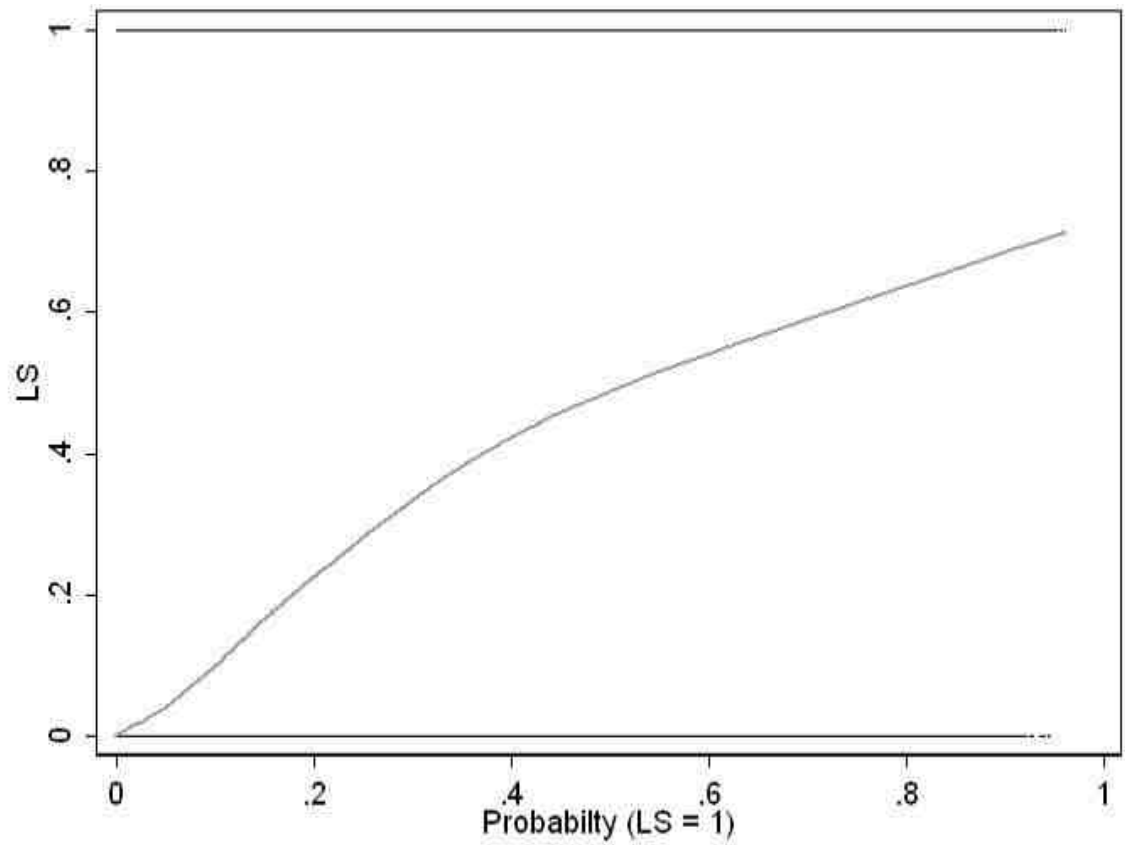


Figure 7.2: Black: Scatter plot of logistic regression predicted landslide probabilities (P_r) and actual landslide occurrence (LS). Grey: symmetric nearest neighbour smoothing line, indicating ratio of actual landsliding by predicted landslide probability.

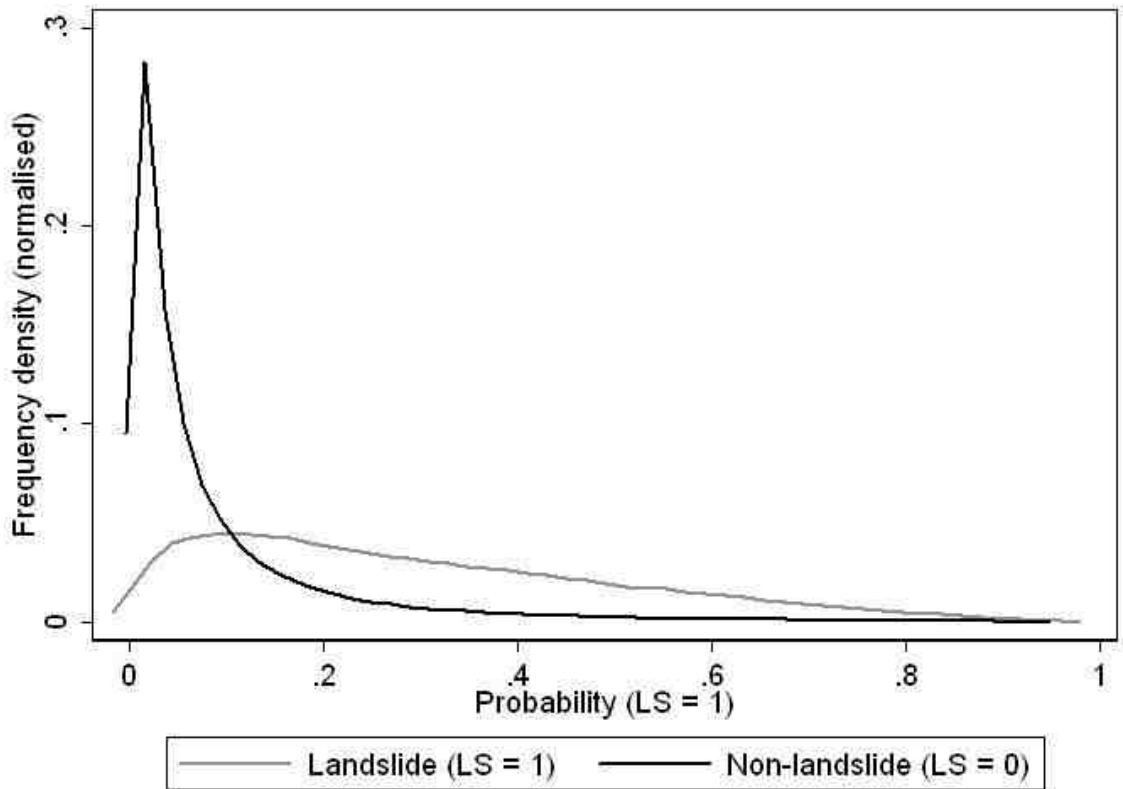


Figure 7.3: Non-cumulative (kernel density) distribution of landslide and non-landslide observations

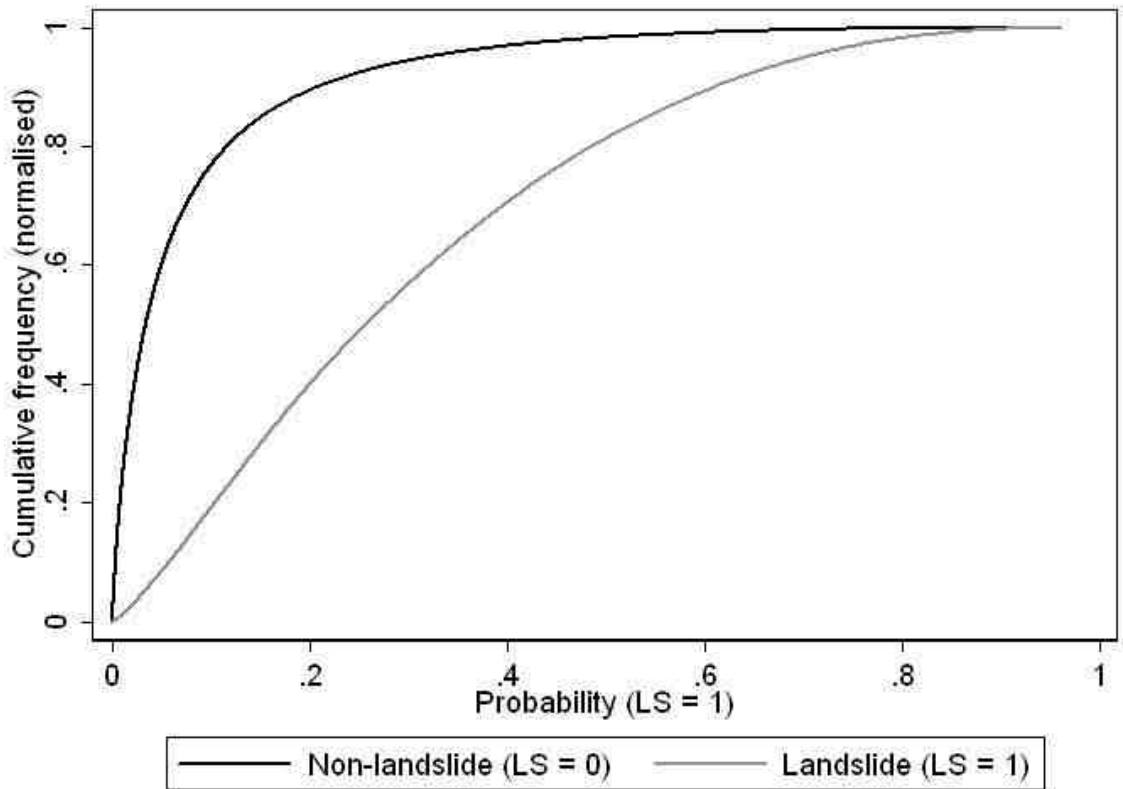


Figure 7.4: Cumulative distribution of landslide and non-landslide observations

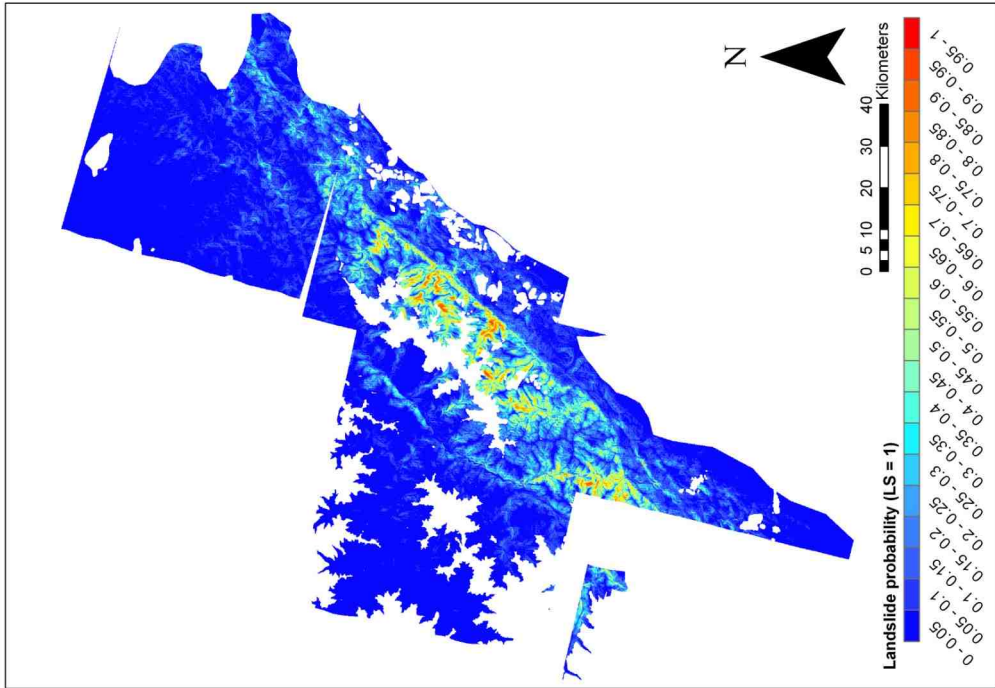
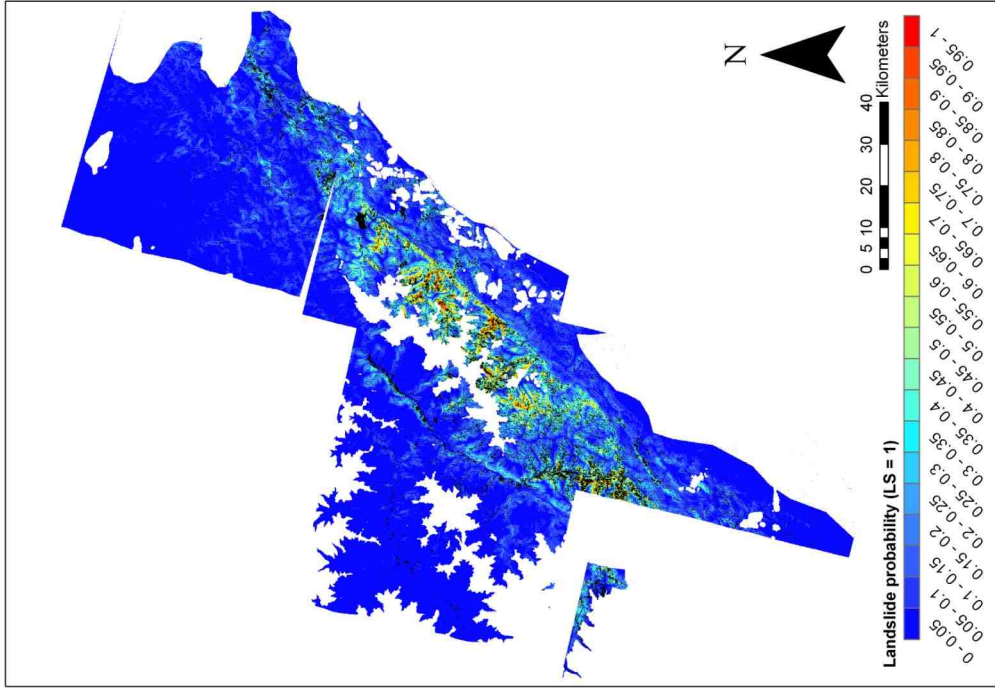


Figure 7.5: Left: Map projected probabilities (P_r) produced using all predictor variables. Right: Probabilities (P_r) overlain by mapped landslides.

7.6 Relative significance of predictor variables and logistic model simplification

While a model using all independent variables will necessarily produce the highest level of correlation and explained variability, not all variables contribute equally to the modelled probability. A model with such numerous variables is also unnecessarily cumbersome, restricted in computational efficiency and has limited application to transfer to other situations. In order to identify the key independent variables controlling the occurrence of landslides the model may be simplified incrementally by removing less significant predictor variables. This serves the purpose of both building an understanding of the relative weighting of different predictors, and identifying the key predictors while removing more redundant ones. Logistic regression output 'p' values and „z' values were used as the primary guide to relative significance of the predictor variables. First, the following variables exhibiting p-values greater than 0.05 (indicating non-statistically significant relationships) were removed:

- *CT*
- *CPL*
- *CPR*
- *Cos(A_r)*

This produced the logistic regression output for all variables exhibiting statistically significant coefficients, show in *Table 7.4*.

Number of observations		1042754.0000				
LR chi²(14)		178592.5800				
Prob > chi²		0.0000				
Pseudo R²		0.2636				
R²		0.2125				
Predictor	Coefficient	Standard error	z	p	95% confidence interval	
<i>FD</i>	-0.0000749	4.38E-07	-170.92	0	-0.0000758	-0.0000741
<i>HF</i>	0.2815552	0.0114335	24.63	0	0.259146	0.3039644
<i>G</i>	0.2672046	0.0031861	83.87	0	0.2609599	0.2734493
<i>SL</i>	0.0552555	0.0004585	120.53	0	0.0543569	0.056154
<i>DEM</i>	0.0004099	0.0000117	34.94	0	0.0003869	0.0004329
<i>LCEL</i>	-0.0021427	0.0000205	-104.52	0	-0.0021829	-0.0021025
<i>R</i>	0.0027028	0.0000237	114.05	0	0.0026563	0.0027492
<i>RD</i>	-0.0000293	2.63E-06	-11.16	0	-0.0000344	-0.0000242
<i>UCA</i>	0.2323459	0.0050685	45.84	0	0.2224117	0.24228
<i>Sin(A_r)</i>	-0.3221622	0.0053155	-60.61	0	-0.3325804	-0.3117441
<i>_cons</i>	-7.281414	0.0344752	-211.21	0	-7.348984	-7.213844

Table 7.4: Logistic regression output for model using statistically significant coefficients

From the result the following logistic regression equation is produced:

$$P_r = 1 \div (1 + e^{-([-7.281414] + [-0.0000749*FD] + [0.2815552*HF] + [0.2672046*G] + [0.0552555*SL] + [0.0004099*DEM] + [-0.0021427*LCEL] + [0.0027028*R] + [-0.0000293*RD] + [0.2323459*UCA] + [-0.3221622*Sin(A_r)])})$$

Equation 7.3

Predictors were then removed sequentially based on their z-value, which is produced by dividing the correlation coefficient by the standard error. The predictor with the lowest z-value (the combination of a low coefficient and high standard error) was removed with each repeated model run, such that predictors with higher coefficients and lower standard errors remained in the model, reducing input predictors to those with the most significant parameters. The sequence of input predictors and the resulting model pseudo R² values are shown in Figure 7.6, to illustrate the impact of input predictor alteration on model performance. Numbering of different model combinations from 1 to 11 is also shown here.

Pseudo R² values are not greatly affected by the removal of CT, CPL, CPR, Cos(A_r) RD and HF. With the removal of DEM the reduction in pseudo R² starts to become more pronounced, and drops off rapidly following model 7. By projecting modelled probabilities back into the map co-ordinate system, it is also clear that

significant changes in the spatial distribution of landslide probabilities also occur beyond this predictor combination (see *Appendix 2*). As such, predictors used in model 7 are core to controlling the spatial distribution of landslides:

- *FD*
- *R*
- *LCEL*
- *SL*
- *G*

Use of these predictors alone results in the five parameter logistic model:

$$P_r = 1 \div (1 + e(-([-6.340695] + [-0.0000645*FD] + [0.33166*G] + [0.0496199*SL] + [-0.0018463*LCEL] + [0.0032465*R])))$$

Equation 7.4

The modelled probabilities produce by models 1 (all parameters) and 7 (core parameters) demonstrate a high degree of correlation ($R^2 = 0.93$), as shown in *Figure 7.7*. The spatial distribution of landslide probabilities also demonstrates a high level of correspondence with mapped landslide areas, as shown in *Figure 7.8*.

In addition to identifying the core predictors, all independent variables exhibiting a significant relationship with landslide occurrence may be ranked based on their removal order in the modelling process, shown in *Table 7.5*.

Rank	Predictor variable
1	Distance from co-seismic fault ruptures
2	Relative relief
3	Local elevation
4	Slope gradient
5	Geology
6	Fault perpendicular component of aspect
7	Upslope contributing area
8	Elevation
9	Hanging wall or footwall
10	Distance from major river channels

Table 7.5: Relative ranking of predictor variables

To focus on the core predictors, this suggests that attenuation of peak ground accelerations exhibits the dominant control on landslide occurrence, with regions closer to the co-seismic fault rupture more prone to landsliding. The high significance of relative relief and slope gradient suggests that within regions experiencing ground motions, steeper and longer topographic slopes are more susceptible to landsliding. The significance of local elevation suggests that landslides preferentially occur on lower on slopes, which may signal preferential proximity to river channels. Following this, geology is also of high significance. This must be considered in terms of both the material properties and hence susceptibility to failure of different rock types, and topographic slope features formed within different geological units. This is illustrated by examining the correlation coefficients of the core variables to one another. As shown in *Table 7.6*, hillslope gradient, local elevation and relative relief all demonstrate positive correlation with ranked geology, showing that geological units more susceptible to landsliding sustain steeper hillslopes with greater relative relief. In addition, geology is also inversely correlated to distance from fault ruptures, showing that geological units with the highest levels of landslide occurrence occur where PGAs are higher. Despite these correlations, the significant decrease in pseudo R^2 with the removal of G from the model suggests that the geological variable is representative of factors not accounted for through topographic and co-seismic variables alone. In addition, there is significant cross-correlation between gradient, local elevation and relative relief. The fact that these all form core predictors of landslide occurrence despite this correlation highlights the importance of the different scales of process which these different features represent.

Variables	FD	G	SL	LCEL	R
FD	1				
G	-0.5294	1			
SL	0.1997	0.0806	1		
LCEL	0.1908	0.1371	0.3148	1	
R	0.3016	0.1437	0.5835	0.5444	1

Table 7.6: Subset of Table7.2, covariance matrix for FD, G, SL, LCEL and R.

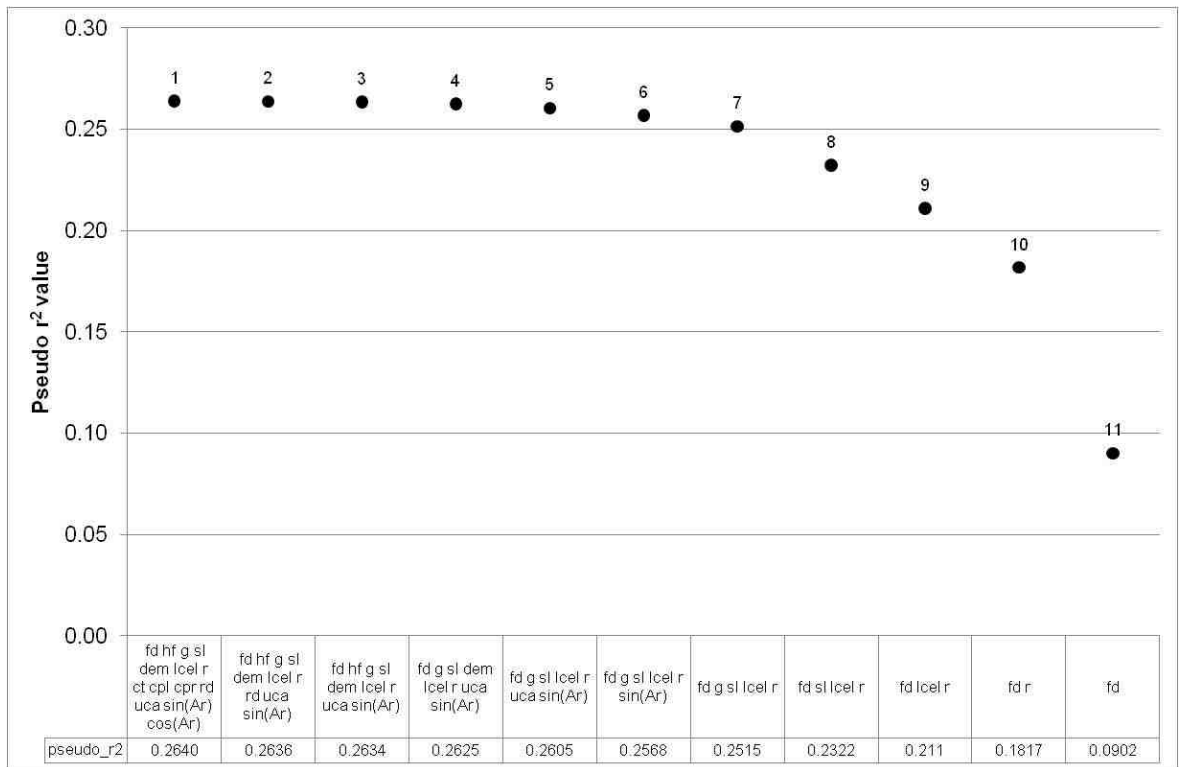


Figure 7.6: Sequence of model input predictors and resulting pseudo R^2 goodness-of-fit values.

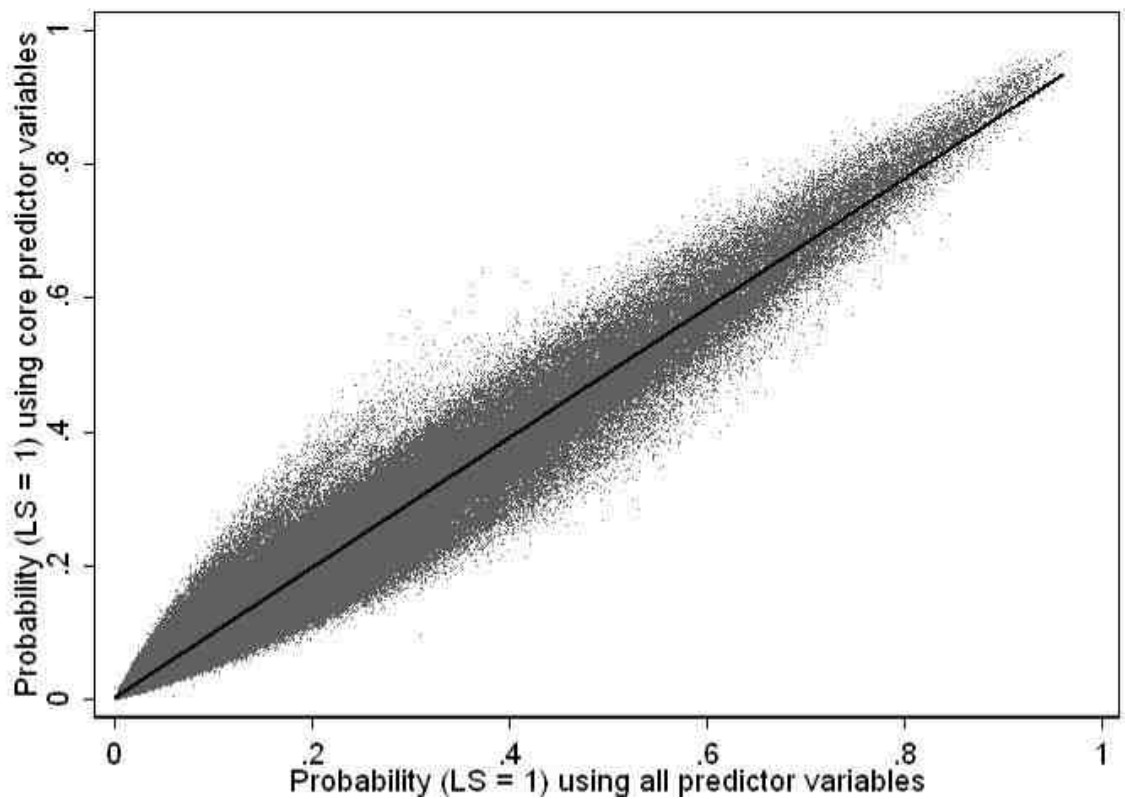


Figure 7.7: Scatter plot comparison of model probabilities produced using all predictors (1) and core predictors (4) logistic regression. $R^2 = 0.93$.

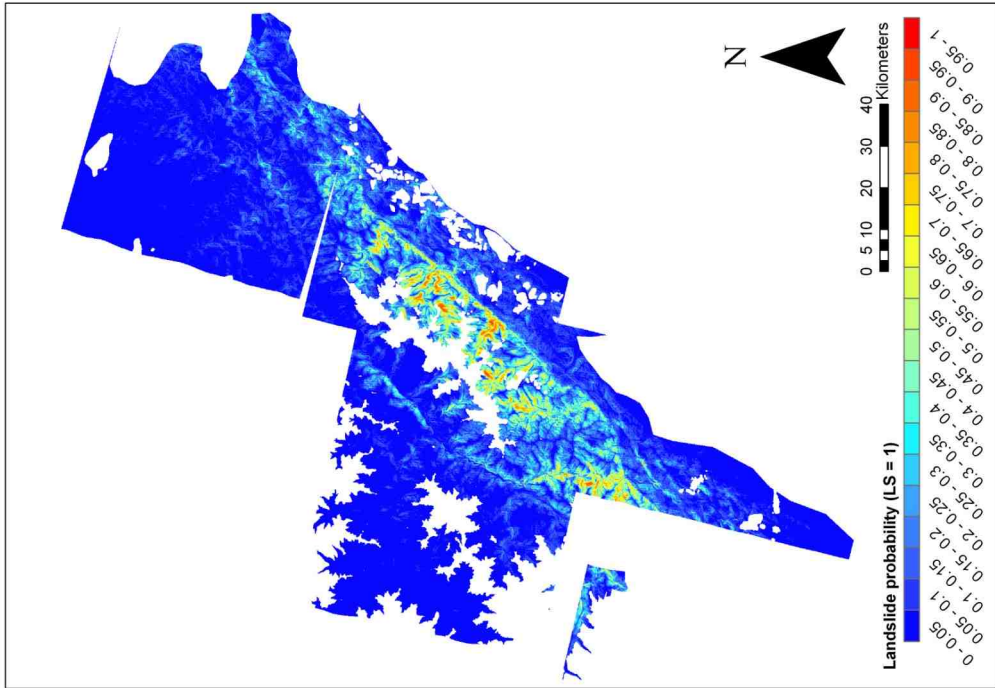
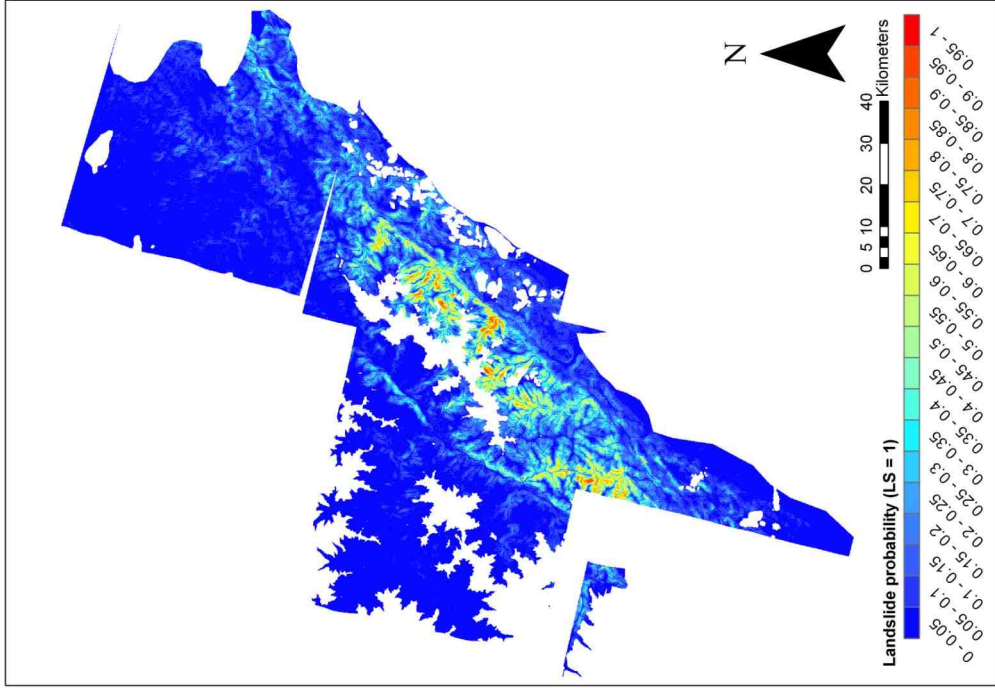
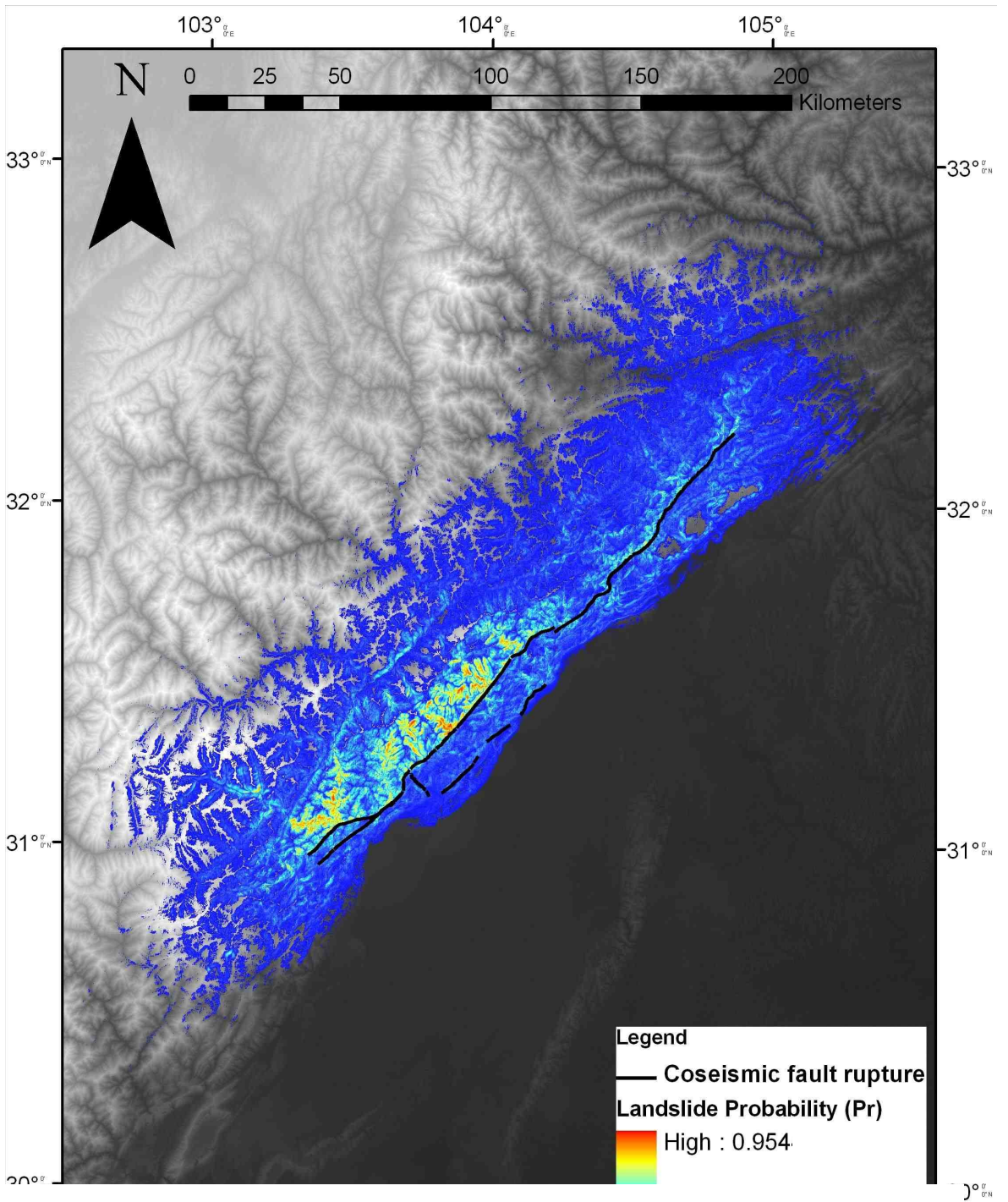


Figure 7.8. Left: Map projected probabilities (P_T) produced using all predictor variables. Right: Map projected probabilities (P_T) produced using core predictor variables.

7.7 Probabilistic landslide occurrence for the full rupture zone

While logistic modelling is useful in understanding controls on the distribution of landslides, the predictor coefficients can also be used to predict landslide occurrence in areas where no observational data on landslides exists or was available. Using coefficients from model 2 (all statistically significant relationships), the logistic regression model was applied to an area of 200,000km² (26,558,400 observations) including the full length of the rupture zone and adjacent areas. The output of this exercise is a complete map of probabilistic landslide occurrence for the Wenchuan earthquake, shown in *Figure 7.9*.

The map suggests that the majority of the main landslide impact zone of the earthquake was covered by sample area (A_T), and it is highly unlikely that regions of significant landsliding extend much further beyond this zone. It is also notable that the area of mapped landslides encompasses variability exhibited by the predictor variables across the remainder of the rupture zone, and hence it is likely that the model performs comparably well in these areas also. In general the predicted landslide impact is focused around the Pengguan massif - an area of steep slopes and granite geology between the Wenchuan and Beichuan faults. However, landslide probabilities > 0.1 continue along the full length of the fault rupture to the northeast, where landslide impact appears to be more evenly distributed on either side of the fault rupture. As the model is based on a uniform decay pattern with distance from the fault rupture in all directions, this effect can be associated with hillslope susceptibility to landsliding rather than variations in peak ground accelerations. In other words, larger areas susceptible to landsliding occur in footwall areas in the northeast of the rupture zone, than is the case to the southwest. In agreement with the actual distribution of landslides, areas of greatest landslide probability occur alongside major rivers, an effect which appears to be mainly linked to topographic characteristics of these areas, rather than a direct hydrological effect.



Legend

<VALUE>



Landslide Probability (Pr)

High : 0.954

Low : 0.001

to

83

7.8 Full rupture zone model evaluation and considerations

While the probabilistic landslide map appears to provide a good first order estimate of the distribution of landslide affected areas, there are several key limitations which must be taken into account when interpreting the result. While the model proposes to predict occurrence of landslides, the training sample included a combination of both landslide scars and deposits. Therefore, some regions with high predicted landslide probabilities may result from essentially stable areas upon which landslide material has been deposited. This may well be the primary cause of overestimation of landslide probabilities in the near-fault region. A more accurate map of landslide occurrence may be attainable by separating landslide source areas and modelling using these alone. However this option was not available, without significant manual reworking of the raw landslide data.

As described in *Section 5.3.9*, the mapping extent did not include areas >3500m. In addition, no variable reflective of topographic amplification of PGA (e.g. normalised distance from ridge crests) was used in the modelling process. The combined absence of training samples at high altitudes and predictor variables incorporating topographic effects is likely to have produced an underestimation of slope failures occurring along ridge crests, as would be expected for earthquake-triggered landslide distributions.

Within the A_T sample region, the dominant co-seismic effect is attenuation with distance from the fault rupture. Given the unilateral rupture propagation which took place during the earthquake (Nishimura and Yagi 2008; Shen *et al.* 2009), larger peak ground accelerations are expected to have occurred to the northeast in areas towards which the rupture propagates, but which fall outside the sample area. No predictor variable reflective of this effect has been included in the model, and it is likely that the modelled probabilities reveal an underestimate of the probable landslide impact in areas to the northeast.

7.9 Chapter summary

Generalised linear modelling of landslide occurrence through logistic regression has revealed the relative influence of different geophysical processes on the occurrence of landslides. To begin with, topographic curvature attributes were identified as being relatively redundant, exhibiting statistically insignificant

relationships to landslide occurrence. Using all predictor variables a maximum of 21 to 26% of variability in landslide occurrence is explained. When comparing landslide probabilities to actual landslide occurrence no distinctive threshold for landsliding is apparent, with a large number of landslide samples occurring in areas with $P_r < 0.4$. Of those variables showing significant relationships, a ranking of relative significance has been achieved, identifying distance from co-seismic fault ruptures, slope gradient, relative relief, local elevation and geology as the key geophysical variables controlling the spatial distribution of landslides. In addition, the fault-perpendicular component of aspect has also been identified as significant.

By applying the model across the entire rupture zone of the earthquake and its adjacent regions, a map of probabilistic landslide occurrence has been generated. This reveals a first order estimate of the complete landslide distribution produced by the Wenchuan earthquake. The result should be interpreted with due consideration to both the limitations of the input data quality, sample, and generalised linear modelling capabilities.

The following chapter provides a further analysis and discussion of these findings, in relation to the wider literature on earthquake-triggered landsliding, before exploring the broader application of the results and techniques used.

Chapter 8

Analysis and Discussion

Despite recent advances, many questions persist in understanding controls on the spatial distribution of earthquake-triggered landslides. The 2008 Wenchuan earthquake presents the opportunity to study these processes for a large continental thrust event with complex faulting mechanisms and diverse geophysical conditions. Through mapping a significant proportion of the landslides triggered by the event this study has generated a landslide inventory dataset for the main rupture and impact zone of the earthquake. This has been examined with respect to seismological, topographic and geological datasets, reflective of various parameters governing the occurrence of landslides. The following section reflects on the characteristics of the landslide distribution in the context of contemporary literature on earthquake-triggered landsliding. Following this, the wider implications and applications of both the dataset produced and techniques developed in this project are explored. As such the findings and implications of this study can be considered at three levels:

1. The processes and mechanisms governing the occurrence of earthquake-triggered landslides
2. Practical implications for landslide inventory investigations
3. Broader applications and contributions of research findings within the fields of hazard management, seismology and geomorphology

8.1 Processes and mechanisms governing the occurrence of earthquake-triggered landslides

The Wenchuan earthquake presents a multifaceted problem in understanding controls on the occurrence of earthquake-triggered landslides, due to the complexity of earthquake mechanisms and broad variation in topographic, geological and hydrological conditions across the rupture zone. As such, to understand the distribution of slope failures a combination of seismological, topographic and geological datasets must be considered, along with the different scales of process they represent and complex interactions between geophysical parameters. The last three decades have seen significant advancement in this understanding, identifying common characteristics of seismic landslide distributions. The research findings of the investigation are discussed in light of this work, framed within the two categories of landslide generating processes considered in this study:

- Seismological triggering parameters
- Topographic and geological landscape characteristics controlling slope stability

8.2 Seismological triggering parameters

During earthquakes landslides are triggered by seismic accelerations, which generate transient, short-lived stresses that overcome the cohesive and frictional strength of hillslope materials (Newmark 1965). As such, the spatial distribution of peak ground accelerations is the most commonly used index to relate ground motion to landslide occurrence (e.g. Khazai & Sitar 2004). The macro-scale distribution of peak ground accelerations can be understood in terms of the following components (e.g. Bolt 2003; Somerville *et al.* 1996, 2003; Abrahamson & Somerville 1996; Meunier *et al.* 2008; Douglas 2002; Campbell 1981; Bommer 2003):

- Seismic moment release
- Rupture directivity
- Attenuation of PGA with distance from the seismic source
- Faulting type and geometry
- Topographic site effects

Each of these components can be both conceptually linked to, and may be reflected in the distribution of seismically triggered landslides.

8.2.1 Seismic moment release: seismic wave generation

In *Section 6.4.2* an apparent correlation between the co-seismic slip distributions and variations in landslide density in the along-strike direction was highlighted. In order to understand the potential mechanism for this link, the relationship between co-seismic slip and ground motion must first be considered. Ground motions are caused by seismic waves, generated by release of energy along the fault plane. Seismic energy released in an earthquake (E_s) can be understood in terms of seismic moment (M_o):

$$E_s \propto M_o = \mu AS$$

Equation 8.1

where μ is the shear modulus (crustal rigidity) of the rocks in which the earthquake occurs (typically 32 GPa in crust or 75GPa in mantle), A is the area of the seismogenic rupture plane (found by multiplying the length and width of the rupture plane), and S is the average co-seismic displacement across the rupture plane (Aki and Richards 1980; *Figure 8.1*). Thus, where variable slip distributions occur (and assuming little along-strike variation in μ and fault width), along-strike variations in co-seismic slip are roughly proportional to variations in the release of seismic energy. However, despite the rough correspondence in spatial patterns of co-seismic surface slip and landslide density, direct positive correlation is not observed.

If there is an empirical link between landslide density and M_o , then this uncertainty may be due to a number of additional geophysical factors. Spatial variations in the distribution of vulnerable slopes - for example the offset of major river valleys relative to 10km fault segments - are likely to spatially offset the impact of higher M_o levels from their source regions. In addition, while M_o may be related to PGA through region specific relationships (e.g. Margaris & Papzachos 1999) site effects may also result in high levels of local variability in PGA. As such, it would be premature to conclude a direct empirical link between landslide density and co-seismic slip based on the results of this study. However, the general patterns of

slip and landslide density suggest this may be discernable through further investigation.

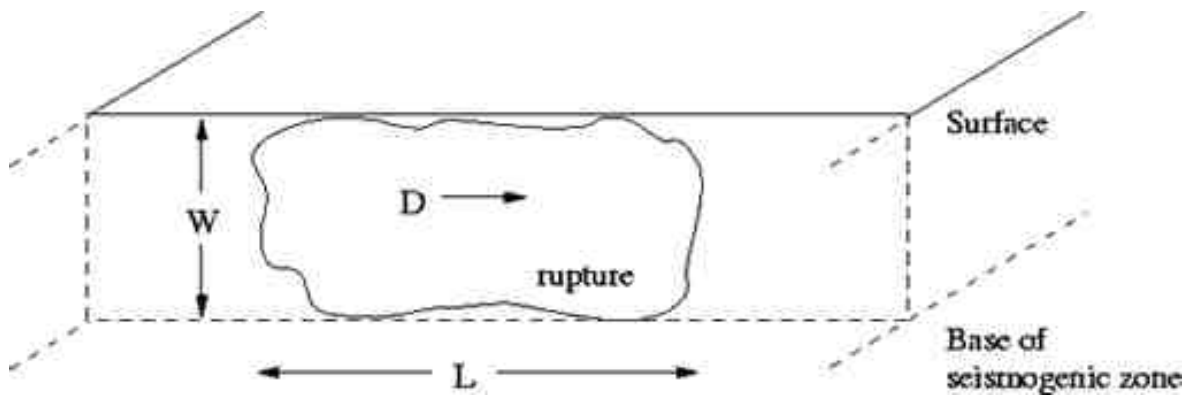


Figure 8.1: Illustration of seismic moment parameters (<http://earthquake.usgs.gov/learn/glossary/?term=seismic%20moment>)

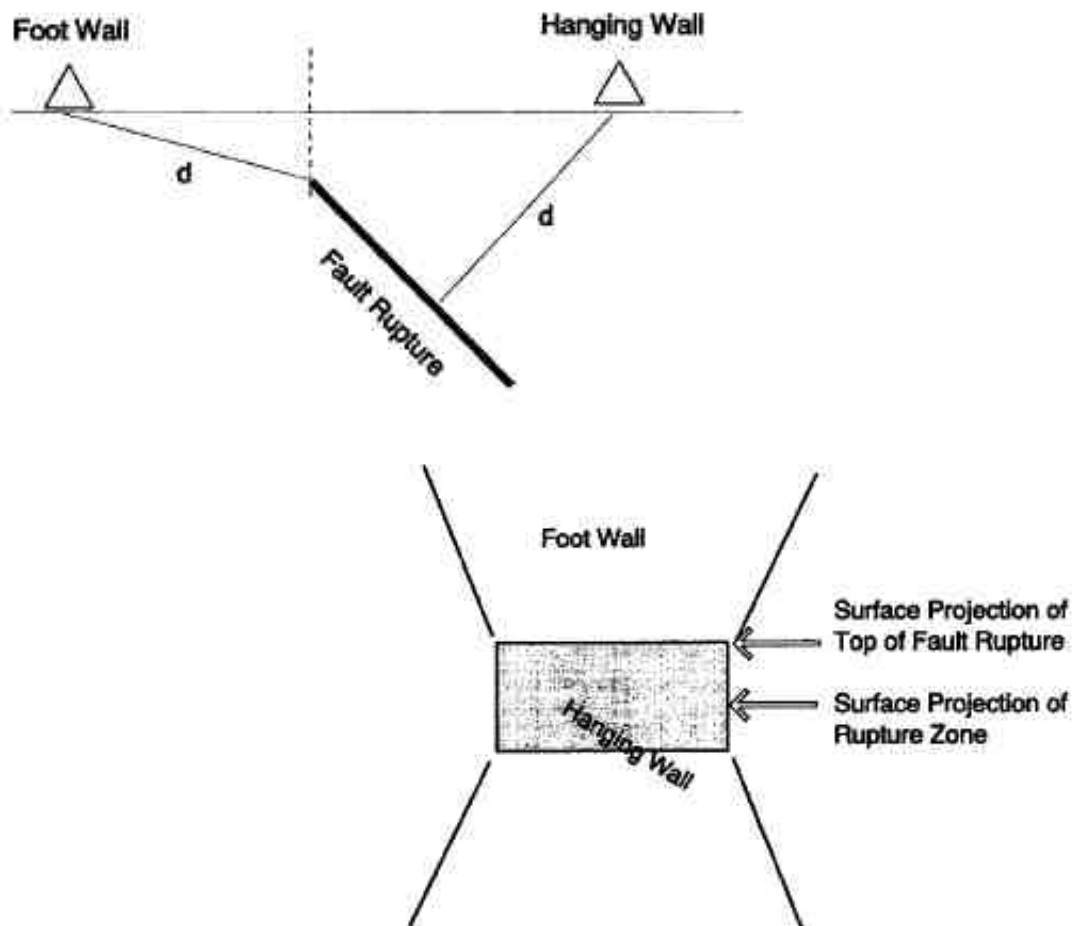


Figure 8.2: Illustration of hanging wall and footwall during thrust fault earthquakes, and their proximity to the coseismic fault rupture (Abrahamson & Somerville 1996)

8.2.2 Directivity

In addition to considering the likely pattern of seismic waves generated by the static slips distribution, the direction of rupture is also an important consideration for understanding shaking intensity. Directivity recognizes the nature of the seismic source as a moving object, rather than a fixed point, line or plane (Shabestrari & Yamazaki 2003). This is particularly important when considering faults which rupture unilaterally, from one end to the other. The result of unilateral rupturing is a marked directional difference in seismic ground motion, with larger amplitudes recorded at sites towards which the rupturing occurs (Bolt 2003; Shabestari & Yamazaki 2003). Spatio-temporal rupture models produced by both Nishimura & Yagi (2008) and Zhang (2009) demonstrate the occurrence of unilateral rupturing in the Wenchuan earthquake, moving from the epicentre in the south-west to the north-east along the fault. As such, continued high levels of landsliding along-strike are likely to also be driven by this factor. While the current dataset shows decay in the occurrence of landslides from an along-strike distance of 140km, this is likely to be an effect of the sample area coverage; other studies suggest high levels of landsliding further to the northeast in accordance with larger, directivity driven PGAs, as is shown in *Figure 4.16* (e.g. Huang & Li 2009a).

8.2.3 Attenuation of seismic waves

While the along-strike pattern of landslide density may be understood in terms of the co-seismic slip distribution and directivity, across-strike landslide density may be understood in terms of the fault geometry and fault perpendicular attenuation of seismic waves.

8.2.4 Hanging wall effect

The most striking component of the across-strike pattern of landslide occurrence is the marked hanging wall effect. This effect, common to thrust events, is recognized to result from systematic differences in ground motion in the hanging wall and footwall of thrust faults. (e.g. Abrahamson & Somerville 1996; Sato *et al.* 2007; Owen 2008; Shabestari & Yamazaki 2003; Jibson *et al.* 2004). Significantly larger PGAs are observed in hanging wall areas, resulting in higher levels of both landslide occurrence and general damage. The hanging wall effect can be understood in terms of the fault geometry, where sites located above the fault

rupture (in the hanging wall) are closer to the source fault plane than areas in the footwall, as illustrated in *Figure 8.2* (Abrahamson & Somerville 1996).

While the hanging wall effect may be explained in seismological terms alone, it is apparent that both topography and geology play a significant role in how this effect is manifested in the Wenchuan earthquake landslide distribution. Whilst landslide occurrence is almost exclusively confined to areas in the hanging wall of the Beichuan and Pengguan faults (*Figure 6.4*), so too is the high, steep topography of the Longmen Shan. As such, the majority of the footwall is comprised of hillslopes of insufficient gradient and relief to generate landslides. Similarly, the fault rupture forms a major boundary for geological units, such that units with higher rates of landslide occurrence are all located on the hanging wall block. This in turn may be related to higher rates of uplift and resulting climatically and seismically driven denudation in hanging wall areas, through which high levels of relative relief are developed in and sustained by particular geology types. This explanation is particularly compelling, as PGAs in immediate footwall areas of thrust faults may be as large as those in the hanging wall, due to the effect of directivity in the up-dip direction (Abrahamson & Somerville 1996). Thus high landslide densities may also be expected here, if steep topography was present. Therefore, while the hanging wall effect is recognized as primarily seismological in nature, its influence on the Wenchuan earthquake landslide distribution appears to be strongly linked to the fault relative distribution of topography. This in turn may be linked to the long term role of the fault geometry in landscape evolution on longer temporal scales.

It is also important to note that while the above discussion generalizes the rupture zones in terms of a hanging wall and footwall, the fault geometry of the Wenchuan earthquake involves two parallel along-strike surface ruptures. A third category of rupture zone may be defined: the mid wall, occurring as the footwall of the Beichuan fault and hanging wall of the Pengguan fault. Landslide occurrence begins to increase moving from the footwall into the mid wall, as both topography and the hanging wall effect have an influence. However, the full severity of the effect is only apparent on the hanging wall side on the Beichuan fault, where topography is steepest and highest.

8.2.5 Attenuation effects with distance from seismic sources

Despite the overall contrast between landslide occurrence in the hanging wall and footwall, both sides of the fault rupture exhibit an exponential decay in landslide density with distance. Through generalized linear modelling in Chapter 7, distance from co-seismic fault ruptures was identified as the highest ranked predictor variable controlling the occurrence of landslides. Within the hanging wall this decay initiates after ~10km with a relatively flat landslide attenuation signal between 5 and 10km, while it begins immediately in the footwall. This fits with the PGA patterns observed for various thrust fault earthquakes where a fairly flat PGA attenuation signal occurs from 6 to 12km on the hanging wall (Abrahamson & Somerville 1996). This effect is expected as a recurring feature of ground motion in reverse thrust events (Abrahamson & Somerville 1996), though it is not fully explained in the literature.

Exponential decay functions with distance from the seismogenic source have long been established for PGA (e.g. Campbell 1981; Taylor *et al.* 1986; Trifunac 1994). Correspondingly, several authors have attempted to demonstrate an exponential decay function for landslide occurrence, both empirically and conceptually. Prior to considering these studies it is important to bear in mind that the source of seismic waves is, in reality, spread out through a volume of rock with spatially variable energy release (Bolt 2003). However, for convenience most landslide investigations generalize this as a point (epicentre) or linear source (surface expression of the fault plain or surface rupture). In addition, the method for measuring landslide occurrence is also inconsistent, with most investigations making reference to either landslide concentration (number of landslides/km²) or landslide density (percentage area affected by landslides). As such, comparisons between studies must be considered with an element of caution and awareness of potential uncertainties.

Keefer (2000) fitted an exponential decay function to the concentration of landslides (landslides/km²) triggered by the 1989 Loma Prieta earthquake, expressed as distance from both the epicentre and the surface projection of the fault plane. Here, distance from the epicentre produced a better goodness-of-fit. For the 1999 Chi-Chi earthquake, data from Khazai & Sitar (2004) suggest an

exponential decay in landslide concentration with distance from the epicentre, while distance from the surface projection of the fault plane appears to produce a roughly linear function, although the authors did not fit curves. Conversely data from Dadson *et al.* 2004 suggest an exponential decay in landslide density with distance from the surface projection of the fault plane of the Chi-Chi earthquake, after a distance of ~20km. Here the use of landslide density is more comparable with this investigation, as opposed to the landslide concentration data of Khazai & Sitar (2004). Meunier *et al.* (2007) demonstrated linear correlation between PGA and landslide density from the Northridge and Chi-Chi earthquakes. Based on this the authors proposed a landslide density attenuation law with an exponential decay function based a common expression for evolution of seismic waves with distance from the hypocenter (Taylor *et al.* 1986; Trifunac 1994). Thus the exponential decay function observed in this study agrees generally with empirical landslide data for past earthquakes and observed relationships between ground motions and landslide occurrence.

8.2.6 Constraining the seismic energy source

A key issue arising out of the above sections is what feature to consider as the source of seismic energy. Of particular concern is the potential for large oversimplifications in the use of the focus (epicentre or hypocenter) defined as: “the point within the earth where an earthquake rupture starts” (USGS) or the “point from which the [seismic] waves first emanate”. This is particularly problematic in the case of the Wenchuan earthquake for a number of reasons. Firstly, there are uncertainties of up to 100km regarding the actual location of the focus (*Figure 8.3*; Shen *et al.* 2009). Secondly, the most widely accepted USGS epicentre location is placed at the southwest limit of the rupture zone, showing that the earthquake ruptured unilaterally from this point, while most of the damage caused by the earthquake occurred to the northeast. Considering landslide density with distance from this epicentre (*Figure 8.4*) produces a very noisy attenuation signal, and is dominated by observations in the along-strike direction. It is also important to note that the point of rupture initiation does not necessarily represent a region of maximum slip or energy release. Use of a linear energy source, split into hanging wall and footwall, solves the problem of confining the energy source

to one end of the fault, while also recognizing the systematic differences between fault perpendicular components of ground motion.

However, categories of hanging wall and footwall remain generalizations of both distance from and location relative to the dip plane of the fault. In addition, fault geometry alone does not account for variations in PGA. The earthquake was generated by a highly variable co-seismic slip distribution, style of faulting and fault geometry (Shen *et al.* 2009), which have all been shown to affect PGA amplitude and attenuation patterns (Campbell & Bozorgina 1994; Bommer *et al.* 2003). Correspondingly, the multiple across-strike landslide density profiles (*Figure 6.9*) suggest variations in the rate of landslide density attenuation depending on along-strike location.

Given the over generalizations produced through the use of point and linear energy sources, it would appear logical that uncertainties arise from failure to consider 3-dimensional fault geometry in landslide attenuation relations. While the use of a volumetric energy sources may be both practically and conceptually challenging, planar fault geometries and displacement fields (made available in the immediate aftermath of seismic events) appear to offer a suitable stepping stone.

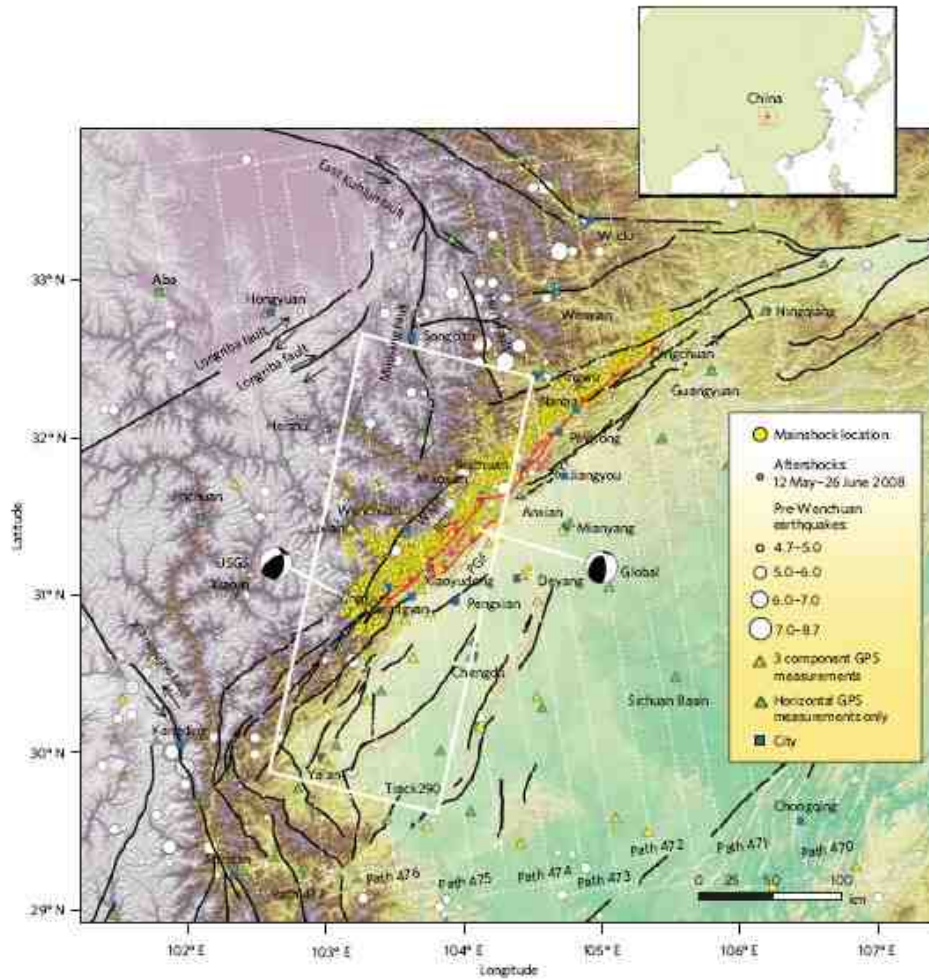


Figure 8.3: Map of Wenchuan earthquake rupture zone, showing disagreement in the location of the epicentre (Shen et al 2009).

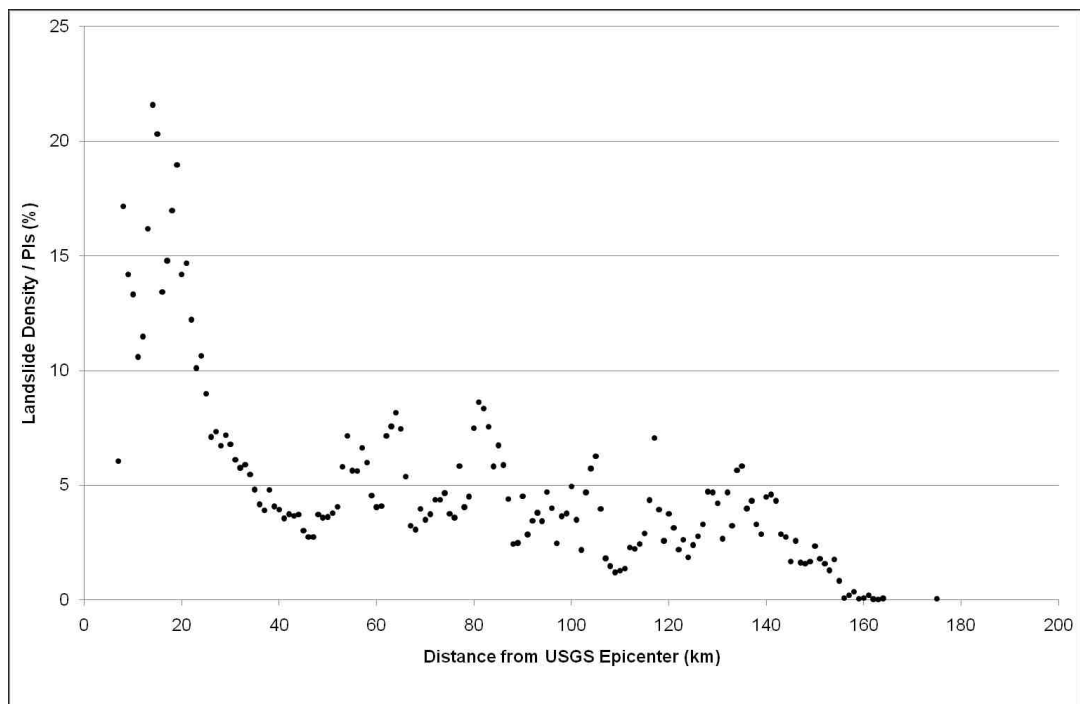


Figure 8.4: Pattern of landslide density with distance from the epicentre within 1km concentric buffers.

8.3 Topographic site effects

While variabilities in seismic wave generation and attenuation act over large horizontal scales of tens of kilometres, at finer scales topographic relief demonstrates a profound influence on the propagation of seismic waves. This results in distinct zones of amplification and damping of ground accelerations in particular topographic locations (Benites and Haines 1994; Bouchon *et al.* 1996; Meunier *et al.* 2008). The impacts of topographic site effects on the location of earthquake-triggered landslides can be examined in terms of two related components:

1. Amplification of ground accelerations at topographic convexities
2. Amplification or damping of ground accelerations due to the incidence angle of seismic waves

8.3.1 Amplification of ground accelerations at topographic convexities

Ground accelerations in several earthquakes have been observed to be significantly larger at ridge crests than those in surrounding flat areas or valley bottoms. For example, Spudich *et al.* (1996) noted that seismic wave amplitudes during the 1987 Whittier Narrows earthquake (California, USA) were an order of magnitude greater at the top of a 60m hill than in the surrounding plains. This topographic amplification occurs as seismic waves entering the base of a topographic ridge are partially reflected back into the rockmass and diffracted along the free surface. Progressive focusing of waves in the upward direction, and constructive interference of their reflections and diffractions increases ground accelerations towards the ridge crest (e.g., Davis and West, 1973; Bouchon, 1996; Geli; *et al.*, 1988; Benites and Haines, 1994). For this reason topographic amplification has been suggested as a significant component affecting the occurrence of seismically induced landslides (e.g. Sepulveda *et al.* 2005a, b; Murphy 2002; Havenith *et al.* 2002; Harp & Jibson 2002; Densmore & Hovius 2000; Meunier *et al.* 2008). In a review of four earthquake-triggered landslide distributions and two rainfall-triggered landslide distributions, Meunier *et al.* (2008) identified a predominant clustering of earthquake-triggered landslides around ridge crests, while rainfall triggered landslides occurred more uniformly across slopes or were clustered near streams. Seismic wave field models and PGA observations in

ridge and valley topographies demonstrated strong amplification of S-waves (though little effect on P-waves) near ridge crests and other convex knick points in the topography such as the edge of inner gorges. Considering the linear relationship between PGA and landslide density demonstrated in Meunier *et al.* (2007), and observed clustering of landslides near ridge crests, both an empirical and conceptual link between landsliding and topographic convexities is inferred.

Despite this, the results of this investigation do not suggest a strong direct link between topographic curvature attributes and landslide density, which proved to be non-statistically significant when correlated directly in logistic regression. Correlation of curvature and landslide density also suggested higher landslide occurrence on slopes with overall (total) and plan concave forms, but higher levels of landslide occurrence on slopes with convex profiles. This uncertainty and contradiction with the literature may well be an artefact of both the mapping and analysis process. In many places, landslide runouts were mapped as well as scars. While failures may have initiated at convex features on hillslopes, their majority area would have been mapped in the concave topography into which landslide material was deposited. In addition, direct correlation of convexity and landslide density may not be applicable to the process, as landslides may not occur directly on convex points, but rather may initiate near to or down slope from them. Due to practical difficulties in mapping ridge crests, distance or normalized distance from these features was not used as a variable in analysis. Thus, while landslides can be visually observed as initiating from ridge crests in the satellite imagery (e.g. *Figure 8.5*) this is difficult to demonstrate graphically at this stage, and requires further work with the dataset. Negative relationships for landslide occurrence with distance from major river channels and local elevation may be linked to topographic amplification and initiation of landslides at convexities along the edge of inner gorges. However, steeply incised hillslopes with steeper gradients also appear to occur along adjacent to river channels. Therefore, a seismic component may not be necessary to explain the preferential occurrence of landslides in these areas, where steep, unstable slopes cluster.

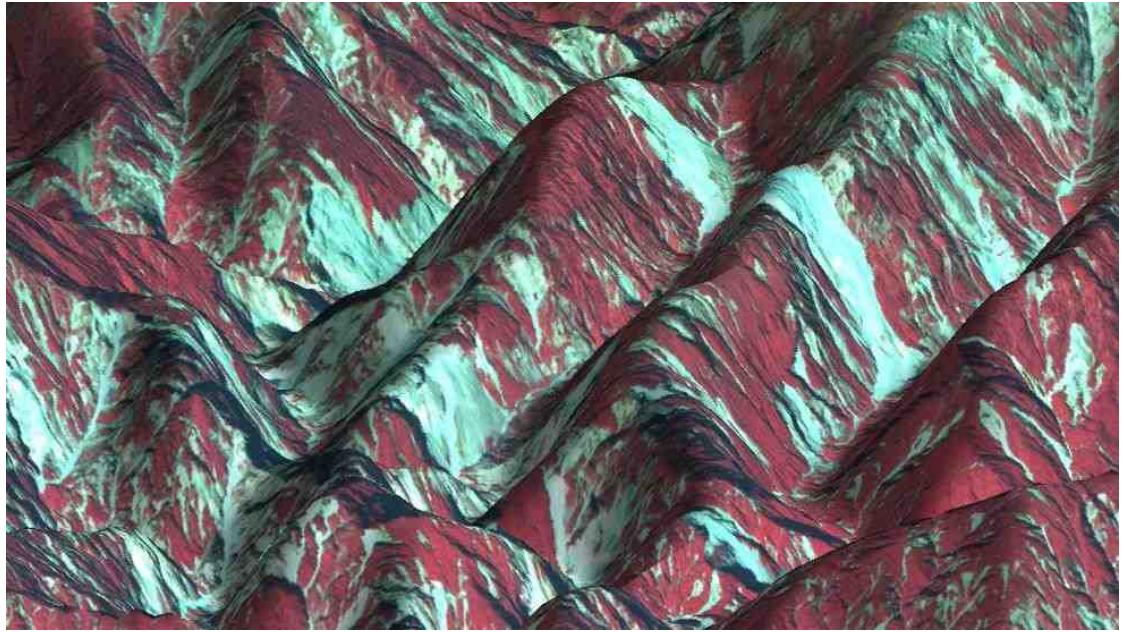


Figure 8.5: Spot imagery draped over DEM, showing landslide initiation from ridge crests.

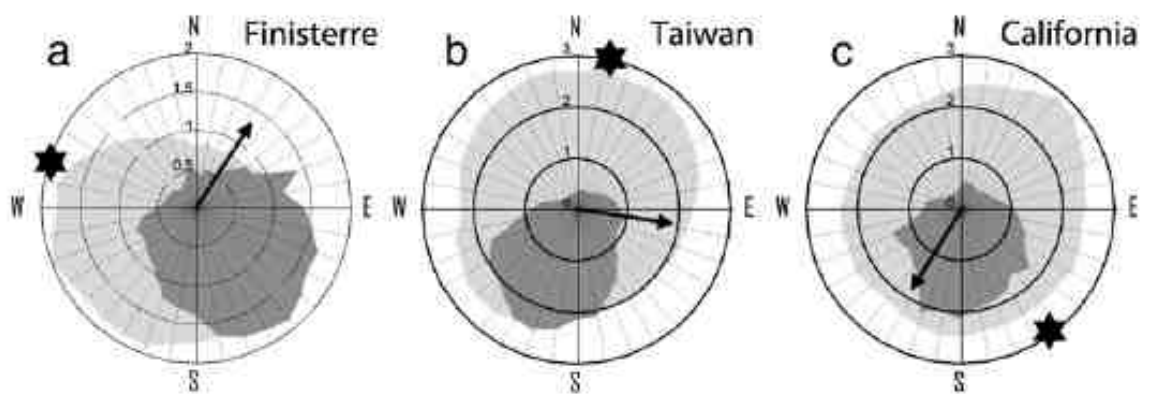


Figure 8.6: Pattern of landslide density by aspect, for the Finisterre (Papa new Guinea), Chi Chi (Taiwan) and Northridge (California) earthquakes. Star shows location of the earthquake focus. Arrows indicate the direction of fault dip.

8.3.2 Amplification or damping of ground accelerations due to the incidence angle of seismic waves

In addition to ground acceleration amplification at major convexities, the seismic wave field models of Meunier *et al.* (2008) also suggested that with increasing seismic wave incidence angle, the amplification maxima shift progressively from the ridge crests into the ridge flanks facing away from the wave source. This is due to constructive interference of the direct wave and the diffracted wave generated at the ridge. In addition, a damping effect is observed on slopes facing towards the wave source. For shallow earthquakes with large incidence angles over much of their impact zone, this suggests a net amplification on slopes facing away from the fault plain and a net damping on slopes facing towards the fault plain. Meunier *et al.* (2008) relate this factor to the normalized aspect distributions of landslides densities produced by the Chi-Chi, Finisterre and Northridge earthquakes (*Figure 8.6*). For Chi-Chi and Finisterre, landslide density is strongly skewed to slopes facing away from the seismic wave source. However, landslide densities in Northridge are strongly skewed to slopes facing towards the source, though this is ascribed to the dominant dip direction of geological strata (Parise and Jibson 2000) and the dependence of the soil production rate on subaerial processes, resulting in large amounts of unstable material on slopes facing south, towards the fault rupture (McFadden *et al.* 2005). Based on both the empirical evidence and conceptual link to PGA, the authors conclude: “*These strongly oriented landslide distributions indicate that topographic site effects dominate the location of earthquake induced landslides in central west Taiwan and the southern Finisterre Mountains, and that the rate of failure of the steepest slopes in mountain ranges is set by the local peak ground acceleration*” (Meunier *et al.* 2008: 230).

In this investigation, relative weighting of the fault perpendicular aspect variable in logistic regression placed it 6th (out of 10) after the core factors (distance from co-seismic fault ruptures, relative relief, local elevation, slope gradient and geology) indicating the relatively significant role played by this variable. However, as shown in (*Figures 6.31 & 6.32*), landslide densities for the Wenchuan earthquake are strongly skewed to the southwest. Given that the majority of landsliding occurred in hanging wall areas, this shows landslides occurred preferentially on slopes facing the seismic wave source. While this effect may be in part due to

topographic shading which obscured northwest facing hillslopes in some of the imagery used for mapping, the finding is also supported by field reports (Petley 2009 pers comm; Densmore 2009 pers comm). As noted for the Northridge earthquake, this may be due to larger amounts of unstable, weathered material produced on slopes with higher levels of solar insolation (Meunier et al 2008). When combined with the findings for the Chi-Chi, Finisterre and Northridge earthquakes, the fact that only two out of four case studies demonstrate the expected pattern of landslide occurrence, suggests that Meunier *et al.*'s (2008) analysis may be overly simplistic.

The Northridge, Chi-Chi and Wenchuan earthquakes all occurred in northern hemisphere mountain ranges at latitudes of over 20°N. In all these events, landslides occurred preferentially on south facing slopes. As such, a subaerial control on the occurrence of landslides may be inferred for any of these events. The Finisterre earthquake occurred in the southern hemisphere. The preferential occurrence of landslides with southeast aspects, on slopes receiving lower levels of solar energy, appears to contradict a subaerial effect. However, the rupture zone, located between 10° and 2° of the equator, experiences high sun zenith angles. The balance of solar energy is therefore more evenly distributed across hillslopes with southerly and northerly aspects, than is the case at higher latitudes. As such, the impact of topographic site effects may be manifest more readily in the landslide distribution in areas where skewing due to subaerial influences is less dominant. However, at higher latitudes, it may well be the case that form of the hillslope surface materials due subaerial processes dominates over seismological effects. In these cases the incidence angle of solar radiation may exhibit a greater influence on landslide occurrence than the incidence angle of seismic waves.

8.4 Other triggering mechanisms

While seismic parameters of the Wenchuan earthquake are the main consideration for triggering of landslides in this investigation, it is important to emphasize that the imagery used for landslide mapping was acquired over a period of seven months after the main earthquake. Thus, while little change is suggested between overlapping areas of earlier and later imagery, it is probable that some mapped landslides were triggered or enlarged after the main

earthquake event, by subsequent rainfalls or aftershocks. Unfortunately, insufficient multi-temporal imagery, as well as seismic or distributed precipitation data, was available to conduct this additional level of analysis into post-seismic triggering. Other investigations, however, have stressed the importance of both subsequent rainfalls and aftershocks in controlling the spatial distribution of landslides (e.g. Tatard & Grasso 2009; Dadson *et al.* 2003; Lin *et al.* 2006). As such, further investigation with the dataset should continue, in order to examine these influences.

8.5 Topographic and geological landscape characteristics controlling slope stability

While failure of hillslopes is triggered by ground accelerations in seismic events, the stability of hillslopes and potential for landslide failure is controlled by their topographic and material properties (Carson & Kirby 1972). As explored above, there are significant interactions between topography, geology and ground accelerations. However, particular topographic parameters alone act to control slope stability, which also form part of the complex range of parameters associated with different geological units.

8.5.1 Hillslope gradient and relative relief

Hillslope gradient is a major factor governing stability, as it controls the balance of normal and shear forces in hillslopes. As such, a strong correlation is shown between landslide density and gradient (*Figure 6.18*), whereby the probability of landslide failure increases with gradient via an exponential function. This pattern of increasing landslide occurrence with gradient is in agreement with findings from other earthquake-triggered landslide distributions (e.g. Keefer 2000; Parise & Jibson 2000; Khazai & Sitar 2004). However, this does not mean that the majority of landsliding occurs on the steepest hillslopes. As shown in this and other investigations, modal gradient values for landsliding occur between $\sim 10^\circ$ and 20° above the mode for the landscape (Keefer 2000; Parise & Jibson 2000). This oversampling of steeper hillslopes should be expected as they are, by definition, more unstable. However, the modal gradient for landsliding occurs where there are still relatively large hillslope areas, dropping off after this point because of the paucity of very steep hillslopes. As such the modal gradients for landslide

occurrence vary between different earthquake events, depending on overall steepness of the topography: 25° for Loma Prieta (Keefer 2000), 30-40° for Northridge (Parise & Jibson 2000), 45° for Chi-Chi (Khazai & Sitar 2004), and 35° for Wenchuan.

However, gradient alone does not fully explain the occurrence of landslides, and relative relief has been shown to generate a similar relationship. However, this must not be understood purely in terms of the relation of relative relief to gradient, both being attributes of change in elevation over a given horizontal distance. Bieniawski & Vanheerden (1975) demonstrated that rock mass strength decreases with increasing spatial scale, due to the influence of spatially distributed discontinuities. Regions which sustain gradients over larger distances therefore have a greater potential to fail. Following on from this, Schmidt & Montgomery (1995) demonstrated that mountain scale material strength is a key limiting factor on topographic relief. In addition, higher relief regions also have the potential to sustain larger landslides, with both longer scar lengths and runout distances due their higher potential energy. Relative relief and gradient demonstrate significant correlation ($R = 0.58$; *Table 7.6*), and both are reflective of the balance of normal and shear forces in hill slopes. However, relative relief combines the balance of forces with the larger scale material strength of hillslopes, reflecting a different scale of the hillslope stability process. These two attributes also share a common feature in that the majority of landsliding occurs at mid-values of slope and relief, where the ratio of landslide to non-landslide areas is <20%. As these are both core factors in landslide probability modelling, this uncertainty regarding the fate of large areas appears to be a key factor in the uncertainties of landslide probability and susceptibility mapping.

8.5.2 Elevation and upslope contributing area

While elevation and upslope contributing area were also included in analysis and probability modelling, these exhibit much less coherent relationships with landslide density. Clustering of landslides at particular elevations appears to be linked with the positioning of major river valleys in the landscape, where the majority of landslide susceptible slopes occur, rather than a particular elevation-dependent control on hillslope stability. The lack of landslides at minimum elevations at the

edge of the Sichuan Basin and higher landslide densities in the mountain range are the likely cause of apparent positive correlation in logistic regression. As such, any relationship between elevation and landsliding is likely to be an artefact of the data analysis and sample methods rather than the result of geophysical conditions. Upslope contributing area (UCA) was primarily included in the analysis due to its relationship to landslide occurrence through soil wetness. While logistic regression suggests an overall positive relationship between UCA and landslide occurrence, the nature of the relationship between these variables is complex. Greater UCA acts to increase groundwater levels, thus higher pore water pressures and enhanced slope instability may be expected. However, there is an inverse relationship between UCA and slope gradient (Montgomery 2001); as UCA increases, slope gradient decreases, countering the destabilizing effect of wetter ground conditions. As such, while both elevation and UCA were included in logistic modelling, their low significance rankings and limited affect on model performance demonstrates that they do not function as direct predictors of landslide occurrence.

8.5.3 Geology

In contrast to other variables used in this investigation, geology is necessarily a categorical variable due to the broad range of lithological attributes and parameters contained within its definition. The geological dataset used in this investigation comprises regional scale geological units, and is thus representative of variations in lithology over reasonably large spatial scales. As described in *Section 4.1.5*, this involves classifying multiple lithologies into single units, where the detailed material properties of individual lithologies are not known. Direct comparison with other studies is difficult, due to the different geological datasets used in analysis. However, the overall pattern of landslide occurrence concurs with the findings of Huang & Li (2009a), with greater levels of landslide occurrence in harder igneous rocks, carbonates and sandy conglomerates, although units containing mudstones, greywacke and shale also feature significantly. An explanation of why particular units are more susceptible to landslides involves a holistic understanding of how a range of different tectonic and topographic attributes vary and interact within geological units, as well as considering lithological material properties.

The general positive correlation of landslide density-ranked geologies with slope gradient and relative relief (shown in *Table 7.2*), shows that, in general, steeper hillslopes of greater relief occur in more susceptible geological units. As such the greater susceptibility of different geologies is explained in part by the topography they sustain. This can be linked to their material strength, in that stronger lithologies may sustain steeper slope gradients and greater relief (Schmidt & Montgomery 1995), explaining the observation of Huang and Li (2009a) that it is in general the harder lithologies which sustain higher rates of landsliding. There is also a significant negative correlation between ranked geology and distance from the surface fault rupture, showing the predictable result that geologies with higher landslide densities are those experiencing high ground accelerations. However, the position of more susceptible geologies in the fault belt may also be related to longer term landscape evolution processes. Due to the rotational nature of the tectonic thrusts (Hubbard & Shaw 2009), higher rates of rock uplift are to be expected in the fault zone, where these high landslide density geological units are located. Combined with this, denudation rates are likely to be higher in these areas due to the high rate of seismicity and location close to the mountain front where higher rates of precipitation are also likely to occur. A combination of both high uplift and denudation rates would explain the steep, incised landscape, and hence slopes susceptible to landsliding. Along with high rates of rainfall, wetter soil moisture conditions and greater pore pressures in this region may also act to decrease slope stability (Selby 2005). In *Section 6.5.1* a correlation between landslide density and age of geological units was observed. This may also be explicable through interactions with topography, in that the exhumation of older units from depth mainly occurs in the near-fault areas of both Beichuan and Pengguan fault hanging walls, close to the fault belt, as shown in *Figure 4.9*.

These spatial associations between lithology, ground accelerations and topographic attributes suggest that geological controls on landslide occurrence may be largely explained through coincidence with other geophysical factors. However, the significant reduction in logistic model performance with the removal of geology demonstrates that the role of this variable is not fully explained through topography and seismic shaking intensity. This may be accounted for through variations in the material properties of different geological units, which affects their

susceptibility to landsliding. This is likely to involve variations in rock and soil strength, dip angle, location of slip planes and other discontinuities in the rock mass (Selby 2005). For example, failures in Mesoproterozoic granite have been observed to predominantly take the form of shallow surface failures, which strip off thin regolith cover along the contact between regolith and bedrock (Petley 2009 pers comm.; Densmore 2009 pers comm.).

While geology exhibits a notable influence on landslide occurrence, the nature of this effect must be understood through intricate relationships between geology, tectonics, topography and climate, as well as the ground acceleration experiences by particular geological units. A more focused understanding of the influence of geology may be attainable through the use of more finely categorised geological maps, and additional geological attributes such as dip angle, material strength and joint spacing (e.g.: Selby 2005; Hales & Roering 2007).

8.6 Practical implications for landslide inventory investigations

Carrying out this investigation involved the development of various techniques to overcome major obstacles in data acquisition and analysis. As such, a major output of the investigation is its practical implications for future investigations of this type. These include methodological implications for landslide mapping, as well as the identification of core attributes for use in the statistical interrogation of landslide inventory datasets, and techniques for extrapolating results from mapped samples.

8.6.1 Landslide inventory data generation and format

The implications of this investigation for landslide inventory data generation, can be summarised three-fold, in terms of the image data used for mapping, the mapping methodology and the geometric dimensions through which landsliding is recorded and analysed.

Although the sub-tropical monsoon climate of the Sichuan region posed a significant challenge in terms of data acquisition, a search of catalogues for major satellite sensors revealed significant cloud free imagery, available within a short period after the earthquake. In addition, the high level of contrast between thickly vegetated areas and bare soil and rock scars produced high levels of spectral separability between landslides and surrounding areas, in agreement with Borghuis *et al.* (2007). Traditional approaches to landslide inventory compilation stress the need for labour-intensive manual delineation of landslides (e.g. Liu *et al.* 2002). However, this investigation emphasises the significant potential of semi-automated classification approaches for the rapid delineation of landslides at regional scales. Here landslide classification has been achieved through a well-established, pixel-based technique, which has been used in image processing for over 20 years (e.g. Strahler *et al.* 1986). As such, there is potential for more modern, sophisticated image segmentation techniques to address both more problematic landslide classification problems, and high contrast classification conditions with greater levels of accuracy (e.g. Barlow *et al.* 2003; 2006).

Many landslide inventory investigations also emphasise the necessity of high resolution aerial or satellite imagery for landslide mapping (e.g. Cardinali 1990; Liu

et al. 2002). Experimentation with classification of imagery data, resampled to lower resolutions, revealed that total mapped landslide areas showed little variation between 5m and 30m pixel resolutions. However, the area-frequency characteristics of mapped landslides were greatly influenced by the mapping resolution. This demonstrates that, for regional scale landslide mapping exercises, imagery as low as 30m in resolution (containing appropriate radiometric bands to separate landslides spectrally from surrounding areas) may be utilised to produce a first order estimate of the landslide impact. This is particularly significant as it applies to Landsat and DMC imagery types which are often freely available, highlighting the potential for low-cost first-order data acquisition. Despite this, higher resolution imagery is required for more in-depth studies, particularly when considering the magnitude-frequency characteristics of landslide events.

Following on from this is a further issue highlighted by this investigation concerning the way in which landsliding is measured. This varies greatly between landslide inventory investigations, from identifying individual landslides as point features located at their source or centroid locations, to delineating landslides areas as 2-dimensional polygons and estimating volumes from scaling relationships (Guzzetti *et al.* 2009). In general, more recent investigations tend towards measuring landslide areas, though there is no strict rule. This results in significant challenges to the comparability of investigations and their results. For example, the linear relationship between landslide concentration and distance from the co-seismic fault ruptures shown by Khazai and Sitar (2004) for the Chi-Chi earthquake is contradicted by the exponential relationship for landslide density shown by Dadson *et al.* (2004), for the same event. This is likely due to underestimates of the landslide impact by only considering the location of failures, while their areas vary over several orders of magnitude. This highlights the need for consistency in practical approaches to landslide inventory mapping. An ideal data format would consist of polygons separately delineating the source and deposit areal bounds of individual landslides, an extension of which are 3-dimensional polygons incorporating landslide depth and thus volumetric characteristics, along with an additional attribute field of landslide type. However, as noted by Hervas & Bobrowsky (2009), all ideally required data fields are rarely available and often difficult to obtain.

This landslide inventory for the period shortly after the Wenchuan earthquake does not incorporate a temporal component. However, several studies have highlighted the potential of multi-temporal landslide inventory data for understanding the post-seismic evolution of landslide failures and valley sedimentation (e.g. Dadson *et al.* 2003; Dadson *et al.* 2004; Lin *et al.* 2008). This is addressed in more detail in the following section. However it is worth noting that, should suitable repeat-pass imagery be available, continued monitoring of landslide distributions should form a key component to landslide inventory studies.

8.6.2 Approaches to landslide inventory analysis

The study also highlights implications for the approaches applied to analyse landslide inventories for seismic events. The identification of core predictors controlling the occurrence of landslides, implies that distance from co-seismic fault ruptures, relative relief, local elevation, hillslope gradient and geology are key variables which should be considered when analysing seismically-triggered landslide distributions. In addition, aspect also appears to play a significant role, and future investigation should examine this in order to help identify the exact nature of the geophysical processes associated with it.

Despite identifying the core predictors, *Chapter 7* also showed that a relatively small proportion of variation in landslide occurrence is explained by the predictor variables. In order to increase the goodness-of-fit of statistical landslide probability models, a wider range of higher resolution attribute fields should be applied to landslide inventory data, based on geophysical processes known to control landsliding. Critical data fields for model improvement are likely to include higher resolution geological maps and data concerning geological structure (dip and fracturing of rocks), as well as higher resolution topographic data and fields reflecting seismic directivity effects.

The combination of bivariate analysis and generalised linear modelling using multiple data fields, allowed for the application of hind-casting, as a powerful tool to estimate the probability of landsliding across the entire rupture zone of the earthquake. This highlights the potential for rapid estimation of post-earthquake landslide impact based on a relatively limited training sample. In addition to generating landslide probability maps, there is also the potential to impose

synthetic landslide distributions based on expected area-frequency relations for events of given magnitude, as identified by Malamud (2004). The application of these techniques may offer significant contributions to both post-disaster management as well as the geomorphological and seismological study of earthquake-landslide events, as discussed further in the following section.

8.7 Application of findings

While investigating controls on the spatial distribution of earthquake-triggered landslides has been the primary focus of this study, both the dataset and techniques developed hold the potential for a range of wider applications within the fields of hazard management, seismology and geomorphology. The following section highlights key areas in which the major outputs of this investigation may afford significant contributions.

8.7.1 Hazard mapping and rapid damage assessment

As acknowledged in *Section 8.6.2*, logistic modelling may be applied to build landslide probability maps from which, it is hypothesized, synthetic landslide inventories may also be inferred. The post-predicting capability of logistic landslide models may offer the potential to overcome a major limitation of optical satellite imagery in rapid damage assessment and post-disaster response for earthquake-landslide events. Satellite data acquisition times in the wake of natural disasters are becoming more rapid, with imagery now often available within hours of events occurring. However, a major limitation, particularly in areas like Sichuan with high levels of cloud cover, is the often limited extent of cloud-free imagery available. This investigation has shown how a sample of landslides may be generated rapidly using semi-automated classification techniques. Logistic models based on core predictors of landslide probability may then be trained using a limited coverage sample, where seismic attributes are available through automatically generated seismic wave inversion results (e.g. USGS earthquake hazards program - <http://earthquake.usgs.gov/earthquakes>). Thus, with the appropriate data processing expertise and resources, maps of probabilistic landslide occurrence may be generated within periods of hours to days, without the need for extensive image coverage. Application of the technique to future events would certainly benefit from more investigation into the impact of sample size and sample location relative to the seismic source.

While deterministic landslide hazard models may be applied globally, locally trained models have been shown to produce more accurate impact estimates. Logistic regression models have been widely applied in landslide susceptibility mapping for future events (e.g. Garcia-Rodriguez *et al.* 2008; Chang *et al.* 2007;

Ayalew & Yamagishi 2005; Dai & Lee 2003), and as such the logistic model may be applied to predictions of the future seismic hazard in Sichuan and surrounding regions. This type of probabilistic hazard data may also feed directly into catastrophe models widely used in the insurance and risk management industries. These combine probabilistic hazard data with a range of vulnerable assets in order to provide estimates of probabilistic risk. Areas in rapidly developing nations such as China are of particular interest due to the growing proportion of insured assets in these regions. While information on spatially distributed death tolls is fairly limited, the main areas affected by higher landslide probabilities appear to coincide with counties exhibiting high earthquake-related fatalities, as shown in *Figure 8.7*. This and the fact that 35% of fatalities caused by the Wenchuan earthquake have been attributed to landslides (Paterson *et al.* 2008), stresses the importance of considering slope failures in seismic damage tolls.

8.7.2 Earthquake dynamics

A key limiting factor for seismological studies of the Wenchuan earthquake is the poor quality of ground motion data available for the region. Given the linear relationship inferred between PGA and landslide density, Meunier *et al.* (2007) highlighted the potential for geomorphologically-derived shakemaps, effectively using landslides as seismometers. Following this investigation, landslide density data are now available for a large portion of the Wenchuan earthquake rupture zone, allowing for the possibility of PGA back-projection in areas where landslides occurred. This in turn may allow for improvements to inversion models of fault rupture dynamics, through the addition of local ground acceleration estimates. However, this exercise would first require intensive normalization to incorporate spatial variations in non-seismic factors affecting slope landslide susceptibility. This may well be achieved through further work with generalized linear modelling. In addition, for areas where seismic data is unavailable, PGA-related features of the landslide distribution discussed in *Section 8.2* may provide valuable estimates of fault rupture dynamics and geometry.

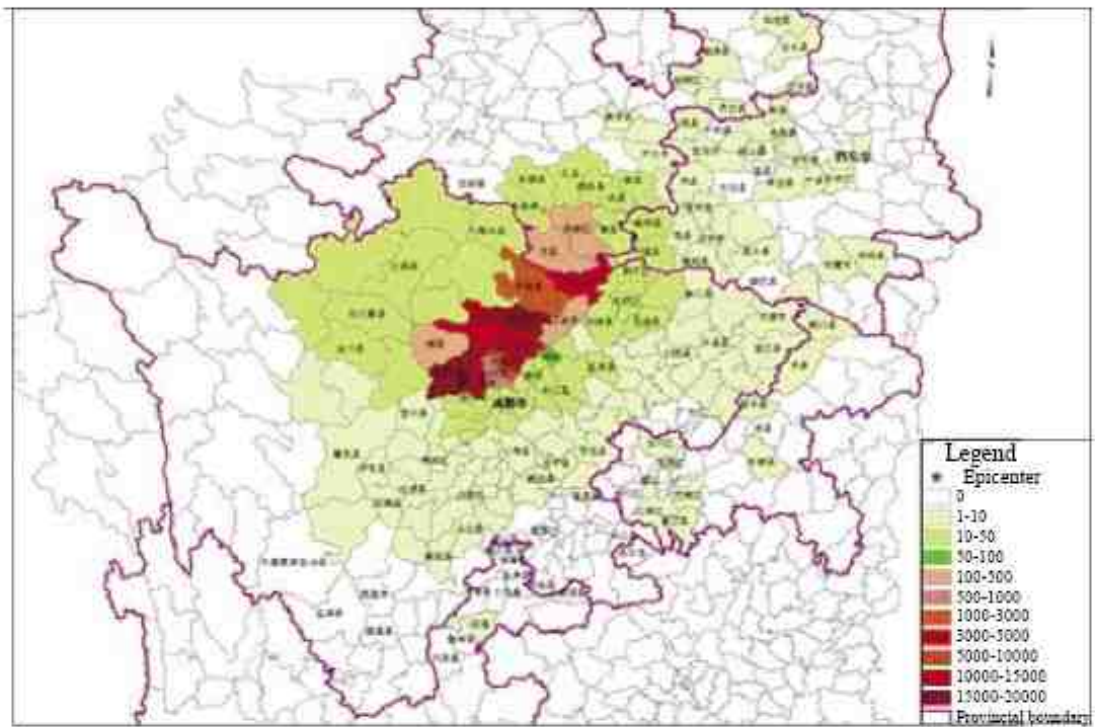


Figure 8.7: Recorded Wenchuan earthquake damage by county (Yuan 2008)

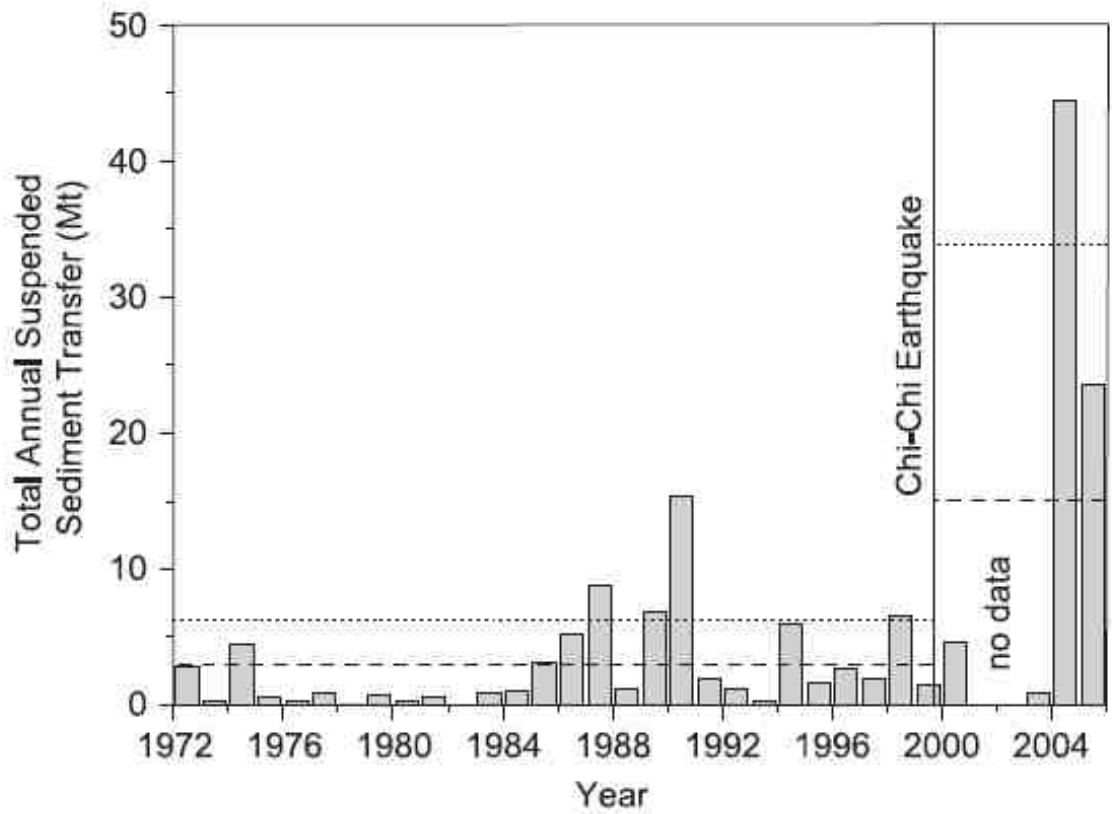


Figure 8.8: Temporal pattern of suspended sediment levels following the Chi Chi earthquake (Lin et al 2008)

8.7.3 Post-seismic evolution of failures, sedimentation and carbon release

While the analysis of this study predominantly focuses on the immediate after-effects of the earthquake, landslide inventory data may also be utilized to explore and understand post-seismic conditions and the longer term effects of the earthquake on the Sichuan region. Key areas for consideration include post-seismic landsliding, remobilization of sediment and carbon release.

While large areas of co-seismic landsliding have been recorded, studies of the Chi-Chi earthquake have shown that the rate of landsliding remains elevated for several years after the event (e.g. Dadson *et al.*, 2004; Lin *et al.*, 2006; Khazai & Sitar 2004; Lin *et al.* 2008). This is attributed to a large number of earthquake-weakened slopes which did not fail co-seismically, but did fail during subsequent monsoon storms (Dadson *et al.*, 2004; Lin *et al.*, 2006). Post-seismic landslides were also found to mimic the distribution of co-seismic failures, an effect ascribed to pervasive fracturing of bedrock throughout the main impact zone of the earthquake. Given the subtropical monsoon climate of the Sichuan region, a similar situation is to be expected. The large number of non-failed hillslopes exhibiting significant landslide probabilities (*Figure 7.9*), are likely to provide a reasonable indication of slopes likely to be affected by post-seismic landsliding. Further monitoring of the post-seismic evolution of slope failures is necessary in order to validate this assumption.

Also related to subsequent, post-seismic rainfall events is the additional hazard concerning the reactivation of landslide deposits. Field evidence suggests that extensive sediment aggradation is at present inundating valley bottom settlements in Sichuan, such as Beichuan town. This is due to the remobilization of sediment by high monsoon rainfalls since the earthquake and transport of large amounts of landslide material through the hydrological network. High suspended sediment levels were also observed for several years following the Chi-Chi earthquake, as shown in *Figure 8.8*. From these data it is estimated that post-seismic landsliding triggered by subsequent typhoon rainfalls resulted in a two- to four-fold increase in suspended-sediment flux (Dadson *et al.*, 2004; Lin *et al.*, 2006; Lin *et al.* 2008). In order to study the activity of this sediment, both actual and synthetic landslide inventory maps may play a major role in producing estimates of sediment volumes mobilized by the earthquake. Simple application of the scaling laws summarized

by Guzzetti *et al.* (2009) to the total mapped landslide area yields a range of total volume estimates from ~20 to 300 km³, with the distribution of landslide areas indicating how this volume is distributed throughout the major catchments. While the high levels of uncertainty in these estimates highlight the need for further work on volume scaling relationships, the landslide inventory map provide a valuable starting point for this investigation.

Finally, there is growing interest the role of landslides in sourcing particulate organic carbon from hillslopes (e.g. Hilton *et al.* 2008a; Hilton *et al.* 2008b). Widespread landsliding may store large amounts of particulate organic carbon, through both the deforestation of affected hillslopes and widespread burial in aggrading river beds. This highlights the need for further investigation into the potentially importance but poorly understood role of landslides in the carbon cycle, for which an essential component is an inventory of mapped landslides. With the datasets now available, the Wenchuan earthquake offers a key opportunity for this field of research.

Chapter 9

Conclusions

9.1 Conclusions

The results of this study can be summarised by revisiting the research objectives in Chapter 1:

1. *To develop semi-automated image classification algorithms in order to map landslides efficiently over large areas of satellite imagery*

Semi-automated, pixel-oriented classification techniques have been developed, which accurately and efficiently delineate landslide scars in SPOT 5 and EO-1 imagery. These techniques utilize both spectral and topographic data, combined with object oriented filtering, to produce a first-order estimate of areas affected by landsliding. The algorithms are most effective in imagery exhibiting high spectral or intensity contrast between landslide scars and surrounding vegetated areas unaffected by landsliding. The accuracy of these techniques has been validated relative to manually-delineated landslides. The combination of accuracy and rapid data generation afforded by these techniques offers significant potential for both the geomorphological study of landslide distributions, and rapid damage assessments in the wake of earthquakes in mountain regions.

Of additional relevance to this objective is the finding that total mapped landslide areas vary little with decreasing pixel resolution. As such, considerably less expensive imagery of lower spatial resolution may be applicable for similar studies, where the primary data interest is 'area affected by landsliding'. However, the area-frequency characteristics of landslide distributions are greatly affected by imagery resolution. As such, high resolution imagery should be used to conduct investigations with this focus, and image resolution should be a key consideration when evaluating studies of this type.

2. *To produce an inventory map of landslides triggered by the Wenchuan earthquake*

A GIS based map of landslide affected areas has been produced for a region of 11,909km², covering the main impact zone of the Wenchuan earthquake. This corresponds to a significant proportion of the total landslide affected area, of which 5% is covered by mapped landslides. The dataset represents the most holistic

mapping of landslides triggered by the earthquake which has been published to date (Parker *et al.* 2009a, b).

Based on the training sample produced by the mapped area, a statistically modelled landslide probability map has been derived for the entire region affected by the earthquake. This predicts landslide occurrence over the entire length of the rupture zone, and also shows that the majority of the landslide impact is captured within the mapped coverage area.

As well as providing the primary data sources for this investigation, both the actual and probabilistic landslide distributions afford significant potential for a broad range of studies into the Wenchuan earthquake and post-seismic evolution of the landscape.

3. To examine spatial relationships between landslide occurrence and geophysical parameters

This study has considered the occurrence of seismically induced landslides relative to 14 seismological, topographic and geological parameters, through which characteristics of the landslide distribution and relationships between landsliding and geophysical parameters have been discerned. The macro-scale landslide distribution demonstrates strong association with expected patterns of peak ground acceleration produced by the earthquake, of which there are three main components. (1) Markedly higher rates of landsliding occur in the hanging wall of the Beichuan fault. However, this appears to be driven by a combination of not only ground accelerations, but also topography, with significant relief limited to hanging wall areas. (2) This effect is superimposed on an exponential attenuation of landslide density with distance from the co-seismic surface rupture, in concurrence with the attenuation function for peak ground accelerations and linear relationships between peak ground acceleration and landslide density, as observed by Meunier *et al.* (2007). (3) In the along-strike direction, landslide densities and distance attenuation signals also suggest probable association with spatial variations in seismic energy release. However, further work is required to distinguish from topographic and geological effects. The preferential occurrence of landslides on hillslopes facing the seismic source was also identified, in clear contradiction with seismic wave field theory for this type of event (Meunier *et al.*

2008). From this finding, the potential dominance of subaerial controls on landslide aspect is suggested for higher latitude regions. As such, further work is required to determine the nature of this effect.

Despite the overarching role of ground accelerations in triggering landslides, the occurrence of slope failures also exhibits strong topographic and geological controls. Topographic attributes relating to the balance of normal and shear forces in hillslopes are central to controlling slope stability. Slope gradient and relative relief demonstrate significant, positive correlation with landslide density, forming core predictors of landslide occurrence; along with local elevation which appears to represent distance from major river channels. Relationships with other topographic attributes are both more complex in nature, and as such do not form major predictors of landslide occurrence.

Oversampling by landslides within particular geological units has also been demonstrated, though the mechanism of this effect is complex. The geological control is strongly tied to the topographic features formed within different geologies, as well as the positioning of geological units in areas of high ground accelerations. However, generalised linear modelling demonstrated that variations in geological susceptibility to landsliding are not fully explained using the available topographic and seismic parameters. This suggests that additional parameters enclosed within geological categories, such as hillslope material strength under seismic acceleration forces, must be considered in order to explain geological controls more fully. Understanding the nature of the geological control is particularly significant, as the modelling in this study has identified geology as a core predictor of landslide occurrence. The significant influence of geology over large spatial scales also suggests that direct correlation of landslide density with peak ground accelerations should be treated with caution. In particular, intensive normalisation of geological influences is likely to be required, in order to achieve the geomorphologically derived shakemaps hypothesised by Meunier *et al.* (2007).

While the relative influence of different parameters on landslide occurrence has been examined, it would be illogical to conclude the dominant role of one particular factor in controlling landsliding, given the range of spatial scales over which different geophysical processes function. However, core variables required to

accurately hind-cast landslide occurrence were: distance from co-seismic fault ruptures, relative relief, local elevation, slope gradient and geology, with aspect also showing a notable but less significant influence. Relationships to geophysical processes of distance from co-seismic fault ruptures, relative relief and slope gradient are well constrained. However, local elevation, geology and aspect may be related to a broader range of processes, and thus the nature of their functions in landslide occurrence is poorly understood. This highlights a perturbing black-box element to the macro-scale understanding of seismically induced landslide distributions which should be addressed in future research, when considering both new and existing datasets.

Appendix 1

McFadden's R^2

$$R^2 = 1 - \ln L(M_{full}) \div \ln L(M_{intercept})$$

M_{full} = Model with predictors

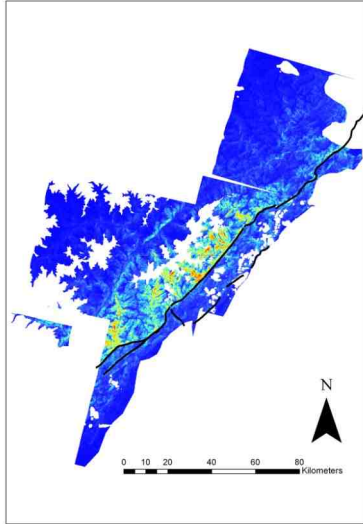
$M_{intercept}$ = Model without predictors

L = Estimated likelihood

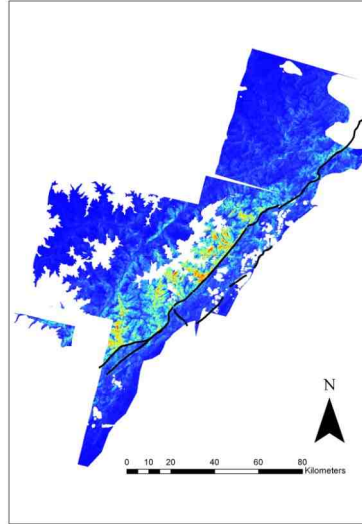
(http://www.ats.ucla.edu/stat/mult_pkg/faq/general/Psuedo_RSquareds.htm)

Appendix 2

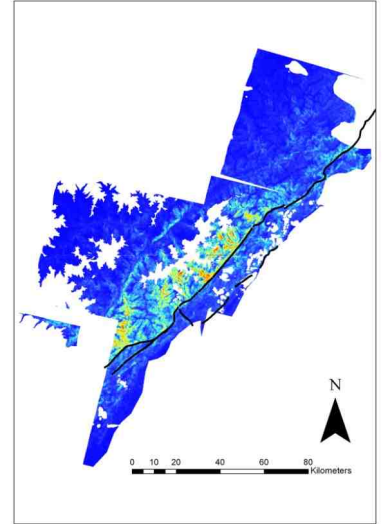
1: FD HF G SL DEM
LCEL R CT CPL CPR RD
UCA $\sin(A_r)$ $\cos(A_r)$



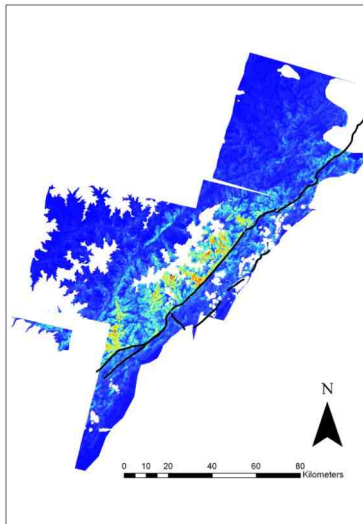
2: FD HF G SL DEM
LCEL R RD UCA $\sin(A_r)$



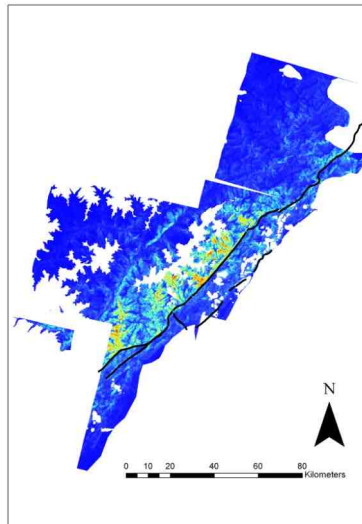
3: FD HF G SL DEM
LCEL R UCA $\sin(A_r)$



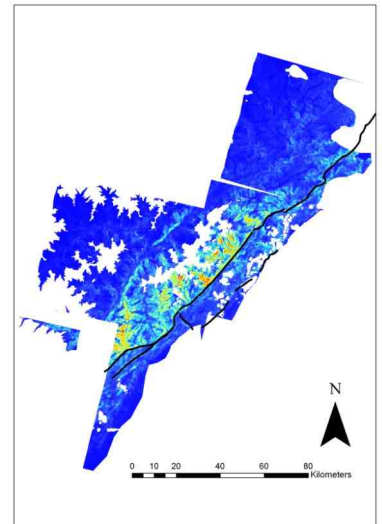
4: FD G SL DEM LCEL R
UCA $\sin(A_r)$



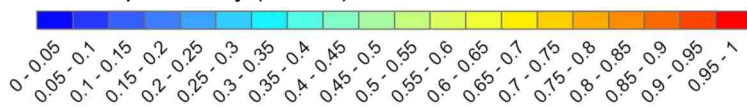
5: FD G SL LCEL R UCA
 $\sin(A_r)$



6: FD G SL LCEL R $\sin(A_r)$



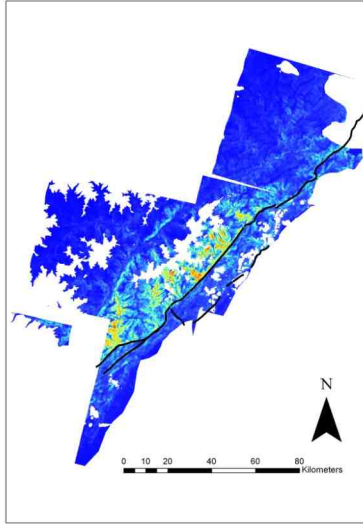
Landslide probability (LS = 1)



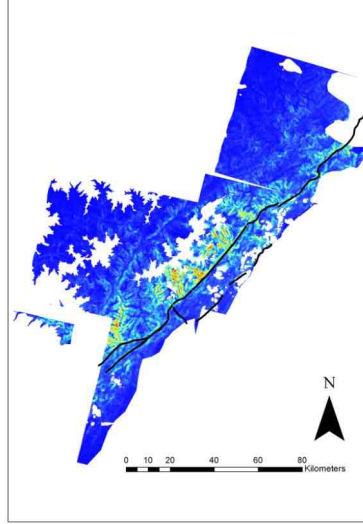
Appendix 2: Map projected landslide probabilities for all parameter combinations. Model number and parameter combinations for each output are given above. (Continues overleaf).

Appendix 2

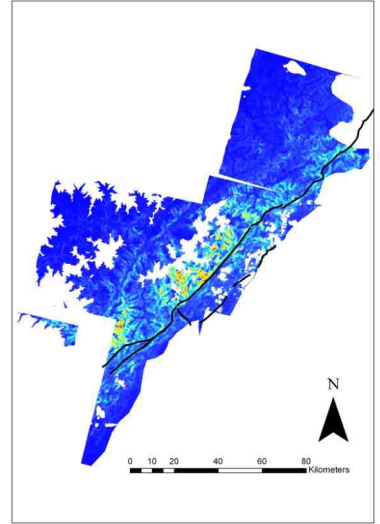
7: FD G SL LCEL R



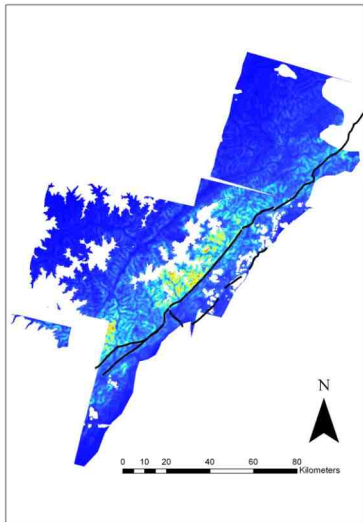
8: FD SL LCEL R



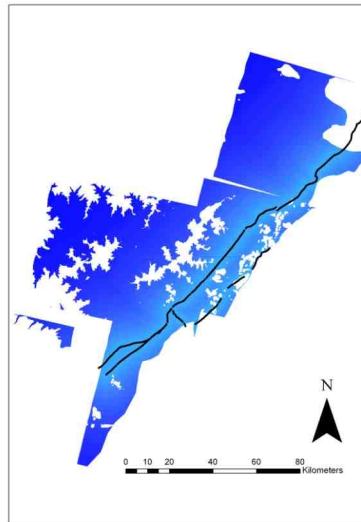
9: FD LCEL R



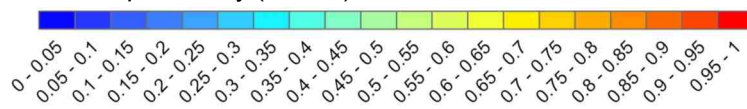
10: FD R



11: FD



Landslide probability (LS = 1)



Appendix 1 continued.

References

- ABRAHAMSON, N. A. & SOMERVILLE, P. G. (1996) Effects of the hanging wall and foot wall on ground motions recorded during the Northridge earthquake. *Bulletin of the Seismological Society of America*, 86, S93-S99.
- AGRESTI, A. (2007) *An Introduction to Categorical Data Analysis*, New Jersey, John Wiley & Sons.
- AKI, K. & RICHARDS, P. G. (1980) *Quantitative Seismology*, San Francisco, W. H. Freeman and Company.
- ALEXANDER, D. (2005) *Natural Disasters*, London, UCL Press Limited.
- AMBRASEYS, N. N. & DOUGLAS, J. (2003) Near-field horizontal and vertical earthquake ground motions. *Soil Dynamics and Earthquake Engineering*, 23, 1-18.
- ANTONINI, G., ARDIZZONE, F., CACCIANO, M., CARDINALI, M., CASTELLANI, M., GALLI, M., GUZZETTI, F., REICHENBACH, P. & SALVATI, P. (2002) Rapporto Conclusivo Protocollo d'Intesa fra la Regione dell'Umbria, Direzione Politiche Territoriali Ambiente e Infrastrutture, ed il CNR-IRPI di Perugia per l'acquisizione di nuove informazioni sui fenomeni franosi nella regione dell'Umbria, la realizzazione di una nuova carta inventario dei movimenti franosi e dei siti colpiti da dissesto, l'individuazione e la perimetrazione delle aree a rischio la frana di particolare rilevanza, e l'aggiornamento delle stime sull'incidenza dei fenomeni di dissesto sul tessuto insediativo, infrastrutturale e produttivo regionale. Unpublished report.
- ANTONINI, G., CARDINALI, M., GUZZETTI, F., REICHENBACH, P. & SORRENTINO, A. (1993) Carta Inventario dei Fenomeni Franosi della Regione Marche ed aree limitrofe. CNR Gruppo Nazionale per la Difesa dalle Catastrofi Idrogeologiche.
- ARGAND, E. & SERVICE GÉOLOGIQUE DE, B. (1928) *Carte tectonique de l'Eurasie*, Congrès géologique internationale.
- ARIAS, A. (1970) Measure of earthquake intensity. IN HANSEN, R. J. (Ed.) *Seismic Design for Nuclear Power Plants*. Cambridge, Mass, Massachusetts Inst. of Tech. Press.

References

- ARMIJO, R., TAPPONNIER, P., MERCIER, J. L. & TONGLIN, H. (1986) Quaternary extension in Southern Tibet. *Journal of Geophysical Research*, 91, 13803-13872.
- ARMIJO, R., TAPPONNIER, P. & TONGLIN, H. (1989) Late Cenozoic right-lateral strike-slip faulting in Southern Tibet. *Journal of Geophysical Research*, 94, 2787-2838.
- AVOUAC, J. P. & TAPPONNIER, P. (1993) Kinematic model of active deformation in central Asia. *Geophysical Research Letters*, 20, 895-898.
- AVOUAC, J. P. & TAPPONNIER, P. (1993) Kinematic model of active deformation in central Asia. *Geophysical Research Letters*, 20, 895-898.
- AYALEW, L. & YAMAGISHI, H. (2005) The application of GIS-based logistic regression for landslide susceptibility mapping in the Kakuda-Yahiko Mountains, Central Japan. *Geomorphology*, 65, 15-31.
- BAEZA, C. & COROMINAS, J. (2001) Assessment of shallow landslide susceptibility by means of multivariate statistical techniques. *Earth Surface Processes and Landforms*, 26, 1251-1263.
- BANERJEE, P. & BURGMANN, R. (2002) Convergence across the northwest Himalaya from GPS measurements. *Geophysical Research Letters*, 29.
- BARLOW, J., FRANKLIN, S. & MARTIN, Y. (2006) High spatial resolution satellite imagery, DEM derivatives, and image segmentation for the detection of mass wasting processes. *American Society for Photogrammetry and Remote Sensing*, 72, 687-692.
- BARLOW, J., MARTIN, Y. & FRANKLIN, S. E. (2003) Detecting translational landslide scars using segmentation of Landsat ETM+ and DEM data in the northern Cascade Mountains, British Columbia. *Canadian Journal of Remote Sensing*, 29, 510-517.
- BARNARD, P. L., OWEN, L. A., SHARMA, M. C. & FINKEL, R. C. (2001) Natural and human-induced landsliding in the Garwhal Himalaya of northern India. *Geomorphology* 40, 21-35.

References

- BARREDO, J. I., BENAVIDES, A. & VAN WESTEN, C. J. (2000) Comparing heuristic landslide hazard assessment techniques using GIS in the Tirajana Basin, Gran Canaria Island, Spain. *International Journal of Applied Earth Observation and Geoinformation*, 2, 9-23.
- BENITES, R. A. & HAINES, A. J. (1994) Quantification of seismic wavefield amplification by topographic features. *Research Report to the Earthquake Commission*. New Zealand.
- BIENIAWSKI, Z. T. & VANHEERDEN, W. L. (1975) Significance of Insitu Tests on Large Rock Specimens. *International Journal of Rock Mechanics and Mining Sciences*, 12, 101-113.
- BIRD, P. (1991) Lateral extrusion of lower crust from under high topography, in the isostatic limit. *Journal of Geophysical Research*, 96, 10275-10286.
- BOLT, B. A. (1999) *Earthquakes*, New York, W. H. Freeman.
- BOMMER, J., DOUGLAS, J. & STRASSER, F. (2003) Style-of-Faulting in Ground-Motion Prediction Equations. *Bulletin of Earthquake Engineering*, 1, 171-203.
- BORGHUIS, A. M., CHANG, K. & LEE, H. Y. (2007) Comparison between automated and manual mapping of typhoon-triggered landslides from SPOT-5 imagery. *International Journal of Remote Sensing*, 28, 1843-1856.
- BOUCHON, M. & BAKER, J. (1996) Seismic response of a hill: the example of Tarzana, California. *Bull. Seismol. Soc. Am.*, 86, 66–72.
- BRABB, E. E. (1993) Proposal for worldwide landslide hazard maps. IN NOVOSAD, S. & WAGNER, P. (Eds.) *Proceedings of 7th International Conference and Workshop on Landslides*. Balkema, Rotterdam.
- BRUNE, J. N. (2001) Shattered rock and precarious rock evidence for strong asymmetry in ground motions during thrust faulting. *Bull. Seismol. Soc. Am.*, 91, 441–447.
- BRUNSDEN, D. (1984) Mudslides. IN BRUNSDEN, D. & PRIOR, D. B. (Eds.) *Slope Instability* Chichester, Wiley.

References

- BUCKNAM, R. C., COE, J. A., CHAVARRIA, M. M., GODT, J. W., TARR, A. C., BRADLEY, L. A., RAFFERTY, S., HANCOCK, D., DART, R. L. & JOHNSON, M. L. (2001) Landslides triggered by hurricane Mitch in Guatemala - inventory and discussion. U.S. Geological Survey Open File Report.
- BURBANK, D. W., LELAND, J., FIELDING, E., ANDERSON, R. S., BROZOVIC, N., REID, M. R. & DUNCAN, C. (1996) Bedrock incision, rock uplift and threshold hillslopes in the northwestern Himalayas. *Nature Geoscience*, 379, 505-510.
- BURCHFIEL, B. C. (2003) Presidential address: New technology, new geological challenges. *GSA Today*, 14, 4-9.
- BURCHFIEL, B. C., ROYDEN, L. H., HILST, R. D. V. D. & HAGER, B. H. (2008) A geological and geophysical context for the Wenchuan earthquake of 12 May 2008, Sichuan, People's Republic of China. *GSA Today*, 18, 4-11.
- CALTECH (2009) The science behind China's Sichuan earthquake. <http://www.tectonics.caltech.edu/outreach/highlights/2008MayChinaEQ/> - accessed 11/11/2008. Tectonics Observatory: California Institute of Technology.
- CAMPBELL, K. W. (1981) Near-source attenuation of peak horizontal acceleration. *Seismological Society of America*, 71, 2039-2070.
- CAMPBELL, K. W. & BOZORGNIA, Y. (1994) Near-source attenuation of peak horizontal acceleration from worldwide accelerograms recorded from 1957 to 1993. *Proceedings of the Fifth US National Conference on Earthquake Engineering*. Chicago.
- CARDINALI, M., ANTONINI, G., REICHENBACH, P. & GUZZETTI, F. (2001) Photo-geological and landslide inventory map for the Upper Tiber River basin. CNR Gruppo Nazionale per la Difesa dalle Catastrofi Idrogeologiche.
- CARDINALI, M., ARDIZZONE, F., GALLI, M., GUZZETTI, F. & REICHENBACH, P. (2000) Landslides triggered by rapid snow melting: the December 1996-January 1997 event in Central Italy. *Proceedings of the 1st Plinius Conference*. Maratea, Bios, Cosenza.

References

- CARDINALI, M., GUZZETTI, F. & BRABB, E. E. (1990) Preliminary map showing landslide deposits and related features in New Mexico. U. S. Geological Survey Open File Report.
- CARRARA, A. (1983) Multivariate models for landslide hazard evaluation. *Mathematical Geology*, 15, 403-426.
- CARRARA, A. & MERENDA, L. (1976) Landslide inventory in northern Calabria, southern Italy. *Geological Society of America Bulletin*, 87, 1153-1162.
- CARSON, M. A. & KIRBY, M. J. (1972) *Hillslope form and process*, Cambridge, Cambridge University Press.
- CEGRP (2008) China Earthquake Geospatial Research Portal. <http://cegrp.cga.harvard.edu/> - accessed 10/10/2009.
- CHANG, J. C. & SLAYMAKER, O. (2002) Frequency and spatial distribution of landslides in a mountainous drainage basin: Western Foothills, Taiwan. *Catena*, 46, 285-307.
- CHANG, K. T., CHIANG, S. H. & HSU, M. L. (2007) Modelling typhoon- and earthquake-induced landslides in a mountainous watershed using logistic regression. *Geomorphology*, 89, 335-347.
- CHEN, Q., FREYMUELLER, J. T., WANG, Q., YANG, Z., XU, C. & LIU, J. (2004) A deforming block model for the present-day tectonics of Tibet. *J. Geophys. Res.*, 109.
- CHEN, S. F. & WILSON, C. J. L. (1996) Emplacement of the Longmen Shan Thrust-Nappe Belt along the eastern margin of the Tibetan Plateau. *Journal of Structural Geology*, 18, 413-430.
- CHEN, Z., BURCHFIEL, B. C., LIU, Y., KING, R. W., ROYDEN, L. H., TANG, W., WANG, E., ZHAO, J. & ZHANG, X. (2000) Global Positioning System measurements from eastern Tibet and their implications for India/Eurasia intercontinental deformation. *J. Geophys. Res.*, 105, 16215–16227.
- CHENG, G. W., WANG, X. D., HE, X. B., FAN, J. H. & FAN, J. R. (2008) Outburst risk of barrier lakes in Sichuan, China. *Journal of Mountain Science*, 5, 189-193.

References

- CHUNG, C. J. & FABBRI, A. G. (2005) Systematic procedures of landslide hazard mapping for risk assessment using spatial prediction models. IN GLADE (Ed.) *Landslide Risk Assessment*. New York, Wiley.
- CLARK, M. K., HOUSE, M. A., ROYDEN, L. H., WHIPPLE, B. C., BURCHFIEL, B. C., ZHANG, X. & TANG, W. (2005) Late Cenozoic uplift of southeastern Tibet. *Geology*, 33, 525-528.
- CLARK, M. K. & ROYDEN, L. H. (2000) Topographic ooze: Building the eastern margin of Tibet by lower crustal flow. *Geology*, 28, 703-706.
- CLARK, M. K., ROYDEN, L. H., WHIPPLE, B. C., BURCHFIEL, B. C., ZHANG, X. & TANG, W. (2006) Use of a regional, relict landscape to measure vertical deformation of the eastern Tibetan Plateau. *Journal of Geophysical Research*, 111, F03002.
- CLARK, W. A. & HOSKING, P. L. (1986) *Statistical Methods for Geographers*, New York, John Wiley and Sons.
- COMPANY, S. R. (2000) Natural catastrophes and man-made disasters in 1999. *Economic Research and Consulting*. Zurich.
- COX, N. J. (2004) Speaking Stata: Graphing distributions. *Stata Journal*, 4, 66-88.
- COX, N. J. (2009) Per coms.
- CUI, P., ZHU, Y. Y., HAN, Y. S., CHEN, X. Q. & ZHUANG, J. Q. (2009) The 12 May Wenchuan earthquake-induced landslide lakes: distribution and preliminary risk evaluation. *Landslides*, 6, 209-223.
- DADSON, S. J., HOVIUS, N., CHEN, H., DADE, W. B., LIN, J. C., HSU, M. L., LIN, C. W., HORNG, M. J., CHEN, T. C., MILLIMAN, J. & STARK, C. P. (2004) Earthquake-triggered increase in sediment delivery from an active mountain belt. *Geology*, 32, 733-736.
- DADSON, S. J., HOVIUS, N., CHEN, H. G., DADE, W. B., HSIEH, M. L., WILLETT, S. D., HU, J. C., HORNG, M. J., CHEN, M. C., STARK, C. P., LAGUE, D. & LIN, J. C. (2003) Links between erosion, runoff variability and seismicity in the Taiwan orogen. *Nature*, 426, 648-651.

References

- DAI, F. C. & LEE, C. F. (2003) A spatiotemporal probabilistic modelling of storm-induced shallow landsliding using aerial photographs and logistic regression. *Earth Surface Processes and Landforms*, 28, 527-545.
- DAVIS, L. L. & WEST, L. R. (1973) Observed effects of topography on ground motion. *Bull. Seismol. Soc. Am.*, 63, 283–298.
- DENSMORE, A. L. (2009) Per cons. Durham University.
- DENSMORE, A. L., ELLIS, M. A., LI, Y., ZHOU, R. J., HANCOCK, G. S. & RICHARDSON, N. (2007) Active tectonics of the Beichuan and Pengguan faults at the eastern margin of the Tibetan Plateau. *Tectonics*, 26, 1-17.
- DENSMORE, A. L. & HOVIUS, N. (2000) Topographic fingerprints of bedrock landslides. *Geology*, 28, 371-374.
- DENSMORE, A. L., YONG, L., RICHARDSON, N. J., RONGJUN, Z., ELLIS, M. & YI, Z. (in review) The role of late Quaternary upper-crustal faults in the 12 May 2008 Wenchuan earthquake. *Bulletin of the Seismological Society of America*.
- DEWEY, J. F., SHACKLETON, R. M., CHEGNEA, C. & YIYIN, S. (1988) The Tectonic Evolution of the Tibetan Plateau. *Philosophical Transactions of the Royal Society London*, 327, 379-413.
- DOUGLAS, J. (2002) Note on scaling of peak ground acceleration and peak ground velocity with magnitude. *Geophysical Journal International*, 148, 336-339.
- DRURY, S. A. (1987) *Image Interpretation in Geology*, London, Allen & Unwin.
- ENGLAND, P. & MOLNAR, P. (1990) Right-lateral shear and rotation as the explanation for strike-slip faulting in eastern Tibet. *Nature* 344, 140 - 142.
- FARINA, P., COLOMBO, D., FUMAGALLI, A., MARKS, F. & MORETTI, S. (2006) Permanent scatterers for landslide investigations: outcomes from the ESA-SLAM project. *Engineering Geology*, 88, 200-217.
- FRUNEAU, B., ACHACHE, J. & DELACOURT, C. (1996) Observation and modelling of the Saint-Etienne-de-Tinée landslide using SAR interferometry. *Tectonophysics*, 265, 181-190.

References

- GALLI, M., ARDIZZONE, F., CARDINALI, M., GUZZETTI, F. & REICHENBACH, P. (2009) Comparing landslide inventory maps. *Geomorphology*, 94, 268-289.
- GAN, W., ZHANG, P., SHEN, Z.-K., NIU, Z., WANG, M., WAN, Y., ZHOU, D. & CHENG, J. (2007) Present-day crustal motion within the Tibetan Plateau inferred from GPS measurements. *J. Geophys. Res.*, 112, B08416.
- GARCIA-RODRIGUEZ, M. J., MALPICA, J. A., BENITO, B. & DIAZ, M. (2008) Susceptibility assessment of earthquake-triggered landslides in El Salvador using logistic regression. *Geomorphology*, 95, 172-191.
- GELI, L., BARD, P.-Y. & JULLIEN, B. (1988) The effect of topography on earthquake ground motion: a review and new results. *Bull. Seismol. Soc. Am.*, 78, 42-63.
- GODT, J., SENER, B., VERDIN, K., WALD, D., EARLE, P., HARP, E. & JIBSON, R. (2009) Rapid assessment of earthquake-induced landsliding. *Proceedings of the World Landslide Forum, 2008*. Tokyo, Japan.
- GORSEVSKI, P. V., GESSLER, P. E., FOLTZ, R. B. & ELLIOT, W. J. (2006) Spatial Prediction of Landslide Hazard Using Logistic Regression and ROC Analysis. *Transactions in GIS*, 10, 395-415.
- GUZZETTI, F., ARDIZZONE, F., CARDINALI, M., ROSSI, M. & VALIGI, D. (2009) Landslide volumes and landslide mobilization rates in Umbria, central Italy. *Earth and Planetary Science Letters*, 279, 222-229.
- GUZZETTI, F., GALLI, M., REICHENBACH, P., ARDIZZONE, F. & CARDINALI, M. (2006) Landslide hazard assessment in the Collazzone area, Umbria, Central Italy. *Natural Hazards and Earth System Sciences*, 6, 115-131.
- HALES, T. C. & ROERING, J. J. (2007) Climatic controls on Frost Cracking and Implications for the Evolution of Bedrock Landscapes. *Journal of Geophysical Research*, 112, F02033.1-F02033.
- HANCOX, G. T., MCSAVENEY, M. J., MANVILLE, V. R. & DAVIES, T. R. (2005) The October 1999 Mt Adams rock avalanche and subsequent landslide dam-break

References

- flood and effects in Poerua River, Westland, New Zealand. *New Zealand Journal of Geology and Geophysics*, 48, 683-705.
- HAO, K. X., SI, H., FUJIWARA, H. & OZAWA, T. (2009) Co-seismic surface-ruptures and crustal deformations of the 2008 Wenchuan earthquake Mw7.9, China. *Geophys. Res. Lett.*, 36, L11303.
- HARP, E. L. & JIBSON, R. L. (1995) Inventory of Landslides Triggered by the 1994 Northridge, California Earthquake. USGS: Open File Report.
- HARP, E. L. & JIBSON, R. W. (1996) Landslides triggered by the 1994 Northridge, California, earthquake. *Bulletin of the Seismological Society of America*, 86, S319-S332.
- HARP, E. L. & JIBSON, R. W. (2002) Anomalous Concentrations of Seismically Triggered Rock Falls in Pacoima Canyon: Are They Caused by Highly Susceptible Slopes or Local Amplification of Seismic Shaking? *Bulletin of the Seismological Society of America*, 92, 3180-3189.
- HAVENITH, H. B., JONGMANS, D., FACCIOLI, E., ABDRAKHMATOV, K. & BARD, P. Y. (2002) Site effect analysis around the seismically induced Ananevo, Rockslide, Kyrgyzstan. *Bulletin of the Seismological Society of America*, 92, 3190-3209.
- HERVAS, J., BARREDO, J. I., ROSIN, P. L., PASUTO, A., MANTOVANI, F. & SILVANO, S. (2003) Monitoring landslides from optical remotely sensed imagery: the case history of Tessina landslide, Italy. *Geomorphology*, 54, 63-75.
- HERVAS, J. & BOBROWSKY, P. (2009) Mapping: Inventories, Susceptibility, Hazard and Risk. IN SASSA, K. & CANUTI, P. (Eds.) *Landslides - Disaster Risk Reduction*. Berlin, Springer.
- HILTON, R. G., GALY, A. & HOVIUS, N. (2008a) Riverine particulate organic carbon from an active mountain belt: The importance of landslides. *Global Biogeochemical Cycles*, 22, GB1017.

References

- HILTON, R. G., GALY, A., HOVIUS, N., CHEN, M.-C., HORNG, M.-J. & CHEN, H. (2008b) Tropical-cyclone-driven erosion of the terrestrial biosphere from mountains. *Nature Geoscience*, 1, 759-762.
- HONG, Y. & ADLER, R. F. (2007) Towards an early-warning system for global landslides triggered by rainfall and earthquake. *International Journal of Remote Sensing*, 28, 3713-3719.
- HOVIUS, N., STARK, C. P. & ALLEN, P. A. (1997) Sediment flux from a mountain belt derived by landslide mapping. *Geology*, 25, 231-234.
- HOVIUS, N., STARK, C. P., CHU, H. T. & LIN, J. C. (2000) Supply and removal of sediment in a landslide-dominated mountain belt: Central Range, Taiwan. *Journal of Geology*, 108, 73-89.
- HUANG, R. & LI, W. (in press) An analysis of the co-seismic fault effects of the geo-hazards triggered by Wenchuan earthquake, China. *Science in China Series E: Technological Sciences*.
- HUANG, R. & LI, W. (2009a) Development and distribution of geohazards triggered by the 5.12 Wenchuan Earthquake in China *Science in China Series E: Technological Sciences*, 52, 810-819.
- HUANG, R. Q. & LI, W. L. (2009b) Analysis of the geo-hazards triggered by the 12 May 2008 Wenchuan Earthquake, China. *Bulletin of Engineering Geology and the Environment*, 68, 363-371.
- HUBBARD, J. & SHAW, J. H. (2009) Uplift of the Longmen Shan and Tibetan plateau, and the 2008 Wenchuan (M = 7.9) earthquake. *Nature*, 458, 194-197.
- HUTCHINSON, J. N. (1968) Mass movement. IN FAIRBRIDGE, R. W. (Ed.) *The Encyclopedia of Geomorphology*. Reinhold Book Corporation.
- IVERSON, R. M. (2000) Landslide triggering by rain infiltration. *Water Resour. Res.*, 36, 1897–1910.
- JI, C. & HAYES, G. (2008) Finite Fault Model: Preliminary Result of the May 12, 2008 Mw 7.9 Eastern Sichuan, China Earthquake USGS Report.

References

- JIBSON, R. W., HARP, E. L., SCHULZ, W. & KEEFER, D. K. (2004) Landslides triggered by the 2002 Denali fault, Alaska, earthquake and the inferred nature of the strong shaling. *Earthquake Spectra*, 20, 669-691.
- JIBSON, R. W., PRENTICE, C. S., BORISSOFF, B. A., ROGOZHIN, E. A. & LANGER, C. J. (1994) Some Observations of Landslides Triggered by the 29-April-1991 Racha Earthquake, Republic-of-Georgia. *Bulletin of the Seismological Society of America*, 84, 963-973.
- JONES, L. M., HAN, W., ZHANG, Y., LUO, Z. & HAUKSSON, E. (1984) Focal mechanisms and aftershock locations of the songpan earthquakes of August 1976 in Sichuan, China. *J. Geophys. Res.*, 89, 7697-7708.
- KEEFER, D. K. (1984) Landslides Caused by Earthquakes. *Geological Society of America Bulletin*, 95, 406-421.
- KEEFER, D. K. (1994) The Importance of Earthquake-Induced Landslides to Long-Term Slope Erosion and Slope-Failure Hazards in Seismically Active Regions. *Geomorphology*, 10, 265-284.
- KEEFER, D. K. (2000) Statistical analysis of an earthquake-induced landslide distribution - the 1989 Loma Prieta, California event. *Engineering Geology*, 58, 231-249.
- KEEFER, D. K. (2002) Investigating landslides caused by earthquakes - A historical review. *Surveys in Geophysics*, 23, 473-510.
- KEEFER, D. K. (2009) Earthquake-triggered landslides, 20 years later. *The next generation of research on earthquake-induced landslides: An international conference in commemoration of the 10th Anniversary of the Chi-Chi Earthquake*. Taipei.
- KELSEY, H. M. (1988) Formation of inner gorges. *Catena* 15, 433-458.
- KHAZAI, B. & SITAR, N. (2004) Evaluation of factors controlling earthquake-induced landslides caused by Chi-Chi earthquake and comparison with the Northridge and Loma Prieta events. *Engineering Geology*, 71, 79-95.

References

- KINCAL, C., AKGUN, A. & KOCA, M. (2009) Landslide susceptibility assessment in the İzmir (West Anatolia, Turkey) city center and its near vicinity by the logistic regression method. *Environmental Earth Sciences*, 59, 745-756.
- KING, R. W., SHEN, F., BURCHFIEL, B. C., ROYDEN, L. H., WANG, E., CHEN, Z., LIU, Y., ZHANG, X. Y., ZHAO, J. X. & LI, Y. (1997) Geodetic measurement of crustal motion in southwest China. *Geology*, 25, 179-182.
- KIRBY, E. P., REINERS, P. W., KROL, M. A., WHIPPLE, K. X., HODGES, K. V., FARLEY, K. A., TANG, W. & CHEN, Z. (2002) Late Cenozoic evolution of the eastern margin of the Tibetan Plateau: Inferences from $^{40}\text{Ar}/^{39}\text{Ar}$ and (U-Th)He thermochronology. *Tectonics*, 21, 1001.
- LEBEDEV, S. & NOLET, G. (2003) Upper mantle beneath Southeast Asia from S velocity tomography. *Journal of Geophysical Research*, 108, 2048.
- LEE, C. T., HUANG, C. C., LEE, J. F., PAN, K. L., LIN, M. L. & DONG, J. J. (2008) Statistical approach to earthquake-induced landslide susceptibility. *Engineering Geology*, 100, 43-58.
- LEE, W. H. K., SHIN, T. C., KUO, K. W., CHEN, K. C. & WU, C. F. (2001) CWB free-field strong motion data from the 21 September Chi-Chi earthquake. *Bull. Seismol. Soc. Am.*, 91, 1370- 1376.
- LEICA-GEOSYSTEMS (2002) *ERDAS Field Guide*, Atlanta, Leica Geosystems.
- LI, X. & HE, S. (2009) Seismically Induced Slope Instabilities and the Corresponding Treatments: the Case of a Road in the Wenchuan Earthquake Hit Region. *Journal of Mountain Science*, 6, 96-100.
- LI, X., ZHOU, Z., YU, H., WEN, R., LU, D., HUANG, M., ZHOU, Y. & CU, J. (2008) Strong motion observations and recordings from the great Wenchuan Earthquake. *Earthquake Engineering and Engineering Vibration*, 7, 235-246.
- LI, X. H., LI, Z. X., LI, W. X. & WANG, Y. (2006) Initiation of the Indosinian Orogeny in South China: Evidence for a Permian Magmatic Arc on Hainan Island. *The Journal of Geology*, 114, 341-353.

References

- LI, Y., P. A. ALLEN, A. L. DENSMORE & QIANG, X. (2003) Evolution of the Longmen Shan Foreland Basin (western Sichuan, China) during the Late Triassic Indosinian Orogeny. *Basin Research*, 15, 117 - 138.
- LI, Y. X., ZHANG, J. H., ZHOU, W., HU, X. K., GUO, L. Q. & ZHANG, Z. F. (2009) The mechanism and dynamics of the generation and occurrence for Wenchuan M(S)8.0 earthquake. *Chinese Journal of Geophysics-Chinese Edition*, 52, 519-530.
- LILLESAND, T. M., KIEFER, R. W. & CHIPMAN, J. W. (2004) *Remote Sensing and Image Interpretation*, New York, John Wiley & Sons.
- LIN, G. W., CHEN, H., HOVIUS, N., HORNG, M. J., DADSON, S., MEUNIER, P. & LINES, M. (2008) Effects of earthquake and cyclone sequencing on landsliding and fluvial sediment transfer in a mountain catchment. *Earth Surface Processes and Landforms*, 33, 1354-1373.
- LIN, J.-C., PETLEY, D., JEN, C.-H., KOH, A. & HSU, M.-L. (2006) Slope movements in a dynamic environment-A case study of Tachia River, Central Taiwan. *Quaternary International*, 147, 103-112.
- LIN, M. L., WANG, K. L. & CHEN, T. C. (2000) Characteristics of the slope failure caused by Chi-Chi earthquake. IN LOH, C. H. & LIAO, W. I. (Eds.) *International Workshop on Annual Commemoration of Chi-Chi Earthquake (III)*. Taipei, National Centre for Research on Earthquake Engineering.
- LIU, J. & WOING, T. (1999) A practical approach to creating a landslide database using Taiwan SPOT mosaic. *Proceedings of the 20th Asia Conference on Remote Sensing*. Hong Kong, China.
- LIU, J. K., WONG, C. C., HUANG, J. J. & YANG, M. J. (2002) Landslide enhancement images for the study of torrential rainfall landslides. *Proceeding of the 23rd Asian conference on Remote Sensing*. Kathmandu.
- LIU, N., ZHANG, J., LIN, W., CHENG, W. & CHEN, Z. (2009) Draining Tangjiashan Barrier Lake after Wenchuan Earthquake and the flood propagation after the dam break *Science in China Series E: Technological Sciences* 52, 801-809.

References

- LIU, X., FU, D. R., YAO, P. Y., LIU, G. F. & WANG, N. W. (1992) *The Stratigraphy, Palaeobiogeography and Sedimentary-Tectonic Development of Qinghai-Xizang (Tibet) Plateau in Light of Terrane Analysis*, Beijing, Geological Publishing House.
- LIU-ZENG, J., ZHANG, Z., WEN, L., TAPPONNIER, P., SUN, J., XING, X., HU, G., XU, Q., ZENG, L., DING, L., JI, C., HUDNUT, K. & WOERD, J. V. D. (2009) Co-seismic ruptures of the 12 May, 2008, Ms 8.0 Wenchuan earthquake, Sichuan: EW crustal shortening on oblique, parallel thrusts along the eastern edge of Tibet. *Earth and Planetary Science Letters*.
- LONG, J. S. (1997) *Regression Models for Categorical and Limited Dependent Variables (Advanced Quantitative Techniques in the Social Sciences)*, London, Sage publications.
- LUO, Z. L. & LONG, X. M. (1992) The uplifting of the Longmenshan orogenic zone and the subsidence of the West Sichuan Foreland Basin. *Acta geologica*, 12, 1-17.
- MA, L. (2002) *Geological Atlas of China*, Beijing, Geological Publishing House.
- MALAMUD, B. D., TURCOTTE, D. L., GUZZETTI, F. & REICHENBACH, P. (2004) Landslide inventories and their statistical properties. *Earth Surface Processes and Landforms*, 29, 687-711.
- MARCELINO, E. V., FONSECA, L. M. G., VENTURA, F. & ROSA, A. N. C. S. (2003) Evaluation of IHS and wavelet transform fusion techniques for the identification of landslide scars using satellite data. *Proceedings of the Anais XI SBSR Symposium*. Belo Horizonte.
- MARGARIS, B. N. & PAPAACHOS, C. B. (1999) Moment-magnitude relations based on strong-motion records in Greece. *Bulletin of the Seismological Society of America*, 89, 442-455.
- MCFADDEN, L. D., EPPES, M. C., GILLESPIE, A. R. & HALLET, B. (2005) Physical weathering in arid landscapes due to diurnal variation in the direction of solar heating. *Bull. Geol. Soc. Am.*, 117, 161-173.

References

- MCKEAN, J. & ROERING, J. (2004) Objective landslide detection and surface morphology mapping using high resolution airborne laser altimetry. *Geomorphology*, 57, 331-351.
- MEADE, B. J. (2007) Present-day kinematics at the India-Asia collision zone. *Geology*, 35, 81-84.
- METTERNICHT, G., HURNI, L. & GOGU, R. (2005) Remote sensing of landslides: An analysis of the potential contribution to geo-spatial systems for hazard assessment in mountainous environments. *Remote Sensing of Environment*, 98, 284-303.
- MEUNIER, P., HOVIUS, N. & HAINES, J. (2007) Regional patterns of earthquake-triggered landslides and their relation to ground motion. *Geophysical Research Letters*, 34, L20408.
- MEUNIER, P., HOVIUS, N. & HAINES, J. A. (2008) Topographic site effects and the location of earthquake induced landslides. *Earth and Planetary Science Letters*, 275, 221-232.
- MOLNAR, P. & ENGLAND, P. (1990) Late Cenozoic uplift of mountain ranges and global climate change: chicken or egg? *Nature*, 346, 29-34.
- MONTGOMERY, D. R. (2001) Slope distributions, threshold hillslopes, and steady-state topography. *Am. J. Sci.*, 301, 432-454.
- MOORE, I. D., GRAYSON, R. B. & LADSON, A. R. (1991) Digital terrain modelling: A review of hydrological, geomorphological, and biological applications. *Hydrological Processes*, 5, 3-30.
- MURPHY, W. (2002) The role of topographic amplification on the initiation of rock slopes failures during earthquakes. IN EVANS, S. G., MUGNOZZA, G. S., STROM, A. & HERMANN, R. L. (Eds.) *NATO Advanced Research Workshop on Massive Rock Slope Failure - New Models for Hazard Assessment*. Celano, ITALY.
- NEWMARK, N. M. (1965) Effects of earthquakes on dams and embankments. *Geotechnique*, 15, 139- 160.

References

- NICHOL, J. & WONG, M. S. (2005) Satellite remote sensing for detailed landslide inventories using change detection and image fusion. *International Journal of Remote Sensing*, 26, 1913-1926.
- NISHIMURA, N. & YAGI, Y. (2008) Rupture Process for May 12, 2008 Sichuan Earthquake (Ver. 2). <http://www.geol.tsukuba.ac.jp/~nisimura/20080512/> - accessed 12/04/2009. University of Tsukuba.
- OLDHAM, R. D. (1899) Report on the great earthquake of 12 June 1897. *Memoirs of the Geological Society of India*, 29, 379.
- OUIMET, W. (2007) Dissecting the eastern margin of the Tibetan Plateau: A study of landslides, erosion and river incision in a transient landscape [PhD Thesis]. Cambridge, Massachusetts Institute of Technology.
- OWEN, L. A., KAMP, U., KHATTAK, G. A., HARP, E. L., KEEFER, D. K. & BAUER, M. A. (2008) Landslides triggered by the 8 October 2005 Kashmir earthquake. *Geomorphology*, 94, 1-9.
- OWEN, L. A., SHARMA, M. & BIGWOOD, R. (1996) Landscape modification and geomorphological consequences of the 20 October 1991 earthquake and the July-August 1992 monsoon in the Garhwal Himalaya. *Zeitschrift für Geomorphologie* 103, 359-372.
- PARISE, M. & JIBSON, R. W. (2000) A seismic landslide susceptibility rating of geologic units based on analysis of characteristics of landslides triggered by the 17 January, 1994 Northridge, California earthquake. *Engineering Geology*, 58, 251-270.
- PARKER, R. N., ROSSER, N., DENSMORE, A. & PETLEY, D. (2009) Automated Landslide Detection Algorithms to Investigate Controls on the Spatial Distribution of Landslides Triggered by the Wenchuan Earthquake, Sichuan Province, China. *Proceedings of The Next Generation of Research on Earthquake-induced Landslides: An International Conference in Commemoration of 10th Anniversary of the Chi-Chi Earthquake*. Taipei.
- PARKER, R. N., ROSSER, N., DENSMORE, A. & PETLEY, D. (2009) Investigating controls on the spatial distribution of landslides triggered by the

References

- Wenchuan Earthquake, Sichuan Province, China. *Proceedings of Annual General Conference of the Remote Sensing and Photogrammetry Society*. Leicester, UK.
- PARUELO, J., GARBULSKY, M., GUERSCHMAN, J., JOBB, AACUTE & GY, E. (2004) Two decades of Normalized Difference Vegetation Index changes in South America: identifying the imprint of global change. *International Journal of Remote Sensing*, 25, 2793-2806.
- PATERSON, E., RE, D. D. & WANG, Z. (2008) The 2008 Wenchuan Earthquake: Risk Management Lessons and Implications. Risk Management Solutions (RMS).
- PAUL, J., BURGMANN, R., GAUR, V. K., BILHAM, R., LARSON, K. M., ANANDA, M. B., JADE, S., MUKAL, M., ANUPAMA, T. S., SATYAL, G. & KUMAR, D. (2001) The Motion and Active Deformation of India. *Geophys. Res. Lett.*, 28, 647–650.
- PETLEY, D. N. (2009) Per coms. Durham University.
- PETLEY, D. N., CRICK, W. D. O. & HART, A. B. (2002) The use of satellite imagery in landslide studies in high mountain areas. *Proceedings of the 23rd Asian Conference on Remote Sensing*. Kathmandu.
- PETLEY, D. N., DUNNING, S. A. & ROSSER, N. J. (2005) The analysis of global landslide risk through the creation of a database of worldwide landslide fatalities. IN HUNGR, O., FELL, R., COUTURE, R. & EBERHARDT, E. (Eds.) *Landslide Risk Management*. Amsterdam, A.T. Balkema.
- PETLEY, D. N., PETLEY, D. J. & ALLISON, R. J. (2008) Temporal Prediction in Landslides - understanding the Saito effect. *10th International Symposium on Landslides and Engineered Slopes*. Xi'an, China.
- RODRIGUEZ, C. E., BOMMER, J. J. & CHANDLER, R. J. (1999) Earthquake-induced landslides: 1980-1997. *Soil Dynamics and Earthquake Engineering*, 18, 325-346.
- ROWLEY, D. B. & CURRIE, B. S. (2006) Palaeo-altimetry of the late Eocene to Miocene Lunpola basin, central Tibet. *Nature*, 439, 677-681.
- SANTACANA, N., BAEZA, B., COROMINAS, J., DE PAZ, A. & MARTURIA, J. (2003) A GIS-based multivariate statistical analysis for shallow landslide

References

- susceptibility mapping in La Pobla de Lillet area (Eastern Pyrenees, Spain). *Natural Hazards*, 30, 281–295.
- SATO, H. P. & HARP, E. L. (2009) Interpretation of earthquake-induced landslides triggered by the 12 May 2008, M7.9 Wenchuan earthquake in the Beichuan area, Sichuan Province, China using satellite imagery and Google Earth. *Landslides*, Online First.
- SATO, H. P., HASEGAWA, H., FUJIWARA, S., TOBITA, M., KOARAI, M., UNE, H. & IWAHASHI, J. (2007) Interpretation of landslide distribution triggered by the 2005 Northern Pakistan earthquake using SPOT 5 imagery. *Landslides*, 4, 113-122.
- SCHMIDT, K. M. & MONTGOMERY, D. R. (1995) Limits to Relief. *Science*, 270, 617-620.
- SELBY, M. J. (2005) *Hillslope materials and processes*, Oxford, UK, Oxford University Press.
- SEPULVEDA, S. A., MURPHY, W., JIBSON, R. W. & PETLEY, D. N. (2005a) Seismically induced rock slope failures resulting from topographic amplification of strong ground motions: The case of Pacoima Canyon California. *Engineering Geology*, 80, 336-348.
- SEPULVEDA, S. A., MURPHY, W. & PETLEY, D. N. (2005b) Topographic controls on co-seismic rock slides during the 1999 Chi-Chi earthquake, Taiwan. *Quarterly Journal of Engineering Geology and Hydrogeology*, 38, 189-196.
- SHABESTARI, K. T. & YAMAZAKI, F. (2003) Near-fault spatial variation in strong ground motion due to rupture directivity and hanging wall effects from the Chi-Chi, Taiwan earthquake. *Earthquake Engineering and Structural Dynamics*, 32, 2197-2220.
- SHEN, Z. K., SUN, J. B., ZHANG, P. Z., WAN, Y. G., WANG, M., BURGMANN, R., ZENG, Y. H., GAN, W. J., LIAO, H. & WANG, Q. L. (2009) Slip maxima at fault junctions and rupturing of barriers during the 2008 Wenchuan earthquake. *Nature Geoscience*, 2, 718-724.

References

- SHEN, Z.-K., ZHAO, C., YIN, A., LI, Y., JACKSON, D. D., FANG, P. & DONG, D. (2000) Contemporary crustal deformation in east Asia constrained by Global Positioning System measurements. *Journal of Geophysical Research*, 105, 5721–5734.
- SKEMPTON, A. W. & DELORY, F. A. (1957) Stability of natural slopes in London clay. *Proceedings 4th International Conference on Soil Mechanics and Foundation Engineering*. London.
- SOMERVILLE, P., SAIKIA, C., WALD, D. & GRAVES, R. (1996) Implications of the Northridge earthquake for strong ground motions from thrust faults. *Bulletin of the Seismological Society of America*, 86, S115-S125.
- SOMERVILLE, P. G. & GRAVES, R. W. (2003) Characterization of earthquake strong ground motion. *Pure and Applied Geophysics*, 160, 1811-1828.
- SPUDICH, P., HELLWEG, M. & LEE, W. H. K. (1996) Directional topographic site response at Tarzana observed in aftershocks of the 1994 Northridge, California, earthquake: implications for mainshock motions. *Bull. Seismol. Soc. Am.*, 86, 193-208.
- SSB (1989) Lithospheric dynamics atlas of China. *Editorial Board: State Seismological Bureau*. Beijing, China Cartographic Publishing House.
- STEPHENS, P. (2009) Per coms. Disaster Monitoring Constellation.
- STRAHLER, A. H., WOODCOCK, C. E. & SMITH, J. A. (1986) On the nature of models in remote sensing. *Remote Sensing of Environment* 20, 121-139.
- TAPPONNIER, P., ZHIQIN, X., ROGER, F., MEYER, B., ARNAUD, N., WITTLINGER, G. & JINGSUI, Y. (2001) Oblique Stepwise Rise and Growth of the Tibet Plateau. *Science*, 294, 1671-1677.
- TATARD, L. & GRASSO, J.-R. (2009) Cross analyses of space distributions for triggered landslide and triggered earthquakes. *Proceedings of The next generation of research on earthquake induced landslides: An international conference in commemoration of the 10th Anniversary of the Chi-Chi earthquake*. Taipei.

References

- TAYLOR, S. R., BONNER, B. P. & ZANDT, G. (1986) Attenuation and scattering of broadband P and S waves across North America. *J. Geophys. Res.*, 91, 7309-7325.
- TERZAGHI, K. & PECK, R. B. (1948) *Soil mechanics in engineering practice*, John Wiley and Sons.
- TRIFUNAC, M. D. (1994) Q and high-frequency strong motion spectra. *Soil Dynamics and Earthquake Engineering*, 13, 149-161.
- USGS (2008a) Preliminary earthquake report: Magnitude 7.9 - EASTERN SICHUAN, CHINA. <http://earthquake.usgs.gov/eqcenter/eqinthenews/2008/us2008ryan/> - accessed 10/10/2008.
- VARNES, D. J. (1978) Transportation Research Board Special Report: Slope movement types and processes. IN L., S. R. & J., K. R. (Eds.) *Landslides, analysis and control*. National Academy of Sciences.
- WALD, D. (2009) Per coms.
- WALD, D. J., QUITORIANO, V., HEATON, T. H., KANAMORI, H., SCRIVNER, C. W. & WORDEN, C. B. (1999) TriNet" ShakeMaps": rapid generation of peak ground motion and intensity maps for earthquakes in southern California. *Earthquake spectra*, 15, 537-556.
- WALD, D. J., WORDEN, B. C., QUITORIANO, V. & PANKOW, K. L. (2006) ShakeMap Manual: Technical Manual, User's Guide, and Software Guide. USGS.
- WANG, F., CHENG, Q., HIGHLAND, L., MIYAJIMA, M., WANG, H. & YAN, C. (2009) Preliminary investigation of some large landslides triggered by the 2008 Wenchuan earthquake, Sichuan Province, China. *Landslides*, 6, 1612-5118.
- WANG, H., SASSA, K. & XU, W. (2007) Analysis of a spatial distribution of landslides triggered by the 2004 Chuetsu earthquakes of Niigata Prefecture, Japan. *Natural Hazards*, 41, 43-60.
- WANG, Q., ZHANG, P.-Z., FREYMUELLER, J. T., BILHAM, R., LARSON, K. M., LAI, X. A., YOU, X., NIU, Z., WU, J., LI, Y., LIU, J., YANG, Z. & CHEN, Q. (2001)

References

- Present-Day Crustal Deformation in China Constrained by Global Positioning System Measurements. *Science*, 294, 574-577.
- WANG, Z. (2009) Avalanches, Landslides and Quake Lakes induced by the Wenchuan Earthquake on May 12, 2008. State Key Lab of Hydroscience and Engineering, Tsinghua University: Report.
- WILSON, J. P. & GALLANT, J. C. (2000) *Terrain analysis: principles and applications*, John Wiley & Sons.
- WILSON, R. C. & KEEFER, D. K. (1985) Predicting aerial limits of earthquake induced landsliding. IN ZIONY, J. (Ed.) *Earthquake hazards in the Los Angeles Region - an earth science perspective*. US Geological Survey.
- WMO (2009) World Meteorological Organisation. http://www.wmo.int/pages/index_en.html - accessed 10/07/2009.
- XIAO, D. (2008) Wenchuan 8.0 earthquake intensity distribution map. http://www.cea.gov.cn/manage/html/8a8587881632fa5c0116674a018300cf/_content/08_09/01/1220238314350.html - accessed 10/03/2009. China earthquake administration earthquake emergency rescue division.
- XU, G. & KAMP, P. J. J. (2000) Tectonics and Denudation adjacent to the Xianshuihe fault, eastern Tibetan Plateau: Constraints from fission-track thermochronology. *Journal of Geophysical Research*, 105, 19231-19251.
- YEE, C. S. & HARR, D. R. (1977) Influence of soil aggregation on slope stability in the Oregon Coast Range. *Environmental Geology*, 1, 367-377.
- YIN, K. L. & YAN, T. Z. (1988) Statistical prediction models for slope instability of metamorphosed rocks. *Proceedings of 5th International Symposium on Landslides*. Lausanne, Switzerland Balkema, Rotterdam
- YIN, Y. P., WANG, F. W. & SUN, P. (2009) Landslide hazards triggered by the 2008 Wenchuan earthquake, Sichuan, China. *Landslides*, 6, 139-152.
- YIN, Y. X. (2008) Researches on the geo-hazards triggered by the Wenchuan Earthquake, Sichuan. *Journal of Engineering Geology*, 16, 433-444 (in Chinese).

References

YUAN, Y. (2008) Impact of intensity and loss assessment following the great Wenchuan Earthquake. *Earthquake Engineering and Engineering Vibration*, 7, 247-254.

ZHANG, P.-Z., SHEN, Z., WANG, M., GAN, W., BURGMANN, R., MOLNAR, P., WANG, Q., NIU, Z., SUN, J., WU, J., HANRONG, S. & XINZHAO, Y. (2004) Continuous deformation of the Tibetan Plateau from global positioning system data. *Geology*, 32, 809-812.

ZHANG, Y., FENG, W., XU, L., ZHOU, C. & CHEN, Y. (2009) Spatio-temporal rupture process of the 2008 great Wenchuan earthquake *Science in China Series D: Earth Sciences*, 52, 1862-2801.

ZHIJUN, N., MIN, W., HANRONG, S., JIANZHONG, S., XINZHAO, Y., WEIJUN, G., GUIJIANG, X., JINXIN, H., SHAOHUA, X., YONGQING, W., YONGXIANG, W. & BAI, L. (2005) Contemporary velocity field of crustal movement of Chinese mainland from Global Positioning System measurements. *Chinese Science Bulletin*, 50, 939-941.

ZHISHENG, A., KUTZBACH, J. E., PRELL, W. L. & PORTER, S. C. (2001) Evolution of Asian monsoons and phased uplift of the Himalaya-Tibetan plateau since Late Miocene times. *Nature*, 411, 62-66.

ZHOU, R., LI, Y., DENSMORE, A. L., ELLIS, M. A., HE, Y. & LI, Y. (2007) Active tectonics of the Longmen Shan region of the eastern margin of the Tibetan Plateau. *Acta Geologica Sinica*, 81, 593-604.

Web pages

http://geog.hkbu.edu.hk/virtuallabs/rs/env_backgr_refl.htm [accessed 11/10/2009]

<http://www.fas.org/irp/imint/docs/rst/Sect2/India.jpg> [accessed 06/05/09]

<http://earthquake.usgs.gov/learn/glossary/?term=seismic%20moment> [accessed 12/07/2009]

http://www.ats.ucla.edu/stat/mult_pkg/faq/general/Psuedo_RSquareds.htm [accessed 12/12/2009]